

UNIVERSIDADE DE VIGO

DOCTORAL THESIS

Search for Planetary Nebulae around Hot Subdwarf stars

Analysis and characterization of these peculiar systems

Author:

Alba ALLER EGEA

Supervisors:

Dr. Luis Felipe Miranda Palacios

Dr. Enrique Solano Márquez

Dr. Ana María Ulla Miguel

*A thesis submitted in fulfillment of the requirements
for the degree of Doctor*

in the

Departamento de Física Aplicada

Universidade de Vigo

Vigo, September 2015



Declaración de Autoría

Yo, **Alba ALLER EGEA**, declaro que soy la autora de la tesis doctoral titulada “Búsqueda de nebulosas planetarias alrededor de estrellas subenanas calientes. Análisis y caracterización de estos sistemas peculiares”, la cual presento a depósito para ser defendida y evaluada en sesión pública. Asimismo, confirmo que:

- Este trabajo ha sido realizado en mi candidatura al grado de Doctor por la Universidad de Vigo, bajo la dirección del Dr. Luis Felipe Miranda Palacios, el Dr. Enrique Solano Márquez y la Dra. Ana María Ulla Miguel.
- La tesis doctoral que presento es una obra original e inédita.
- En la realización de este trabajo se han respetado siempre los derechos de autor, proporcionando apropiadamente las fuentes cuando se citan los resultados y publicaciones de otros. Con excepción de dichas citas, el trabajo es enteramente mío.
- Donde esta tesis haya sido fruto del trabajo conjunto con otros investigadores, queda también explícitamente indicado y referenciado.

En Vigo, a 7 de Septiembre de 2015



Alba Aller Egea

Universidade de Vigo

Luis Felipe Miranda Palacios, Doctor en Ciencias Físicas y Científico Titular del Instituto de Astrofísica de Andalucía, Consejo Superior de Investigaciones Científicas

Enrique Solano Márquez, Doctor en Ciencias Matemáticas y Científico Titular del Centro de Astrobiología (INTA-CSIC), y

Ana María Ulla Miguel, Doctora en Ciencias Físicas y Profesora Titular de la Universidad de Vigo,

CERTIFICAN que la presente memoria

Búsqueda de nebulosas planetarias alrededor de estrellas subenanas calientes.

Análisis y caracterización de estos sistemas peculiares

ha sido realizada por la licenciada en Física **Alba Aller Egea** bajo nuestra dirección. Así, consideramos que esta memoria contiene aportaciones suficientes para constituir la Tesis Doctoral de la interesada. Asimismo, AUTORIZAMOS la presentación de la citada Tesis por Alba Aller Egea para optar al título de Doctor con Mención Internacional por la Universidad de Vigo, y bajo la modalidad de compendio de publicaciones, dado que reúne las condiciones necesarias para su defensa.

En Vigo, a 7 de Septiembre de 2015



Luis Felipe Miranda Palacios



Enrique Solano Márquez



Ana María Ulla Miguel

UNIVERSIDADE DE VIGO
TESIS DOCTORAL

**Búsqueda de nebulosas planetarias alrededor
de estrellas subenanas calientes**
Análisis y caracterización de estos sistemas peculiares

Autor:
Alba ALLER EGEA

Directores:
Dr. Luis Felipe Miranda Palacios
Dr. Enrique Solano Márquez
Dra. Ana María Ulla Miguel

*Tesis depositada en cumplimiento de los requerimientos
para la obtención del grado de Doctor*

por la

Universidade de Vigo
Departamento de Física Aplicada

Vigo, September 2015



A mi abuelo, a mis padres y a Jorge

Agradecimientos

Y por fin llegó el momento de escribir estas líneas. Espero que el cansancio de todos estos meses no torpedee las palabras que mi mente quiere dictarme, ya que son muchas las personas a las que quiero dedicar este rincón. Algunos sé que quizás no las leerán pero, aún así, quiero aprovechar este momento para agradecer a toda la gente que ha marcado mi vida y me ha ayudado a llegar hasta aquí. Aquí van...

Empezaré por el principio, por los que siempre han estado allí y seguirán estando. Mi familia. Gracias a mis padres, por todo. Por darme esta vida que aprecio tanto y por inculcarme los valores que ahora tengo. Por enseñarme a no rendirme nunca y el valor del esfuerzo. Por estar siempre, incluso en mis peores momentos (¡que no son pocos!). Por darme la oportunidad de hacer lo que siempre he soñado, aún sabiendo que mis sueños me llevarían lejos de casa. Sabéis mejor que nadie que no todos los momentos han sido buenos pero siempre, siempre, estáis ahí para decirme que todo irá mejor y para recordarme que todas las cosas pasan por algún motivo. Mami, sé que tenerme lejos ha sido y es especialmente duro para ti, porque soy todavía tu niña, y sé que te cuesta muchísimo ir soltando la cuerda de la cometa. Pero también sé que tus malos ratos se pasan cuando piensas que esto es lo que me hace feliz. No te preocupes porque esté donde esté, siempre seguiré siendo tu niña. Gracias de corazón a los dos porque vosotros más que nadie sabéis lo que significa esto para mí.

Gracias también a mi hermano, Gus, que aunque no recuerdo muy bien cómo comenzó todo, estoy segura de que fue él quien me metió el gusanillo del “Universo” en el cuerpo. Sin ti, muy probablemente no estaría escribiendo estas líneas. Has sido siempre y serás un referente para mí y, aunque a veces no nos aguantásemos de pequeños, todo forma parte de la increíble experiencia de tenerte como hermano mayor. Por muchos pajaritos que tengas en la cabeza, no te cambiaría por nadie. Dentro de unos días comienzas una nueva etapa, al lado de una persona maravillosa: Lidia. Gracias también a ti por entrar en mi vida para quedarte. Eres la mejor mujer que podía haber encontrado mi hermano. Gracias a los dos por estar siempre ahí. Os deseo todo lo mejor. Estoy deseando celebrarlo con vosotros por todo lo alto.

Y siguiendo con la familia, no podías faltar tú, muchas gracias Lu. Porque eres mi pri, mi hermana, mi melliza, mi amiga, todo en una persona. Porque toda la vida hemos estado lejos pero es como si estuvieras aquí al lado. Porque has sido y eres mi punto de apoyo. A quien sé que puedo llamar a cualquier hora del día sin ninguna razón y con la que necesito hablar cada vez que me sucede algo nuevo. No sé qué haría sin ti. Millones de gracias por estar siempre ahí. Muchas gracias al resto de los pris (¡no podíais faltar!) y por supuesto gracias también a los *consuertes*. Os adoro a todos, ¡a pesar de que os metáis conmigo sabiendo que voy a entrar al trapo! Gracias Elo, Jesu, Vicky, Dami, Jaco y Vane. Son demasiadas las anécdotas, recuerdos y

momentos que nos han marcado y siempre han sido para bien. Gracias por transmitirme desde pequeña este amor por Galicia que me acompaña allá donde vaya.

Gracias también a mis papis adoptivos, Maribel y Chucho, por acogerme siempre con tanto cariño y por preocuparse siempre de que estuviera bien, sobre todo en Vigo, cuando no me faltaba nunca una llamada. Gracias a mi abuela por ser tan auténtica y muy especialmente a mi abuelo, porque siempre ha sido y será mi persona favorita de este mundo. Hace ya más de 7 años que no estás con nosotros y te has perdido gran parte de mi vida pero para mí es como si siguieras estando. Gracias por los paseos a caballo, por los trucos de cartas (todos los años eran los mismos pero me encantaban), por pedirme que te echara siempre *vino blanco* y por las lágrimas que no te permitían salir a despedirnos cuando nos íbamos cada verano. Has sido una persona clave en mi vida y por eso quería dedicarte este trabajo a ti. Gracias también a mis tíos Manolo y María, que nunca se olvidaban de preguntarme... ¿Qué tenemos nuevo por ahí arriba? Mi familia es demasiado grande como para nombrarlos a todos así que pararé aquí. Gracias a todos, tíos y primos de ambos lados porque todos me aportáis algo en mi vida.

Gracias también a la familia Lillo-Box (la *cosi-family*), que ahora son parte también de mi familia. Gracias por todo el cariño que me habéis dado desde el principio y los ánimos de estos últimos meses, que nunca vienen mal. En especial gracias a mi *cosi-cuñi*, porque eres la alegría personificada y es que es verte y tener una sonrisa en la boca ;)

Por supuesto, gracias a mis tres directores de tesis (sí, ¡tres!), Luis, Enrique y Ana, porque sin ellos estas líneas no tendrían ni un principio ni un final. Gracias Luis y Ana por elegirme a mí y darme la oportunidad de comenzar esta tesis. Y gracias Enrique por darme la oportunidad de continuarla. Gracias a todos por estos largos años de aprendizaje, con momentos buenos, malos, duros y satisfactorios, que de todo ha habido, y en particular gracias por el esfuerzo de estos últimos meses. Muy especialmente, muchas gracias a Luis, por las largas discusiones científicas y por las continuas charlas al teléfono de las que he aprendido tanto, y que me han permitido avanzar en esta etapa.

Gracias a Jorge Losada por la preciosa portada que me has regalado. Es perfecta para cerrar esta tesis, como también lo fue el dibujo de Saturno que me hiciste a carboncillo cuando era una niña y que hoy sigue colgado en mi pared. ¿Quién iba a creer entonces que mi locura por el cielo no era transitoria y que muchos años después estaría escribiendo esta tesis? Me alegro de que formes parte de esto porque al fin y al cabo eres como de la familia. Gracias.

Gracias a mi gente de Zaragoza que ha estado ahí siempre. Gracias a mi Ani por los casi 28 años incondicionalmente a mi lado. Literalmente, toda una vida juntas. Todavía guardo el libro “Astronomía para niños” que me regalaste cuando apenas cumplí los... ¿10 años?. Buf, no sé, ¡hace demasiado tiempo! Creo que nadie más que tú conoce cada rincón de mi cerebro y de mi corazón. Hemos pasado juntas guardería, colegio, instituto, baloncesto, clases de guitarra, mil

y una historias pero siempre juntas. Solo nos ha faltado compartir mesa en la Universidad, y porque tú eres *de letras* y yo *de ciencias* que si no... Porque sigamos tan unidas siempre, a pesar de la distancia con la que ya hemos aprendido a lidiar. Gracias a Carlota, que también ha estado ahí desde el principio. Nos cuesta ponernos de acuerdo para hablar pero cuando lo hacemos es como si no hubiera pasado el tiempo y esa sensación me encanta. Hace más de doce años que nuestros caminos se separaron y seguimos igual que el primer día, así que no tengo duda de que seguirá siendo así. Es increíble la complicidad que tenemos solo con mirarnos. Muchas gracias por todo. Gracias también a mi Sandri, aquí tienes a tu *astronauta flipada* terminando esta etapa, quién te lo diría, ¿eh? Gracias por tus dosis de locura, que nunca faltan.

Gracias a mi salvadora de tortuguis preferida, Prin! Sabes que te seguiremos allá donde vayas. Gracias por ser tan, tan especial. Porque es imposible no quererte más y me encantas. Gracias por la sonrisa que tienes siempre, por los mensajes de ánimo y las llamadas de apoyo. Gracias a San, por todas las risas y momentos (que han sido muchos y los seguirán siendo), ¡aunque estoy segura de que todavía no sabes a qué me dedico! ¡jajaja! Y muchas gracias también a Lari por todos los momentos juntas. Gracias a las tres por compartir conmigo vuestra pasión por el basket.

Y cómo no, a mis guapas epilenses que me cuidaron siempre y crecieron conmigo. Bueno, mejor dicho, yo crecí con ellas. Porque somos muchas y todas y cada una me ha aportado algo. Muchas gracias en especial a mi rubia y a Patri, porque sé que siempre estáis. Gracias a todas y todos, porque es genial pasar tiempo con vosotros, aunque sea de boda en boda, ya que la distancia no permite mucho más. Me encanta que nuestra gran familia siga creciendo!

Gracias a Rachel, por tu compañía en las infinitas horas de estudio en Filosofía, por las canciones que animan, por las moras de energía y por descubrirme a Quique González, entre otros. Y gracias por todas las cenas, cafés, trinas, desayunos o lo que hiciera falta para ponernos al día en mis visitas fugaces a Zaragoza. Siempre tienes un hueco para mí. ¡Ánimo con la tesis!, ahora estoy en condiciones de decir que esto se acaba algún día.

A Larry, Carlos y Eli. De todas las personas que la vida te pone en el camino, el tiempo te deja solo unas pocas. De mi paso por la Uni de Zaragoza sois sin duda vosotros. Gracias a las interminables horas de clase que nos hicieron conocernos cada día un poquito más. Apenas compartimos tres años (¡o incluso dos!) de nuestras vidas pero fueron más que suficiente.

A Canarias, “sol y playa”. A los canarios, los de allí y los de aquí. Porque juntos nos adentramos en este lado oscuro de la Astrofísica. Porque de allí me volví con grandes recuerdos y sobre todo con grandes amigos. Fueron dos años increíbles y en su mayor parte gracias a vosotros. Gracias en especial a Rubo, Zaira, Parda, Andre, Bea, Lore, Eneko e Itzi. Y a todos los demás con los que me crucé en esa maravillosa isla.

A Juan Antonio Belmonte, porque con él comencé en esto que llaman Investigación. Gracias por contagiarme esas ganas de aprender y ese amor por lo que haces. Gracias por darme la oportunidad de trabajar contigo y de sentir lo que se siente al combinar dos de mis pasiones: las civilizaciones antiguas y la astronomía. Espero algún día tener la oportunidad de volver a experimentarlo.

Gracia también a Alicia, cómo olvidarme, que fue un constante apoyo en Vigo, e hiciste las veces de madre cuando hacía falta. Fue genial encontrarte y tenerte en la mesa de al lado! Contarnos nuestros fines los lunes y hacernos tanta compañía todos los días. Fue un placer conocerte y tenerte allí.

A Madrid por devolverme las ganas que algún día perdí. Porque las cosas al final llegan y esto también llegó. Y sobre todo gracias a la gente que encontré aquí. Es el lugar de trabajo perfecto con el que todo el mundo sueña y es gracias a vosotros. De manera especial, gracias a mis compis de despacho, Mario y Bea, por tantos y tantos días de apoyo, trabajo y risas. Va a ser difícil superar esto. Millones de gracias a Bea de manera muy especial. Ya van unos cuantos años. Nos conocimos en nuestra querida isla y la vida nos cruzó unos años más tarde en Madrid. Gracias por las charlas interminables de casi cualquier cosa y el apoyo incondicional. Eres una de esas personas que te encuentras con las que tienes una conexión especial, y espero que podamos seguir contándonos nuestras cosas muchos años más (de momento, espero que el siguiente reencuentro sea en Chile...). Muchas gracias a Benja, por tu siempre dispuesta ayuda, tus ánimos, tus sorpresas, tus libros de Egipto que me esperan para cuando acabe éste al que le he dedicado estos últimos meses. Ha sido y es un placer poder contar contigo. Gracias a todos en general y en particular a Jesús, Irene, Álvaro, Nacho, Paco, Pablo, Natalia, Nuri, Julia y Miri. Gracias también a Mauro por la ayuda prestada en el entendimiento y manejo de los métodos de clasificación descritos en el capítulo 7. Para los profanos en la materia como yo, no es fácil enterarse de esto y tú lo haces siempre fácil con tus ejemplos. Muchas gracias.

Gracias a México lindo y a su gente, que me acogieron con los brazos bien abiertos. Gracias a Roberto por tratarme y cuidarme tan bien durante mi estancia en Ensenada. Mis padres y yo te lo agradeceremos eternamente. Gracias a todos los “planetosos” por los cafés tan agradables en aquel café tan piqui. Mención especial a Paco, Mónica y Carmen (la pipitilla) por sus clases de vocabulario mexicano. Gracias Mally y Tito de corazón por sacar tiempo de debajo de las piedras para pasearme por la linda Ensenada. Gracias Mally porque me llevé de allí una gran amiga. Espero que la vida nos cruce de nuevo algún día. De momento, tendré que volver a Ensenada para comprobar que la gran bandera del puerto no es una leyenda urbana... Muchas gracias también a Lorenzo, es un gusto siempre trabajar contigo. Finalmente, gracias a los Tacos El Zarpazo que marcaron un antes y un después. Por todo y más, gracias a todos por hacer que mi estancia allí fuera tan *chingona*. Desde que volví estoy deseando regresar.

Gracias a la maravillosa gente del Observatorio de Calar Alto. Allí fueron mis primeras observaciones, que no pudieron ser mejores. Siempre que me acuerdo de vosotros lo hago con una sonrisa. Da gusto estar fuera de casa, trabajando, y sentirte como en casa. Y así ha sido siempre que he estado allí. Muchísimas gracias a todo el personal.

Y gracias a ti, Jorge. Te he reservado este párrafo final, pero en realidad estás también al principio y a lo largo de todas estas líneas. Conoces a todas y cada una de las personas de esta lista, sabes lo que significan estas palabras (las que hay escritas y las que no) y eso es, sin duda, porque eres parte fundamental de mi vida. Gracias por estar ahí desde el principio de esta aventura. Sin duda, eres lo mejor que me llevé de Canarias. Gracias por cuidarme y quererme tan bien y por no dejarme tirar nunca la toalla. Gran parte de este trabajo te pertenece, porque has estado ahí siempre para ayudarme, enseñarme, corregirme, y leerte lo que hiciera falta, por muy ocupado que estuvieses. Gracias por las risas, las tonterías, los desayunos, por transmitirme las fuerzas cuando me hacían falta y la serenidad y la calma cuando me faltaban (¡que suele ser a menudo!). Porque contigo todo es mucho más fácil. Gracias por ser el mejor compañero de viaje que jamás hubiera imaginado tener. Y también por ser el mejor compañero de viajes, porque me encanta recorrer mundo contigo y cada escapada es una experiencia. Dentro de poco nos embarcamos en una aventura más, que estoy segura de que, como siempre, será perfecta a tu lado. Porque eres mi equilibrio, mi equipaje... Tú eres mi paracaídas. Millones de gracias.

Y para terminar, gracias a todas las personas que se han cruzado en mi camino en algún momento de mi vida y que de un modo u otro han dejado huella. De todo y de todos se aprende.

Resumen de la tesis en castellano

Hace apenas un año del 250 aniversario del descubrimiento de la primera nebulosa planetaria (NP), la nebulosa *Dummbell* o M27, por Charles Messier en 1764. Sin embargo, no fue hasta unos años más tarde (en 1780) cuando el término *nebulosa planetaria* fue acuñado por primera vez por el astrónomo británico William Herschel. A pesar de su nombre, estos objetos nada tienen que ver con lo que conocemos como planetas. Su origen se debe a que la apariencia de estos objetos difusos era muy similar a la de los planetas gigantes gaseosos del Sistema Solar, como Urano, al ser observados con los telescopios ópticos de la época. Más tarde, el inicio de las observaciones espectroscópicas marcó un antes y un después en el entendimiento de estos fascinantes objetos (al igual que en el resto de los objetos astronómicos). William Huggins obtuvo el primer espectro de una nebulosa planetaria en 1864 (un siglo después del descubrimiento de M27) y fue entonces cuando la naturaleza de estos objetos comenzó a entenderse. Más de otro siglo y medio después podemos decir con absoluta certeza que las nebulosas planetarias se forman al final de la vida de las estrellas de masa baja o intermedia, es decir, aquellas que tienen entre aproximadamente 0.8 y 8 veces la masa de nuestro sol (M_{\odot}). En esta fase, la estrella pierde gran cantidad de masa, expulsando hacia el medio interestelar las capas más externas de su atmósfera. Por esta fase pasarán aproximadamente el 95% de todas las estrellas del Universo. Sin embargo, todavía hoy muchas preguntas acerca de la formación y evolución de estos objetos continúan sin resolver.

Actualmente, el número de nebulosas planetarias que se conocen en nuestra Galaxia es de aproximadamente 3000, aunque se estima que podrían ser muchas más. Esta gran muestra no es ni mucho menos homogénea ya que presentan una gran variedad de formas, tamaños y brillos. La formación de estas estructuras tan variadas y complejas es actualmente un tema de intenso debate. En situaciones normales, esperaríamos que la pérdida de masa de un astro ocurriese de forma radial y homogénea. Sin embargo, lo que vemos es bien distinto. Aproximadamente el 80% de todas las nebulosas planetarias presentan formas no esféricas, lo que implica tener que recurrir a mecanismos de formación que involucran la presencia de estrellas binarias, campos magnéticos o alta rotación estelar. En cualquier caso, las estrellas centrales (así llamadas) que dan lugar a estas nebulosas planetarias juegan un papel fundamental en la formación de las mismas. Sin embargo, no todas las estrellas centrales son iguales. Al contrario, las estrellas centrales exhiben una gran variedad de propiedades como la composición química, la temperatura o la gravedad superficial, lo que se traduce en distintos rasgos espectrales. Esto hace que se les haya clasificado en diferentes tipos espectrales. Entre estos tipos espectrales, encontramos las estrellas subenanas calientes de tipo O (o sdO por sus siglas en inglés), que han sido el objeto de este trabajo.

Las estrellas subenanas calientes se encuentran en una fase previa a las enanas blancas aunque su origen continúa siendo tema de intenso debate desde que se descubrieron en 1947. Se cree que sus progenitores son estrellas de baja masa. En este estado evolutivo se encuentran también todas las estrellas centrales de nebulosas planetarias. Sin embargo, sorprendentemente, solo alrededor de un 3% de las estrellas subenanas calientes que se conocen tienen una nebulosa planetaria a su alrededor. Explicar este bajo porcentaje es todavía una incógnita que aguarda a ser respondida. Las estrellas subenanas calientes se sitúan al final de la Rama Horizontal Extendida en el diagrama Hertzsprung-Russell. Esta zona es un cruce de caminos donde confluyen las trazas evolutivas de estrellas procedentes de la rama de gigantes rojas (o post-RGB, por sus siglas en inglés), de la rama horizontal (o post-HB) y de la rama asintótica de gigantes (o post-AGB). Por eso, saber cuál de estos caminos evolutivos es el que han seguido las estrellas subenanas calientes no es una tarea trivial.

La presencia de nebulosas planetarias alrededor de estas estrellas, implicaría un posible origen post-AGB para estas estrellas. Sin embargo, debido a las finas envolturas de hidrógeno ($< 0.02 M_{\odot}$) que poseen, que hace que su masa total sea prácticamente igual a la masa de su núcleo ($\sim 0.5 M_{\odot}$), se cree que éstas son incapaces de ascender la rama AGB. A pesar de esto, algunas estrellas subenanas calientes, como ya hemos dicho, sí tienen una nebulosa planetaria. Los primeros sistemas NP+sdO descubiertos datan de finales de los años 70 y principios de los 80. Cuatro nebulosas fueron descubiertas entonces alrededor de las estrellas LSS 2018, LSE 125, RWT 152 y LSS 1362. Unos años más tarde, a finales de la década de los 80, varios autores se embarcaron en la búsqueda de más nebulosas planetarias alrededor de estas estrellas, aunque con muy poco éxito. Desde entonces, esta búsqueda (y quizás también el interés por estos sistemas) cesó, principalmente motivado por la falta de nuevas detecciones. Solo unas pocas estrellas centrales de nebulosas planetarias ya conocidas fueron posteriormente catalogadas como sdOs, lo que amplió la muestra a unos 18 sistemas de este tipo.

En esta tesis, investigamos este campo empleando instrumentación moderna y telescopios de mayor tamaño. Nuestra contribución se centra en la búsqueda y análisis de sistemas NP+sdO y presentamos, por primera vez, un estudio conjunto de los sistemas que se conocen de este tipo. El objetivo principal es tratar de obtener características comunes que puedan trazar un mismo escenario de formación para estos sistemas. Además, presentamos un nuevo catálogo actualizado de las nebulosas planetarias que se conocen en nuestra Galaxia, que ha sido construido con la ayuda de las herramientas del Observatorio Virtual. Este catálogo es una contribución fundamental al campo de las nebulosas planetarias ya que actualmente no se dispone de ninguna base de datos donde se pueda consultar toda la población conocida de estos objetos.

Motivación y objetivos de la tesis

Esta tesis nace con el principal objetivo de estudiar las nebulosas planetarias alrededor de estrellas sdOs. Como ya hemos comentado, estas estrellas son precursoras inmediatas de las enanas blancas, sin embargo, su origen y estado evolutivo continúan siendo tema de debate. La razón es que ocupan una zona muy amplia en el diagrama HR, con temperaturas efectivas (T_{eff}) que van desde los $\sim 40\,000$ K hasta más allá de los $100\,000$ K y gravedades superficiales ($\log g$) entre ~ 4.0 y ~ 6.5 , por la que pasan trazas evolutivas de diferentes estrellas. Este amplio abanico de posibilidades y la alternativa de escenarios binarios contribuyen a que no exista una teoría única que explique sus orígenes.

Así pues, la asociación de sdOs con nebulosas planetarias (NPs) es esencial para determinar qué fracción de sdOs podría tener un origen post-AGB. Hasta la fecha, solo se conocen unas pocas sdOs asociadas con NPs. Entre ellas se encuentran las “clásicas” LSE 125 y LSS 2018, LSS 1362 y RWT 152, que son las primeras nebulosas que se descubrieron alrededor de estrellas sdO, así como unos pocos casos de estrellas centrales de NPs que han sido clasificadas como sdOs.

En este contexto, el objetivo principal de esta tesis es dar respuestar a dos cuestiones fundamentales:

- (i) *¿Son o no frecuentes las nebulosas planetarias alrededor de estrellas sdO?. Como ya hemos mencionado, la fracción de sdOs que tienen nebulosa a su alrededor es muy baja ($\sim 3\%$). Sin embargo, si las presuntas nebulosas esperadas alrededor de estos objetos son muy débiles, muchas de ellas no se habrían podido detectar. Por lo tanto, para contestar a esta pregunta es necesario obtener imágenes profundas de un muestra amplia de sdOs, que confirmen o descarten la posible presencia de nebulosas planetarias, y que puedan arrojar luz sobre el posible origen post-AGB de estas estrellas.*
- (ii) *¿Comparten los sistemas NP+ sdO propiedades comunes?. Como un segundo punto, analizar en profundidad y caracterizar todos los sistemas NP+sdO que se conocen para poder estudiarlos en un marco común, es imprescindible. Así, estudiar sus propiedades físicas, abundancias químicas, cinemática, morfología, etc., con el fin de buscar posibles similitudes, puede ayudarnos a trazar el origen y la evolución de estos objetos.*

Metodología

El primer paso que realizamos antes de comenzar nuestra investigación fue una revisión y búsqueda bibliográfica exhaustiva de todos los trabajos realizados anteriormente en el campo

concreto de las estrellas sdOs, nebulosas planetarias y, especialmente, aquellos que trataban ambos objetos conjuntamente. Esto nos permitió definir con precisión cuál era el estado de este campo en el momento de comenzar esta tesis, qué se había investigado, con qué medios, cuáles habían sido los resultados positivos y cuáles las posibles carencias de dichas investigaciones (la mayoría de ellas realizadas en la década de los ochenta). Una de las conclusiones de esta búsqueda bibliográfica fue constatar el bajo número de asociaciones NP+sdO así como la alta dispersión de la información de estos objetos en la bibliografía. Todo ello nos ayudó a establecer el marco concreto de trabajo y planificar la investigación con una aproximación mucho más moderna.

Con el objetivo de comprobar si el número tan bajo de asociaciones NP+sdO era real o, por el contrario, existía algún tipo de sesgo en las observaciones previas, diseñamos un programa de búsqueda sistemática de nebulosas planetarias alrededor de sdOs conocidas basado en imagen directa y espectroscopia de baja resolución en el rango óptico. Este programa se llevó a cabo a lo largo de tres campañas de observación desde tres observatorios diferentes: dos campañas en el Observatorio de Calar Alto (Almería, España), una en el Observatorio de Roque de los Muchachos (La Palma, España) y otra en el Observatorio de Sierra Nevada (Granada, España). Los instrumentos CAFOS, WFC y CCDT150 se utilizaron en cada uno de estos telescopios, respectivamente. En total se observaron 109 sdOs. Estas observaciones se realizaron siguiendo siempre la misma estrategia: obtención de imágenes profundas en los filtros estrechos $H\alpha$ y/o $[O III]\lambda 5007$, líneas típicas de nebulosas planetarias, con el objetivo de detectar emisión procedente de estas bandas. Aquéllos objetos que pudieran presentar signos de emisión difusa en dichas imágenes, eran subsecuentemente observados con espectroscopia (con el instrumento CAFOS) con el objetivo de determinar la naturaleza de dicha emisión.

Además de esta búsqueda de nebulosas planetarias alrededor de sdOs, también obtuvimos imágenes y espectros de algunas de las nebulosas planetarias con estrellas centrales sdOs (tanto confirmadas como probables), con el objetivo de constreñir la naturaleza sdO de estas estrellas. Para este trabajo, los instrumentos CAFOS y WFC fueron utilizados. Estas observaciones fueron complementadas, en algunos de los casos, con espectros de rendija larga de alta resolución obtenidos con el instrumento MES del Observatorio de San Pedro Mártir (Baja California, México). Estos espectros permiten construir los llamados mapas de posición-velocidad, que proporcionan información sobre la cinemática interna y morfología de las nebulosas de una manera muy detallada.

También hicimos uso del instrumento OSIRIS del Gran Telescopio de Canarias, en el Observatorio de Roque de los Muchachos. Este telescopio de clase 10-m nos ha permitido obtener información de la nebulosa RWT 152 (uno de los sistemas NP+sdO) que no es posible obtener con telescopios de clase 2-m. Para ello, obtuvimos imágenes con el filtro sintonizable rojo,

que permite variar la longitud de onda transmitida según se requiera, y espectros de resolución intermedia en todo el rango óptico.

Para la parte más teórica de este trabajo, que fue el análisis espectral de uno de los posibles sistemas NP+sdO con el objetivo de confirmar la naturaleza sdO de su estrella central, hicimos uso de los modelos de atmósferas estelares para estrellas calientes y compactas, desarrollados por el Observatorio Virtual Alemán y accesibles a través del servicio TheoSSA.

Finalmente, también hemos trabajado con datos de archivo para la compilación de un nuevo catálogo de nebulosas planetarias. Esto ha sido posible mediante el uso de las herramientas del Observatorio Virtual, como Topcat, Aladin, etc., que permiten trabajar con enormes cantidades de datos de una manera eficiente y amigable.

Resultados

A continuación resumimos brevemente los principales resultados científicos obtenidos durante esta tesis. Estos resultados se dividen en una búsqueda de sistemas NP+sdO, el análisis y la caracterización de cinco de estos sistemas (uno de ellos aún sin confirmar) y la compilación de un nuevo catálogo de nebulosas planetarias.

- **Búsqueda de sistemas NP+sdO:** En el programa observacional de búsqueda de nuevos sistemas NP+sdO, 109 sdOs fueron finalmente observadas. Esta búsqueda fue complementada con una inspección visual de las imágenes públicas del archivo del telescopio WISE para una muestra de 774 sdOs. WISE proporciona imágenes en el infrarrojo medio en cuatro bandas (desde 3.4 a 22 μm). Estas búsquedas dieron como resultado el descubrimiento de una nueva nebulosa planetaria alrededor de la sdO 2M 1931+4324. Por otro lado, y como resultado de la búsqueda de estrellas centrales sdOs en nebulosas ya conocidas, clasificamos por primera vez la estrella central de la nebulosa planetaria DeHt 2 como sdO y proponemos la misma clasificación para la estrella central de K 2-2.
- **2M1931+4324:** Presentamos la detección esta nueva nebulosa, resultado del programa de búsqueda de nebulosas planetarias alrededor de sdOs. Las imágenes revelan una nebulosa extremadamente débil con una morfología compleja, compuesta de una envoltura bipolar y otra elíptica, cuyos ejes son perpendiculares. Además, también es posible reconocer un filamento exterior a estas estructuras, visible solo en la imagen de [O III], lo que sugiere una alta excitación para el mismo. Las regiones internas de la nebulosa también muestran emisión en el infrarrojo medio (concretamente a 12 μm y 22 μm), según revelan las imágenes de archivo del telescopio espacial WISE. El análisis morfo-cinemático de esta nebulosa, obtenido a partir de espectros de rendija larga de alta resolución, es consistente con la presencia de una cavidad bipolar y otra cilíndrica o elipsoidal, cuyos ejes están

orientados perpendicularmente a la línea de visión. El espectro nebuloso, que solo presenta las líneas de emisión $H\alpha$, $H\beta$ y $[O III] \lambda\lambda 4959,5007$, sugiere una baja excitación para la nebulosa, en contraste con la ausencia de líneas de baja excitación como las de $[N II]$, lo que resulta bastante peculiar, pudiendo sugerir una deficiencia en elementos pesados.

- **Abell 36** Las imágenes de esta nebulosa planetaria presentan una morfología elíptica con dos arcos con simetría puntual. El análisis morfo-cinemático sugiere que varios eventos de eyección pudieron tener lugar en la formación de esta nebulosa planetaria. Proponemos la presencia de una estructura esferoidal inicial que probablemente fue perforado posteriormente por la eyección de dos flujos colimados bipolares y que dieron lugar a los arcos que hoy vemos en las imágenes. Además de las líneas de emisión de hidrógeno y $[O III] \lambda\lambda 4959,5007$, el espectro nebuloso presenta líneas de alta excitación como $He II \lambda 4686$ y $[Ar IV] \lambda\lambda 4711,4740$. La estrella central de Abell 36 ya estaba previamente clasificada como sdO, clasificación que también confirman nuestros espectros estelares.
- **DeHt 2** Las imágenes de esta nebulosa presentan una morfología elíptica con ligeras desviaciones en las regiones polares. Además revelan la existencia de un anillo elíptico que parece estar embebido en la estructura elíptica principal. Las orientaciones de ambas estructuras son bastante diferentes, indicando que el anillo no estaría trazando el plano ecuatorial de la envoltura elíptica principal. El análisis morfo-cinemático de esta nebulosa indica que la formación de la misma ha sido compleja, con al menos dos procesos de eyección diferentes, como el caso de Abell 36. Con el objetivo de explicar los sucesos involucrados en esta formación, proponemos una estructura esferoidal inicial con una región en forma de anillo trazando su plano ecuatorial. Probablemente, una posterior eyección bipolar tuvo lugar, deformando el esferoide original, lo que provocó las protuberancias que ahora vemos en las regiones polares de la envoltura elíptica. Además, el espectro nebuloso presenta las líneas de emisión $H\alpha$, $H\beta$, $[O III] \lambda\lambda 4959,5007$ y $He II \lambda 4686$, sugiriendo una alta excitación. Sin embargo, la ausencia de otras líneas típicas de alta excitación es muy peculiar, sugiriendo una deficiencia en elementos pesados. Por primera vez, clasificamos esta estrella como una sdO, lo que añade un nuevo sistema NP+sdO objeto a los pocos identificados de este tipo.
- **RWT 152:** Por primera vez presentamos una descripción detallada de la morfología de RWT 152. Nuestras imágenes CAFOS/CAHA sugieren una morfología bipolar para esta nebulosa. Esta estructura bipolar es confirmada también por las imágenes posteriores obtenidas con OSIRIS/GTC, las cuales añaden más detalles a esta descripción morfológica. Los lóbulos bipolares están compuestos de pequeñas burbujas o lóbulos menores mientras que una región brillante parece trazar el plano ecuatorial de la nebulosa. Además, la envoltura bipolar aparece rodeada por un débil halo circular desplazado respecto al centro de la nebulosa. El análisis morfo-cinemático derivado de los correspondientes

espectros de alta resolución confirma la morfología bipolar de la nebulosa, aunque con algunas desviaciones, posiblemente consecuencia de las pequeñas burbujas que se observan en las imágenes de OSIRIS. El espectro nebular obtenido con CAFOS solo revela las líneas de emisión $H\alpha$, $H\beta$ y $[O\ III]\ \lambda\lambda\ 4959,5007$, como en el caso de la nebulosa 2M1931+4324, sugiriendo una deficiencia en elementos pesados. Para comprobar dicha deficiencia, obtuvimos espectros con OSIRIS/GTC, que confirmaron la presencia de otras líneas de emisión muy débiles de metales doblemente ionizados (e.g., $[Ne\ III]$, $[Ar\ III]$ and $[S\ III]$) así como de H y $He\ I$. Las bajas abundancias químicas obtenidas y la alta velocidad peculiar derivada para este objeto apuntaría a que RWT 152 es probablemente una nebulosa del disco grueso o del halo, las llamadas nebulosas tipo III o tipo IV, respectivamente.

- **BD+30°623:** Presentamos un análisis espectral de BD+30°623, la estrella central *peculiar* de la nebulosa planetaria NGC 1514. Esta estrella pertenece a un sistema binario compuesto por una estrella fría de tipo A, responsable del espectro de absorción, y una estrella compañera caliente que es la responsable de la fotoionización de la nebulosa y que ha sido clasificada por varios autores como sdO. La presencia de esta compañera caliente es, en muchas ocasiones, apenas perceptible en el espectro óptico lo que dificulta mucho el análisis de ambas componentes. En este trabajo presentamos un nuevo método que hemos desarrollado para el análisis espectral para este tipo de objetos, que nos permite obtener simultáneamente los parámetros atmosféricos de ambas componentes del sistema binario. Esto proporciona, en última instancia, información sobre el origen y el estado evolutivo actual del sistema. A partir del análisis espectral obtenemos que el mejor modelo corresponde a una estrella A0 en la Rama Horizontal con $T_{\text{eff}} = 9850 \pm 150\text{ K}$, $\log g = 3.50 \pm 0.25$ y una estrella caliente con temperaturas entre los 80 000 y los 95 000 K y $\log g \simeq 5.5$. Aunque una naturaleza sdO es la más plausible para la estrella caliente, la determinación de su tipo espectral no ha podido ser determinada con los datos actuales. Este método de análisis nos abre una ventana para poder estudiar sistemas similares.
- **Nuevo catálogo de nebulosas planetarias:** Finalmente, presentamos un nuevo catálogo actualizado de nebulosas planetarias conocidas en nuestra Galaxia. Dicho catálogo será de gran utilidad en el campo ya que el último de este tipo fue publicado en el año 2001 y, desde entonces, el número de nuevos descubrimientos se ha incrementado constantemente. Nuestro catálogo tiene en cuenta estos nuevos hallazgos, la mayoría de ellos resultado de grandes proyectos diseñados para buscar nuevas nebulosas planetarias en nuestra Galaxia. Además de esto, hemos diseñado un método de clasificación de estrellas de diferentes clases. El fin último de este procedimiento era tratar de clasificar la muestra completa de estrellas centrales de nebulosas planetarias incluidas en nuestro catálogo, de una manera automática y utilizando datos de archivo. Aunque los criterios seleccionados para dicha clasificación pudieron aplicarse con éxito a la muestra de entrenamiento de estrellas de campo, encontramos dificultades para aplicar esta técnica a la muestra de

estrellas centrales. Concluimos entonces que la obtención de espectros es crucial para determinar los tipos espectrales de las mismas.

Conclusiones

Los resultados de este trabajo nos han permitido profundizar en el conocimiento de los sistemas NP+sdO, un campo que llevaba prácticamente inexplorado desde finales de la década de los ochenta. Las principales conclusiones de este trabajo son:

- Los sistemas NP+sdO son escasos: solo alrededor de 18 sistemas de este tipo se conocen actualmente, lo que representa menos de un 1% de todas las nebulosas conocidas en nuestra Galaxia. Sin embargo, éste solo es un límite inferior, ya que podría estar sesgado principalmente por dos motivos. En primer lugar, no todas las estrellas centrales de nebulosas planetarias han sido clasificadas espectroscópicamente (apenas un 13% lo han sido), por lo que otras sdOs podrían formar parte de la muestra de estrellas centrales que aún está por identificar. En segundo lugar, la debilidad intrínseca de las nebulosas planetarias eyectadas por sdOs, podría reducir de manera considerable la fracción de detección de las mismas, debido a la necesidad de imágenes muy profundas para su detección.
- Si la evolución de las sdOs se produce muy lentamente, como esperamos para estrellas de muy baja masa, la nebulosa planetaria eyectada podría haberse disipado en el medio interestelar mucho antes de que la estrella central hubiera alcanzado la suficiente temperatura como para ionizarla. Por lo tanto, dichas estrellas podrían haber pasado ya por la fase de nebulosa planetaria pero sin embargo, no hubieran sido detectadas. Esta evolución extremadamente lenta sería compatible con las altas latitudes galácticas a las que se encuentran estos objetos, ya que esta localización implica que son objetos muy viejos desde el punto de vista evolutivo.
- El estudio detallado llevado a cabo en esta tesis de algunos de los sistemas NP+sdO que se conocen, nos ha permitido estudiar por primera vez las características de estos sistemas en un marco común y extraer conclusiones sobre su formación y origen. Encontramos que la mayoría de las nebulosas tienen un bajo brillo superficial y que se encuentran en un estado evolutivo avanzado. Además, presentan morfologías bipolares y/o elípticas, revelando también otras estructuras complejas así como signos de eyecciones colimadas. Por lo general, sus espectros nebulares sugieren una posible deficiencia de elementos pesados. Finalmente, una alta fracción de estos objetos pertenecen (o podrían pertenecer) a sistemas binarios. Estudios detallados como los llevados a cabo en esta tesis para todos los objetos de la muestra, nos permitiría confirmar estas posibles propiedades para poder trazar el camino evolutivo de estas estrellas.

Abstract

About 95% of all stars in the Universe come from low- and intermediate- mass progenitors ($0.8 \leq M/M_{\odot} \leq 8$). Most of these stars (including our Sun) will pass through the planetary nebula (PN) phase before ending their lives as white dwarfs. Therefore, studying their formation and evolution is crucial to understand the whole process of stellar evolution. From the discovery of the first PN in 1764, the number of PN detected has been continuously increasing. Currently, there are roughly 3000 confirmed or probable PNe in the Milky Way. They have been extensively studied in the last decades although many aspects of these amazing objects still remain not fully understood. They exhibit a wide variety of morphologies and properties, what seems to be closely related to the evolution of their central stars (CSs). For this reason, the study of PNe also requires a high knowledge of the properties of these CSs.

This thesis is focused on the study of PNe with hot subdwarf O-type (sdO) CSs. sdOs are blue, low-mass stars evolving towards the white dwarf phase, although their origin remains unknown. Their progenitors could be, among others, post-Asymptotic Giant Branch (AGB) stars. Thus, investigating the association of sdOs with PNe is essential to establish the fraction of sdOs with a post-AGB origin. We have found that, currently, only 18 objects have a reliable classification as PN+sdO systems in the literature. This low fraction could be a consequence of the very slow evolution expected for sdOs, which would make difficult the detection if the presumed ejected PNe had been dissipated before being photoionized by the CS. In this thesis, we perform a systematic search for new PNe around a large sample of sdOs in order to determine how frequent these systems are. In addition, we carry out an analysis and characterization of some of these systems, which allows us to obtain information about their morphology, internal kinematics, stellar properties and/or chemistry. All this information is crucial in order to trace the origin and evolution of these systems.

The work performed during this thesis resulted in the discovery of a new PN+sdO system. In addition, the detailed analysis carried out for this and other PN+sdO systems has allowed, for the first time, studying their properties in a common framework. Our results suggest that most of them show common characteristics: they are generally evolved PNe, show complex morphologies with very low surface brightness, and host binary central stars. In addition, some of their nebular spectra suggest a possible deficiency in heavy metals. Finally, we also present a new catalogue of Galactic PNe that has been compiled during this thesis. All these results are extensively described and discussed along this dissertation.

*El pueblo de mi padre dice que cuando nacieron el Sol y su hermana la Luna su madre murió.
El Sol le ofreció a la Tierra el cuerpo de su madre del cual surgió la vida y de su pecho extrajo
las estrellas y las lanzó hacia el cielo nocturno en memoria de su espíritu.*

El último mohicano (1992)

Contents

Declaración de Autoría	iii
Autorización de los directores	v
Agradecimientos	xi
Resumen de la tesis en castellano	xvii
Contents	xxix
List of Figures	xxxiii
List of Tables	xxxv
Acronyms & Abbreviations	xxxvii
Symbols	xxxix
Physical Constants	xli
1 Introduction	1
1.1 The life of an ordinary star: birth and evolution	1
1.2 Planetary nebulae phase: the chronicle of a death foretold	4
1.2.1 Physics in PNe	5
1.2.2 PN Morphology	9
1.2.3 Models for the formation of PNe	10
1.2.4 Central stars of planetary nebulae	13
1.3 Hot subdwarf stars: why not ordinary stars?	15
1.3.1 Properties of hot subdwarf stars	16
1.3.2 Spectral classification and analysis	18
1.3.3 Formation and evolution channels for hot subdwarfs	20
1.3.3.1 Canonical HB and post-HB evolution	20
1.3.3.2 Hot He-flashers in the post-RGB	22
1.3.3.3 Binary scenarios for hot subdwarf evolution	23

1.4	Putting in common Planetary Nebulae and Hot Subdwarf stars	25
1.5	Motivation and structure of this thesis	26
2	Searching for Planetary Nebulae around sdOs	29
2.1	Previous work in the field: 1978-1989	29
2.2	Search for new PNe around sdOs in the optical range	31
2.2.1	Sample selection	31
2.2.2	Optical observations and data reduction	33
2.3	Hints of possible PNe around sdOs in infrared wavelengths	38
2.4	Search for sdO central stars in known PNe	42
2.5	Discussion	48
2.6	Summary and outcomes of this chapter	48
3	Detection of a multishell planetary nebula around the sdO 2M1931+4324	51
3.1	Introduction	51
3.2	Observations and results	52
3.2.1	Optical imaging	52
3.2.2	Mid-infrared imaging	53
3.2.3	Intermediate-resolution optical spectroscopy	55
3.2.3.1	The stellar spectrum of 2M1931+4324	55
3.2.3.2	The stellar spectral energy distribution: from g band to WISE	56
3.2.3.3	The nebular spectrum	57
3.2.4	High-resolution spectroscopy	59
3.3	Discussion	63
3.4	Summary and outcomes of this chapter	65
4	The physical structure of planetary nebulae around sdO stars: Abell 36, DeHt 2, and RWT 152	67
4.1	Introduction	67
4.2		68
4.2.1	Optical imaging	68
4.2.2	Spectroscopy	69
4.2.2.1	High-resolution long-slit spectroscopy	69
4.2.2.2	Intermediate-resolution, long-slit spectroscopy	70
4.3	Results	70
4.3.1	Abell 36	70
4.3.1.1	Imaging	70
4.3.1.2	High-resolution, long-slit spectroscopy	72
4.3.1.3	Intermediate-resolution, long-slit spectroscopy	75
4.3.2	DeHt 2	76
4.3.2.1	Imaging	76
4.3.2.2	High-resolution, long-slit spectroscopy	78
4.3.2.3	Intermediate-resolution, long-slit spectroscopy	79
4.3.3	RWT 152	81
4.3.3.1	Imaging	81
4.3.3.2	High-resolution, long-slit spectroscopy	81
4.3.3.3	Intermediate-resolution, long-slit spectroscopy	83

4.4	Discussion	84
4.5	Summary and outcomes of this chapter	87
5	Observations of RWT 152 with OSIRIS/GTC	91
5.1	Introduction	91
5.2	Observations and data reduction	92
5.2.1	Optical imaging	92
5.2.2	Intermediate-resolution, long-slit optical spectra	94
5.3	Results	95
5.3.1	Morphology	95
5.3.2	The optical spectrum: physical conditions and chemical abundances	96
5.4	Discussion	100
5.5	Summary and outcomes of this chapter	104
6	Spectral analysis of BD+30° 623, the peculiar binary central star of the planetary nebula NGC 1514	107
6.1	Introduction	107
6.2	Observations and results	108
6.2.1	Intermediate-resolution optical spectra	108
6.2.2	Low-resolution ultraviolet spectra	111
6.3	Synthetic stellar spectra	111
6.4	Spectral analysis	113
6.4.1	Composite models	113
6.4.2	Parameters of the cool component	114
6.4.3	First filter: UV continuum and Balmer jump	116
6.4.4	Second filter: optical continuum and He II λ 5412	118
6.4.5	Reassessment of the parameters of the cool star	118
6.4.6	Final results for the hot star	118
6.4.7	Extinction	119
6.5	Discussion	120
6.6	Summary and outcomes of this chapter	124
7	An updated catalogue of Galactic Planetary Nebulae by means of VO tools	127
7.1	Introduction	127
7.2	The PN Catalogue: gathering data from archives	129
7.3	Classification of CSPNe	132
7.3.1	The machine-learning algorithms	133
7.3.2	Application and validation of the methods	135
7.3.2.1	The field star sample	135
7.3.2.2	Selection criteria	136
7.3.2.3	Results of the classification for the field star sample	138
7.3.3	Our case study: classification of CSPNe	139
7.3.3.1	The CSPNe sample	139
7.3.3.2	Selection criteria	140
7.3.3.3	Results of the classification for the CSPNe sample	141
7.4	Summary and outcomes of this chapter	142
8	Conclusions and Future Work	145

8.1	General Conclusions	145
8.2	Future prospects	147

List of Publications	151
-----------------------------	------------

Bibliography	153
---------------------	------------

List of Figures

1.1	Evolutionary track for a star with an initial mass of $2 M_{\odot}$	2
1.2	Scheme of the internal structure of an AGB star	3
1.3	Example of infrared and optical spectra of PNe	6
1.4	Scheme for excitation class of PNe	7
1.5	Energy level diagrams for [O III] and [N II] (left) and [O II] and [S II] (right)	8
1.6	Example of different morphologies and structures in PNe	10
1.7	Sketch of the possible mechanisms involved in the formation of PNe	12
1.8	Scheme of the possible evolutionary channels for H-deficient CSPNe from the AGB phase to the white dwarf sequence	14
1.9	Sketch of a HR-diagram showing the position of sdOs and sdBs	16
1.10	Comparison of typical spectra of sdB and He-sdO stars	19
1.11	Possible post-HB evolution channels for different envelope masses.	21
1.12	Evolutionary tracks for different mass-loss rates.	24
2.1	Snapshot of the Subdwarf Database query form	32
2.2	Location of CSPNe and sdOs above post-AGB evolutionary tracks	33
2.3	Galactic distribution of PNe and sdOs	34
2.4	WISE relative response per photon	38
2.5	NGC 1514 as seen in infrared and optical wavelengths	39
2.6	W2, W3, and W4 images of sdOs with hints of nebular emission	40
2.6	Continued.	41
2.6	Continued.	42
2.7	Normalized spectra of some PN+sdO systems	44
2.8	H α images, WISE images, and nebular spectra of Abell 63, NGC 1360 and K 2-2	46
2.9	[O III] images and CS spectra of Be UMa (top) and HFG 1 (bottom)	47
3.1	H α and [O III] images of 2M1931+4324	53
3.2	WISE 2, WISE 3, and WISE 4 images of 2M1931+4324	53
3.3	Colour-composite image of PN G 075.9+11.6	54
3.4	CAFOS CAHA spectra of the CS 2M1931+4324	55
3.5	Spectral energy distribution of 2M1931+4324	57
3.6	Light and radial velocity curves of 2M1931+4324.	58
3.7	CAFOS CAHA nebular spectra of PN G 075.9+11.6.	59
3.8	Simulated high-resolution, long-slit spectra constructed from specific image+slit configurations.	61
3.9	PV maps derived from the high-resolution, long-slit H α spectra of 2M1931+4324	62

4.1	H α and [O III] images of Abell 36	71
4.2	PV maps derived from the high-resolution, long-slit [O III] spectra of Abell 36	71
4.3	Sketch of Abell 36 as derived from our morphokinematical analysis	73
4.4	Nebular spectrum of Abell 36	76
4.5	Normalized optical spectrum of the CS of Abell 36	76
4.6	H α and [O III] images of DeHt 2	77
4.7	PV maps derived from the high-resolution, long-slit [O III] spectra of DeHt 2	77
4.8	Sketch of DeHt 2 as derived from the morphokinematical analysis	79
4.9	Nebular spectrum of DeHt 2	80
4.10	Normalized optical spectrum of the CS of DeHt 2	81
4.11	H α and [O III] images of RWT 152	82
4.12	PV maps derived from the high-resolution, long-slit [O III] spectra of RWT 152	82
4.13	Nebular spectrum of RWT 152	84
4.14	Normalized optical spectrum of the CS of RWT 152	86
5.1	OSIRIS/GTC field of view for tunable filter mode	93
5.2	Transmission curves of the OS filter	94
5.3	Grey-scale reproductions of the OSIRIS/GTC H α image of RWT 152	96
5.4	RTF image with the optical centre at $\lambda_6=6600 \text{ \AA}$	97
5.5	OSIRIS/GTC spectrum of RWT 152 in the spectral range 3800–7250 \AA	98
5.6	Plot of $12+\log(S/H)$ vs $12+\log(O/H)$ for different Peimbert types of PNe	101
5.7	Position of RWT 152 in the $\log g - T_{\text{eff}}$ diagram	102
6.1	[O III] image of NGC 1514	109
6.2	CAFOS CAHA blue spectrum of BD+30°623	110
6.3	IUE-SWP spectra of BD+30°623	112
6.4	Flow chart with all the steps of the fitting procedure	115
6.5	Best fit to the observed spectrum of BD+30°623	117
6.6	Fitting of the observed absorption lines used for the spectral analysis	117
6.7	Location of the hot component on the post-AGB evolutionary tracks	121
6.8	Location of the cool component on the evolutionary tracks	122
7.1	Snapshot of our catalogue of Galactic PNe available in the webpage	131
7.2	Galactic latitude distribution of our catalogue as compared with previous compilations	132
7.3	Examples of kernel functions available in support vector machines methods	133
7.4	Examples of graphics constructed with Bayesian Networks	134
7.5	Reduced proper motion diagram for the field star sample	136
7.6	Colour-colour diagrams from 2MASS photometry for the field star sample	137
7.7	Galactic distribution of the field star sample	138
7.8	Reduced proper motions diagram for CSPNe training sample	140
7.9	Colour-colour diagrams from 2MASS photometry for the CSPNe training sample	141
7.10	Galactic distribution of CSPNe training sample	142
8.1	Deep nebular spectra of PN Abell 36 and DeHt 2	148
8.2	Slit positions used for high-resolution, long-slit spectra of NGC 1514	150
8.3	PV maps derived from the high-resolution, long-slit spectra of NGC 1514	150

List of Tables

2.1	Summary of the observational campaigns	35
2.2	Summary of imaging observations.	36
2.2	continued.	37
2.2	continued.	38
2.3	Confirmed and possible PN+sdO systems compiled from the literature	43
3.1	Emission line intensities in PN G 075.9+11.6.	60
4.1	Main information of CSPNe Abell 36, DeHt 2, and RWT 152	68
4.2	Emission line intensities in Abell 36.	75
4.3	Emission line intensities in DeHt 2.	80
4.4	Emission line intensities in RWT 152.	85
4.5	Properties of PN+sdO systems	89
5.1	Emission line intensities in RWT 152	99
5.2	Mean ionic abundances relative to H ⁺ of RWT 152.	100
5.3	Elemental abundances of RWT 152	100
6.1	List of the IUE spectra used for the spectral analysis of BD+30°623	113
6.2	Spectroscopic solutions derived for the hot component of BD+30°623	119
6.3	Stellar parameters of the two components of BD+30°623.	120
7.1	Previous catalogues used for the preparation of our catalogue of PNe	129

Acronyms & Abbreviations

2MASS	T wo M icron A ll S ky S urvey
AGB	A symptotic G iant B ranch
CAFOS	C alar A lto F aint O bject S pectrograph
CAHA	C entro A stronómico H ispano A lemán
CE	C ommon E nvelope
CSPN	C entral S tar of P lanetary N ebula
E-AGB	E arly A symptotic G iant B ranch
EHB	E xtrême H orizontal B ranch
ESO	E uropean S outhern O bservatory
FOV	F ield O f V iew
FWHM	F ull W idth H alf M aximum
GTC	G ran T elescopio C anarias
HB	H orizontal B ranch
INT	I saac N ewton T elescope
IRAF	I mage R eduction and A nalysis F acility
IUE	I nternational U ltraviolet E xplorer
MIDAS	M unich I mage D ata A nalysis S ystem
NLTE	N on- L ocal T hermodynamic E quilibrium
ORM	O bservatorio R oque de L os M uchachos
OSIRIS	O ptical S ystem for I maging and low- I ntermediate- R esolution I ntegrated S pectroscopy
OS	O rders S orter
OSN	O bservatorio de S ierra N evada
PA	P osition A ngle
PN	P lanetary N ebula

PV-map	P osition- V elocity map
RGB	R ed G iant B ranch
SED	S pectral E nergy D istribution
sdB	H ot S ub D warf B -type star
sdO	H ot S ub D warf O -type star
SDSS	S loan D igital S ky S urvey
SPM	S an P edro M ártir
SVO	S panish V irtual O bservatory
TF	T unable F ilter
TMAP	T übingen M odel A tmosphere P ackage
TP-AGB	T hermally P ulsing A symptotic G iant B ranch
UV	U ltra V iolet
VO	V irtual O bservatory
WD	W hite D warf
WFC	W ide F ield C amera
WR	W olf R ayet
WISE	W ide- F ield I nfrared S urvey E xplorer
ZAHB	Z ero A ge H orizontal B ranch

Symbols

Symbol	Description	Units
b	Galactic latitude	degrees
l	Galactic longitude	degrees
$c(\text{H}\beta)$	Logarithmic extinction coefficient	dex
M	Stellar mass	M_{\odot}
R	Stellar radius	R_{\odot}
L	Stellar luminosity	L_{\odot}
N_e	Electron density	cm^{-3}
T_e	Electron temperature	K
$\log g$	Surface gravity	dex (cm s^{-2})
T_{eff}	Effective temperature	K
V_{sys}	Systemic radial velocity	km/s
$E(B-V)$	Colour excess	magnitude
A_V	Extinction coefficient	magnitude

Physical Constants

Speed of Light	c	$=$	$2.997\,924\,58 \times 10^8 \text{ m s}^{-1}$
Gravitational constant	G	$=$	$6.6742799 \times 10^{-11} \text{ m}^3 \text{ kg}^{-1} \text{ s}^{-2}$
Solar radius	R_{\odot}	$=$	$6.9634202 \times 10^8 \text{ m}$
Solar mass	M_{\odot}	$=$	$1.9891001 \times 10^{30} \text{ kg}$
Solar luminosity	L_{\odot}	$=$	$3.846 \times 10^{33} \text{ erg s}^{-1}$

On the evening of the 29th of August, 1864, I directed the telescope for the first time to a planetary nebula [...] I looked into the spectroscope. No spectrum such as I expected! A single bright line only! At first, I suspected some displacement of the prism [...] then the true interpretation flashed upon me. [...] The riddle of the nebulae was solved. The answer, which had come to us in the light itself, read: Not an aggregation of stars, but a luminous gas.

William Huggins, "The New Astronomy: A Personal Retrospect", Nineteenth Century, 41 (1897), pp. 916-17.

Introduction

Planetary nebulae (PNe) are one of the most photogenic objects in the Universe. These wonderful and astonishing objects have fascinated astronomers during many decades. The first PN discovered was the Dumbbell Nebula (M27), by Charles Messier in 1764, although the term “planetary nebula” was coined some time later by William Herschel, in the 1780s. This term is certainly not appropriate since this type of objects have nothing to do with planets; Herschel proposed this name due to the appearance of these objects with his recent discovery of the planet Uranus. Since these first discoveries, the number of detected PNe has been increasing in leaps and bounds. However, one year after the 250th anniversary of the discovery of the first PN, many questions about the nature and formation of these objects remain open. It is clear that their central stars play an important role in their evolution. Among the wide variety of types of central stars that one can find in PN nuclei, hot subdwarf stars are of special interest due to the very small number of known hot subdwarf stars that have associated a PN. In this chapter, a brief review on stellar evolution of low- and intermediate-mass stars will be introduced, since it is the natural starting point to understand how both planetary nebulae and hot subdwarf stars are formed. The joint study of these two *a priori* different objects can provide clues to understand their origin and evolution.

1.1 The life of an ordinary star: birth and evolution

The evolution and fate of a star is inevitably determined by its initial mass. Briefly, if the star has an initial low- or intermediate mass, i.e., between approximately 0.8 and $8 M_{\odot}$, it will evolve slowly until becoming a planetary nebulae (PNe) and definitively cooling down. On the contrary, if the initial mass of the star is higher than $\sim 8 M_{\odot}$, it will experience a short and hectic life and finally a violent death in the form of supernova explosion. We will focus our attention on the former group since they will be the subject matter of this work.

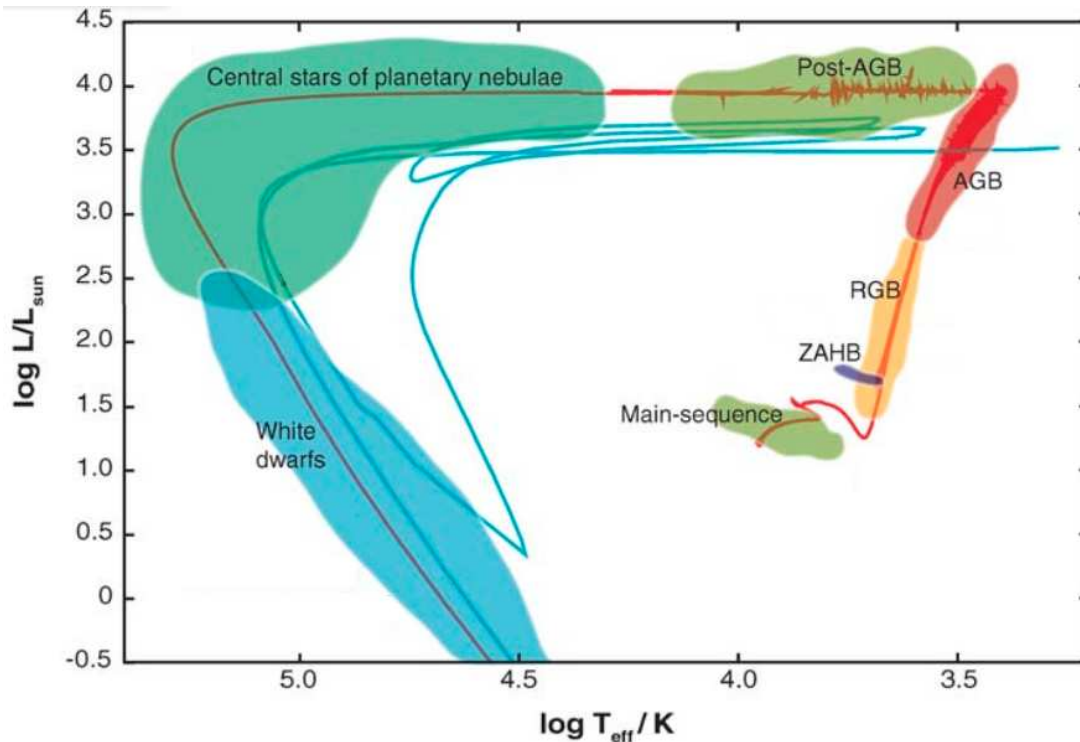


FIGURE 1.1: Evolutionary track for a star with an initial mass of $2 M_{\odot}$ for solar metallicity. The blue track shows a born-again evolution (see Sect. 1.2). The colour clouds mark the different phases of the evolution of a low- and intermediate-mass star, from the main-sequence (in green) to the white dwarf cooling sequence (in blue). Image credit: Herwig (2005)

Figure 1.1 shows the evolutionary track followed by one of these stars (specifically a star with an initial mass of $2 M_{\odot}$) in the $\log(L/L_{\odot})$ versus $\log T_{\text{eff}}$ diagram, i.e., in the Hertzsprung-Russell (HR) diagram. The life of the star will be a constant fight between the radiation pressure, resulting from the internal energy generated by nuclear reactions, and the gravitational contraction. After the star forms in a molecular cloud, it will enter in the so-called main-sequence where the star will pass most of its life. This phase is characterized by hydrogen (H) burning in the core in hydrostatic and thermal equilibrium. When all the hydrogen fuel in the core is exhausted and transformed into helium (He), the core begins to contract since there is no radiation pressure to support the gravitational collapse.

The core continues to contract and, in order to maintain the thermal equilibrium, the envelope expands according to the mirror principle. This causes an increment of the radius and a decrement of the effective temperature. This contraction of the core increases the star's central temperature enough to move H fusion into a shell surrounding the core. The star moves to the right in the HR diagram (lower T_{eff} , higher L), along the so-called sub-giant branch, to settle on the base of the Red Giant Branch (RGB). As a consequence of the H-burning in the shell, the core grows in mass, the luminosity also grows and the star climbs up the RGB. Meanwhile, the core continues to contract until it reaches the temperature required to ignite He fusion in the core by means of the triple-alpha (3α) process, in which three ${}^4\text{He}$ nuclei (i.e., alpha particles) are transformed

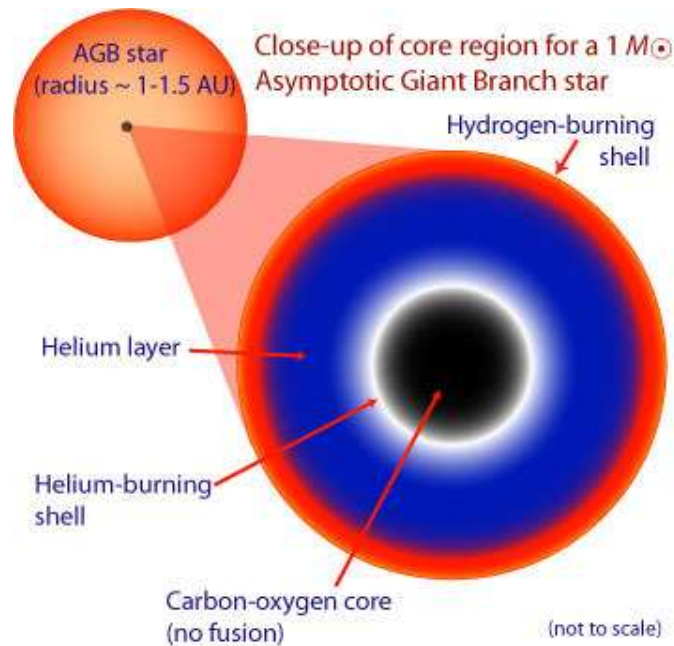


FIGURE 1.2: Scheme of the internal structure of an AGB star. Credits: <http://www.atnf.csiro.au/>.

into carbon. This He-burning phase, however, will start in a different way depending on the initial mass of the star. If the initial mass is lower than $\sim 1.8 M_{\odot}$, its core will become electron-degenerate when it reaches the tip of the RGB. Then, the He-burning will start with a He flash, in which a very quick and violent nuclear fusion of the He is produced. By contrast, if the star has an initial mass higher than $1.8 M_{\odot}$, the He-burning in the core will start in a non-violent way.

After these episodes, the star will enter in the zero-age horizontal branch (ZAHB) where He burning in the core is produced in a stable way. This phase is also known as the *helium-burning main-sequence* for its similarities with the *normal* main-sequence, in which the hydrogen is being burned. The location of a star at this point strongly depends on its metal content. Those with a high metallicity will occupy a close region to the RGB, called *red clump*. In contrast, stars with lower metal content will sit in the HB. Although both clump giants and HB stars are fusing helium to carbon in their cores, their different structures result in different types of stars in terms of radii, effective temperatures and colour. Therefore, the position of stars on the HB also depends on other factors such as their envelope mass. Thus, depending on the size of the H-envelope, the star will occupy different regions in the ZAHB (bluewards or redwards in the HR diagram), but having almost constant luminosity (this will be discussed in further detail in Sect. 1.3). In this stage, the star has now two sources of energy generation: He is being fused into carbon (C) and oxygen (O) in the core while H is being fused in a shell.

After the He core exhaustion, the star will not have the required gravitational energy to trigger the fusion of C and O. Thus, core fusion will no longer take place in the remaining life of

these stars. As in the RGB phase, the contraction of the core will result in an expansion of the outer layers, causing a decrease of the effective temperature and an increment of the radius and luminosity of the star. On the other hand, the heating from the C/O core is high enough to ignite the He in a surrounding shell. The star moves upwards in the HR-diagram along the Asymptotic Giant Branch (AGB). At this stage, the structure of the star consists (from the nucleus outwards) of an inert C/O core, an He-burning concentric shell, an He layer, an H-burning shell, and finally, an outer H convective envelope (see Figure 1.2).

The AGB phase can be divided into two phases: the early-AGB (E-AGB) phase and the thermally-pulsing AGB (TP-AGB) phase. During the E-AGB phase, the H-burning shell remains inactive being the He-burning shell the only energy source in the star. The He-burning adds mass to the C/O core, increasing the density until becoming degenerate. Eventually, when the burning shells are thin enough, the burning becomes unstable and the star enters the TP-AGB phase, where the H- and He- shells are burning intermittently, mixing material from the shells to the convective envelope. In this last phase, the star undergoes a heavy mass loss of $\dot{M} \sim 10^{-4}$ - $10^{-5} M_{\odot} \text{ yr}^{-1}$ led by a slow wind ($v_{exp} \sim 10$ - 15 km s^{-1}), which induces the star to lose more than 50% of its mass. Almost all the H-envelope is rapidly removed as a consequence of this *superwind*¹, determining the end of the AGB phase. This stage will therefore determine the final mass of the star as well as the maximum luminosity to be reached. The timescales of the thermal pulses strongly depend on the mass loss rate of the star.

It is worth noting that the AGB phase is the more important factory for the production of elements in low- and intermediate-mass stars. In this phase, the nucleosynthesis leads to the production of carbon, nitrogen, neon, sodium, and magnesium, among others (see, e.g., Karakas, 2010a). The mixing convection episodes bring the new synthesized elements from the core to the envelope, and finally these elements are expelled to the interstellar medium through strong winds. Thus, AGB stars provide a fundamental source of chemical enrichment for the Universe.

1.2 Planetary nebulae phase: the chronicle of a death foretold

During the post-AGB phase, where H is burning in a shell, the remnant central star (CS) decreases in radius at almost constant luminosity, reaching higher effective temperatures. As a consequence, the star moves leftwards in the HR-diagram (see Fig. 1.1). In this phase the mass loss does not cease but decreases abruptly until values of $\dot{M} \sim 10^{-8} M_{\odot} \text{ yr}^{-1}$.

Simultaneously, the CS develops a very fast wind ($\sim 1000 \text{ km s}^{-1}$), which interacts with the fossil superwind from the AGB phase, forming a compressed optically thin shell. When the CS reaches a $T_{\text{eff}} \geq 30000 \text{ K}$, the high energy of its ultraviolet (UV) photons is able to ionize

¹The term *superwind* refers to the large amount of material ejected, not to the velocity of the wind.

the envelope. We can now say that a new PN has been born. The typical timescales for the post-AGB phase is really short as compared with the rest of evolution. After $\sim 10^4$ yrs, the nebula will have been dissipated in the interstellar medium. Finally, when the H-burning shell is extinguished (for $T_{\text{eff}} \sim 10^5$ K), the luminosity starts to drop and the remnant of the star starts to cool down until becoming a white dwarf.

Although the evolution described above is the usual one for most of the stars, there are some cases in which the evolution of the star is truncated by several reasons (generally not well understood yet). In some cases, and as we will see later, the star can experience a last thermal pulse (also called late He-flash) during the post-AGB phase or the white dwarf cooling sequence, activating the fusion of the He again (Iben et al., 1983). This can temporarily bring the star back to the AGB, evolving again to the post-AGB phase but this time driven by the combustion in the He-burning shell. This “second life” is also known as *born-again* scenario (see Section 1.2.4). In other cases, the very low-mass stars (those with $\lesssim 0.55 M_{\odot}$ in the ZAHB) cannot ascend the AGB due to their thin H envelopes after the RGB phase and evolves along different channels, sometimes having a late He-core flash, analogous to that in the post-AGB phase, after departure from the RGB.

About 95% of all stars in the Galaxy are born with low- and intermediate mass (Kwok, 2004, Werner, 2010). Therefore, it is expected that most of these stars (including our Sun) will pass through the PN phase before ending their lives as white dwarfs. Nowadays, according to Frew & Parker (2010), there are more than 3000 confirmed or probable PNe in the Milky Way. However, this number is really low as compared with the theoretical Galactic PN population estimates. As an example, Frew & Parker (2006) predicted a total number of $28\,000 \pm 5\,000$ and Moe & De Marco (2006) estimated $46\,000 \pm 13\,000$ with radii < 0.9 pc. By contrast, if it is assumed that close binaries are required to form PNe (see below), the number falls until 6 600, within a factor of 3 uncertainty according to De Marco & Moe (2005).

1.2.1 Physics in PNe

- **The nebular spectrum**

The first spectrum of a PNe was taken in 1864 by the English astronomer William Huggins. The nature of these objects was then unveiled. He observed the PN NGC 6543, the *Cat's Eye Nebula*, and found a very different spectrum than expected. Instead of a continuum spectrum with absorption lines, typical of stars, the spectrum showed a bright emission line at about 5007 \AA . This emission line did not correspond to any familiar element at that time so it was assigned to a new hypothetical element, named *nebulium*. It was only in the early 20th century, when this line was identified by Ira Bowen and his

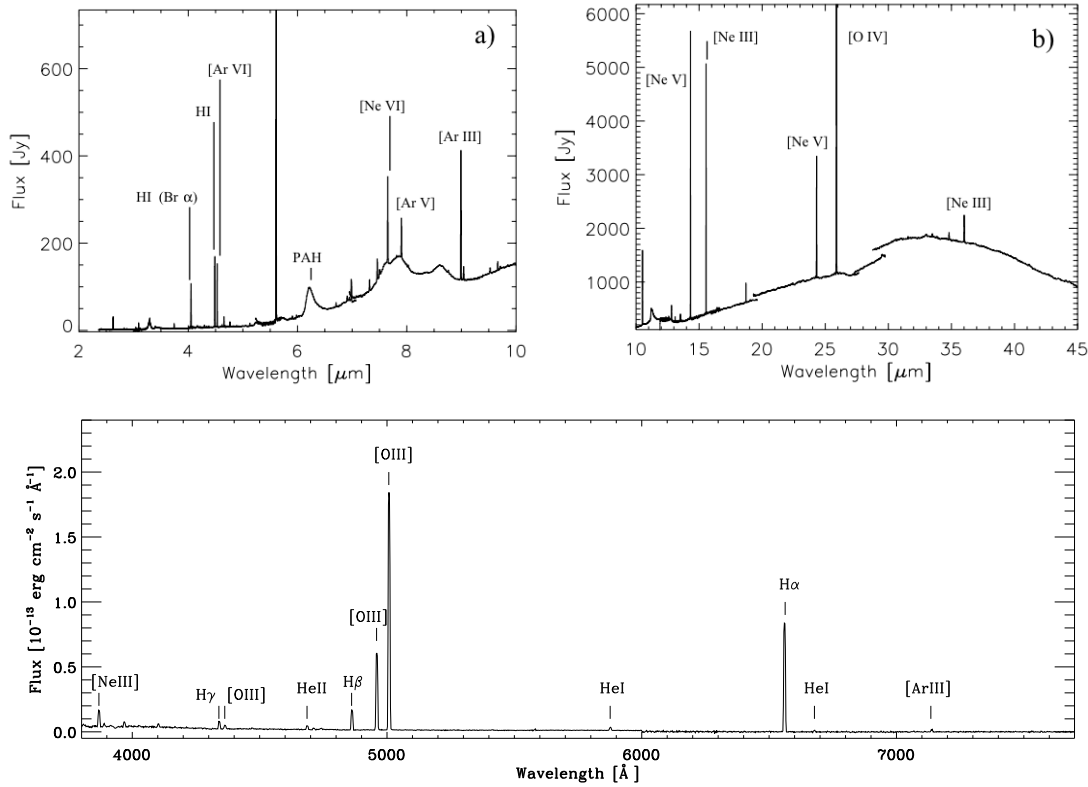


FIGURE 1.3: Infrared (top) and optical (bottom) spectra of the PNe NGC 7027 and NGC 1514, respectively. Some of the recombination and collisionally excited lines are identified. Credits for the IR spectra: [Bernard Salas et al. \(2001\)](#)

team with emission from double-ionized oxygen, which was produced in a very rarefied ionized gas.

Nowadays, we know that spectra of PNe are characterized by emission lines at different wavelengths. As an example, Figure 1.3 shows the infrared spectra (upper panels) of the PN NGC 7026, taken from [Bernard Salas et al. \(2001\)](#), and the optical spectrum of the PN NGC 1514, obtained with CAFOS in one of our observational campaigns. The physical processes which originate these lines are also well-known today. The high energy of the ultraviolet light from the CS removes electrons from the atoms in the process called photoionization. These free electrons, can either recombine with ions or collide with other atoms and ions. In the first case, the recombined electrons fall to the lower levels emitting photons and generating a recombination line. The strongest recombination lines are produced by hydrogen and helium. This process can also occur in metals, although much less often, resulting in very weak lines difficult to measure. However, most of the stronger lines observed in PNe are produced by the second process, which leads to collisionally excited lines. The collisions with the atoms and ions are able to excite the lowest energy levels electrons. These excited electrons can then be de-excited collisionally, where no radiative emission takes place, or by a spontaneous transition, emitting a photon. Because of the low density conditions in PNe – typically of order 10^3 atoms per cubic centimeter –,

Excitation class	Middle					High				
p	4	5	6	7	8	9	10	11	12	12 ⁺
$\log(N_1 + N_2)/4686 \text{ He II}$	2.7	2.5	2.3	2.1	1.9	1.7	1.5	1.2	0.9	0.6

Excitation class	Low		
p	1	2	3
$N_1 + N_2/H\beta$	1-5	5-10	10-20

FIGURE 1.4: Excitation class (p of PNe according to their intensity ratios $\log(N_1+N_2)[\text{O III}]/\text{He II } \lambda 4686$ and $(N_1+N_2)[\text{O III}]/H\beta$. PNe can be classified in low- ($p = 1-3$), middle- ($p = 4-8$) and high- ($p = 9-12$) PNe. Credits image: [Gurzadian & Egikian \(1991\)](#)

the probability of collisional de-excitations are low, favoring spontaneous de-excitations radiatively.

According to the relative intensities of emission lines, PNe are classified into low- middle- and high-excitation PNe. [Gurzadian & Egikian \(1991\)](#) proposed a quantitative system where the excitation class of a PN (p) is obtained from the intensity ratios $(N_1+N_2)[\text{O III}] / \text{He II } \lambda 4686$ and $(N_1+N_2)[\text{O III}] / H\beta$, where N_1 and N_2 refers to the line intensities of $[\text{O III}] \lambda 4959$ and $[\text{O III}] \lambda 5007$. Figure 1.4 shows this classification scheme, where p can take values from 1 up to 12. If the spectrum shows the emission line $\text{He II } \lambda 4686$, then it will be a middle- ($p = 4-8$) or high- ($p = 9-12$) excitation PNe, depending on the magnitude of the ratio $[\text{O III}] / \text{He II } \lambda 4686$. If this line is not present in the spectrum, then it will be a low-excitation PN with $p = 1-3$. The excitation class of PNe is related to the effective temperature of the CS: the higher this temperature, the higher excitation is and the spectrum will show highly ionized elements, such as He II , $[\text{Ne V}]$, $[\text{Ar IV}]$, etc.

- **Physical conditions and chemical abundances**

Line intensity ratios in PNe allow to determine the physical conditions of the gas. The population of the energy levels depends on the temperature of the gas, that is the electron temperature (T_e). Due to this dependence, T_e can be derived by measuring line intensity ratios of emission lines from different excitation levels of the same atom/ion. This is illustrated in Figure 1.5 (left panel), which shows the energy level diagrams for $[\text{O III}]$ and $[\text{N II}]$ ions, usually used to measure T_e . For example, in the case of the $[\text{O III}]$ diagram, the photon emitted at $\lambda 4326 \text{ \AA}$ due to the de-excitation of an electron from 1S level is more energetic than photons emitted in the de-excitations from 1D level ($\lambda 5007 \text{ \AA}$ or $\lambda 4959 \text{ \AA}$). Thus, the intensity ratio between both de-excitations, $I(\lambda 4959 + \lambda 5007)/I(\lambda 4326)$, provides information about the relative population between the levels and thus, on the

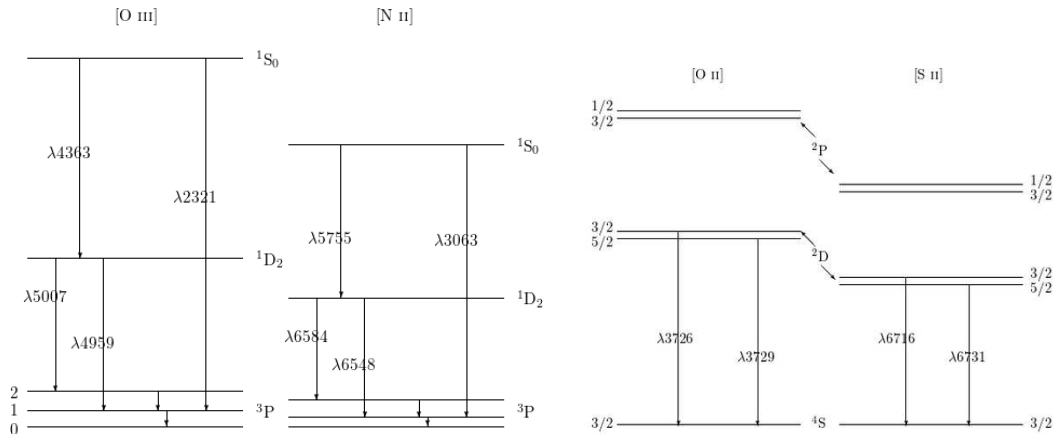


FIGURE 1.5: Left: Energy level diagrams for [O III] and [N II], the most commonly used temperature diagnostic ratios. Right: Energy level diagram for [O II] and [S II], the most commonly used density diagnostic ratios.

electron temperature. Similarly for [N II], the ratio $I(\lambda 6548 + \lambda 6584)/I(\lambda 5754)$ can be used to measure the electron temperature.

On the other hand, to derive the electron density (N_e), line intensity ratios originated from levels with similar energies are required. In this case, the probability of sending an electron from the bottom level to one or other level is about the same so both levels have the same chance to be populated. Therefore, the dependence with the temperature is practically cancelled. The most commonly used intensity ratio is that of the [O II] lines $\lambda 3726 \text{ \AA}/\lambda 3729 \text{ \AA}$ and [S II] lines $\lambda 6716 \text{ \AA}/\lambda 6731 \text{ \AA}$ (see Figure 1.5, right panel). Also, lines from [Cl III] and [Ar IV] can be used.

Finally, once the electron temperature and density have been derived, chemical abundances can be determined relative to hydrogen. The abundance of a particular ion (ionic abundance) can be obtained from the observed intensity ratio of an ionic line relative to $H\beta$ and the corresponding emission coefficients (which depend on T_e and N_e). The total abundance of a particular element (i.e., its elemental abundance) is calculated by the sum of all the ionic contributions of the different stages of ionization. However, not all these stages are observed so the unseen ionic contributions have to be estimated. This is possible by using the ionization correction factors (ICFs, Peimbert & Costero, 1969), which are based on ionization potential similarities. These ICFs can be also derived from photoionization models (see, e.g., Kingsburgh & Barlow, 1994, Kwitter & Henry, 2001, Delgado-Inglada et al., 2014).

Peimbert (1978) divided PNe into four types on the basis of their chemical composition, spatial distribution and kinematical properties. Type I PNe are those with high He and N ($\text{He}/\text{H} \geq 0.125$; $\log(\text{N}/\text{O}) \geq -0.30$) abundances (Peimbert & Torres-Peimbert, 1983). They result from the most massive stars ($2.4\text{--}8.0 M_\odot$) so they are the youngest population. Type II PNe are intermediate population, generally older than type I members and, therefore,

more deficient in heavy elements such as O, S and Ne. They do not present He and N enrichments. Type III PNe belong to the thick disk and present peculiar velocities of $|\Delta V_{pr}| \geq 60 \text{ km s}^{-1}$, which is the difference between the observed radial velocity and that expected velocity on the basis of Galactic rotation (assumed circular). Finally, type IV PNe are halo objects with $|\Delta V_{pr}| \geq 60 \text{ km s}^{-1}$ and $\log(\text{O}/\text{H})+12 \leq 8.1$.

1.2.2 PN Morphology

In spite of the large number of known PNe and the many published studies devoted to understand their formation and evolution, many aspects of these amazing objects remain not well understood yet. One of the most puzzling issues is the wide variety of observed morphologies (see Fig. 1.6) and, accordingly, the varied physical processes that may be involved in their shaping. Morphologically, PNe were originally classified in round, elliptical, bipolar and irregular. Later, observations at higher angular resolution of PNe revealed more complex features and structures, which led to other morphological types like quadrupolar, multipolar and point-symmetric (see, e.g. [Manchado et al., 1996a,b](#)). In addition, other structures like jets, knots, and disks are also identified in many PNe, which complicates enormously the classification.

[Stanghellini et al. \(2002\)](#) analyzed the correlation between the PNe morphology and the physical parameters of their CSs. They found that bipolar PNe appear to come from higher-mass (and short-lived) progenitors than elliptical or round PNe, confirming their different Galactic distributions: bipolar PNe tend to be located in the Galactic plane whereas elliptical and specially round PNe are spread along a wide range of latitudes. In addition, recent simulations carried out by [Huarte-Espinosa et al. \(2012\)](#) show that young bipolar PNe may evolve to mature elliptical ones, which is consistent with the Galactic distribution mentioned above. It is clear that the PN zoo and their properties must be closely related to the evolution of their CSs and, specially with the mass-loss history of their progenitors. It is worth noting that round PNe seem to represent only about 20% of all PNe ([Parker et al., 2006](#), [Jacoby et al., 2010](#)) so it is necessary to invoke complex formation processes to explain the diversity of morphologies found in the rest of the PNe sample.

The existence of highly collimated outflows or jets in PNe was an unexpected fact because no mechanism was foreseen that could produce high collimation in this evolutionary phase. The first detection of bipolar jets in a PN was reported by [Gieseking et al. \(1985\)](#) in NGC 2392 (“Esquimo” nebula), which was followed by the detection of jets in NGC 6543, ([Miranda & Solf, 1992](#)), M 1-16, ([Schwarz, 1992](#)), and Fleming 1 ([Lopez et al., 1993](#)). Since then, the presence of jets in PNe is a well-established fact (Gonzalvez). Although they are known to originate in the rapid transition from the AGB phase to the pre-PN phase, the formation of the jets remains not well understood. They present high velocities of about $\sim 100 - 150 \text{ km s}^{-1}$ up to more than

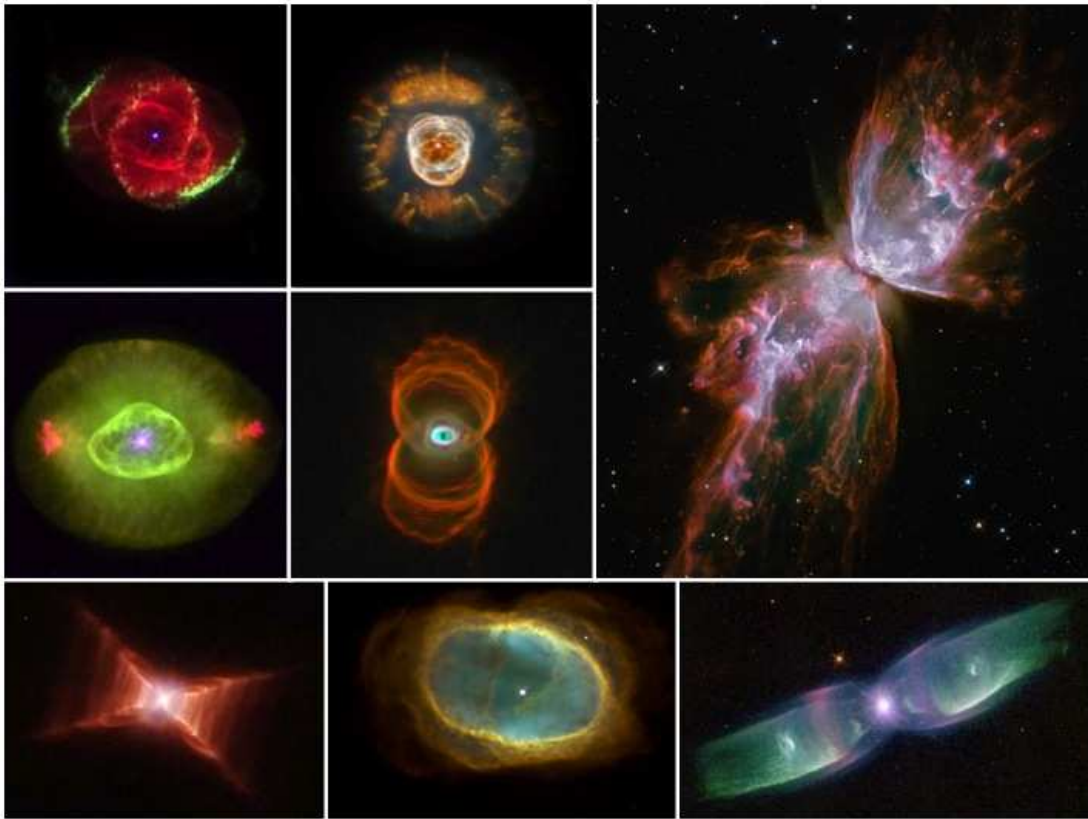


FIGURE 1.6: Mosaic of planetary nebulae with different morphologies, such as bipolar and elliptical. In addition, other structures like jets can be recognized. Images credits: NASA, ESA, and The Hubble Heritage Team (STScI/AURA).

500 km s^{-1} (O'Connor et al., 2000). In addition, these jets show in many cases changes in the orientation with respect to the CS, suggesting precession or rotation of the collimating agent (see Sect. 1.2.3). Collimated outflows ejected at different directions are thought to be responsible for the formation of quadrupolar (Manchado et al., 1996b) and multipolar PNe (see Sahai, 2000)).

1.2.3 Models for the formation of PNe

The basic model for the formation of PNe was firstly introduced by Kwok et al. (1978) and called the interacting stellar wind (ISW) model. In this model, the fast wind of the post-AGB phase interacts with the fossil slower and denser wind (or “superwind”) expelled in the latter stages of the AGB phase, forming a compressed optically thin shell. This model easily explains the formation of spherical PNe but it fails to explain more complex morphologies as bipolar, which seems to require asymmetries in the mass-loss process. To solve this problem, Balick (1987) proposed the generalized interacting stellar wind (GISW) model, previously suggested by Kahn & West (1985). This model (see Figure 1.7, *a.I*) assumed a density gradient in the AGB envelope, so that the maximum density is reached in the equatorial region, forming a circumstellar torus or disk in the equatorial plane of the CS, which is able to drive the winds toward

the polar regions and form bipolar lobes. Analytic calculations and numerical simulations of this model were later carried out by [Mellema & Frank \(1995\)](#), [Icke \(1988\)](#), [Icke et al. \(1989\)](#), who were able to reproduce the observed elliptical and bipolar shapes. We note that the origin of the assumed density gradient in the AGB envelope was not considered in the GISW model. Remarkably, GISW model was completely unable to explain jets, point-symmetric features and multi-lobe structures. In fact, the huge number of PNe with this kind of components led [Sahai & Trauger \(1998\)](#) to propose that collimated outflows are indeed the main shaping mechanism of PNe and not the wind interaction. To explain the origin of these components, magnetic fields, binary evolution and/or stellar rotation have been invoked. We briefly discuss these scenarios below.

Among the magnetohydrodynamic (MHD) models, (MWBB, [Chevalier & Luo, 1994](#)) proposed the first magnetic wind blown bubble (MWBB) scenario. In this model (see Fig. 1.7, *a.2*), a weak toroidal magnetic field, generated by a rapid rotation of the star, is embedded in the fast wind and it is strengthened when passing through the wind shock. Numerical simulations of MWBB model by [Rozyczka & Franco \(1996\)](#) and [García-Segura et al. \(1999\)](#) were capable of reproducing elliptical and bipolar PNe as well as collimated jets. According to the model, higher rotation and stronger magnetic field produce the highest collimation. In addition, by introducing precession of the magnetic axis, point-symmetric features are also reproduced (see Fig. 1.7, *a.4*, [García-Segura, 1997](#)). In other scenario, [Blackman et al. \(2001a\)](#) proposed a model in which a single AGB star generates a strong magnetic field, consequence of a dynamo effect induced by the rapidly rotating core of the AGB star and the slowly rotating envelope. Eventually, a “magnetic explosion” associated with toroidal pressure takes place, which is able to drive the outflows. The observations show that magnetic fields around AGB and post-AGB stars are indeed present. Polarized maser (H_2O , SiO, OH) emission have been detected in some PNe like, e.g., K 3-35 ([Miranda et al., 2001a](#), [Gómez et al., 2009](#)) and IRAS 20406+2953 [Bains et al. \(2004\)](#), which is usually interpreted as due to a magnetic field. In addition, polarization caused by the alignment of the dust grains has been also measured in some post-AGB stars like, e.g., NGC 6537, 7027, 6302 and CRL 2688 ([Sabin et al., 2007](#)) as well as in some proto-PN like CRL 618 and OH 231.8+4.2 ([Sabin et al., 2014](#)). Recently, non-thermal emission compatible with synchrotron emission has been also detected for the first time in a PN (IRAS 15103-5754, [Suárez et al., 2015](#)) and clearly indicates the presence of a magnetic field which is probably related with the water maser jet observed in the object ([Gómez et al., 2015](#)).

The question is whether a single star can produce the magnetic fields or rotation required for the described models. In this respect, [Soker \(1997\)](#) concluded that the rotation in the later phases of the evolution of a Sun-like star is very slow and, therefore, it is not possible to produce a strong magnetic field. A binary companion (either stellar or substellar) seems to be necessary to spin up the envelope in the AGB phase and to supply the angular momentum via tidal force or common envelope (CE) evolution. In a recent work, [García-Segura et al. \(2014\)](#) also concluded that single

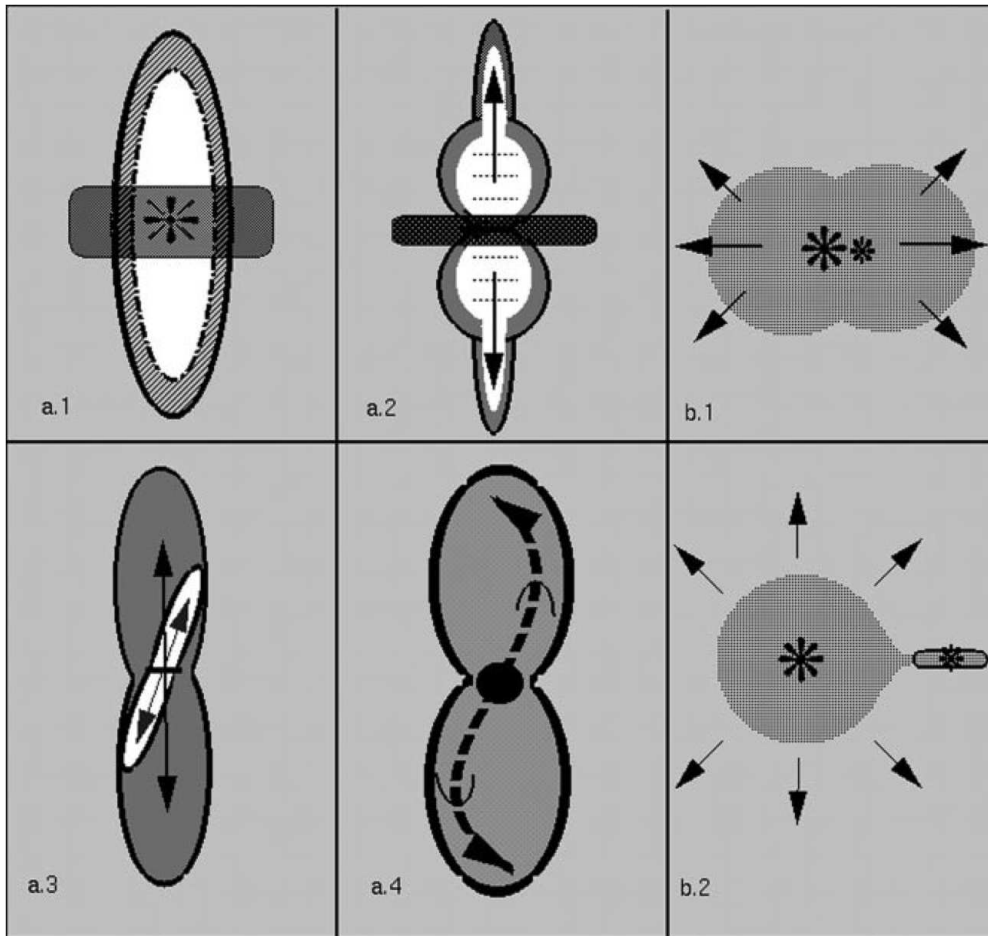


FIGURE 1.7: Sketch of the possible mechanisms involved in the formation of PNe. (a.1) Generalized interacting stellar wind (GISW) model. (a.2) Magnetic wind blown bubble (MWBB) model. (a.3) Magneto-centrifugal model. (a.4) Precessing of the jets can create point-symmetric features. (b.1) CE formation in a short-period binary system. (b.2) Accretion disk formation via Bondi wind. See the text for details. Image credit: [Balick & Frank \(2002\)](#)

star cannot sustain the high rotation velocities required in the current MHD models to reproduce bipolar PNe. In this framework, binary interactions have become the most suitable candidates to account for the formation of axisymmetric mass loss on the AGB phase and, therefore, to explain the complex morphologies seen in the PN phase.

In the last years, searches for binary systems in CSPNe have been carried out through photometric variations ([Bond, 2000](#), [Miszalski et al., 2009a](#), [Hillwig et al., 2010](#)), radial velocity variations ([Van Winckel et al., 2014](#), [Méndez, 1989](#)), infrared excess detections ([De Marco et al., 2013](#), [Douchin et al., 2015](#)), and direct images ([Ciardullo et al., 1999](#)). Although the number of the observed objects is still small the results point out that binarity in CSPNe is a key ingredient in the shaping of PNe.

Most of the confirmed binary CSs have very short orbital periods (less than 3 days, [Miszalski et al., 2009a, 2011](#)). They are thought to have undergone through the so-called CE phase ([Iben & Livio, 1993](#), see Fig. 1.7, *b.1*). In this scenario, two main-sequence stars with different masses

evolve in a binary system. The more massive star evolves faster and reaches first the RGB phase, filling its Roche lobe. Then, mass is transferred from the giant to the companion star and, if the mass transfer is unstable, the envelope of the giant engulfs the companion and forms a CE. During this phase, the two components spiral-in towards each other resulting in a much closer binary system. Bipolar PNe are expected to have experienced the CE phase. This phase is, however, poorly understood. On the other hand, our understanding about the shaping of PNe could be extremely limited if we only take into account those PNe formed in a CE phase. Many authors highlight the need to focus on the search of wider binaries (see, e.g., [Miszalski et al., 2009a](#), [Bond, 2000](#)).

Finally, and also as a result of binary interactions, accretion disks are another proposed mechanism to explain the high-velocity, collimated outflows or jets in many PNe and proto-PNe. Basically, disks have been proposed to be formed through two different ways: (i) they can be formed around the secondary star via Bondi-Hoyle-type accretion ([Morris, 1987](#), [Mastrodemos & Morris, 1998, 1999](#), see Fig. 1.7, *b.2*), or (ii) around the primary star after the CE-phase ([Soker & Livio, 1994](#)). Recent detailed 3D simulations of the first scenario were carried out by [Huarte-Espinosa et al. \(2013\)](#), by using three different orbital separations for the binaries (10, 15 and 20 au). They found that the size of the disk as well as the accretion rates decrease with the orbital radii. Simulations also show that a white dwarf as a companion can produce high enough wind accretion rates to generate the highly collimated outflows seen in PNe. However, if the companion is a main-sequence star, the wind accretion rates is not sufficiently high to account for them. In this latter case, closer binaries are likely involved in the formation of the jets, which would favor the scenario of an accretion disk formed after a CE phase and a subsequent Roche-lobe overflow (RLOF) of the secondary. Restrictions about the formation of the disks under these circumstances are discussed in detail in [Reyes-Ruiz & López \(1999\)](#). Finally, MHD models have also investigated the presence of a disk, resulted from binary disruption and coupled with a star ([Blackman et al., 2001b](#)). In this scenario (see Fig. 1.7, *a.3*), the misalignment of the disk with respect to the axis of the rapidly rotating star result in multipolar features.

1.2.4 Central stars of planetary nebulae

As it has been described above, the mass-loss history of the CSs plays an important role in the mechanisms for shaping PN. CSPNe show a large range of temperatures, gravities, masses and chemical compositions which may result in a rich diversity of PNe properties. For these reasons, the study of PNe needs to go hand in hand with the analysis of their CSs. However, this is not always the case and CSPNe are often treated as simply ionization sources, without taking into account their specific characteristics. In previous sections, we have described the progenitors of CSPNe as low- or intermediate-mass stars which finally will end as a C/O core with He and H shells and a H envelope. However, in its long way until this stage, the star can suffer different

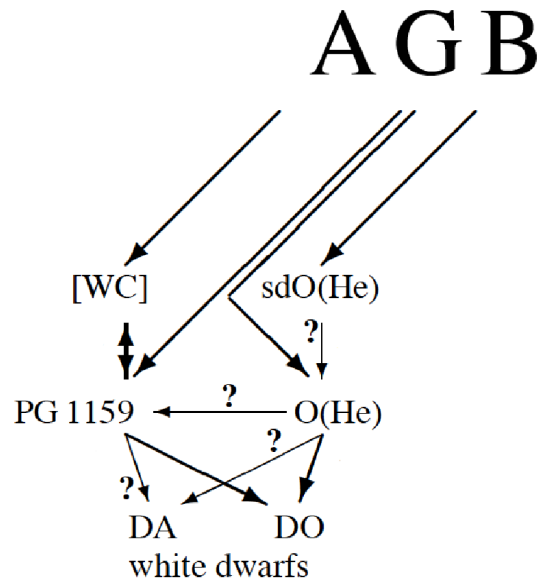


FIGURE 1.8: Scheme of the possible evolutionary channels for H-deficient CSPNe from the AGB phase to the white dwarf sequence. See the text for details. Image credit: [Rauch et al. \(1998\)](#)

deviations from the expected normal evolution which may lead to different compositions and properties.

According to [Mendez \(1991\)](#), most of the CSs can be divided in two different groups: the H-rich CSs (those with hydrogen features identified in their spectra) and the H-poor or H-deficient CSs (those with non-detectable hydrogen features). This is a very general scheme and within these two wide groups, different classes with different features and properties can be found. [Weidmann & Gamen \(2011\)](#) compiled a total of 26 different spectral types well differentiated.

Knowing whether a CSPN is H-rich or H-deficient is crucial to understand the evolution undergone by the progenitor star. In the most general scenario of stellar evolution, it is assumed that low- and intermediate-mass stars leave the AGB with a H-rich envelope. As a consequence, it is expected that all CSPNe are H-rich. In contrast, observations show that roughly 30% of CSPNe are H-deficient (see, e.g., [Weidmann & Gamen, 2011](#), [Mendez, 1991](#)). For the majority of these stars, the more accepted scenario to explain this H deficiency is the already described born-again phenomenon (see Sect. 1.2). The Sakurai's object, A 30, A 58 and A 78 are examples of born again PNe (see, e.g., [Toalá et al., 2015](#)). However, this observational evidence is not supported by the predictions of the theoretical models, which estimate that only 20-25% of the AGB stars are expected to become H-deficient ([Blöcker et al., 2001](#)) and just 10-15% will experience a very late He-flash ([Lawlor & MacDonald, 2001](#)). Therefore, other mechanisms, as binary evolution, are also necessary together with the born again scenario, to explain the relatively high fraction of H-deficient CSPNe (see, e.g., [Tylenda & Gorny, 1993](#)).

Among H-deficient CSPNe, one can find O(He) stars, PG 1159 stars, He-rich sdB and He-rich sdO stars, DO white dwarfs and Wolf-Rayet (WR) CSs. The latter group, that have nothing to do with their massive analogous Population I W-R stars, are the most numerous within the H-deficient CSPNe sample.

The possible evolutionary channels for the H-deficient CSPNe (especially W-R and PG 1159 stars) have been further discussed in the literature. Apart from the well-established carbon-rich evolutionary sequence [WC] \rightarrow PG 1159 \rightarrow DO (Werner & Herwig, 2006), the discovery of the first unambiguous [WN] CSPNe (IC 4663, Miszalski et al., 2013) opened a new equivalent helium-rich evolutionary sequence [WN] \rightarrow O(He) \rightarrow DO. This could explain the poorly understood O(He) stars, for which the most accepted evolutionary sequences until then had been He-sdO \rightarrow O(He) \rightarrow DO (Rauch et al., 1998) and RCrB \rightarrow O(He) \rightarrow DO (Rauch et al., 2006). RCrB refers to the post-AGB R Coronae Borealis, which are cool stars ($T_{\text{eff}} < 10\,000$ K) with helium-dominated atmospheres. Figure 1.8, taken from Rauch et al. (1998), shows a scheme of the possible evolutionary sequences for some of the He-rich stars. The origin of He-sdOs (and, also, of the “normal” sdOs) is still controversial (see Sect. 1.3.3).

H-rich CSs seems to be more frequent among the population of CSPNe. In this group, one can find spectral types as O-type stars, hydrogen rich white dwarfs (i.e, DA), hot subdwarf stars (“normal” sdBs and sdOs, see Sect. 1.3), and hybrid stars. The former, also called O(H), are the most common among the H-rich CSPNe. From a evolutionary point of view, they are less interesting than their H-deficient analogous W-R stars, since the current status of O(H) stars does not require deviations from a normal post-AGB evolution. In contrast, other CSPNe in this group, such as sdBs and sdOs, are not easily explained and deserve more detailed consideration (Sect. 1.3).

In a general context, WR and O-like stars appear to dominate the initial evolution stages in the PN phase. They have “cooler” effective temperatures and relatively high surface gravities. In contrast, the hotter PG1159 and white dwarf CSs correspond to a more evolved evolutionary status of CSPNe. An illustrative scheme of this evolution can be seen in Werner & Herwig (2006), their figure 1. In the following, we will focus our attention on hot subdwarf stars (especially sdOs), since they are the CSPNe studied in this work.

1.3 Hot subdwarf stars: why not ordinary stars?

Hot subdwarf stars are usually defined as compact ($R \simeq 0.1\text{-}0.3 R_{\odot}$) core He-burning stars at the blue end of the HB, the so-called Extreme or Extended Horizontal Branch (EHB), or beyond (see Figure 1.9). They are low-mass ($M \simeq 0.5 M_{\odot}$), blue subluminous objects mainly located at high Galactic latitudes (Heber, 2009). They would be “normal” HB stars if it were not for

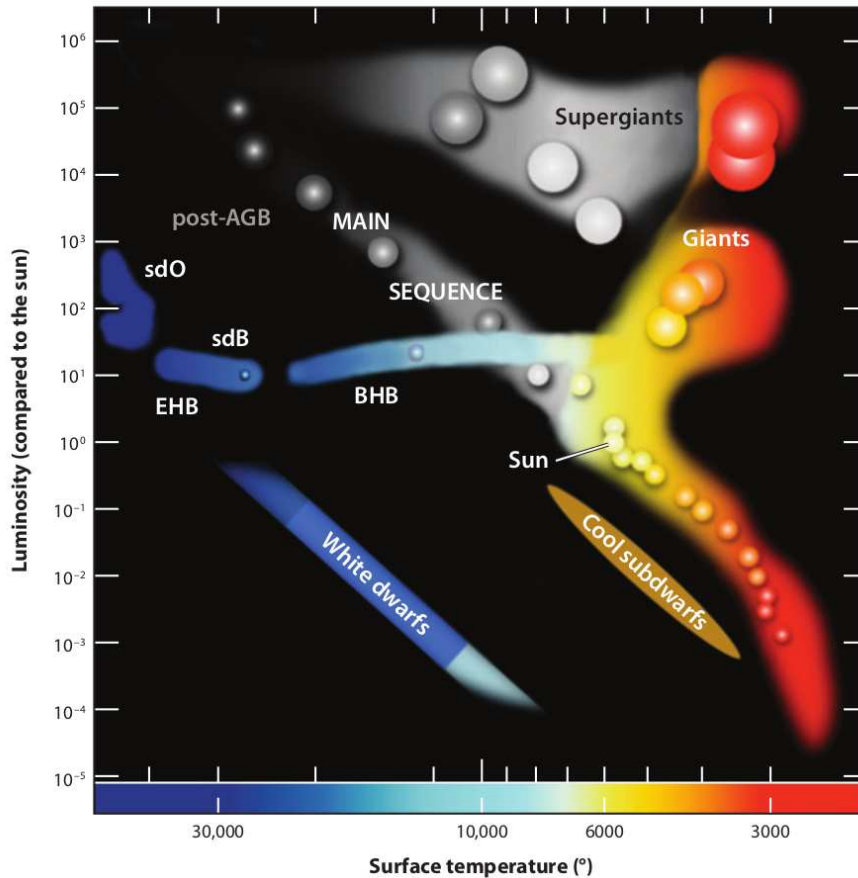


FIGURE 1.9: Sketch of a HR-diagram showing the position of hot subdwarf (sdB and sdO) stars in the extreme horizontal branch (EHB) and beyond. Image credit: Heber (2009).

their extremely thin ($<0.02 M_{\odot}$) hydrogen envelopes. In contrast to the normal HB stars, this thin envelope is unable to sustain H-burning in the shell and, most of the times, prevents the star from ascending the AGB and continuing its expected evolution. As a consequence, the star evolves towards higher temperatures to finally descend along the WD cooling track. In this Section, we will briefly discuss the main properties of hot subdwarfs and the possible evolutionary channels that have been proposed to explain their controversial origins.

1.3.1 Properties of hot subdwarf stars

Hot subdwarfs were firstly discovered by Humason & Zwicky (1947) in a photometric survey of the North Galactic Pole region searching for faint blue stars. Later on, many works were published related to the search and analysis of blue stars, including hot subdwarfs (see. e.g., Luyten & Miller, 1951, Haro & Luyten, 1962, Greenstein, 1966). Sargent & Searle (1968) divided, for the first time, hot subdwarf stars into two main subclasses: *hot subdwarf B* (sdB) and *hot subdwarf O* (sdO), depending on whether they are chemically similar to the corresponding B and O main-sequence stars, respectively. An intermediate class (sdOB) was defined a few years

later (Baschek & Norris, 1975) to describe those hot subdwarfs that showed spectral features from the two types.

While the sdB subclass forms a homogeneous group that populates a reduced region in the $\log T_{\text{eff}} - \log g$ plane, sdOs are spread across a broad region in the same diagram. The former have effective temperatures (T_{eff}) generally in the range 20 000- 40 000 K, and surface gravity ($\log(g)$) from 5.0 to 6.5 (see, e.g., Saffer et al., 1994). sdOBs are considered to be in the hotter range of sdBs, with T_{eff} from 30 000 K to 40 000 K approximately. In contrast, sdOs have hotter temperatures (exceeding 40 000 K to above 100 000 K) and a wide range in $\log(g)$ from 4.0 to 6.5 (see, e.g., Rodríguez-López et al., 2010). In addition, while sdBs usually present helium deficient atmospheres due to diffusion, which inhibits the development of HeII convection zone in their photospheres (Heber, 1986), the hotter sdOs, with HeII convection zones which reach up to their photospheres (Groth et al., 1985), show a wide variety of helium abundances, which contributes to the heterogeneity of this group. Stroeyer et al. (2007) found a correlation between this helium abundance in sdOs and the presence of carbon and/or nitrogen in their spectra. Thus, the helium-enriched sdOs (i.e, He-sdOs) can be grouped into carbon strong-lined and nitrogen strong-lined.

The widespread location of sdOs in the HR diagram led to classify them into *luminous* and *compact*, depending on their luminosity (Husfeld, 1987, Husfeld et al., 1989). Thus, the “low gravity”, luminous sdOs, which are located in the region of the CSPNe evolutionary tracks, are assumed to have a post-AGB origin. On the other hand, the compact, He-deficient sdOs would have directly evolved from the EHB, being the possible outcome of sdBs (see, e.g., Heber, 2009).

A remarkable property of hot subdwarfs is the presence of pulsations, which allows to study them by means of asteroseismology (see, e.g., Brassard et al., 2001). Pulsations in sdB stars were theoretically predicted and observationally discovered at almost the same time, by Charpinet et al. (1996) and Kilkeny et al. (1997a), respectively. Since then, many sdB pulsators have been discovered (see, e.g., Silvotti et al., 2000, 2001, Oreiro et al., 2009). In contrast, pulsations in sdOs appear less frequent than in sdBs. To date, only one sdO pulsating is known: SDSS J160043.6+074802.9, that was discovered serendipitously by Woudt et al. (2006). Later on, Rodríguez-López et al. (2007) carried out the first extensive search for new sdO pulsators and found 2 very promising candidates out of 56 of the observed sdOs. However, to our knowledge, their pulsating nature has still to be confirmed. Pulsation instabilities in sdOs have been recently modeled by Rodríguez-López et al. (2010), who reported the first sdO models capable of driving high-radial-order g modes.

1.3.2 Spectral classification and analysis

As mentioned above, the first spectral classification for hot subdwarf stars, into two main classes, was introduced by [Sargent & Searle \(1968\)](#). However, even within these only two groups, hot subdwarfs show a large variety of spectra, specially amongst sdOs, making difficult their classification. Many works have been published attempting to classify these objects accounting for all the spectral features of the numerous subclasses (see [Green et al., 1986](#), [Moehler et al., 1990](#), [Drilling, 1996](#), [Jeffery et al., 1997](#), [Drilling et al., 2003](#)). The most generally used classification scheme is, up to then, that from [Moehler et al. \(1990\)](#):

- **sdB.** They show Balmer absorption lines abnormally broader as compared with the Population I main-sequence B stars. Some of them show weak He I lines in absorption, being specially notable He I $\lambda 4472$.
- **sdO.** They present some He II absorption lines in their spectra (specially intense He II $\lambda 4686$). Balmer lines are strong relative to the Population I main-sequence O stars although they are shallower than in sdBs. For sdOs in the coolest temperature range, some He I lines can be present in their spectra.
- **sdOB.** This class describes the spectra with sdB appearance but with weak He I and He II lines also present.
- **He-sdO.** It refers to the helium-enriched sdOs. Their spectra is dominated by strong He II lines, resulting from the Pickering series. In contrast, Balmer lines are rarely visible. Depending on the T_{eff} , some He I lines can also be visible.
- **He-sdB.** This is a scarcely populated class. It designates sdB stars with unusually strong He I lines.

In [Figure 1.10](#), we include an example that illustrates the main differences between typical spectra of sdB and He-sdO stars. However, the most recent work related to this topic is that reported by [Drilling et al. \(2013\)](#), in which the authors present an MK (Morgan-Keenan)-like system of spectral classification for hot subdwarfs. This systems is mainly based in the He abundance, the presence or absence of carbon, and the luminosity class, and represents the most homogeneous classification system for hot subdwarf stars to date.

Atmospheric parameters (T_{eff} , $\log(g)$) and chemical abundances of hot subdwarfs can be derived by means of spectral analysis. [Kudritzki \(1976\)](#) showed that taking into consideration the deviations from local thermodynamic equilibrium (LTE) as well as of opacities of elements heavier than H have a significant influence on the determination of effective temperature and surface gravity in spectral analysis of hot subdwarfs. This is specially critical at high temperatures since

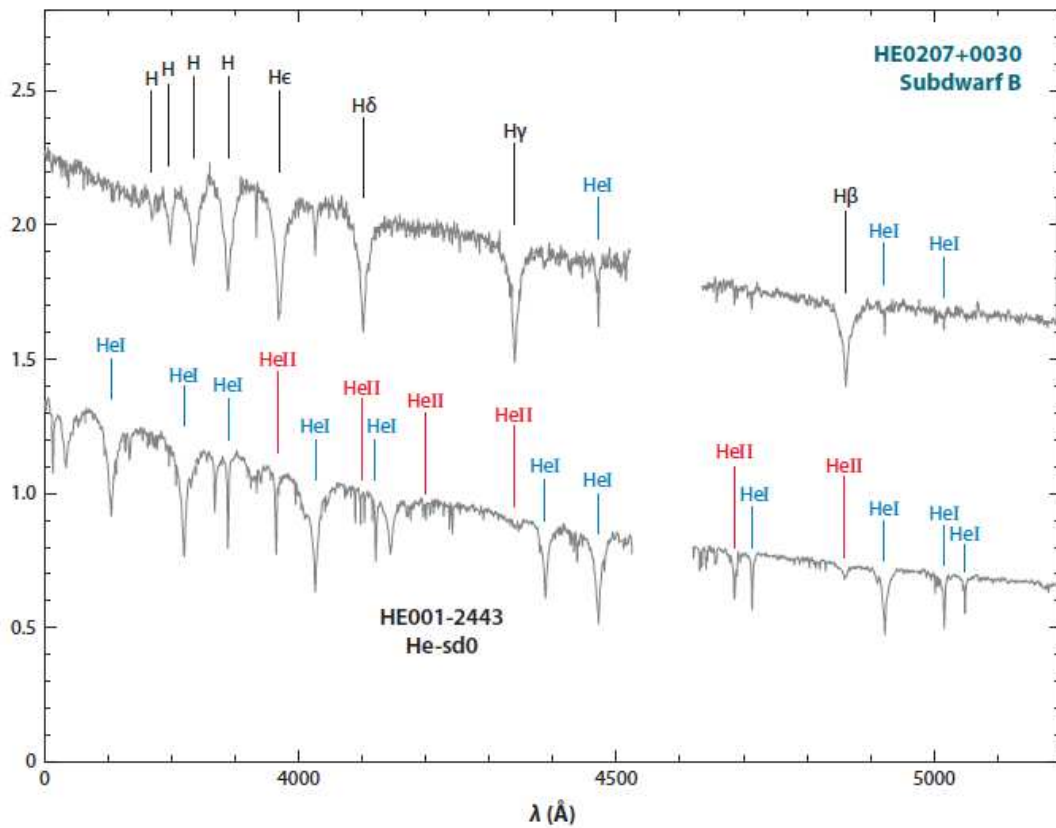


FIGURE 1.10: Comparison of a typical spectrum of a sdB star (top) and one of a He-sdO star (bottom). While the sdB spectrum is dominated by the Balmer lines with the presence of some weak He I lines, in the He-sdO spectrum Balmer lines are blended with the He II Pickering lines. Image credit: [Heber \(2009\)](#).

deviations from LTE strongly increase with effective temperature. [Napiwotzki \(1997\)](#) drew the line in $T_{\text{eff}} > 30\,000$ K, temperature above which the non-LTE effects start to be pronounced. According to this *rule of thumb*, the use of LTE model atmospheres seems to be appropriate for the coolest sdBs (those with T_{eff} between 20 000 and 30 000 K) but not for sdOs. [Latour et al. \(2014\)](#) showed that, theoretically, NLTE effects also depend on surface gravity and helium content. However, their spectral analysis of Feige 48, an sdB with $T_{\text{eff}} > 29\,850 \pm 60$ K, showed that NLTE effects have small effects in the determination of the parameters, as compared with those analyses carried out with LTE atmosphere models. The influence of the metal line blanketing has been also further treated in the development of model atmospheres. This effect strongly depends on the metallicity since metal components block part of the flux from the UV, which is redistributed along redder wavelengths. This affects to the depth of the absorption lines in the optical and can mimic hotter temperatures. Finally, atmospheric models have to account for the enormous range of He abundances that hot subdwarfs (specially sdOs) present.

The most used codes of non-LTE atmosphere models are TMAP² (Tübingen NLTE - Model Atmosphere Package; [Werner & Dreizler, 1999](#), [Werner et al., 2003](#)) and TLUSTY ([Hubeny & Lanz, 1995](#)). Both of them provide plane-parallel, non-LTE, line-blanketed model atmospheres in radiative and hydrostatic equilibrium for hot stars. The models computed by TMAP code were designed to analyze hot and compact objects such as white dwarfs, CSPNe, hot subdwarfs, and PG1159 stars. The service TMAW³, recently developed in the framework of the German Astrophysical Virtual Observatory (GAVO), provides access to such theoretical stellar spectra. This collection of models has been successfully used for spectral analysis of hot, compact stars (see, e.g., [Rauch et al., 2007, 2013](#), [Ziegler et al., 2012](#)). On the other hand, TLUSTY code is divided into two different grids: model atmospheres for O stars ([Lanz & Hubeny, 2003](#), OS-TAR2002) and early B stars ([Lanz & Hubeny, 2007](#), BSTAR2006). These models have been also used to analyze sdOs (see, e.g., [Latour et al., 2013](#)). The TLUSTY models are available from the Spanish Virtual Observatory theoretical spectra server⁴ and also from the Virtual Observatory Sed Analyzer (VOSA⁵).

1.3.3 Formation and evolution channels for hot subdwarfs

The formation and evolution paths of hot subdwarf stars (both sdBs and sdOs) remain still unclear. The main problem is to find which mechanism (or mechanisms) causes the high mass loss that these objects presumably have to undergo ($\gg 0.1\text{-}0.3 M_{\odot}$, which are the typical mass loss in the RGB phase for low mass stars; [Dorman et al., 1993](#)) before they reach their current position in the HR diagram (see Figure 1.9). They occupy a broad region that is crossed by evolutionary tracks of post-AGB, post-RGB and post-EHB ([Heber, 2009](#)). This degeneracy in evolutionary paths and the possibility of binary formation scenarios (e.g., [Napiwotzki, 2008](#), [Heber, 2009](#)) hamper a reliable determination of their origins. In the following, we briefly describe the most plausible scenarios that have been proposed to account for their current evolutionary status.

1.3.3.1 Canonical HB and post-HB evolution

After the He flash takes place at the tip of the RGB, the remnant helium core mass is restricted to be $0.46 \leq M_c / M_{\odot} \leq 0.5$, depending on the metallicity and He abundance ([Heber, 2009](#)). The thinner the H envelope is, the bluest the ZAHB location is. The post-HB evolution followed by the star depending on this position on the ZAHB was extensively explored by [Dorman et al. \(1993\)](#). They calculated post-HB evolutionary tracks for envelope masses in the ZAHB (M_{env}^0) in the range $0.002 \leq M_{env}^0 / M_{\odot} \leq 0.531$ and found that if the M_{env}^0 is lower than a critical value

²[http://astro.uni-tuebingen.de/\\$\sim\\$TMAP/](http://astro.uni-tuebingen.de/\simTMAP/)

³[http://astro.uni-tuebingen.de/\\$\sim\\$TMAW/](http://astro.uni-tuebingen.de/\simTMAW/)

⁴<http://svo2.cab.inta-csic.es/theory/newov/index.php?mtype=star>

⁵<http://svo2.cab.inta-csic.es/theory/vosa/>

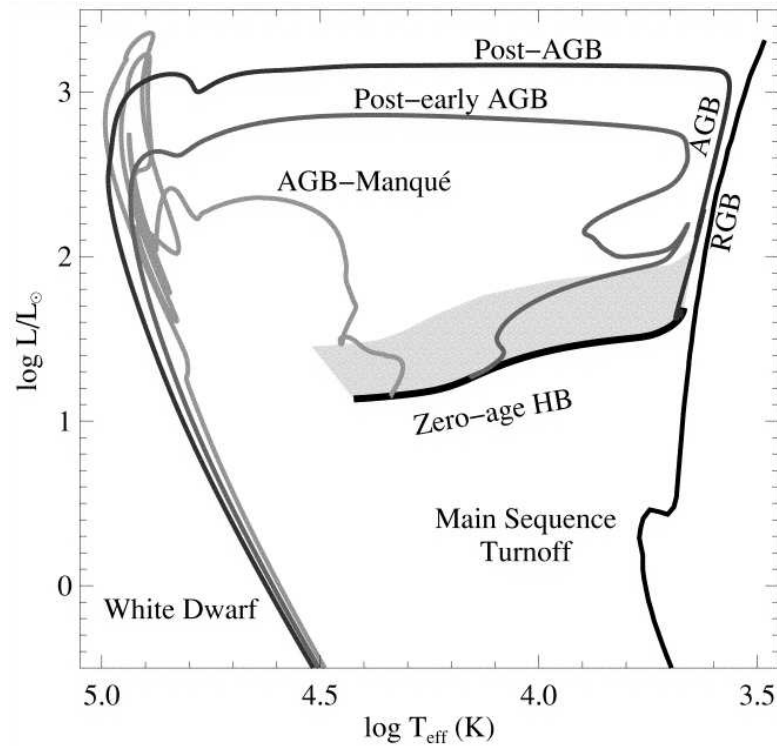


FIGURE 1.11: Possible post-HB evolution channels (post-AGB, post-early AGB and AGB-Manqué) for different envelope masses and effective temperatures in the ZAHB. Image credit: [Brown et al. \(2000\)](#).

named $\sim 0.05 M_{\odot}$, the star will not be able to continue the normal AGB evolution after core helium exhaustion. Then, depending on their envelope masses, they will evolve following either of the two evolutionary tracks:

1. Post-early AGB (p-EAGB). The stars will evolve through the early stages of the AGB but leave this phase before the thermal pulsating phase ([Brocato et al., 1990](#)).
2. AGB-Manqué. The stars with the lowest M_{env}^0 will never develop extensive convective envelopes and, therefore, never reach the AGB ([Greggio & Renzini, 1990](#)).

Figure 1.11 shows these two scenarios for post-HB evolution. As already mentioned, the main problem is the identification of the mechanism (or mechanisms) causing the strong mass-loss required to remove almost completely the H envelope and end in the HB with tiny envelopes of $<0.02 M_{\odot}$ [Geier \(2013\)](#). One mechanism would be strong stellar winds. The most common parametrizations used to describe these mass loss episodes are that of [Reimers \(1975\)](#), and its revised version by [Schröder & Cuntz \(2005\)](#). It is estimated that RGB stars lose a considerable amount of mass in this phase (~ 0.1 - $0.3 M_{\odot}$), prior to reach the ZAHB (see, e.g., [Dorman et al., 1993](#)). This amount, however, is far from being the needed mass-loss to obtain the mentioned thin H envelopes found in hot subdwarf stars.

1.3.3.2 Hot He-flashers in the post-RGB

For low-mass stars, the He core-flash usually takes places at the tip of the RGB (see Sect. 1.1). However, if the mass loss prior to this point is extreme, the star can lose enough mass to remove the envelope making the total mass on the order of the core mass. Under these circumstances, the star can leave the RGB before experiencing the He-flash (see [Castellani & Castellani, 1993](#)). Instead, a late He core-flash can occur for specific parameters. These stars are called “hot-flashers”. This scenario is analogous to the born-again mechanism that takes place in the post-AGB phase and produces some of the H-deficient stars (see above).

[D’Cruz et al. \(1996\)](#) computed models for initial masses lower than $1.1M_{\odot}$, different metallicities and a large range of the mass-loss efficiency parameter (η_R) from the Reimers formula:

$$\dot{M} = -4 \times 10^{-13} \cdot \eta_R \cdot \frac{L}{gR} M_{\odot} \text{yr}^{-1}, \quad (1.1)$$

where L is the luminosity, g the surface gravity, and R is the radius of the star. Their simulations showed that after these late He-core flashes, the remnants of the hot flashers ended at the very end of the EHB.

This scenario was further explored by [Brown et al. \(2001\)](#). Figure 1.12 (taken from that work), shows the different paths followed by the star depending on the time when the late flash (marked with asterisks) occurs. In the lower left corner of each panel, the η_R value used for the calculation is showed. Solid lines correspond to the evolution until the ZAHB and dotted lines from the HB onwards. In a typical evolutionary track of a low-mass star (Fig. 1.12a) the He-flash occurs at the tip of the RGB and the star finally evolves along the post-AGB phase. If the He-flash takes place shortly after the tip of the RGB, the position in the ZAHB becomes hotter and the star evolves as a p-EAGB star (Fig. 1.12b). In contrast, if the He core-flash occurs after the departure of the RGB, at constant luminosity, or early in the with dwarf cooling track (see Fig. 1.12c and Fig. 1.12d, respectively), the star evolves as an AGB-manqué. For higher values of η_R , the He core-flash takes places in the late white dwarf cooling sequence (Fig. 1.12e) and the star would enter in the white dwarf cooling curve for a second time. Finally, for $\eta_R > 0.818$ no He core-flash occurs (Fig. 1.12f).

Evolutionary simulations by [Lanz et al. \(2004\)](#) showed that for the later hot flashers (that is, those occurring in the white dwarf cooling curve), the interior convection zones could penetrate into the H envelope leading to strong enrichment of He (and sometimes C and N) in the surfaces. They found two types of “flash mixing” depending on whether the H envelope is mixed deeply into the site of the flash (*deep mixing*, Fig. 1.12e) or only in the convective shell of the outer layers of the core (*shallow mixing*, Fig. 1.12d). In the early hot flasher (Fig. 1.12c) no mixing takes place and hot subdwarfs with standard H/He envelopes result. Hence, the hot-flasher

scenarios may explain from sdBs (result of early flashes) to He-sdOs (remnants of late flashes with deep mixing).

1.3.3.3 Binary scenarios for hot subdwarf evolution

In the last years, the observational evidence seems to focus the debate on the binary formation channels (see, e.g., [Stark & Wade, 2003](#), [Girven et al., 2012](#), [Geier et al., 2011b](#)). Radial velocity surveys have demonstrated that a high fraction of sdBs ($\sim 40\text{-}70\%$) reside in close binaries (with periods from 0.07 to 30 days, see, e.g., [Maxted et al., 2001](#), [Morales-Rueda et al., 2003](#), [Napiwotzki et al., 2004](#)), being most of the companions from white dwarfs to late-type main-sequence stars. This large fraction seems not to be applicable to He-sdOs as reported by [Napiwotzki et al. \(2004\)](#), who found that only 4% of He-sdOs are binaries. However, more recent studies show that this fraction could be higher than expected ([Green et al., 2008](#), [Geier et al., 2011b](#)).

Three different binary channels are generally used to explain the formation of hot subdwarfs:

- CE channel. Most binary sdBs have very short orbital periods (less than 1 day). They are thought to have undergone a CE phase. In this scenario (see Sect. 1.2.3), a giant star fills its Roche-lobe, transferring mass to the companion. If mass transfer is unstable, the envelope of the giant engulfs the companion forming the CE. The result is the core of the giant (that will become an sdB star), and a main-sequence companion. A second CE phase may occur when the companion reaches the RGB and fills its Roche-Lobe, which can result in a closer binary with an sdB star and a white dwarf.
- Stable Roche-lobe overflow (RLOF) channel. In this case, the red giant star fills its Roche-lobe and, if mass transfer is dynamically stable, the companion accretes matter but without forming a CE. This results in a binary system with an sdB and a main-sequence companion of long orbital period from 10 to 500 days, according to [Heber \(2009\)](#) and $\gtrsim 1000$ days according to [Han et al. \(2002\)](#). An example of these systems is the sdB+G0 binary PG 1104+243 ([Vos et al., 2012](#)).
- The merger of two helium white dwarfs. In this scenario, a short-period binary system of two helium core white dwarfs loses orbital energy due to radiation of gravitational waves. The less massive one is accreted onto its companion, which will eventually get enough mass to start helium burning (for a detailed description of this process, see [Webbink, 1984](#), [Iben & Tutukov, 1986](#), [Iben, 1990](#)). As argued by [Saio & Jeffery \(2000\)](#), this would result in an He-enriched sdO with nitrogen lines, consequence of the CNO-processed matter from the donor that has been transferred to the newly formed He-sdO. [Jeffery \(2002\)](#) suggested that the sdB V 652 Her could be the product of this merging process. However,

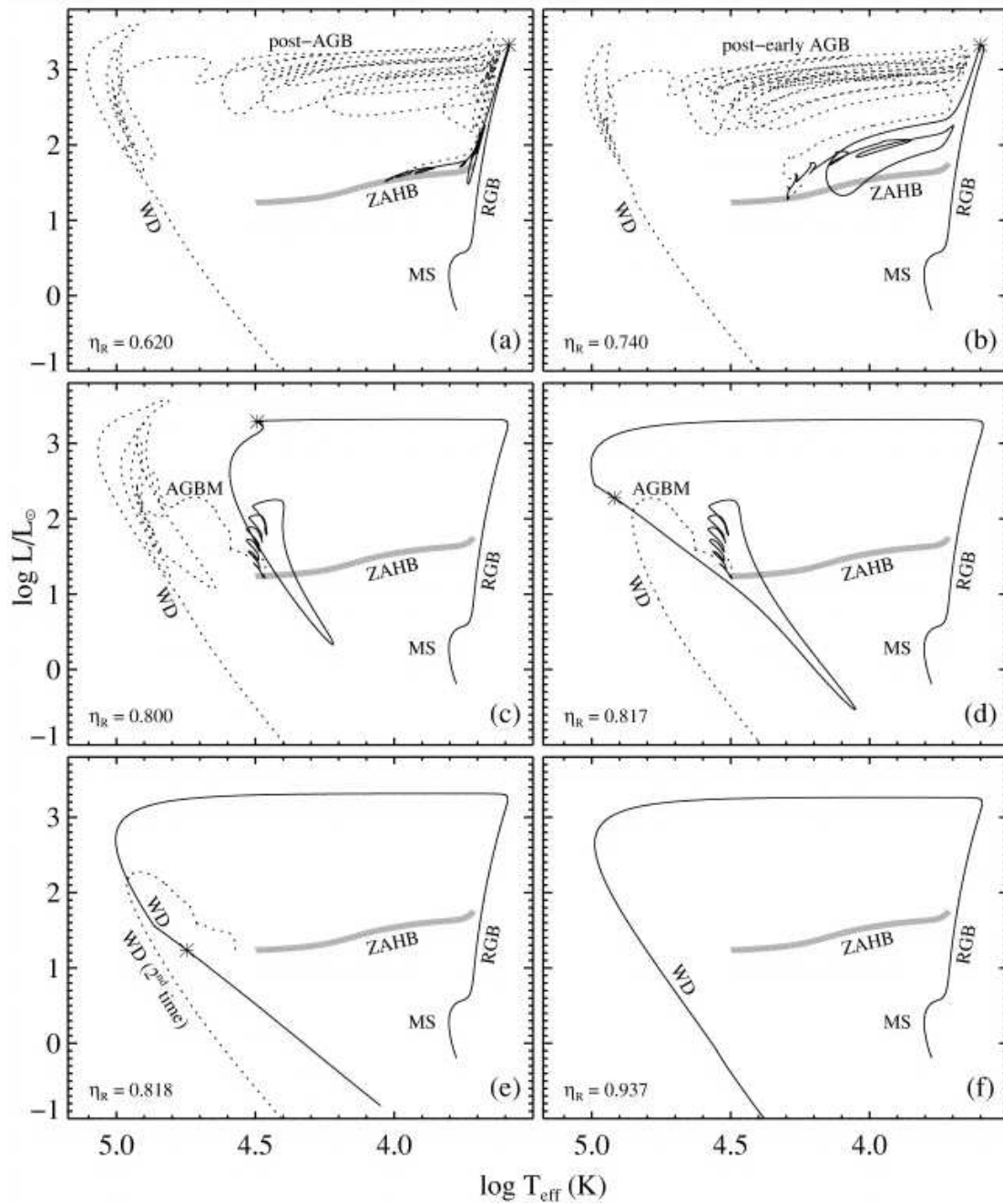


FIGURE 1.12: Evolutionary tracks from the MS to the white dwarf cooling sequence for different values of the Reimers mass-loss efficiency parameter η_R (lower left corner of each panel). This illustrates the possible evolutionary paths that hot subdwarfs have followed until their current position in the HR diagram, as well as their future evolution. Solid lines correspond to the evolution until the ZAHB and dotted lines from the HB onwards. The moment in which the He-core flash occurs is indicated with an asterisk. Depending on whether this moment occurs sooner or later, the star will lie in cooler or hotter region of the ZAHB, respectively, and it will evolve along different channels (as post-AGB, post-early AGB and AGB-Manqué). See the text for the details. Image credit: [Brown et al. \(2001\)](#).

[Gourgouliatos & Jeffery \(2006\)](#) concluded, assuming total conservation of angular momentum, that the rotation velocity of the He mergers products would be high enough to cause breakup, so the star must lose angular momentum at some point in its evolution.

1.4 Putting in common Planetary Nebulae and Hot Subdwarf stars

As we have already mentioned, sdOs are also found as CSPNe. In these cases, it is clear that the star has ascended the AGB phase before ejecting the nebula. However, observational evidence seems to point that this is not the preferred evolutionary path for sdOs. An exhaustive search in the literature leads to a very few sdOs with associated PNe, hereafter PN+sdO systems, (~ 18), which represent only $\sim 3\%$ of all sdOs. This number includes both PNe discovered around sdOs, that we will refer to as “classical” systems in this thesis, and those already known CSPNe that have been classified as sdOs. In Chapter 2 we will discuss this point in detail. In this context, the question that naturally arises is: what is the difference between sdO CSPNe and sdOs without, *a priori*, an associated nebula?. Both PNe and sdOs have been extensively studied independently. However, there are only a few works dealing with both PNe and sdO simultaneously in the same context (see, e.g. [Mendez et al., 1988](#), [Kwitter et al., 1989](#)). The reasons for the scarcity of PN hosting sdOs was already addressed by [Heber & Hunger \(1987\)](#), who proposed three possible explanations that could account for the non-detection of the nebula in most of the cases:

- (i) The star simply does not eject the nebula during the AGB phase. This scenario hardly explains the enrichment of helium and carbon found in many sdOs. If the H-envelope has not been expelled, hydrogen should dominate the photospheric abundances of these stars, and this is not the case for the majority of sdOs.
- (ii) The evolution of the star is extremely slow. This would imply that the ejected nebula has been dissipated in the interstellar medium before the central star becomes hot enough to ionize it.
- (iii) They are “born again” post-AGB stars. As mentioned above, in this scenario a late thermal pulse may occur in the post-AGB phase or white dwarf cooling sequence. This would lead the star again to the RGB phase, which will evolve along the post-AGB phase for a second time. No nebula will be ejected at this time and the first one would have already been dissipated.

It this framework, it is clear that knowing the number of sdOs with PNe as well as to study in detail their properties is very relevant in order to constrain the fraction of sdOs that indeed have a post-AGB origin. This would help us to understand the evolution of the puzzling sdOs, which remains unclear today.

1.5 Motivation and structure of this thesis

The core of this thesis is the analysis and characterization of PN+sdO systems in a common framework. As it has been described in the previous sections, many questions regarding the formation and evolution of sdOs remain still open. Several scenarios have been proposed to explain the origins of these stars and the post-AGB scenario is a less explored channel due to the low number of known sdOs with associated PN. The detection of PNe in a large sample of sdOs is crucial to tip the balance to a post-AGB origin or other scenarios. Hence, this thesis was conceived with the aim of answering two fundamental questions:

- (i) *How frequent PNe around sdOs are.* As already mentioned, among the large sample of known sdOs, the fraction of those with PNe around them is extremely small. If the progenitors of sdOs are normal low-mass stars, the question which arises is why most of the known sdOs do not have associated PNe. The first step to resolve this question is to search for the expected PNe around a large sample of sdOs, in order to confirm or discard a possible AGB origin.
- (ii) *Whether or not PN+sdO systems share common properties.* The study of all known PN+sdO systems in a general context is very important in order to elucidate why these sdOs have suffered a different evolution than those sdOs without associated PNe. Thus, analysis of their physical properties, chemical abundances, internal kinematics, morphology as well as the possibility of a binary evolution is mandatory to study whether PN+sdO systems present similar characteristics that may trace a same evolutionary channel.

Answering the above questions is the main objective of this thesis, which is outlined as follows:

In Chapter 2, we describe our observational program designed to search for new extended emission around known sdOs by means of imaging and intermediate-resolution long-slit spectroscopy. The observations and the general results of this survey are presented. The most relevant result of these surveys was the detection of a multi-shell PN around the sdO binary 2M1931+4324. This discovery adds a new object to the small sample of PN+sdO systems. In addition, we also obtained imaging and intermediate-resolution, long-slit spectra of some of the already known PNe with confirmed or possible sdO CSs, in order to constrain the sdO nature of these objects. These observations are also described in this chapter.

A detailed analysis of 2M1931+4324 including both optical and mid-infrared imaging, and intermediate- and high-resolution, long-slit spectra of the nebula is described in Chapter 3. This is the first analysis published of this PN. Since no other new PNe were discovered in the course of our survey, we focused the subsequent analysis on a sample of known PNe with sdO CSs, mainly motivated by the detailed study carried out for 2M1931+4324. Thus, in Chapter 4 we present the

results of the analysis of three more PN+sdO systems, Abell 36, DeHt 2 and RWT 152, obtained from a morpho-kinematic study of their PNe as well as from their intermediate-resolution long-slit spectra. Also in this chapter, we will discuss the main properties and characteristics that seem to share PN+sdO systems in order to put these peculiar objects in a common context. Finally, in Chapter 5, we present a more detailed study of the PN RWT 152. In particular, we analyze deeper subsecond images and spectra of the nebula and discuss the chemical abundance study carried out for this object.

Chapter 6 is dedicated to the spectral analysis of BD+30°623, the *peculiar central star* of the PN NGC 1514. The nucleus of this PN consists of a cool star and a hot (and faint) companion which is the responsible for the photoionization of the nebula. This hot star has been historically classified as sdO although previous classification and modeling have not taken into account the complexity of this system. We present an innovative spectral analysis of BD+30°623 by using an extensive composite grid of Kurucz and Tübingen NLTE Model Atmosphere spectra.

In Chapter 7, as a by-product of our investigation, we present a new and updated catalogue of true, probable and possible PNe in our Galaxy. This catalogue has been motivated by the large number of new PNe discovered in the last few years and the complete lack of a database that gathers all these objects. The catalogue has been built up by means of Virtual Observatory tools. We also present a classification method to distinguish different classes of blue stars. The ultimate goal of this method is to obtain the spectral class of the whole sample of CSPNe in our catalogue in an automatic way, on basis of archival data.

Finally, Chapter 8 closes the thesis with a summary of the main conclusions of the work and some prospective projects for future research.

Searching for Planetary Nebulae around sdOs

This chapter is devoted to describe the work carried out at the beginning of this thesis in order to detect new PNe around sdOs. To contextualize this work, the first discoveries and systematic searches previously carried out in the field are summarized in Sect. 2.1. Later, we explain the motivation for a new search with a more suitable and recent instrumentation than the previous ones and describe our contribution in the field. We have imaged at optical wavelengths more than 100 sdOs with a new positive detection (Sect. 2.2). WISE archive images have also been inspected to search for hints of nebular emission around more than 700 sdOs (Sect. 2.3). Diffuse extended emission can be guessed in a handful of them. Imaging and intermediate-resolution, long-slit spectra of some CSPNe classified as sdOs, obtained in the course of this work, are also presented. Finally, an overview of the confirmed and possible PN+sdO systems is described in Sect. 2.4.

2.1 Previous work in the field: 1978-1989

The first detections of nebular emission around sdOs date back to the late seventies and early eighties. [Holmberg et al. \(1978\)](#) detected a very diffuse and obscured PN around the sdO LSS 2018, in the ESO/UPPSALA survey of the ESO (B) Atlas of the southern sky. It was designated as 215-PN?04. Later, [Drilling \(1983\)](#) confirmed the presence of this faint nebula by means of image-tube spectroscopy. In that work, in which the spectra of 12 newly discovered sdOs were analyzed, Drilling also reported the detection of a faint nebula around the sdO LSE 125. By inspecting the ESO-SRC Sky Survey (J) prints, he concluded that both nebulae were roughly circular with diameters of ~ 180 arcsec but also noted that the nebula surrounding LSE 125 appeared to have more a shell-like structure than that surrounding LSS 2018.

The third detected nebula around an sdO was RWT 152. Although the CS of this PN was initially classified as an O4-5 star on or near the main sequence (Chromey, 1980), Ebbets & Savage (1982) estimated the stellar mass, radius and metallicity and concluded that were in good agreement with those of the hot subdwarf population. The evolutionary state proposed by Ebbets & Savage (1982), very close to that of the already known PN NGC 6543, and the detected interstellar absorptions lines at velocities close to that of the CS of RWT 152 –possibly indicative of the presence of a photoionized nebula–, led Pritchett (1984) to search for a possible nebula around this object with a positive result. His $H\alpha + [N\text{ II}]$ image showed a small, low surface brightness nebulosity, after subtracting from the image of RWT 152 itself, the image of a nearby star scaled to the central intensity of RWT 152.

In parallel with the detection of RWT 152, Heber & Drilling (1984) reported the detection of a very faint PN with a diameter of 1.5 arcmin around the sdO LSS 1362, after an inspection of the ESO survey. This object had been observed by Drilling (1983), but no nebular emission was reported then.

From these discoveries, the interest on these peculiar objects grew rapidly and some authors started systematic searches for nebulosity traces surrounding more known sdOs. It is the case of Mendez et al. (1988), who carried out long-slit spectroscopy of 12 sdOs to search for extended emission around them. The observations were obtained with the Boller & Chivens spectrograph mounted in the 2.2m telescope at La Silla Observatory (Chile). Exposure times ranged from 5 to 50 min. For comparison, they also observed, with the same instrumentation, three of the four already known PNe around sdOs: RWT 152, LSS 2018, and LSS 1362. The search resulted in six positive detections: HD 49798 ($H\gamma$ and $H\beta$); LSS 630 ($H\beta$ and $[O\text{ III}]\lambda 5007$); LSE 44 and 153 ($H\beta$ and possibly a very weak $[O\text{ III}]\lambda 5007$); SB 705 and KPD 0720-0003 (possibly a very weak $H\beta$). However, the authors concluded that these emissions were not associated to a PN but due to diffuse, low-excitation ionized regions in the galactic disk. The arguments that support these conclusions were mainly two: no intensity variations were detected along the slit and the low excitation of the obtained nebular spectra. However, the authors also conclude that an image survey was necessary to analyze the morphology of the detected extended emission.

Shortly after, Kwitter et al. (1989) carried out spectroscopy and imaging of a larger sample (45 sdOs, including the already known RWT 152). For the long-slit spectroscopy, the 0.9m telescope at Kitt Peak National Observatory (KPNO) was used. For imaging, two telescopes were used: the 0.9m telescope at KPNO and the 2.2m telescope at Mauna Kea (Hawaii), with field size of 5.7 arcmin^2 and 5 arcmin^2 , respectively. Filters $H\beta$ and $[O\text{ III}]\lambda 5007$ were used in both telescopes as well as the $H\alpha + [N\text{ II}]\lambda 6584$ filter in the second one. Exposure times ranged from 3 to 60 min. The results were discouraging since no convincing detections associated with the sdO stars were observed. They obtained positive results just for the case of RWT 152, for which its spectrum clearly showed $H\beta$ and $[O\text{ III}]$ in emission. Only in three cases (KPD 0549+1948,

KPD 2104+3407, and KPD 2145+4216) they detected faint $H\beta$ in the spectrum. However, they concluded that these emissions were not associated with the sdOs, following the same arguments that those reported by [Mendez et al. \(1988\)](#). Finally, strong $[O\ II]\lambda 3727$ and Balmer lines were also detected in the surroundings of LS IV-12° 1, but they concluded, by measuring the radial velocities of $H\beta$ and $H\gamma$ lines, that the detected emission was associated with the ξ Oph emission nebula, very close on the sky to the sdO.

After these discoveries, the search for nebular emission around sdOs ceased mainly motivated for the lack of detections, and the association of PNe with sdOs was limited to the identification of some already known CSPNe as sdO (see Sect. 2.4).

2.2 Search for new PNe around sdOs in the optical range

As already discussed in Chapter 1, the association of sdOs with PNe is crucial to constrain the origin of these stars. If a large number of sdOs are associated with PNe, a post-AGB origin can be firmly established. If not, post-RGB and post-EHB scenarios would be favored. In this context, searching for new PNe around sdOs is needed to understand whether these systems are the rule or the exception. In addition, studying in detail the properties (morphology, kinematics, chemical abundances, etc.) of all the known PN+sdO systems could shed some light on their formation, that is relevant to understand their scarcity so far.

Although, as stated previously, these searches for new PNe around sdOs have been already conducted at the late eighties, we considered that a new search around a larger number of sdOs, and with modern and advanced instrumentation would be very helpful to contribute drawing definitive conclusions on these systems. It is worth noting that the instrumental characteristics of previous surveys (relatively short exposure times, small field of view) may have prevented from detecting large and/or very faint PNe. Therefore, a new complementary search for PNe around sdOs that accounts for these concerns is desirable. In this framework, we started such a systematic survey with the main goal of increasing the number of identified PN+sdOs systems.

2.2.1 Sample selection

Most of the objects to be imaged were selected from the Subdwarf Database¹ by [Østensen \(2006\)](#). This database is the largest and latest compilation of spectroscopically confirmed hot subdwarfs to date. It contains 2399 entries among sdBs, sdOs and sdOBs. For each entry, the database returns the finding chart of the object, and information such as photometric data, spectral classification and physical properties, if available, with the corresponding references.

¹<http://www.ing.iac.es/ds/sddb/>

FIGURE 2.1: Snapshot of the Subdwarf Database query form, from Østensen (2006).

Figure 2.1 shows a snapshot of the search form from the Subdwarf Database. As can be seen, it permits queries by different fields such as name, coordinates, class, magnitudes, etc. Additionally, we also included in the sample some objects observed by the *Kepler*² mission (Borucki et al., 2003, 2010) and classified as sdOs (Østensen et al., 2010, 2011) but not still incorporated in the Subdwarf Database. In total, we compiled 774 stars, among sdOs and sdOBs, from both northern and southern hemispheres, in our initial sample.

A good selection of the objects (among the so heterogeneous class of sdOs) is very important in order to obtain a high detection ratio. Therefore, from the whole sdOs sample, only those accomplishing certain criteria were selected:

- Firstly, we imposed the condition that the effective temperature (T_{eff}) was higher than ~ 45000 K in order to guarantee the existence of strong ionizing radiation; at these effective temperatures, [OIII] emission is strong in PNe.
- Among those sdOs with available atmospheric parameters (both T_{eff} and surface gravity $-\log g$), we prioritized those located along the post-AGB evolutionary tracks of PNe. In Figure 2.2 we show the position of our sample of sdOs (those having T_{eff} and $\log g$ in the literature, blue symbols) in a $\log g$ versus T_{eff} diagram as compared with a sample of CSPNe (red symbols) taken from Mal'Kov (1997). Post-AGB evolutionary tracks by Bloeker (1995) and Schoenberner (1983) have also been plotted. Although this diagram shows a clear segregation between both samples, there are some sdOs (roughly thirty) that

²<http://kepler.nasa.gov/>

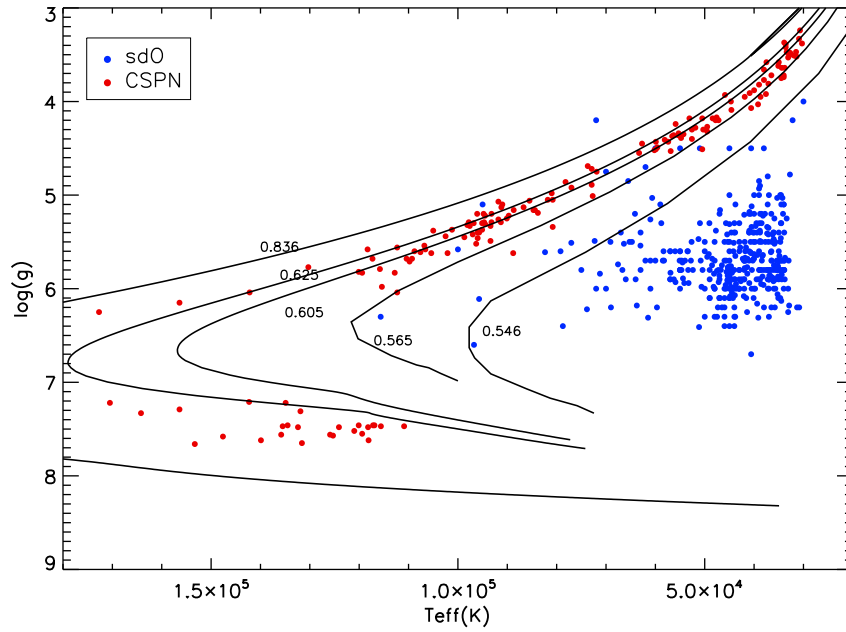


FIGURE 2.2: Location of CSPNe (red) and sdOs (blue) on post-AGB evolutionary tracks by [Bloecker \(1995\)](#) and [Schoenberner \(1983\)](#). Each evolutionary track is labelled with the corresponding stellar mass (in M_{\odot}).

lie in the expected region of CSPNe. Therefore, these sdOs are the best candidates to be CSPNe so we included them with high priority in our final sample.

- Finally, since the large majority of sdOs lacks information about T_{eff} , we also selected those sdOs located at relatively low galactic latitudes ($b \leq |15^{\circ}|$) to increase the probability of being associated to a PN. This is a quite restrictive criterion since sdOs are mainly found at high galactic latitudes while most PNe are located near the galactic plane (see [Fig. 2.3](#)). This distribution is shown in [Figure 2.3](#), where we plot our whole sample of sdOs together with the PNe sample from the catalogue of Galactic PNe that we have built up in this thesis (see [Chapter 7](#)).

Applying all these criteria to the initial sample, we ended up with a final sample of 311 objects.

2.2.2 Optical observations and data reduction

Data were obtained in four different observational campaigns in the course of 2010, 2011 and 2012 (see [Table 2.1](#)). We performed the observations with three different instruments and the observing strategy was similar in all the cases (see below).

In total, 109 objects out of 311 were observed (10 of them in common with the search by [Kwitter et al. \(1989\)](#) and none in common with the search by [Mendez et al. \(1988\)](#)), all visible from the

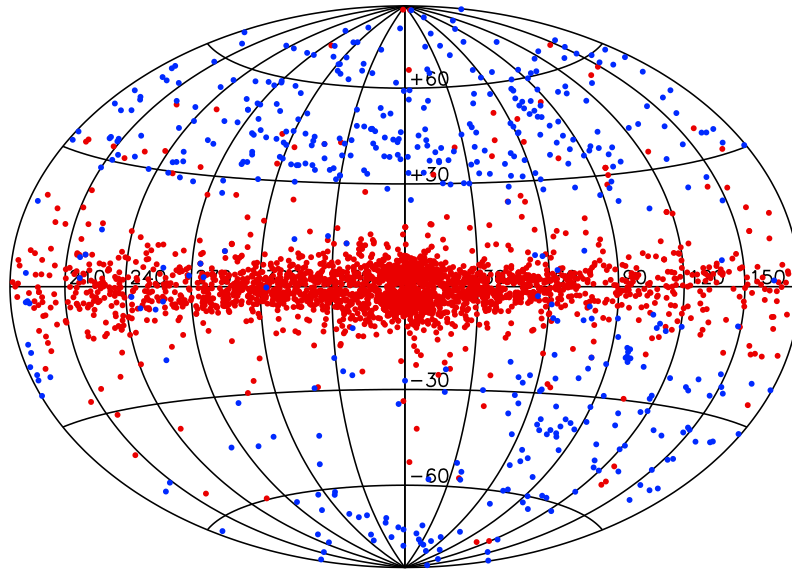


FIGURE 2.3: Galactic distribution of PNe (red) and sdOs (blue). As can be seen, PNe are mainly found near the galactic plane while sdOs are generally located at high latitudes. The PNe sample used in this plot has been obtained from the catalogue of Galactic PNe that we have built up during this thesis (see Chapter 7) for details.

northern hemisphere. The rest of the objects of the final sample could not be observed due to lack of more observational time. Table 2.2 lists the common names of the objects observed (col 1), their equatorial coordinates (col 2 and 3), the instrument used (col 4), and both the filter and exposure time in each case (col 5). A summary of the instrumentation used in each case is described as follows.

We used Calar Alto Faint Object Spectrograph (CAFOS) at the 2.2-m telescope at Calar Alto Observatory³ (Almería, Spain), which permits a rapid change between both direct image and long-slit spectroscopic modes. A SITE 2k×2k-CCD was used as detector, with a plate scale of $0''.53 \text{ pixel}^{-1}$ and a circular field of view (FOV) of $16'$. Images were obtained through the narrow-band filters 501/9 ($\lambda_0 = 6563 \text{ \AA}$, FWHM = 15 \AA) and 656/2 ($\lambda_0 = 6563 \text{ \AA}$, FWHM = 15 \AA), which isolate the $[\text{OIII}]\lambda 5007$ and $\text{H}\alpha$ emission lines, respectively. If extended emission was suspected or detected, long-slit spectra of the brightest nebular region were subsequently obtained. For intermediate-resolution, long-slit spectroscopy gratings B-100 and R-100 were used, that provide a wavelength coverage between 3500 and 9600 \AA (where relevant nebular emission lines of H, N, O, S exist) at a dispersion of 2 \AA pixel that is enough to resolve most of the expected emission lines.

³The Centro Astronómico Hispano Alemán (CAHA) at Calar Alto is operated jointly by the Max-Planck Institut für Astronomie and the Instituto de Astrofísica de Andalucía (CSIC).

TABLE 2.1: Summary of the observational campaigns dedicated to search for new PNe around sdOs.

Semester	Telescope	Instrument	Observatory	Nights
2010B	2.2m	CAFOS	CAHA	14
2010B	INT	WFC	ORM	9
2011B	2.2m	CAFOS	CAHA	8
2012B	1.5m	CCD Vers Array	OSN	13

The Wide Field Camera (WFC) at the 2.5m Isaac Newton Telescope (INT) on El Roque de los Muchachos Observatory⁴ (La Palma, Canary Islands, Spain) was also used. The detector was a four 2k×4k-CCD mosaic with a plate scale of $0''.33 \text{ pixel}^{-1}$ and a FOV of $34' \times 34'$. This large FOV provides a noticeable improvement with respect to the previous searches for PNe around sdOs since allows us to detect very large objects. The filters WFC5008 ($\lambda_0 = 5008 \text{ \AA}$, FWHM = 100 \AA) and WFC6568 ($\lambda_0 = 6568 \text{ \AA}$, FWHM = 95 \AA) were used, which contain the [O III] and $\text{H}\alpha + [\text{N II}]$ emission lines, respectively.

Finally, we also used the CCD Camera mounted at the 1.5m telescope of the Observatorio de Sierra Nevada⁵ (Granada, Spain). This camera provides a FOV of $7.92 \times 7.92 \text{ arcsec}^2$ with a plate scale of $0''.232 \text{ pixel}^{-1}$. The filters #32 and #50 were used, which contain the $\text{H}\alpha + [\text{N II}]$ and [O III] emission lines, respectively.

Images were reduced following standard procedures with specific softwares for image processing and data reduction. First, a careful cosmic ray removal was carried out with ESO-MIDAS⁶ (European Southern Observatory Munich Image Data Analysis System; Banse et al., 1983). Then, the bias subtraction and flat-field correction was performed with IRAF⁷ (Image Reduction and Analysis Facility; Tody, 1986, 1993). Finally, when more than one image was obtained for the same object, we aligned and combine them in order to get a higher signal-to-noise ratio and so detect fainter emissions (if present).

Once completed our survey, nebular emission was only detected around one object: the sdO 2MASS J19310888+4324577. The analysis of this object will be described in detail in Chapter 3. In addition, the low detection ratio of new PNe around sdOs will be discussed in Section 2.5 at the end of this chapter.

⁴The Isaac Newton Telescope is operated on the island of La Palma by the Isaac Newton Group in the Spanish Observatorio de El Roque de los Muchachos of the Instituto de Astrofísica de Canarias.

⁵The Observatorio de Sierra Nevada (OSN) is operated by the Consejo Superior de Investigaciones Científicas through the Instituto de Astrofísica de Andalucía

⁶<http://www.eso.org/sci/software/esomidas/>

⁷<http://iraf.noao.edu/>

TABLE 2.2: Summary of imaging observations.

Object	$\alpha_{(2000.0)}$	$\delta_{(2000.0)}$	Instrument	Exposure time (s)/Filter
PG0011+221	00:14:19.28	22:24:18.14	CAFOS	3x1200/[O III]
LBQS 0015+0216	00:17:57.08	+02:33:31.5	CCDT150	2x2700/[O III]; 2x2700/H α + [N II]
HS0019+3944	00:21:47.32	40:01:23.08	WFC	3x1800/[O III]
HS0024+3331	00:27:22.95	33:48:17.24	CAFOS	(1x1800+1x2700)/[O III]; 1x2700/H α
KPD0033+5229	00:35:52.36	52:45:49.34	CCDT150	2x2700/[O III]; 2x2700/H α + [N II]
PG0039+135	00:42:16.54	13:45:40.55	WFC	3x1800/[O III]
PG0045+251	00:47:55.28	25:20:27.62	CAFOS	3x1800/[O III]
FBS B4	00:49:04.42	+39:50:22.6	CCDT150	2x2700/[O III]; (2x2700 + 1x1200)/H α + [N II]
FB10	00:52:15.07	-10:39:46.00	CAFOS	3x900/[O III]
PG0105+276	01:08:16.65	27:52:51.22	WFC	3x1800/[O III]
J01276+4043	01:27:39.40	40:43:58.00	WFC	3x1800/[O III]; 1x1800/H α
BD+37 442	01:58:33.43	38:34:23.82	CAFOS	1x600/1x400/[O III]
PHL1256	02:19:18.91	03:26:53.21	CAFOS/WFC	3x1800/[O III]
PG0217+155	02:20:35.53	15:44:07.55	CAFOS	3x1800/[O III]
PHL1359	02:34:02.73	-12:42:56.89	CCDT150	2x2700/[O III]; 1x2700/H α + [N II]
Feige26	02:40:04.36	03:55:42.60	WFC	3x1800/[O III]
FBS0244+366	02:47:35.05	36:45:51.10	WFC	3x1800/[O III]
PG0245+182	02:48:07.48	18:26:15.73	CCDT150	2x2700/[O III]; 1x2700/H α + [N II]
HS0258+3003	03:01:27.99	30:15:36.91	CAFOS	(2x1200 + 1x900)/[O III]
PG0310+149	03:13:37.19	15:06:21.53	CAFOS	3x1200/[O III]
HS0312+2225	03:15:15.07	22:36:20.72	WFC	2x1800/[O III]
PG0314+146	03:17:38.05	14:46:25.71	WFC	3x1800/[O III]
KPD0319+4553	03:22:38.95	46:04:34.12	CCDT150	2x2700/[O III]; 2x2700/H α + [N II]
FB29	03:29:05.68	64:04:42.20	CCDT150	2x2700/[O III]; 2x2700/H α + [N II]
HZ3	03:53:31.30	10:45:04.43	CAFOS	(2x900 + 1x1200)/[O III]
KUV 04233+1502	04:26:07.99	15:08:29.01	CAFOS	(2x1200 + 1x1800)/[O III]
KUV 04402+1455	04:43:03.31	15:00:24.67	CAFOS	3x1800/[O III]
KUV 04456+1502	04:48:29.77	15:07:39.92	CAFOS	3x1800/[O III]
HZ1	04:50:13.51	17:42:06.18	CAFOS	(2x600 + 1x900)/[O III]
RWT114	05:11:51.29	41:41:29.14	CCDT150	2x2700/[O III]; 2x2700/H α + [N II]
KUV 05109+1739	05:13:49.72	17:42:03.39	CCDT150	2x2700/[O III]; 2x2700/H α + [N II]
KPD0549+1948	05:52:40.12	19:49:14.04	CAFOS	3x300/[O III]
KPD0552+1903	05:55:40.39	19:04:26.24	CAFOS	3x1200/[O III]
KPD0553+1755	05:56:02.29	17:56:13.57	CAFOS	(2x900 + 1x600)/[O III]
JL129	07:07:03.86	-03:08:54.57	CAFOS	3x1800/[O III]
UVO0711+22	07:14:29.82	22:17:00.20	CCDT150	2x2700/[O III]; 2x2700/H α + [N II]
KPD0720-0003	07:22:56.25	-00:09:37.3	WFC	1x1800/[O III]
HS0735+4026	07:38:56.98	40:19:42.11	CCDT150	2x2700/[O III]; 2x2700/H α + [N II]
FBS0759+413	08:02:59.83	41:14:38.15	CAFOS	3x1800/[O III]
J0828+4040	08:28:01.90	40:40:09.00	CAFOS	3x1800/[O III]
J08396+0308	08:39:36.00	03:08:40.99	CAFOS	1x1800/[O III]
J08443+0753	08:44:23.09	07:53:05.99	CAFOS	1x1800/[O III]
PG0844+232	08:47:18.91	23:00:30.80	CAFOS	1x1800/[O III]
PG0845+129	08:48:44.77	12:41:49.13	CCDT150	2x2700/[O III]; 2x2700/H α + [N II]
PG0848+249	08:51:37.84	24:41:50.71	CAFOS	3x1800/[O III]
FBS0913+819	09:21:19.92	81:43:28.59	CAFOS	(2x900 + 1x1200)/[O III]
BD+37 1997	09:24:26.38	36:42:53.29	CCDT150	3x2700/[O III]; 2x2700/H α + [N II]
PG0924+565	09:28:30.55	56:18:12.25	CAFOS	3x1800/[O III]
FBS0932+627	09:36:12.66	62:27:00.60	CAFOS	3x1800/[O III]
EC09445-0905	09:47:03.37	-09:19:49.07	CAFOS	3x1800/[O III]
J1000-0034	10:00:19.99	-00:34:13.41	CAFOS	3x1800/[O III]
PG1009+069	10:12:13.28	06:40:31.37	CAFOS	1x1800/[O III]

TABLE 2.2: continued.

Object	$\alpha_{(2000.0)}$	$\delta_{(2000.0)}$	Instrument	Exposure time (s)/Filter
PG1036+434	10:39:36.73	43:06:10.64	CAFOS	(3x120 + 1x60)/[O III]; 1x120/H α
HE1047-0637	10:50:28.84	-06:53:25.38	CAFOS	3x1800/[O III]
PG1102+499	11:05:23.15	49:34:59.72	WFC	1x1800/[O III]
HE1106-0942	11:09:08.23	-09:58:47.34	CCDT150	2x2700/[O III]; 2x2700/H α + [N II]
PG1125+295	11:28:29.33	29:15:04.56	CAFOS	3x1800/[O III]
PG1134+463	11:37:30.94	46:00:06.89	CCDT150	1x2700/[O III]; 1x2700/H α + [N II]
J1214+5502	12:14:24.70	55:02:26.00	CAFOS	1x1800/[O III]
TON129	12:48:19.06	03:50:04.49	CAFOS	3x1800/[O III]
J16007+0748	16:00:43.60	07:48:02.99	CAFOS	3x1800/[O III]
J1614+0040	16:14:31.39	00:40:04.00	CAFOS	3x1800/[O III]
J1614+0821	16:14:42.30	08:21:45.00	CAFOS	3x1800/[O III]
PG1624+382	16:26:16.73	38:07:09.90	WFC	3x1800/[O III]
J1628+3532	16:28:25.90	35:32:04.99	CAFOS	4x1800/[O III]
PG1654+322	16:55:52.93	32:08:25.41	CCDT150	2x2700/[O III]/ (2x2700 + 1x600)/H α + [N II]
PG1708+602	17:09:15.90	60:10:10.8	CCDT150	2x2700/[O III]; 1x2700/H α + [N II]
HS1732+7023	17:32:18.97	70:21:28.49	CAFOS	2x1800/[O III]; 1x1800/H α
HS1736+7023	17:35:36.70	70:21:06.99	CAFOS	3x1800/[O III]; 1x1800/H α
HS1736+5521	17:37:23.83	55:20:16.68	WFC	3x1800/[O III]
HS1800+7252	17:59:32.43	72:52:41.22	WFC	3x1800/[O III]; 1x1800/H α
HS1804+4632	18:05:43.60	46:33:10.00	CAFOS	1x1800/[O III]
HS1831+6432	18:31:27.21	64:34:41.45	CCDT150	(2x2700 + 1x600)/[O III]; 1x2700/H α + [N II]
KPD1856+2301	18:58:22.01	23:05:47.32	CCDT150	2x2700/[O III]; 1x2700/H α + [N II]
KPD1903+2540	19:05:36.04	25:45:53.49	CCDT150	2x2700/[O III]; 2x2700/H α + [N II]
J19100+4640	19:10:00.18	+46:40:24.41	WFC	3x1800/[O III]
J19153+4256	19:15:18.9	42:56:13	WFC	3x1800/[O III]
J19244+5305	19:24:29.70	53:05:54	WFC	3x1800/[O III]
J19311+4324	19:31:08.9	43:24:58	WFC	3x1800/[O III]
			CAFOS	(1x1800 + 1x2400)/H α
HS1939+6728	19:39:32.59	67:35:22.49	WFC	3x1800/[O III]; 1x1800/H α
KPD1938+4220	19:39:39.94	42:28:01.79	CCDT150	2x2700/[O III]; 2x2700/H α + [N II]
J19477+4347	19:47:42.88	+43:47:30.68	WFC	3x1800/[O III]
J19569+4350	19:56:55.56	+43:50:17.19	CAFOS	1x1800/[O III]
LSII+2221	20:04:57.58	22:20:40.21	CAFOS	(2x1800 + 1x1459)/[O III]
KPD2048+3515	20:50:03.52	35:27:26.07	CAFOS	2x1800/[O III]
HS2100+0650	21:02:47.65	07:02:28.52	CAFOS	3x1800/[O III]
PG2106+1042	21:06:04.99	10:42:15.00	CAFOS	1x1800/[O III]
KPD2104+3407	21:06:15.67	34:19:14.72	CCDT150	2x2700/[O III]; 1x2700/H α + [N II]
J2024+1337	20:24:40.90	13:37:28.99	CCDT150	2x2700/[O III]; 2x2700/H α + [N II]
PHL4	21:26:21.16	00:58:35.06	CAFOS	1x1800/[O III]
PG2129+151	21:31:40.82	15:16:49.63	CAFOS	1x1800/[O III]
KPD2145+4216	21:47:24.27	42:31:34.69	CCDT150	2x2700/[O III]; 1x2700/H α + [N II]
BD+28 4211	21:51:11.05	28:51:50.90	CCDT150	2x2700/[O III]; 2x2700/H α + [N II]
J2200+1236	22:00:48.70	12:36:11.99	CAFOS	3x1800/[O III]
PG2158+082	22:01:02.37	08:30:49.65	CCDT150	2x2700/[O III]; 1x2700/H α + [N II]
PG2201+145	22:04:03.79	14:46:38.54	CAFOS	1x1800/[O III]
FBS2207+392	22:09:26.04	39:30:18.69	CCDT150	2x2700/[O III]; 2x2700/H α + [N II]
HS2225+2344	22:27:59.8	23:59:36.43	CAFOS	1x1800/[O III]
HS2234+8457	22:32:37.99	85:13:20.29	CAFOS	1x1200/[O III]
HS2231+0749	22:34:18.98	08:05:33.43	CAFOS	1x1800/[O III]
PB5164	22:49:01.54	01:17:23.24	CCDT150	2x2700/[O III]; 1x2700/H α + [N II]
HS2304+0118	23:06:38.14	01:35:10.07	CAFOS	1x1800/[O III]; 2x1800/H α
PG2304+193	23:07:14.57	19:32:19.64	CAFOS	2x1800/[O III]

TABLE 2.2: continued.

Object	$\alpha_{(2000.0)}$	$\delta_{(2000.0)}$	Instrument	Exposure time (s)/Filter
HS2307+3345	23:10:13.90	34:01:55.90	WFC	3x1800/[O III]
PG2321+214	23:24:27.46	+21:38:51.26	CCDT150	1x2700/[O III]; 3x2700/H α + [N II]
KPD2322+4933	23:24:32.74	49:50:55.29	CAFOS	3x1800/[O III]
HS2333-0014	23:35:41.46	00:02:19.74	CAFOS	3x1800/[O III]
PG2352+180	23:55:17.24	18:20:15.50	WFC	3x1800/[O III]

2.3 Hints of possible PNe around sdOs in infrared wavelengths

PNe are strong emitters not only at optical wavelengths but also at other wavelengths as, e.g., the infrared, in many cases revealing different morphologies in different wavelength ranges. For this reason, the studies related to the search for PNe emission in the infrared wavelengths have increased in the late years, by means of large telescopes like the Spitzer Space Telescope (see, e.g., Kwok et al., 2008, Chu et al., 2009) and the Infrared Astronomical Satellite (IRAS). Another example in the mid-IR is the Wide-Field Infrared Survey Explorer (WISE), which provides a database with images of the entire sky taken in four infrared bands: $3.4 \mu\text{m}$ (W1), $4.6 \mu\text{m}$ (W2), $12 \mu\text{m}$ (W3), and $22 \mu\text{m}$ (W4), with angular resolutions of 6.1, 6.4, 6.5, and 12.0 arcsec, respectively. The quantum-efficiency-based response of these bands, taken from Wright et al. (2010), is shown in Fig. 2.4.

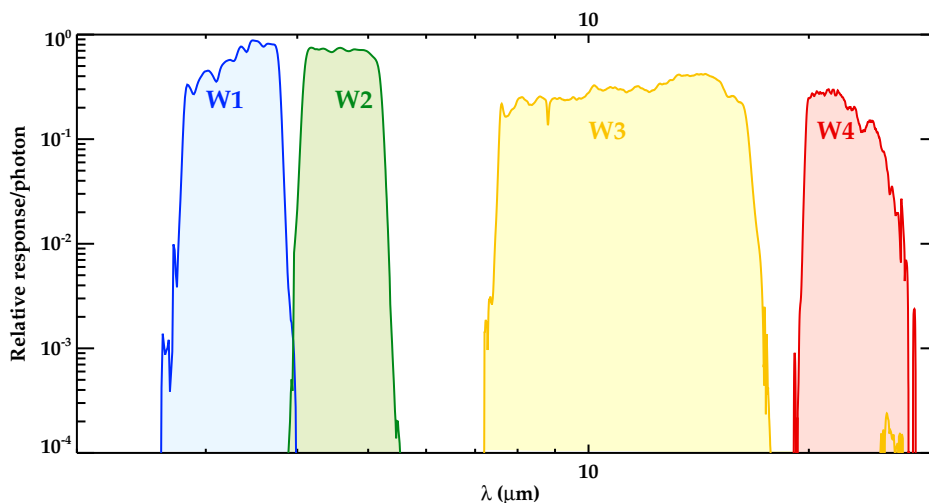


FIGURE 2.4: The quantum-efficiency-based (response per photon) relative system response curves normalized to a peak value of unity, on a logarithmic scale. Transmission data from Wright et al. (2010).

A very illustrative case of how different the morphology of PNe can be at optical and infrared wavelengths is provided by the PN NGC 1514 (a possible PN+sdO system with a binary central

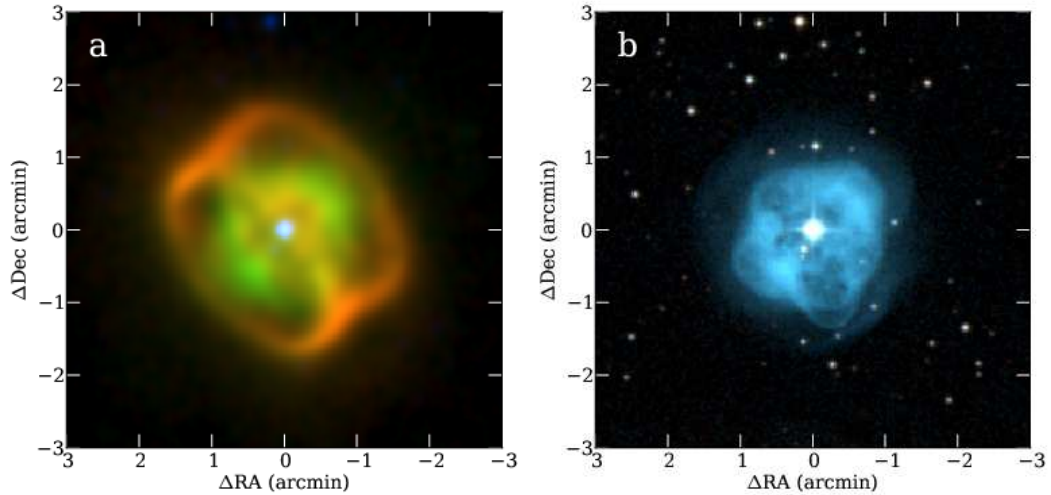


FIGURE 2.5: NGC 1514 as seen in different wavelengths. Left: WISE 3-colour image (blue = W2, green = W3, and red = W4). Right: Visible 3-colour image derived from POSS (blue = B, green = B+R, red = R+I). Credits: [Ressler et al. \(2010\)](#)

star which will be analyzed in detail in Chapter 6). Fig. 2.5 shows both WISE and optical images of NGC 1514 taken from [Ressler et al. \(2010\)](#). As can be appreciated, the WISE 3-colour image reveals well defined structures that are not recognizable in the optical image.

Within this context, we visually inspected in detail the WISE archive images of our whole sdOs sample (774 objects) with the main goal of searching for extended and/or diffuse emission in their surroundings, which may trace the presence of new PNe. This inspection was carried out by checking the four bands of the WISE archive and selecting potential candidates that show extended emission in at least one WISE band either surrounding the star or relatively close to it. We constraint our search to a field of 3×3 arcmin² around the stars to increase the probability that the detected emission was associated to the star. In 12 sdOs nebular emission was detected that fulfilled those criteria, including the recently detected 2M1931+4324 (the WISE data of this object will be further discussed in Chapter 3). Fig. 2.6 shows the mentioned detections for the bands W2, W3, and W4 (W1 images are not shown here because no emissions were detected). Most of them present diffuse emission specially at W3 ($12 \mu\text{m}$) and W4 ($22 \mu\text{m}$) bands, while no nebular emission can be recognized in the W1 and W2 images.

These successful mid-IR detections were consequently requested for imaging in service mode in CAFOS/CAHA, to search for the optical counterparts. Unfortunately, time was only available to observe two objects (FB 29 and UVO 1419-09) but no nebulae were detected in both cases. For the rest of the objects, observing time has not been awarded yet.

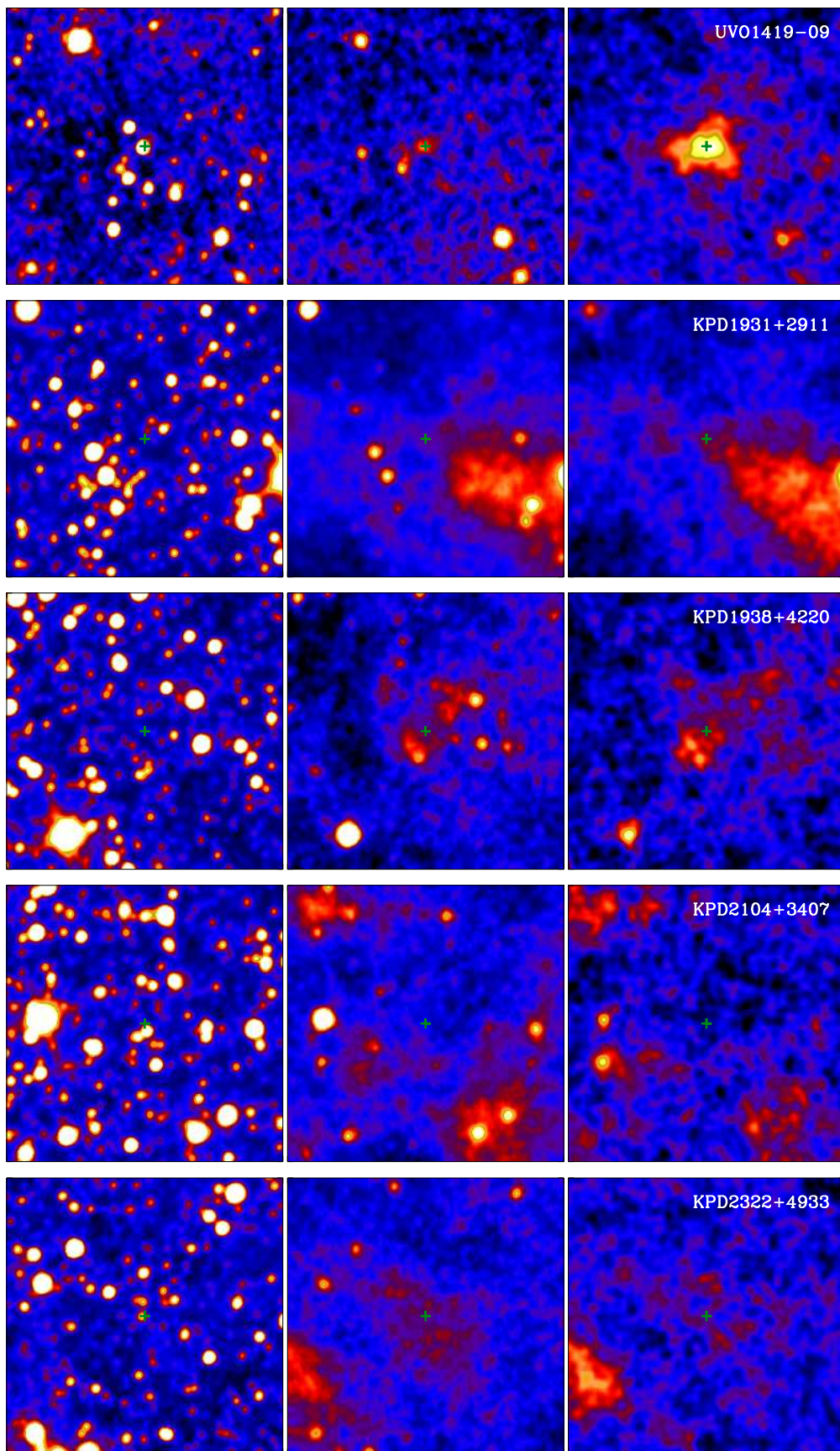


FIGURE 2.6: False colour of W2 (left), W3 (centre), and W4 (right) images of those sdOs with possible traces of nebular emission in their surroundings. The field of view of the images is the same in all cases ($3 \text{ arcmin} \times 3 \text{ arcmin}$) and the orientation is north up, east left. In each panel, the sdO is located at the centre and indicated with a green plus symbol.

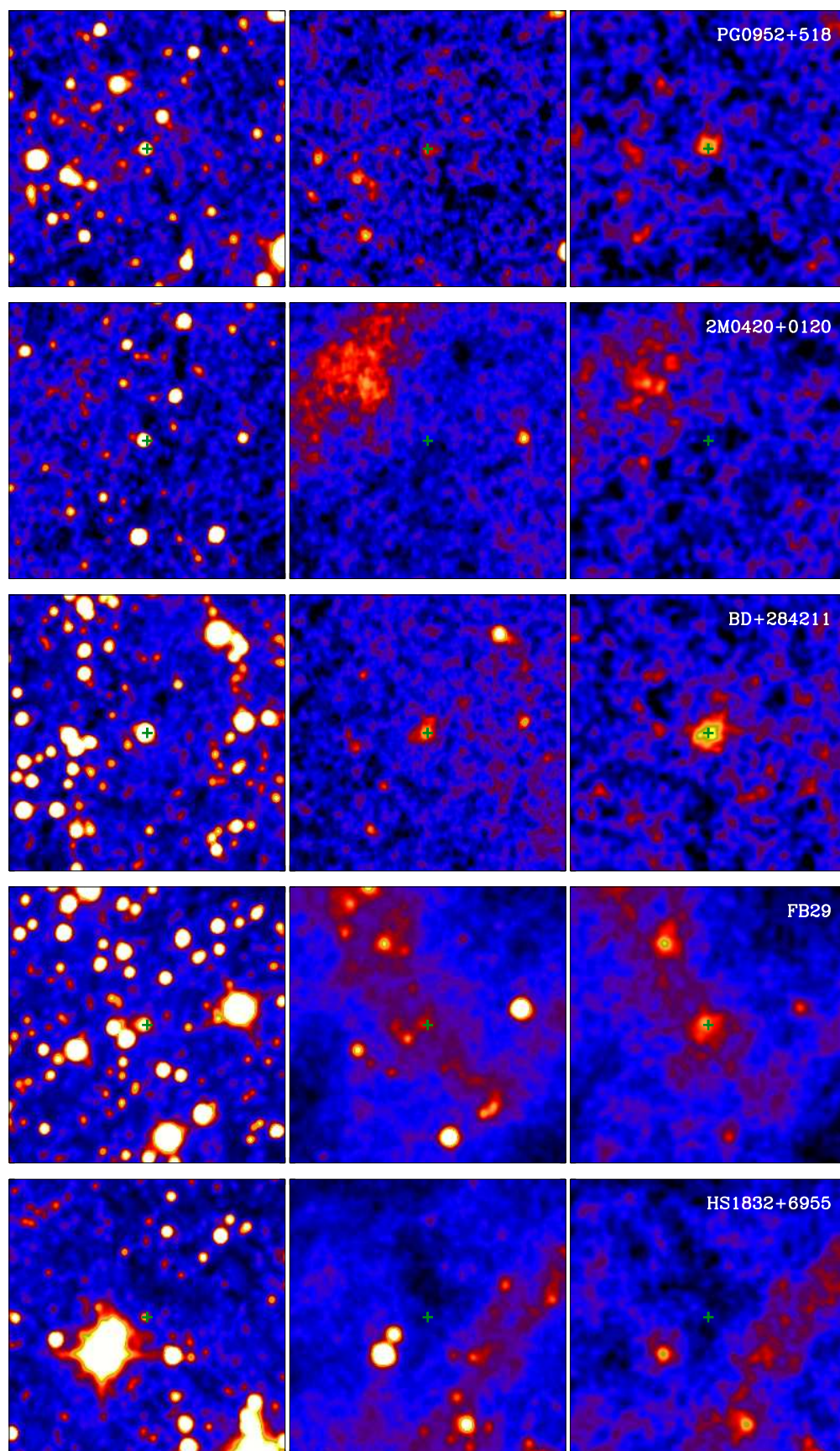


FIGURE 2.6: Continued.

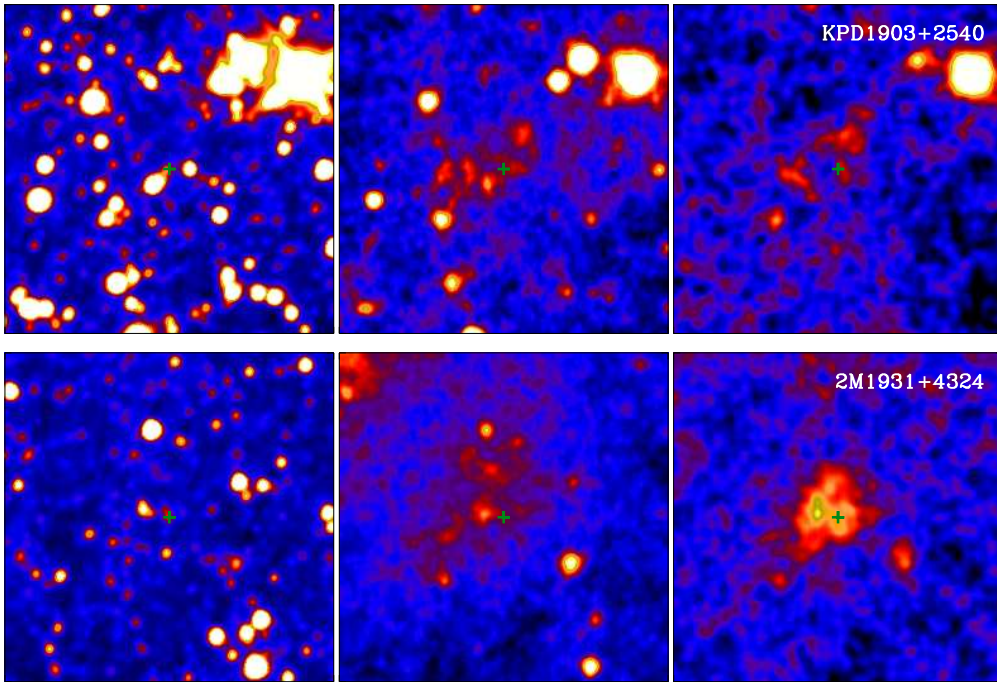


FIGURE 2.6: Continued.

2.4 Search for sdO central stars in known PNe

Up to now throughout this chapter, we have focused on the search for new PNe around sdOs. However, the study of PN+sdO systems can be also addressed from a different point of view: “searching” for sdOs in the nuclei of known PNe. Apart from the already mentioned PNe discovered around sdOs, there is also a small number of known CSPNe that have been classified as sdO by one or more authors. While this classification is firmly established in some of the cases, it is doubtful or controversial in others, with different classifications (including sdO) having been proposed by several authors. For instance, the CS of NGC 2371 is classified as sdO in SIMBAD but as WR-PG 1159 by [Herald & Bianchi \(2004\)](#); the CS of NGC 6026 is classified as WD/sdO by [De Marco \(2009\)](#), as a pre-WD/WD by [Hillwig et al. \(2010\)](#) but as OB by [Weidmann & Gamen \(2011\)](#); in the case of NGC 1514, the hot star in its binary CS has been classified as sdO ([Kohoutek, 1967](#)) but as we will see in Chapter 6, our spectral analysis does not allow us to establish a firm classification.

After an exhaustive search in the literature, we compiled 29 sdOs, either confirmed or possible (i.e., those for which the spectral type has not been confirmed yet), that have been proposed to be the CSs of known PNe. In Table 2.3 we list these systems. In addition, two more objects (K 2-2 and DeHt 2) are included, since we noted in already published spectra ([Napiwotzki & Schoenberner, 1995](#)) that they have similar spectral features to those found in sdOs, although this spectral type has not been previously proposed for these two objects. Table 2.3 contains the common names of the objects (col 1), their equatorial coordinates (col 2 and 3), whether or not

TABLE 2.3: Confirmed and possible PN+sdO systems compiled from the literature (see the text for details).

Object	$\alpha(2000.0)$	$\delta(2000.0)$	Own data	Semester	Instrument	Section
Confirmed PN+sdO systems						
HFG 1	03 ^h 03 ^m 47:0	+64°54′35″.7	✓	2010B	CAFOS	§ 2.4
NGC 2346	07 ^h 09 ^m 22:5	−00°48′23″.6	✗	-	-	-
RWT 152	07 ^h 29 ^m 58:5	−02°06′37″.5	✓	2010B	CAFOS	§ 4.3.3/ 5
He 2–36	09 ^h 43 ^m 25:6	−57°16′55″.6	✗	-	-	-
LSS 1362	09 ^h 52 ^m 44:5	−46°16′47″.5	✗	-	-	-
NGC 3132	10 ^h 07 ^m 01:8	−40°26′11″.1	✗	-	-	-
LSS 2018 (DS 1)	10 ^h 54 ^m 40:6	−48°47′02″.8	✗	-	-	-
LoTr 5	12 ^h 55 ^m 33:7	+25°53′30″.6	✗	-	-	-
Abell 36	13 ^h 40 ^m 41:3	−19°52′55″.3	✓	2013	Mexman-B&Ch	§ 4.3.1
LSE 125 (DS 2)	15 ^h 43 ^m 05:0	−39°18′14″.6	✗	-	-	-
Hen 3–1357	17 ^h 16 ^m 21:1	−59°29′23″.3	✗	-	-	-
Abell 41	17 ^h 29 ^m 02:0	−15°13′04″.4	✗	-	-	-
Abell 46	18 ^h 31 ^m 18:3	+26°56′12″.9	✗	-	-	-
GJC 1	18 ^h 36 ^m 22:8	−23°55′18″.3	✗	-	-	-
2M1931+4324	19 ^h 31 ^m 08:9	+43°24′57″.7	✓	2010B/2011B	WFC/CAFOS	§ 3
Abell 63	19 ^h 42 ^m 10:3	+17°05′14″.4	✓	2010B/2011B	WFC/CAFOS	§ 2.4
K 648	21 ^h 29 ^m 59:4	+12°10′27″.5	✗	-	-	-
Possible PN+sdO systems						
NGC 246	00 ^h 47 ^m 03:3	−11°52′18″.9	✗	-	-	-
NGC 1360	03 ^h 33 ^m 14:6	−25°52′17″.9	✓	2010B	CAFOS	§ 2.4
NGC 1514	04 ^h 09 ^m 16:9	+30°46′33″.5	✓	2011	CAFOS	§ 6
Abell 15	06 ^h 27 ^m 01:8	−25°22′49″.6	✗	-	-	-
NGC 2371	07 ^h 25 ^m 34:7	+29°29′26″.4	✗	-	-	-
Abell 33	09 ^h 39 ^m 09:1	−02°48′32″.0	✗	-	-	-
Be UMa	11 ^h 57 ^m 44:8	+48°56′18″.5	✓	2010B	CAFOS	§ 2.4
PG 1520+525	15 ^h 21 ^m 46:6	+52°22′04″.1	✓	2011B	CAFOS	§ 2.4
NGC 6026	16 ^h 01 ^m 21:1	−34°32′35″.8	✗	-	-	-
NGC 6337	17 ^h 22 ^m 15:6	−38°29′03″.5	✗	-	-	-
Abell 65	19 ^h 46 ^m 34:2	−23°08′12″.9	✗	-	-	-
NGC 7293	22 ^h 29 ^m 38:5	−20°50′13″.6	✗	-	-	-
New candidates for PN+sdO systems (this work)						
K 2-2	06 ^h 52 ^m 23:17	+09°57′55″.7	✓	2010B	CAFOS	§ 2.4
DeHt 2	17 ^h 41 ^m 40:9	+03°06′57″.3	✓	2010B	WFC	§ 4.3.2

our own data were obtained (col 4), the observing date (col 5), and the section where they will be described (col 6).

All the objects marked with a check in the table (except Abell 36 and NGC 1514) were observed in some of the observing runs listed in Table 2.1. Data of Abell 36 and NGC 1514 were obtained during other campaigns (see col 5) and the corresponding observations will be described in detail in the chapters dedicated to these objects. Deep optical images (in H α and/or [OIII] filters) and intermediate-resolution, long-slit spectra were acquired for each object. All images were reduced following the procedure described in Sect. 2.2.2. On the other hand, spectra were reduced following standard procedures for long-slit spectroscopy within the IRAF and MIDAS packages. The first steps of the reduction process are identical to those used for imaging reduction. Firstly, a cosmic ray removal is performed followed by the bias subtraction and flat-field correction. After this basic correction, spectra have to be wavelength calibrated. To do this, arc calibration

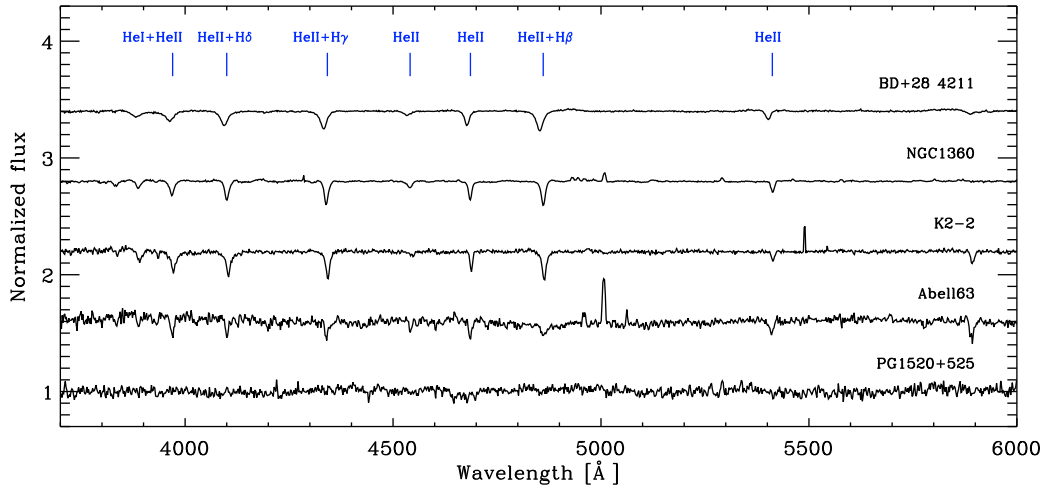


FIGURE 2.7: Normalized spectra of four possible PN+sdO systems as compared with the known sdO BD+28°4211 (top).

images (e.g., ThAr, HgCdAr arc lamps) are obtained, in order to identify and measure the position of the visible spectral features. Once the dispersion axis has been transformed from pixels to wavelengths, the next step is to subtract the background sky from the spectra. Finally, the spectra are flux calibrated using a spectrophotometric standard obtained in the same night as the target.

For some of the objects, a detailed study (sometimes complemented with high-resolution spectroscopy of the nebulae) have been carried out. These objects will be extensively discussed in subsequent chapters: 2M 1931+4324 (Chapter 3), Abell 36 (Chapter 4), DeHt 2 (Chapter 4), RWT 152 (Chapter 4 and 5), and NGC 1514 (Chapter 6). For the remaining observed objects, we present in the following the acquired observations as well as a summary of their main properties:

- *Abell 63*: The nucleus of this evolved and low-surface brightness PN (UU Sagittae) is a well-known eclipsing close-binary system whose primary star has been classified as an sdO star by several authors (Bond et al., 1978, Walton et al., 1993). It has already passed through the CE phase and is currently a pre-cataclysmic (pre-CV) variable star. Pre-CVs refer to semi-detached binaries with a white dwarf (or white dwarf precursor) as a primary and a low-mass secondary that is filling its Roche lobe. The similarities of the CS spectrum of Abell 36 with that of the known sdO BD+28°4211 (see Fig. 2.7) clearly support the sdO classification. Our $H\alpha$ image (taken with WFC/INT), W4 image and the CAFOS nebular spectrum of this PN is shown in Fig. 2.8 (top). In the light of $H\alpha$, the PN shows a cylinder-like structure with a constriction at the waist and bipolar caps connected to the main nebula by faint emission, as already reported by Pollacco & Bell (1997).

Mitchell et al. (2007) confirmed with kinematical data that these caps are likely to be high-velocity outflows from the central binary that have excavated a cavity through the remnant AGB envelope. In W4 image the nebula shows a very different morphology, revealing a non-defined structure much more larger in size than in the optical counterpart. This structure can be only recognized in the W4 filter since in the W3 one (not shown here), the nebula presents the same size as at optical wavelengths. Finally, the nebular spectrum only shows $H\alpha$, $H\beta$, $[O\text{ III}]$ (4959Å, 5007Å, and probably 4363Å) and $He\text{ I}$ (5876Å, 6678Å) emission lines. The $[Ar\text{ III}]\lambda 7135\text{Å}$ emission line may be also present. The spectrum indicates a low excitation, which is atypical for the relatively high effective temperature of the central star (75000-85000 K, Wawrzyn et al., 2009). Furthermore, the lack of low-excitation emission lines as $[N\text{ II}]$ or $[S\text{ II}]$ is highly peculiar. We will see in the next chapters that this characteristic seems to be common in some of the PN+sdO systems.

- *NGC 1360*: The CS of this PN (CPD°389) was initially classified as an sdO (Mendez & Niemelä, 1977, Gleizes et al., 1989) although the O(H) spectral classification was later proposed (Acker et al., 1992). However, the spectral features of our CAFOS spectrum, dominated by strong and narrow ionized helium absorption lines (see Fig. 2.7) clearly points out an sdO classification. Therefore, we can propose this classification for this star. As Fig. 2.8 (middle panels) shows, the nebula presents an elliptical morphology both in the $H\alpha$ and W3 images. A similar morphology is also presented in all WISE bands (not shown here). As in the case of Abell 63, collimated outflows are also present in NGC 1360 (Goldman et al., 2004). Finally, the nebular spectrum indicates a high excitation showing, e.g., $He\text{ II}\lambda 4686$, $[O\text{ III}]\lambda 4363\text{Å}$, 4959Å, and 5007Å.
- *K 2-2*: Although the CS of this PN was classified as a high-gravity O star -hgO(H)- by Napiwotzki & Schoenberner (1995), it was selected in the course of this work since its absorption spectrum shows similar spectral features than those found in the sdO BD+28°4211 (see Fig. 2.7). In view of these similarities, we can tentatively classify it as an sdO and this would add another object to the PN+sdO sample. The nebula (see Fig. 2.8 bottom) shows an irregular morphology that is very similar in the $H\alpha$ and W3 images. It is worth noting that no hints of nebular emission can be recognized in the other WISE bands (not shown here). Our CAFOS nebular spectrum shows $[O\text{ II}]\lambda 3727$, $H\gamma$, $H\beta$, $H\alpha$, $[O\text{ III}]\lambda\lambda 4959, 5007$, $[S\text{ II}]\lambda\lambda 6716, 6731$, and $[N\text{ II}]\lambda\lambda 6548, 6584$, indicating a low excitation.
- *PG 1520+525*: This extremely faint nebula was discovered by Jacoby & van de Steene (1995), who presented an $H\alpha$ image revealing a spherical PN of 11 arcmin of diameter. Surprisingly, our CAFOS $H\alpha$ and $[O\text{ III}]$ images (not shown here) do not reveal any nebular emission. WISE images neither reveal nebular emission in any of its bands. Also, our long-slit blue and red spectra of 1800 s each fail to detect nebular emission. The extreme

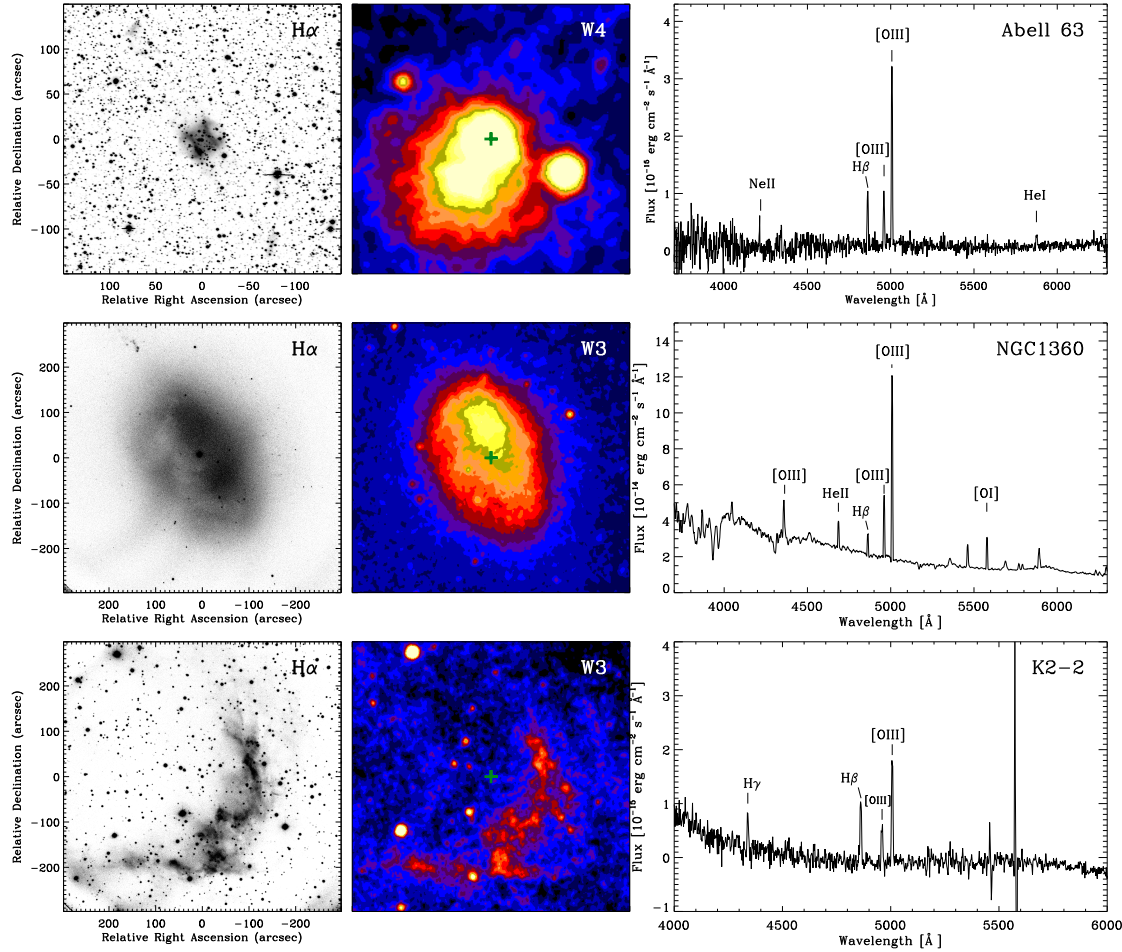


FIGURE 2.8: H α images (left), WISE images (middle), and nebular blue spectra (right) of the PNe Abell 63, NGC 1360 and K 2-2 (from top to bottom respectively). The field of view and orientation of both H α and WISE images are the same in each row. In each panel, the sdO is located at the centre and indicated with a green plus symbol in the WISE image.

faintness of the nebula and the sky conditions (a bright moon) of our CAFOS observations could prevent us from the detection of the nebula. The CS of this PN has been classified as PG1159 and as sdO, sometimes indistinctly, by several authors (see, e.g., [Kwitter et al., 1989](#), [Jacoby & van de Steene, 1993](#)). Our CAFOS CS spectrum is also included in Fig. 2.7. Although the signal-to-noise is very poor, it is clear that the spectrum of PG 1520+525 does not show typical features of sdO, so this PN can be definitively discarded from the PN+sdO sample.

- *Be UMA*: Our CAFOS [O III] image is shown in Figure 2.9 (left upper panel). The nebula presents a barrel-like morphology, and a filament extending towards the northwest. Although no filament can be recognized towards the southeast, it cannot be ruled out that the nebula may be point-symmetric. Deeper images are needed to confirm this. WISE images do not reveal nebular emission in any of its bands. The CS of this faint PN has been classified as an sdO/DAO by [Liebert et al. \(1995\)](#) but as an O(H) by [Napiwotzki](#)

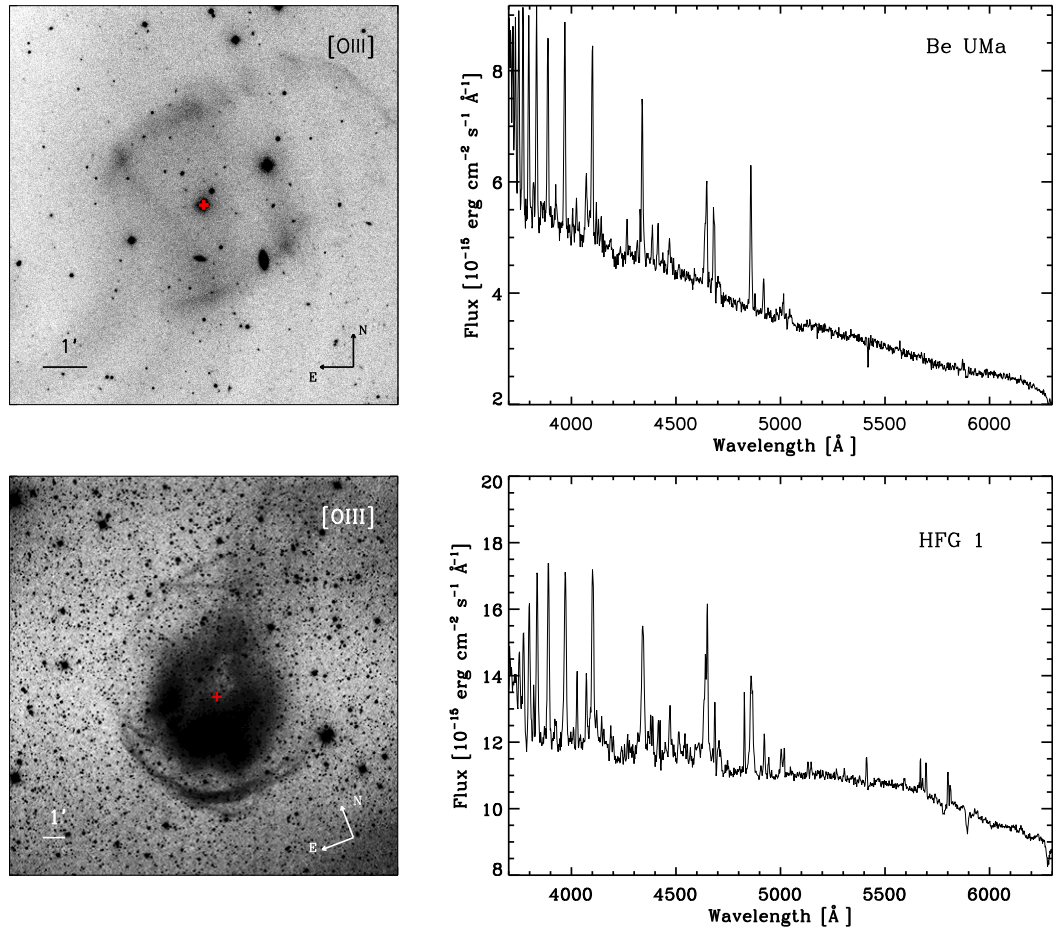


FIGURE 2.9: [O III] images (left) and central star spectra (right) of the PNe Be UMa (top) and HFG 1 (bottom). The red plus symbol in the images mark the position of the central star. Credit of the HFG 1 image: Ken Crawford, <http://www.imagingdeepsky.com/Nebulae/HFG1/HFG1.htm>.

(1999). Our CAFOS CS spectrum (Fig. 2.9, upper right panel) is dominated by emission lines from the nebula, which prevents us from a spectral classification for the CS.

- *HFG 1*: This PN (also known as V664 Cas) is another pre-CVs containing an sdO (Ritter & Kolb, 2003). Our CAFOS images do not reveal the nebula because of its extreme faintness. Fig. 2.9 (left lower panel) shows the image by Ken Crawford, where the singular bock sock-tail morphology of HFG 1, discovered by Boumis et al. (2009), can be recognized. As in the case of Be UMa, our CS spectrum of HFG 1 (see Fig. 2.9, lower right panel) is dominated by emission lines from the nebula and stellar features cannot be observed.

2.5 Discussion

Despite the great efforts dedicated in this thesis to search for new PNe around sdOs, the low detection rate is surprising. Only one new PNe has been identified by imaging in the optical range, which barely represents less than 1% of all the observed sample. In addition, a dozen of our sample of sdOs reveal signs of extended emission in the mid-infrared, although this emission has definitively to be confirmed with optical imaging and spectroscopy. These results appear to be consistent with the low total number of known PN+sdO systems (~ 18 , see Sect. 2.4 and Chapter 4), which represents, as we said, only $\sim 3\%$ of the total spectroscopically classified CSPNe.

This number, however, could be biased by the intrinsic faintness of the associated PNe, and by the lack of a firm classification for many CS of PNe. Very deep images of more sdOs, preferably with large telescopes ($\geq 2\text{m}$ class), and analysis of high-quality CS spectra are necessary to identify new PN+sdO systems. On the other hand, and as already mentioned in Chapter 1, if sdOs originate from low-mass progenitors, the non-detection of more PN+sdO systems could be, at least for a certain fraction of sdOs, a consequence of the dissipation of the nebula before being photoionized, due to the slow evolution of the CS.

It would be very interesting, as already mentioned by [Kwitter et al. \(1989\)](#), to carry out detailed analysis of all of the PN+sdO systems in order to study whether or not systematic trends in their properties are present. These analyses could help us to understand the rarity of finding an sdO with a PN in its surroundings. However, these analysis have never been carried out before. In this context, we will dedicate the next chapters (Chapter 3, 4 and 5), to analyze in detail the morphology, kinematics and spectral characteristics of some of these systems, and to search for properties that may be shared by them.

2.6 Summary and outcomes of this chapter

The main conclusions of this chapter can be summarized as follows:

- (1) By using narrow-band $H\alpha$ and $[OIII]$ filters, we have imaged 109 sdOs as part of a survey to search for new PNe around sdOs. This search resulted in the detection of nebular emission around one object: the sdO 2MASS J19310888+4324577.
- (2) A sample of 774 sdOs was visually inspected in the WISE archive, which provides images in four bands ($3.4\ \mu\text{m}$, $4.6\ \mu\text{m}$, $12\ \mu\text{m}$, and $22\ \mu\text{m}$) in the mid-infrared. 12 of these objects (including 2MASS J19310888+4324577) were selected based on the detection of possible

extended emission, to subsequently be observed in the optical range. Two of them were imaged with CAFOS but no nebulosity were identified in these images.

- (3) A compilation of all known PN+sdO systems from the literature was done. In total, we report 31 confirmed, possible and new candidates sdOs as CSPNe. We describe the observations and the main properties of some of the observed systems in this sample.

Detection of a multishell planetary nebula around the sdO 2M1931+4324

In this chapter we report the discovery of a complex PN around the sdO 2M1931+4324, as a result from our survey to search for new PNe around sdOs. A detailed morpho-kinematic analysis of this PN based on imaging and high-resolution spectroscopy is presented. Narrow-band optical images reveal, for the first time, a very faint multishell PN around 2M1931+4324. We also show mid-IR images from the WISE archive¹, in which the nebula is detected. Complementary intermediate- and high-resolution, long-slit spectra allow us to confirm the sdO/central star nature of 2M1931+4324, to describe the nebular emission spectrum, and to analyze the internal kinematics of this complex nebula. This discovery adds a new object to the small sample (~ 18) of known PN+sdO systems. This chapter has been adapted from [Aller et al. \(2013\)](#) (A&A, 552, A25) and updated with the more recent information published on the object.

3.1 Introduction

As mentioned in the previous chapters, studying the association of sdOs with PNe is essential for obtaining the fraction of sdOs that have a post-AGB origin. To briefly remind the reader, only a few (~ 18) PN+sdO systems have been reported to date. This number includes the four “classical” PNe discovered around known sdOs in the early eighties: LSE 125 and LSS 2018 ([Drilling, 1983](#)), LSS 1362 ([Heber & Drilling, 1984](#)), and RWT 152 ([Pritchett, 1984](#)); and several already known PNe (~ 14) whose central stars have been later classified as sdOs (see [Chapter 2](#) for a review of this topic).

In this framework, and as a part of the results obtained in our survey carried out to observationally search for and to analyze PN+sdO associations (see [Chapter 2](#)), we present the discovery of

¹<http://irsa.ipac.caltech.edu>

a PN around 2MASS J19310888+4324577 (hereafter 2M1931+4324; $\alpha(2000.0) = 19^h 31^m 8^s.9$, $\delta(2000.0) = +43^\circ 24' 58''$; $l = 075^\circ.99$, $b = 11^\circ.6$), which has been firstly spectroscopically classified as an sdO by Østensen et al. (2010). The discovered PN is extremely faint and presents a complex structure. We note that in the red and blue plates of the Palomar Observatory Sky Survey (POSS), the nebula can be guessed only at very low intensity levels. Recently, De Marco et al. (2015) have analyzed *Kepler* photometric data of 2M1931+4324 (Kepler ID 7755741²) and found that it is a non-eclipsing, post-CE binary star with a period of 2.928 days. In such analysis, the authors conclude that the companion of the sdO is most likely a white dwarf.

3.2 Observations and results

3.2.1 Optical imaging

A narrow-band [O III] image was obtained on 2010 August 22 with the WFC at the INT on El Roque de los Muchachos Observatory, with the same configuration to that described in Chapter 2. We used an [O III] filter ($\lambda_0 = 5008 \text{ \AA}$, FWHM = 100 \AA) to obtain three images with an exposure time of 1800 s each. The sky was clear with an average seeing value of $\approx 1''.3$.

A narrow-band $H\alpha$ image was obtained on 2011 July 12 with CAFOS at the 2.2m telescope on Calar Alto Observatory, also with the same configuration to that described in Chapter 2. We used an $H\alpha$ filter ($\lambda_0 = 6563 \text{ \AA}$, FWHM = 15 \AA) to obtain two images of 1800 s and 2400 s. Weather conditions were fair and seeing was $\approx 2''$. The images were reduced using standard procedures for direct image within the IRAF and MIDAS packages.

Figure 3.1 shows the $H\alpha$ and [O III] images of 2M1931+4324 that reveal the existence of a very faint and complex nebula around the star. In $H\alpha$ two structures can be recognized: a bipolar shell with a size of $\approx 4'.3 \times 1'.7$ and the major axis oriented at position angle (PA) $\approx 55^\circ$, and an elliptical shell with a size of $\approx 5' \times 1'.8$ and the major axis oriented at PA $\approx 145^\circ$. The polar regions of the elliptical shell are very faint and, in fact, the elliptical shell seems to be open. The nebula is particularly bright in the regions where both shells cross each other, while the shells enclose regions of lower intensity. The nebula is very weak in [O III], suggesting low excitation (see Sect. 3.2.3.3). Additionally, the [O III] image reveals a long filament outside the two shells, which extends from the north towards the southeast of the two shells, ending in a diffuse emission region. While the diffuse emission could also be present in $H\alpha$, the filament is not detected in this line, indicating very high excitation. We note that 2M1931+4324 is not located at the centre of the shells but displaced $\approx 10''$ towards PA $\approx 235^\circ$, approximately coinciding with the orientation of the minor (major) axis of the bipolar (elliptical) shell. The presence of two axisymmetric shells around a hot sdO star (see Sect. 3.2.3.1) strongly suggests

²http://archive.stsci.edu/kepler/data_search/search.php

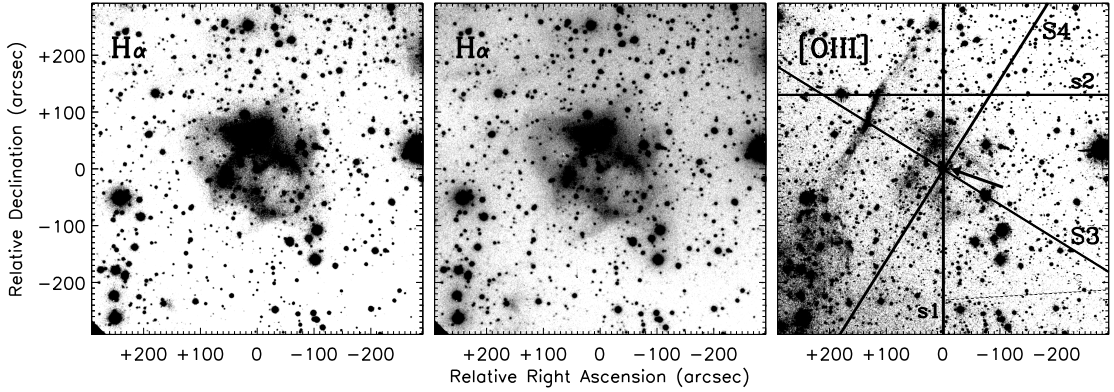


FIGURE 3.1: Grey-scale reproductions of the $H\alpha$ (left and centre) and $[O\text{ III}]$ (right) images of 2M1931+4324. Grey levels are linear and two different levels are used to show the $H\alpha$ image. The slits s1 and s2 (S3 and S4) used for intermediate (high) resolution, long-slit spectroscopy are plotted on the $[O\text{ III}]$ image (slit width not to scale) in which 2M1931+4324 is also arrowed.

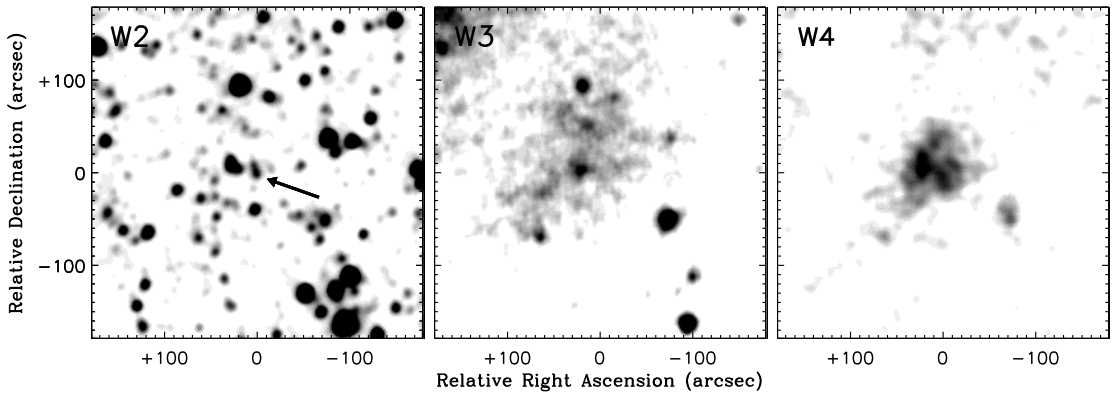


FIGURE 3.2: Grey-scale reproductions of the WISE 2 ($4.6\ \mu\text{m}$), WISE 3 ($12\ \mu\text{m}$), and WISE 4 ($22\ \mu\text{m}$) images of 2M1931+4324. The grey levels are linear and arbitrary, and have been chosen to emphasize the more relevant nebular features. 2M1931+4324 is arrowed in the WISE 2 image, while it is not detected in the WISE 3 and WISE 4 images.

a PN nature for the nebula. Following the designation scheme for Galactic PNe by [Acker et al. \(1992\)](#), we tentatively propose the name PN G 075.9+11.6 for this nebula, and we refer to it hereafter as such.

3.2.2 Mid-infrared imaging

To investigate this PN further, we inspected the NASA's WISE database which, as mentioned in Chapter 2, is a space telescope designed to map the entire sky in four infrared bands: $3.4\ \mu\text{m}$ (W1), $4.6\ \mu\text{m}$ (W2), $12\ \mu\text{m}$ (W3), and $22\ \mu\text{m}$ (W4). Because we are interested in the nebular morphology, we retrieved the W1 to W4 images in the atlas, which have a spatial scale of $1''.375\ \text{pixel}^{-1}$.

Figure 3.2 shows the W2, W3, and W4 images around 2M1931+4324 (W1 is not shown here). While no nebula can be recognized in the W1 and W2 images, the W3 and W4 ones show

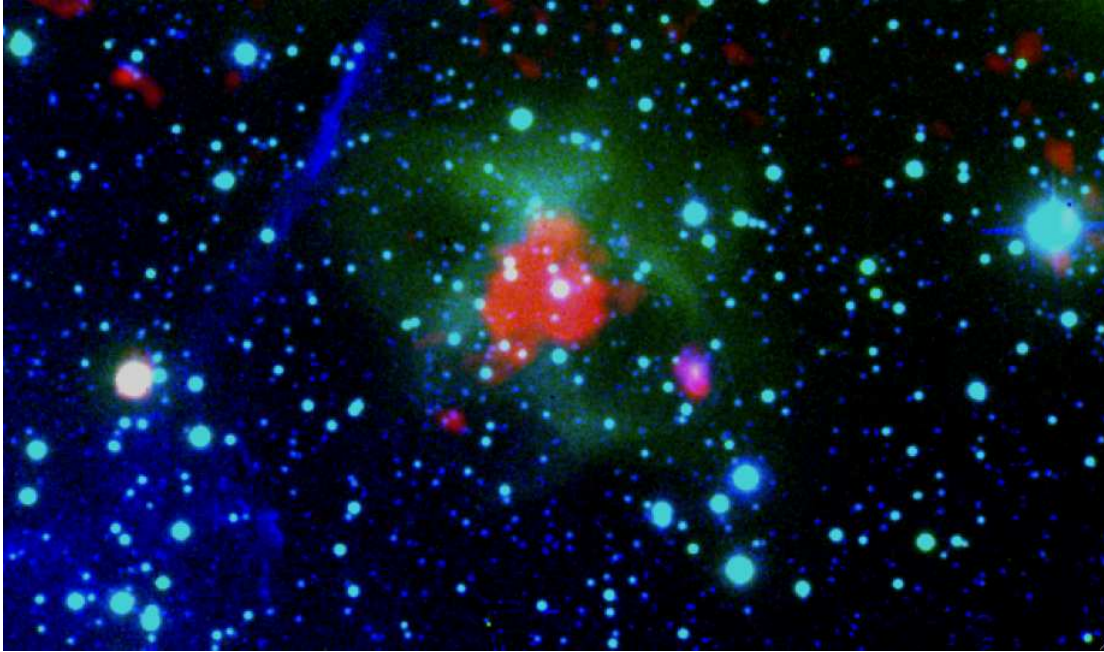


FIGURE 3.3: Colour-composite image of PN G 075.9+11.6. Red corresponds to WISE 4 ($22\ \mu\text{m}$), green to $\text{H}\alpha$, and blue to $[\text{O III}]$. North is up, east to the left. The size of the field shown is $10'.5 \times 6'.1$. The red knot near the tip of the southwestern bipolar lobe is probably a galaxy that is also observed in the optical images.

nebulous emission that seems to be related to PN G 075.9+11.6. In W3, very weak extended emission is detected in a region of $\approx 3'.1 \times 1'.5$ in size oriented at $\text{PA} \approx 145^\circ$. The orientation is similar to that of the elliptical shell described in Sect. 4.2.1, although the nebulosity observed in W3 is displaced towards the northeast with respect to the elliptical shell observed in $\text{H}\alpha$. In W4, extended emission is observed in a region of $\approx 50''$ in size at the centre of the nebula, and it presents an irregular, knotty morphology. The origin of the $12\ \mu\text{m}$ and $22\ \mu\text{m}$ emission associated to PN G 075.9+11.6 is difficult to establish without a spectrum. In principle, $[\text{S IV}]$ and $[\text{Ne III}]$ emission lines could contribute to the emission observed in W3, and $[\text{O IV}]$ emission line could be partially included in what is observed in W4 (see Ressler et al., 2010). However, the absence of (prominent) high-excitation emission lines in the optical spectrum (e.g., $[\text{Ne III}]$, see Sect. 3.2.3.3) seems to suggest that the mid-infrared emission is due to cool dust associated to the nebula. We also note that 2M1931+4324 itself is detected in W1 and W2, but not in W3 and W4.

To analyze the morphological relationship between the emission observed at $22\ \mu\text{m}$ (W4) and in the optical images, we present a colour-composite image obtained by combining $\text{H}\alpha$, $[\text{O III}]$, and W4 in Figure 3.3. This image shows that the $\text{H}\alpha$ emission dominates in the bipolar shell and outer regions of the elliptical shell. The $[\text{O III}]$ emission comes mainly from the regions where the bipolar and elliptical shells cross each other, and it is the dominant emission in the high-excitation filament and diffuse region. The emission at $22\ \mu\text{m}$ traces only a part of the

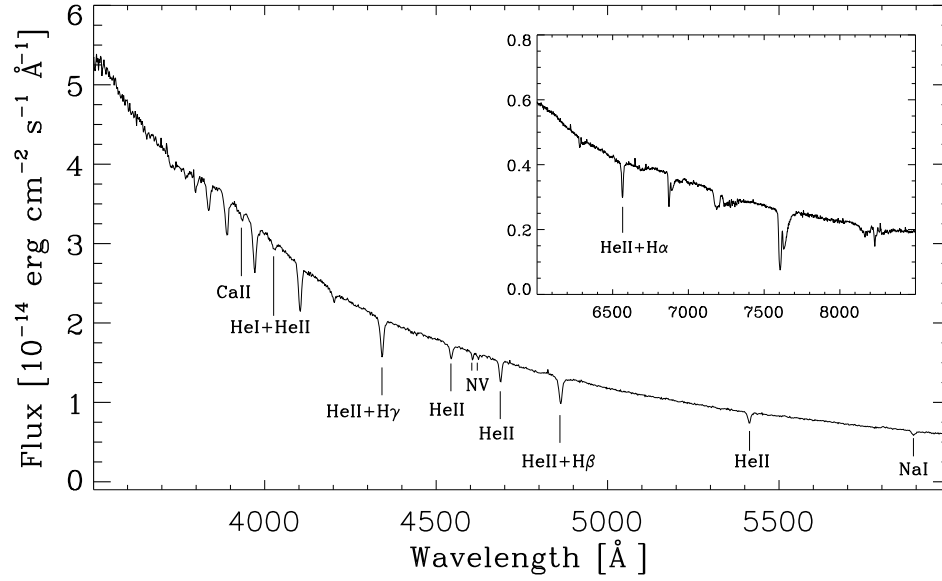


FIGURE 3.4: CAFOS CAHA blue spectrum of 2M1931+4324 in the range 3500–6000 Å. The inset shows the CAFOS CAHA red spectrum. Some helium, hydrogen, and N v absorption lines are indicated, as well as the Ca II λ 3968 and Na I λ 5895 in absorption.

northwestern border of the elliptical shell, and it is also detected in a region surrounding the central star.

3.2.3 Intermediate-resolution optical spectroscopy

Intermediate-resolution, long-slit spectra were acquired on 2011 July 13 with CAFOS. Gratings B-100 and R-100 were used to cover the 3200–6200 Å and 5800–9600 Å spectral ranges, respectively, both at a dispersion of $\approx 2 \text{ \AA pixel}^{-1}$. The slit width was $2''$ and spectra were obtained at two slit positions: one (denoted s1) with the slit oriented north–south, centred on 2M1931+4324 and with an exposure time of 3600 s for each grism, in order to cover 2M1931+4324 and the brightest nebular regions; and another (s2) with the slit oriented east–west, centred $2.2''$ northern of 2M1931+4324 and with an exposure time of 2400 s for each grism, in order to register the outer filament. These slits are also shown in Fig. 3.1. The spectrophotometric standard HZ 44 was also observed for flux calibration. The sky was clear and seeing was $\approx 2''$. The spectra were reduced using standard procedures for long-slit spectroscopy within the IRAF and MIDAS packages.

3.2.3.1 The stellar spectrum of 2M1931+4324

Figure 3.4 shows the optical spectrum of 2M1931+4324. It is dominated by strong ionized helium and hydrogen Balmer absorptions that are blended with the corresponding He II Pickering lines. The narrowness of the absorption lines and the presence of the He II λ 4686 line indicate

an sdO nature for 2M1931+4324, in agreement with the classification by [Østensen et al. \(2010\)](#). We also note the presence of $N\text{v}\lambda\lambda 4604, 4620$ absorption lines that are observed in some sdOs ([Husfeld et al., 1989](#), [Rauch et al., 1991](#)) and which indicate a maximum limit for the T_{eff} of 115 000 K ([De Marco et al., 2015](#)). On the other hand, the lack of $\text{He}\text{I}\lambda 4471$ in absorption suggests a $T_{\text{eff}} \geq 60\,000$ K ([Rauch et al., 1991](#)), which is high enough to produce the ionization of the nebula. Therefore, we can say, with a high probability, that 2M1931+4324 is the central star of the nebula. Finally, a careful inspection of the spectrum reveals $\text{Ca}\text{II}\lambda 3934$ and $\text{Na}\text{I}\lambda\lambda 5890, 5895$ absorption lines. These absorptions lines could be attributed to a late type companion, although they also are strong features of the interstellar medium. The first possibility can be now ruled out on the basis of the variability analysis recently carried out by [De Marco et al. \(2015\)](#) (see below).

3.2.3.2 The stellar spectral energy distribution: from g band to WISE

To obtain more information about 2M1931+4324, we constructed its spectral energy distribution (SED) with the available photometry: the g, r, i, and z magnitudes from the *Kepler* Input Catalog (KIC, [Brown et al., 2011](#)), the J, H, and K_s magnitudes from the 2MASS Point Source Catalog³, and the W1 and W2 magnitudes from the WISE archive. Figure 3.5 presents the SED, including our optical spectrum. Because the red part of the SED is barely sensitive to T_{eff} for hot central stars, we have plotted in Fig. 3.5 a blackbody with $T_{\text{eff}} = 70\,000$ K, as a guide to what could be expected from extrapolating the stellar continuum of our red spectrum. The blackbody has been reddened by $A_V = 0.04$ (corresponding to $c(H\beta) = 0.02$, see Sect. 3.2.3.3) and normalized at the r_{KIC} magnitude. Fig. 3.5 shows that the KIC, near-, and mid-infrared magnitudes agree reasonably well with those we expected from a blackbody with $T_{\text{eff}} \geq 60\,000$ K. Moreover, no noticeable infrared excess can be recognized in the SED of 2M1931+4324.

Atmospheric parameters of 2M1931+4324 have been recently determined by [De Marco et al. \(2015\)](#), who obtained $T_{\text{eff}} = 70\,000$ K and $\log g = 5.2\text{--}5.4$ cm s^{-2} by fitting TMAP atmospheres models with pure hydrogen and helium composition and a helium mass fraction of 0.4. Also in that work, an exhaustive variability study of 2M1931+4324 (named J19311) is presented, which allows us to put constraints on the nature of the companion. By using light and radial velocity curves obtained with *Kepler*, they concluded that 2M1931+4324 is a short-period (2.928 days), post-CE binary with a compact companion, most likely a white dwarf. Figure 3.6 shows the light and radial velocity curves reported by [De Marco et al. \(2015\)](#). While no signs of eclipses are found in the light curve, the authors interpret the variability as due to both Doppler beaming and ellipsoidal effects. They obtained a range for the inclination of the system of $40^\circ\text{--}88^\circ$, and constrained the radius and mass of the CS to $0.27 < R_{\text{CS}}/R_{\odot} < 0.35$ and $0.55 < M_{\text{CS}}/M_{\odot} < 0.70$,

³<http://irsa.ipac.caltech.edu>

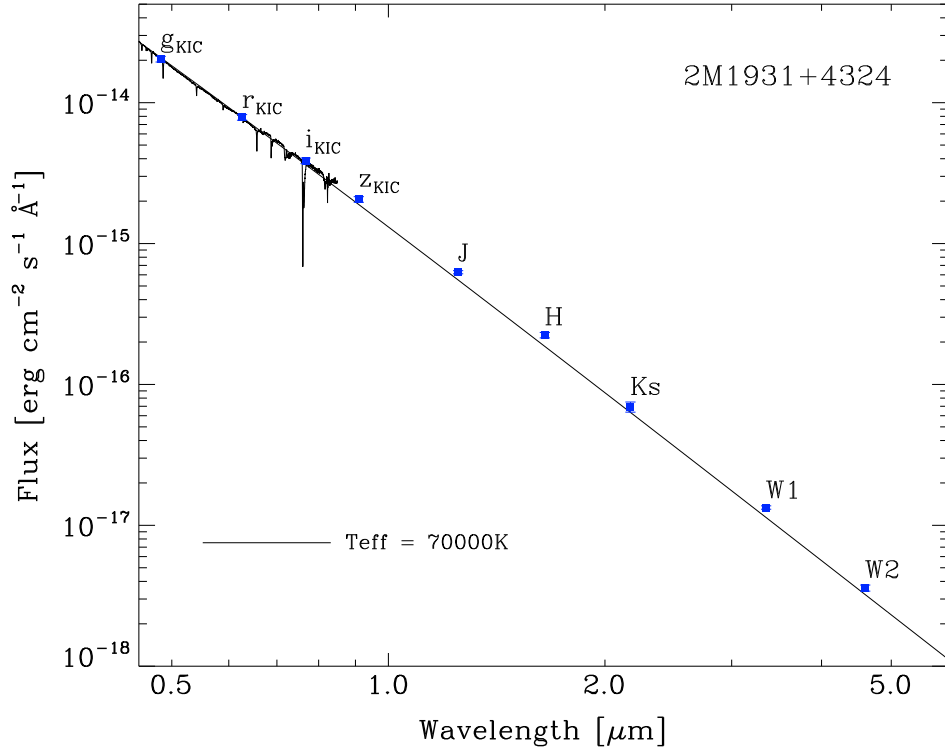


FIGURE 3.5: Spectral energy distribution (SED) of 2M1931+4324 constructed with the magnitudes from the Kepler Input Catalog (KIC), 2MASS Point Source Catalog, and WISE archive. The blue and red CAPOS spectra (see Fig. 3.4) are also included. The solid line corresponds to a blackbody with $T_{\text{eff}} = 70000$ K, reddened by $A_V = 0.04$ (see text) and normalized to the r_{KIC} magnitude.

respectively. Finally, a range for the companion mass of $0.68 < M_{CS}/M_{\odot} < 1.4$ was found. This result is compatible with the lack of infrared excess in the SED of 2M1931+4324.

3.2.3.3 The nebular spectrum

In the nebular spectrum obtained at s1 (Fig. 3.1), only faint $H\alpha$, $H\beta$, and $[\text{O III}]\lambda\lambda 4959, 5007$ emission lines are detected. Figure 3.7 presents the integrated spectra around these lines. The underreddened line intensities and their Poissonian errors are listed in Table 3.1. They have been obtained using the extinction law of Seaton (1979) and a logarithmic extinction coefficient $c(H\beta) \approx 0.02$ derived from the observed $H\alpha/H\beta$ ratio, assuming Case B recombination ($T_e = 10^4$ K, $N_e = 10^4 \text{ cm}^{-3}$) and a theoretical $H\alpha/H\beta$ ratio of 2.85 (Brocklehurst, 1971).

The $[\text{O III}]/H\beta$ line intensity ratio of ≈ 1.6 (Table 3.1) and the absence of $\text{He II}\lambda 4686$ indicates a very low-excitation PN. However, the lack of prominent low-excitation emission lines, in particular due to $[\text{N II}]$, is highly peculiar. In fact, (low-excitation) bipolar PNe usually present strong $[\text{N II}]$ line emission that is not detected from the bipolar shell of PN G 075.9+11.6. It could be that PN G 075.9+11.6 is a density bounded PN with no low-excitation region or a very high-excitation PN with very weak $[\text{O III}]$ line emission due to the prevalence of O^{3+} in the nebula.

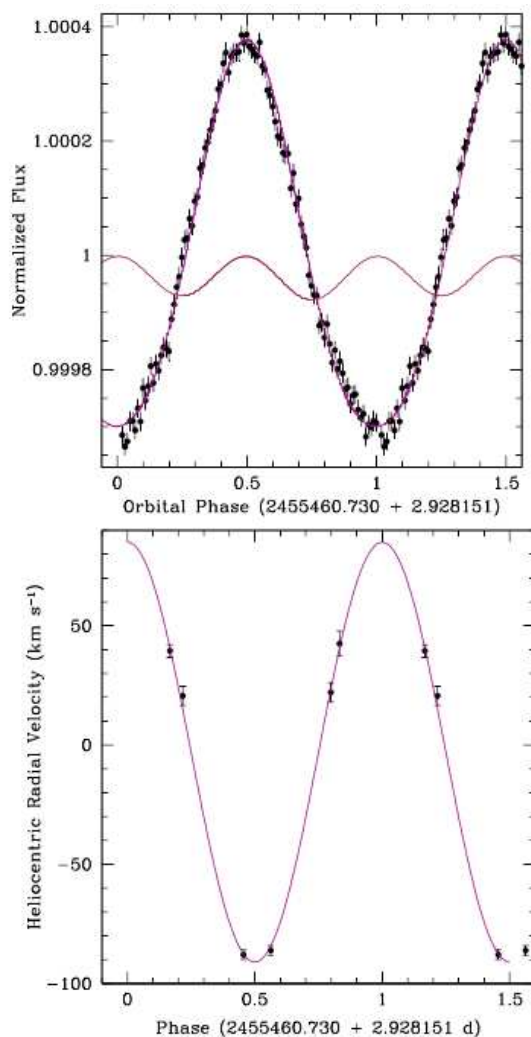


FIGURE 3.6: Light (upper panel) and radial velocity curves (lower panel) of 2M1931+4324. The solid line corresponds to the best model fitting to the curves. In particular, the small amplitude curve in the upper panel represents the fit to the ellipsoidal modulation. Credits Image: [De Marco et al. \(2015\)](#).

Although the existence of (very) high-excitation is suggested by the outer filament, the absence of other high-excitation emission lines (e.g., He II, [Ar V], [Ne IV]) in the optical spectrum makes these possibilities questionable. Alternatively, the nebula could be strongly deficient in heavy elements. This possibility would be compatible with both low and high excitation in the nebula, and seems to be the only one that accounts for the observed spectrum. This strong deficiency of heavy elements may also provide information about the progenitor of the central star. Since one would expect that metal-poor PNe had formed in the early stages of the Galaxy, this would mean that they took long time to evolve. This would point to a low-mass progenitor of say, $\leq 1 M_{\odot}$ (see, e.g., [Vázquez et al., 2002](#)) for 2M1931+4324. This value is compatible with the range of masses obtained by [De Marco et al. \(2015\)](#) for the central star (see above) and also with the relatively high Galactic latitude of the object (see [Stanghellini et al., 2002](#)). A much deeper nebular spectrum is needed to identify more (presumably extremely faint) emission lines and to

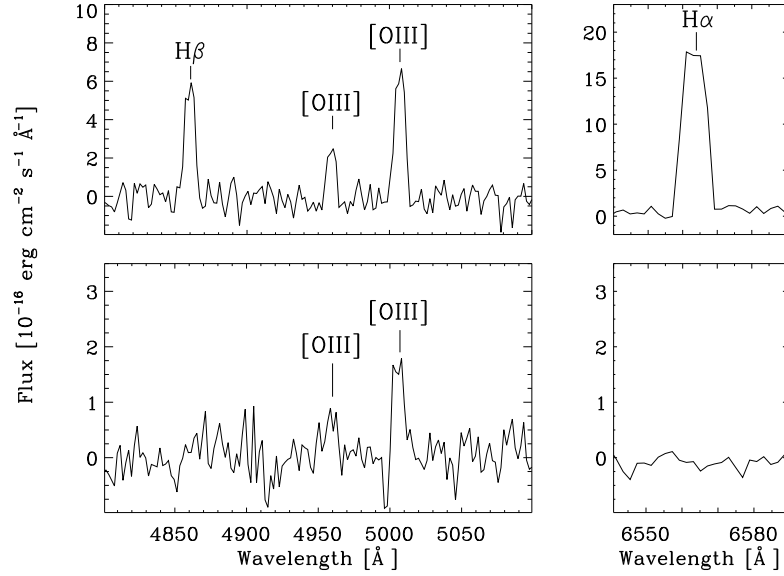


FIGURE 3.7: (*top*) CAFOS CAHA spectra of the detected nebular emission lines from PNG 075.9+11.6. The spectrum has been obtained by integrating the detected emission lines at s1 (see Fig. 1) between 38'' and 75'' north of 2M1931+4324. (*bottom*) Spectrum of the high-excitation filament. The spectrum has been obtained by integrating the detected [O III] λ 5007 emission line at s2 (see Fig. 1) in a region of 8'' centred on the filament.

obtain elemental abundances, which will allow us to derive a much more accurate initial mass for the central star.

The spectrum of the outer filament obtained at s2 (see Fig. 3.1) is also shown in Fig. 3.7. Only very faint [O III] $\lambda\lambda$ 4959,5007 line emission is detected (observed [O III] λ 5007 flux $\sim 1.7 \times 10^{-15}$ erg cm $^{-2}$ s $^{-1}$), confirming its very high-excitation. Similar outer filaments and knots are observed in other PNe (e.g. NGC 40 Balick et al., 1992). In the case of PNG 075.9+11.6, our data do not allow us to establish whether the outer structures are related to mass ejection from 2M1931+4324, or whether they are instead ambient gas ionized by the central star. Nevertheless, we note that the optical and mid-infrared images do not show any nebulosities (except for those detected in our images) in the environment of PNG 075.9+11.6.

3.2.4 High-resolution spectroscopy

High-resolution, long-slit spectra were obtained on 2012 May 14 and 15 with the Manchester Echelle Spectrometer (Meaburn et al., 2003) at the 2.1 m telescope on the OAN San Pedro Mártir Observatory⁴ (Baja California, Mexico). The detector was a 2k \times 2k Marconi CCD that was employed with a 4 \times 4 binning, resulting in spectral and spatial scales of 0.11 Å pixel $^{-1}$ and 0''.702 pixel $^{-1}$, respectively. A $\Delta\lambda = 90$ Å filter was used to isolate the 87th order containing the H α emission line. The slit (6' long, 2'' wide) was set on 2M1931+4324 and spectra were

⁴The Observatorio Astronómico Nacional at the Sierra de San Pedro Mártir (OAN-SPM) is operated by the Instituto de Astronomía of the Universidad Nacional Autónoma de México

TABLE 3.1: Emission line intensities in PN G 075.9+11.6.

Line	$f(\lambda)$	$I(\lambda) (I(\text{H}\beta)=100)$
H β λ 4861	0.000	100 \pm 3
[O III] λ 4959	-0.023	37 \pm 3
[O III] λ 5007	-0.034	113 \pm 3
H α λ 6563	-0.323	285 \pm 4
$c(\text{H}\beta) = 0.02$		
$\log F_{\text{H}\beta}(\text{erg cm}^{-2} \text{s}^{-1}) = -14.31$		

obtained at two slit PAs: PA 58° (denoted S3) and PA 148° (S4). These slits are also shown in Fig. 3.1. In the case of PA 58°, two spectra were secured with the slit on 2M1931+4324 but displaced from each other along PA 58°, and these two spectra were combined in a single long-slit spectrum. Exposure time was 1800 s for each spectrum. A Th-Ar lamp was used for wavelength calibration to an accuracy of $\pm 1 \text{ km s}^{-1}$. The resulting spectral resolution (FWHM) is 12 km s^{-1} . Seeing was $\simeq 2''$ during the observations. The spectra were reduced with standard routines for long-slit spectroscopy within the IRAF and MIDAS packages.

Observing through a long slit allows us to simultaneously obtain spectra of each point of the PNe covered by the slit. Each spectrum provides information about both intensity of the emission lines and their wavelengths, at each specific point (spatial position). The intensity and wavelength may vary along the slit, tracing variations in the different parts of the nebula. If the long-slit spectrum is obtained at high resolution, different kinematic components of the PN can be observed, as they are separated according to their radial velocity (i.e., their wavelength) due to the Doppler effect. By easily transforming the wavelength axis into radial velocity (by using the corresponding rest wavelength of the observed emission line) and the spatial axis into an angular scale (by using the plate scale of the instrument), we directly obtain a so-called position-velocity (PV) map. This is basically the radial velocity profile of the PN along the slit in a specific emission line, which contains the intensity information in each point (usually represented with a colour map). Figure 3.8 shows an illustration for the most simple case: a spherical PN. In the top panel, we show a front-view of the nebula with the position of the slit (orange vertical lines) overplotted. In the bottom left panel, the expansion velocity vectors of the PN are shown (in yellow) together with their radial (i.e., those in the line of sight, in blue) and perpendicular (i.e., those perpendicular to the line of sight, in white) velocity components. Finally, in the bottom right panel, the resulting high-resolution spectrum along the slit, with the wavelength (or radial velocity) in the x-axis and the pixel of the CCD (or angular scale) in the y-axis. As the radial velocity decreases from the middle of the nebula towards its edges (where the radial velocity component vanishes), a velocity ellipse results in the high-resolution, long-slit spectrum. In this ellipse, one can identify the parts of the nebula that are blueshifted (that is, moving towards us) and those redshifted (that is, moving away from us). As mentioned, this is

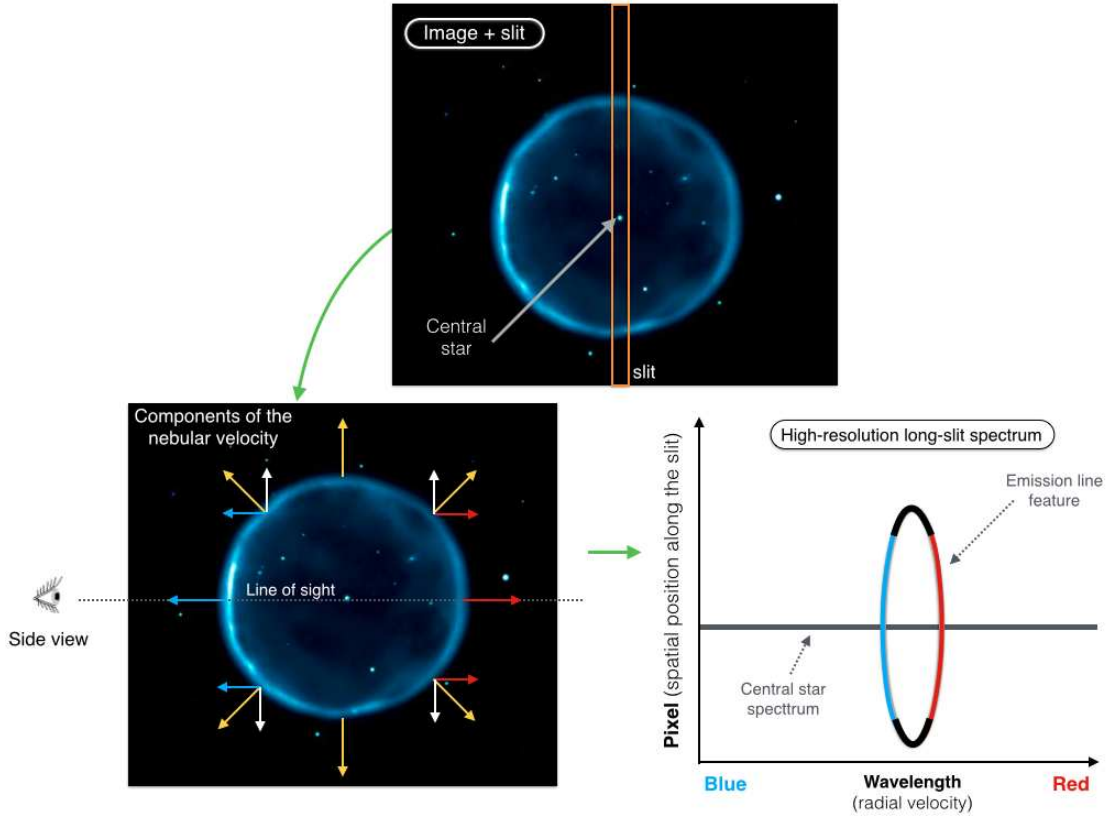


FIGURE 3.8: Illustration of simulated high-resolution, long-slit spectra (right lower panel) constructed from specific image+slit configurations (upper panel). In the left lower panel, the radial velocity components are plotted. The high-resolution spectra can be easily transformed to position-velocity maps by using the pixel scale of the instrument and the Doppler effect equation (see the text for details).

the most simple case; depending on the kinematical components present in the nebula, the PV map may be very complex.

Figure 3.9 shows PV maps of the $H\alpha$ emission line at the two observed PAs. Although the $H\alpha$ emission is weak, it shows details of the internal kinematics of PNG 075.9+11.6. From the velocity centroid of the line emission feature we derive a heliocentric systemic velocity of $-16 \pm 2 \text{ km s}^{-1}$. Internal radial velocities will be quoted hereafter with respect to the systemic velocity.

The PV map at PA 148° (Fig. 3.9) mainly covers the major axis of the elliptical shell. It shows two extended velocity components with almost constant radial velocities of $\approx \pm 16 \text{ km s}^{-1}$. The two components appear mainly parallel to the spatial axis in the PV map, although a slight tilt ($\approx 1\text{--}2 \text{ km s}^{-1}$ in $\approx 4'$) could be present with the northwestern (southeastern) region slightly blueshifted (redshifted). The PV map at PA 58° (Fig. 3.9) covers the major axis of the bipolar shell and shows a more complex kinematics. Two velocity components are observed at the stellar position with radial velocities of $\approx \pm 16 \text{ km s}^{-1}$. Towards the southwest, the radial velocity of the two components increases up to $\approx \pm 23 \text{ km s}^{-1}$ at $\approx 50''$ from the central star and then it

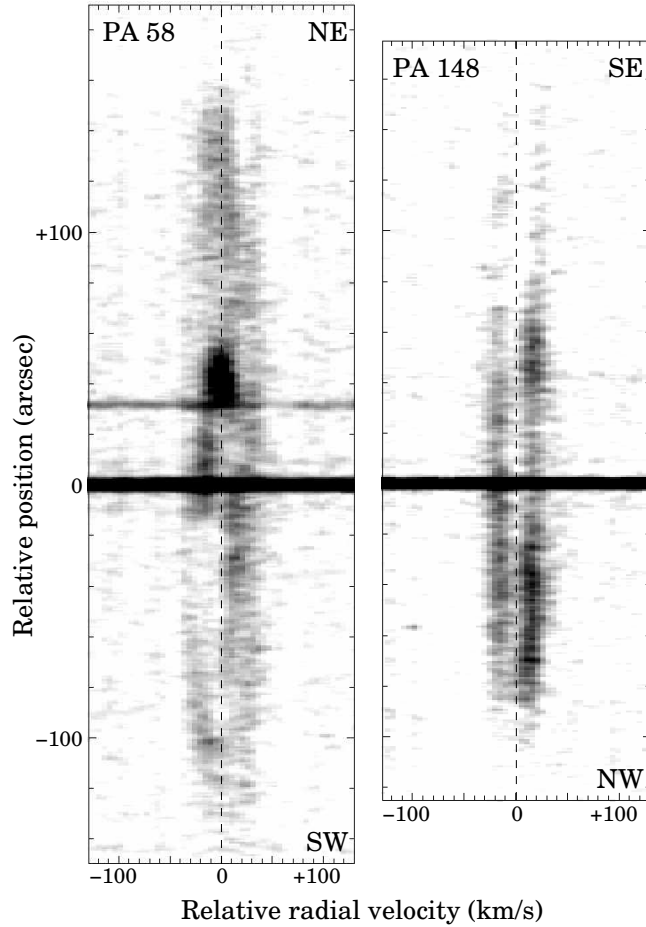


FIGURE 3.9: Grey-scale position-velocity maps of the $H\alpha$ line observed at two slit position angles (upper left). The origin (0,0) corresponds to the systemic velocity and the position of the central star. The grey-scale is linear. A 3×3 box smooth was used for the representation.

decreases until the two velocity components merge at the systemic velocity, at the southwestern tip of the bipolar shell. An additional, faint velocity component can be identified between $\approx 20''$ and $\approx 80''$ southwestern from the central star, with radial velocities between ≈ 10 and $\approx 0 \text{ km s}^{-1}$, respectively. This component could be related to the elliptical shell or indicate complex motions in the southwestern lobe of bipolar shell. Towards the northeast, up to $35''$ from the central star, two velocity components are also recognized with radial velocities of $\approx -15 \text{ km s}^{-1}$ and $\approx 25 \text{ km s}^{-1}$. At $\approx 40''$ from the central star, a bright feature is observed at the systemic velocity, which coincides with a bright region observed in the images (Fig. 3.1) and may correspond to the northeastern edge of the elliptical shell. At angular distances $> 50''$ towards the northeast, the emission feature does not show two velocity components but a single, relatively broad feature mainly at the systemic velocity. This suggests that the northeastern lobe may contain material expanding at lower velocities than the surface of the shell. Finally, the radial velocity of the northeastern tip of the bipolar shell coincides with the systemic velocity.

The kinematics of the elliptical shell observed at $PA 148^\circ$ rules out that this shell corresponds to the projection of a tilted ring, as the images could suggest. If this was the case, one would

not detect emission from the inner regions of the shell, but only from the two “points” of the ring intersected by the slit. The possibility of an oblate (equatorial) ellipsoid, such as the one identified in Mz 3 (Guerrero et al., 2004), may also be ruled out because one would expect to see in the PV map at PA 148° decreasing radial velocities from the position of the central star to the tips of the elliptical shell, which is not observed. The presence of two spatially extended velocity components almost parallel to the spatial axis is compatible with a cylindrical (or open ellipsoidal) shell whose major axis is in (or close to) the plane of the sky. The equatorial expansion velocity of this shell is $\approx 16 \text{ km s}^{-1}$, and if we assume homologous expansion (velocity proportional to radius), the expansion velocity at the observed maximum size ($\approx 2'.5$, see Sect. 4.2.1) is $\approx 45 \text{ km s}^{-1}$. From the equatorial expansion velocity and the equatorial radius of the elliptical shell ($\approx 0'.9$, Sect. 4.2.1), a kinematic age of $\sim 1.6 \times 10^4 \times D[\text{kpc}] \text{ yr}$ is obtained for this structure.

The PV map at PA 58° , along the main axis of the bipolar shell, is compatible with the kinematics expected from bipolar motions in an hour-glass-like shell. The main axis of the bipolar shell should be located in the plane of the sky, as indicated by the absence of tilt of the $\text{H}\alpha$ emission feature on the PV map. The equatorial expansion velocity of the bipolar shell is $\approx 16 \text{ km s}^{-1}$, while the polar one is $\approx 43 \text{ km s}^{-1}$ (also assuming homologous expansion), which are virtually identical to those of the cylindrical shell. From the equatorial expansion velocity and equatorial radius ($0'.85$, Sect. 4.2.1) of the bipolar shell, a kinematic age of $\sim 1.5 \times 10^4 \times D[\text{kpc}] \text{ yr}$ is obtained for this structure, which is very similar to that of the cylindrical shell. The kinematic ages of the shells are compatible with an evolved PN. Moreover, the similarity between the kinematic ages suggests that the formation of the two shells has occurred in a short time span, as compared with the age of the nebula.

3.3 Discussion

The detection of PNG 075.9+11.6 around the sdO/central star 2M1931+4324 adds a new object to the known sample of sdO+PN associations and, therefore, a new sdO whose origin can be ascribed to post-AGB evolution. It is worth noting that 2M1931+4324 is quite bright ($r_{\text{KIC}} \approx 13^m.9$) compared to most central stars of PNe. That such a “bright” central star has gone unnoticed to date can be understood by its association with an extremely faint PN that cannot be recognized in the POSS with a simple visual inspection of the plates. In this respect, it should be mentioned that Jacoby et al. (2010) have recently identified a relatively large number of new PNe using the POSS plates, most of them at the detection limit of the plates. It is also noteworthy that PNG 075.9+11.6 and a large fraction of the new PNe identified by Jacoby et al. (2010) are located at relatively high Galactic latitudes ($|b| > 6^\circ$) and, therefore, cannot be identified in recent PN surveys that are concentrated more towards the Galactic plane (e.g., Parker et al., 2005, Drew

[et al., 2005](#)). A survey for PNe at higher Galactic latitudes may result in the identification of many new PNe (see [Miszalski et al., 2011](#), and references therein).

The existence of two shells in PNG 075.9+11.6 indicates that complex ejection processes have been involved in the formation of the nebula. As already mentioned, the ejection of the two shells should have occurred in a relatively short time span (as compared with the age of the nebula). Moreover, the location of the two major axes, mainly in the plane of the sky, and the difference of $\simeq 90^\circ$ in their orientation indicate that the major axes are (virtually) perpendicular to each other. Therefore, the central star has been able to eject two shells in a relatively short time span, including, in addition, a large change of $\sim 90^\circ$ in the orientation of the main ejection axis. These results, involving episodic ejections and changes in the orientation of the main ejection axis, are difficult to interpret within a single star scenario but fit in the framework of binary central stars in which they may be explained as a result of stellar interactions, mass transfer, and precession of the collimating agent. In fact, PNe with multiple structures at different orientations, such as quadrupolar or multipolar ones, are usually interpreted invoking a binary central star (e.g., [Manchado et al., 1996a](#), [Guerrero et al., 2013](#), and references therein). In this respect, the structure of PNG 075.9+11.6 and the binary nature of 2M1931+4324 ([Jacoby et al., 2012](#), [De Marco et al., 2015](#)) provide support for a binary star scenario in multishell PNe and reinforce the idea that binary stars are an important ingredient in the formation of complex PNe ([De Marco 2009](#), and references therein; [Miszalski et al. 2009b](#), [Miszalski 2012](#), [Boffin et al. 2012](#)).

Within the context of PNe with binary central stars, we note the off-centre position of 2M1931+4324 with respect to the nebular shells. This situation has already been observed in other PNe (e.g., [Sahai et al., 1999](#), [Miranda et al., 2001b](#)) and interpreted as a result of a possible binary central star ([Soker et al., 1998](#), and references therein). The binary nature of 2M1931+4324 supports this interpretation. Peculiar in PNG 075.9+11.6 is the very large difference between the orientation of the two shells. Other quadrupolar or multipolar PNe do not usually show such large differences in the orientation of the shells ([Manchado et al., 1996a](#)), although they have been observed in a few cases (see [Guillén et al., 2013](#), and references therein). In an axisymmetric PN with a binary central star, the orientation of the main nebular axis may be expected to be perpendicular to the orbital plane of the binary. If so, the orbital plane of 2M1931+4324 should have been almost parallel to the line of sight (or somewhat tilted, as eclipses are not observed, [De Marco et al., 2015](#)) when each shell was formed, but it has rotated by $\sim 90^\circ$ between the ejections. This would imply a dramatic change in the angular momentum of the binary star system, which is not easy to explain. On the other hand, the generation of axisymmetric shells in PNe may be due to other mechanisms (collimated outflows, magnetic fields, see, e.g., [Balick & Frank, 2002](#)) so that the main nebular axis should not be necessarily related to the orbital plane of a binary central star. Nevertheless, very large changes in orientation of the collimating agent would still be required. In any case, PNG 075.9+11.6 and its binary central star 2M1931+4324 present characteristics that make this system another interesting case for studying the formation

of PNe with binary central stars, as, e.g., ETHOS 1 and Fleming 1 (Miszalski et al., 2011, Boffin et al., 2012).

The role of the binary 2M1931+4324 in the formation of PN G 075.9+11.6 could be even more crucial if the nebula is strongly deficient in heavy elements and the central star evolves from a low-mass progenitor, since single stars with low initial mass are expected to form spherical PNe but not axisymmetric and multishell ones (e.g., Vázquez et al. 1999, 2002; Stanghellini et al. 2002, and references therein). Besides obtaining elemental abundances in the nebula, in order to confirm a possible deficiency of heavy elements, estimating the atmospheric parameters of 2M1931+4324 will allow us to constrain the initial mass of the progenitor.

3.4 Summary and outcomes of this chapter

Using deep $H\alpha$ and $[O\text{ III}]$ images we have detected a very faint nebula around the sdO 2M1931+4324, recently found to be a binary star. The nebula presents a bipolar and an elliptical shell, as well as high-excitation structures outside the two shells. Faint emission from the central nebular regions is also detected at $12\ \mu\text{m}$ and $22\ \mu\text{m}$ in archive WISE images. Analysis of the internal nebular kinematics, by means of high-resolution, long-slit spectroscopy, reveals a bipolar shell and a cylindrical (or open ellipsoidal) shell with their major axes mainly perpendicular to each other. In addition, very similar expansion velocities are found in the two shells that were formed within a relatively short time span.

Our intermediate-resolution spectrum of 2M1931+4324 confirms its sdO classification and indicates a $T_{\text{eff}} \geq 60\ 000\ \text{K}$, strongly suggesting a PN nature for the detected nebula that is tentatively referred to as PN G 075.9+11.6. The detection of 2M1931+4324 adds a new object to the known sdOs associated with a PN and to the sdOs with a post-AGB origin.

A recent spectral analysis of the central star carried out by De Marco et al. (2015) have determined $T_{\text{eff}} = 80\ 000$ and $\log g = 5.2\text{-}5.4\ \text{cm s}^{-2}$ for the sdO 2M1931+4324. In that work, a variability study of this star has also revealed a short period (2.928 days), post-CE binary system, with a most likely a white dwarf as a companion.

The spectrum of PN G 075.9+11.6 exhibits only $H\alpha$, $H\beta$, and $[O\text{ III}]$ emission lines that indicate a very low-excitation ($[O\text{ III}]$ to $H\beta$ intensity ratio ≈ 1.6), in strong contrast to the absence of other low-excitation emission lines. The possibility of a very high nebular excitation is difficult to reconcile with the absence of other high-excitation emission lines, suggesting that PN G 075.9+11.6 might be deficient in heavy elements, a fact that should be confirmed by means of very deep spectroscopy and elemental abundance calculations.

The analysis of the spatiokinematical structure of PN G 075.9+11.6 indicates that 2M1931+4324 has been able to eject two axisymmetric shells in a relatively short time span, as compared with the age of the nebula of $\sim 1.6 \times 10^4 \times D[\text{kpc}]$ yr, as derived in the present work. Between these two events, the main ejection axis has rotated by $\sim 90^\circ$ in such a way that the two main nebular axes are perpendicular to each other and, in both cases, oriented almost in the plane of the sky. The complexity of PN G 075.9+11.6 and the binary nature of 2M1931+4324 provide strong support to the idea that binary central stars are a key ingredient for generating complex PNe.

The physical structure of planetary nebulae around sdO stars: Abell 36, DeHt 2, and RWT 152

In this chapter we present the first detailed morpho-kinematic analysis of Abell 36, DeHt 2, and RWT 152, three PNe with sdO central stars, by means of narrow-band H α and [O III] images, and high-resolution, long-slit spectra. These data are complemented with intermediate-resolution, long-slit spectroscopy of the three objects, which allow us to describe the spectral properties of the CSs and nebulae. Finally, we report a compilation of the *bona fide* classified PN+sdO systems to date and discuss their possible common properties. This chapter has been adapted from [Aller et al. \(2015a\)](#) (MNRAS, 446, 317).

4.1 Introduction

Abell 36 and RWT 152 are two faint PNe with sdO CSs and neither their morphology nor their kinematics have previously been analysed in detail. Abell 36 was discovered by [Abell \(1966\)](#) using the Palomar Observatory Sky Survey (POSS) plates and was later imaged by [Hua & Kwok \(1999\)](#). Its bright ($B \simeq 11.3$ mag) CS was initially classified as O(H) by [Acker et al. \(1992\)](#) and as sdO by [Kilkenny et al. \(1997b\)](#). Later, it was incorporated to the Subdwarf Database¹ by [Østensen \(2006\)](#). RWT 152 is also included in this data base as an sdO, although it was previously classified as an O5 star by [Chromey \(1980\)](#). The PN around RWT 152 was discovered by [Pritchett \(1984\)](#) who found a slightly elongated nebulosity after subtracting the image of a nearby star from the image of RWT 152 itself. We have also noticed that the CS of DeHt 2 has similar spectral features to those found in sdOs (see [Napiwotzki & Schoenberner, 1995](#), their

¹<http://www.ing.iac.es/ds/sddb/>

TABLE 4.1: Common names, PNG designations, coordinates, and atmospheric parameters of the CSPNe for the objects discussed in this chapter.

Object	PNG	$\alpha(2000.0)$	$\delta(2000.0)$	ℓ	b	$T_{\text{eff}}[\text{K}]$	$\log g [\text{cm s}^{-2}]$
Abell 36	PNG 318.4+41.4	13 ^h 40 ^m 41 ^s .3	-19°52'55".3	318°:4	41°:4	93 000 ^b – 113 000 ^c	5.3 ^b – 5.6 ^c
DeHt 2	PNG 027.6+16.9	17 ^h 41 ^m 40 ^s .9	+03°06'57".3	027°:6	16°:9	117 000 ^d	5.64 ^d
RWT 152	PNG 219.2+07.5 ^a	07 ^h 29 ^m 58 ^s .5	-02°06'37".5	219°:2	07°:5	45 000 ^e	4.5 ^e

^a Designation proposed in this work following the designation for Galactic PNe by Acker et al. (1992). ^bHerrero et al. (1990). ^cTraulsen et al. (2005). ^dNapiwotzki (1999). ^eEbbets & Savage (1982)

fig.3) and, therefore, we included it in this investigation. DeHt 2 was discovered by Dengel et al. (1980) after inspecting the POSS plates. Its CS was classified as an O-type star by Acker et al. (1992) and as a hybrid-high luminosity object by Napiwotzki (1999).

Table 4.1 lists a summary of the three objects: the common names and PNG designations, the equatorial and Galactic coordinates, together with the atmospheric parameters (effective temperature and surface gravity) of their CSs.

4.2 Observations

4.2.1 Optical imaging

Narrow-band $\text{H}\alpha$, $[\text{O III}]$, and $[\text{N II}]$ images of Abell 36 were obtained with the Mexman filter-wheel at the 0.84 m telescope on San Pedro Mártir Observatory (OAN-SPM). The $[\text{N II}]$ image was taken on 2013 February 19 with a seeing of ≈ 2.8 arcsec, and the $[\text{O III}]$ and $\text{H}\alpha$ images were obtained on 2013 April 7 with a seeing of ≈ 2.8 arcsec. A Marconi (e2v) CCD with 2048×4612 pixels each of 15 μm in size, was used as detector in both campaigns. A 2×2 binning was employed providing a field of view (fov) of $\approx 8.2 \times 18.4$ arcmin² and a plate scale of 0.468 arcsec pixel⁻¹. Total exposure time was 3600 s in the $[\text{N II}]$ filter ($\lambda_0 = 6585$ Å, FWHM = 10 Å), 4800 s in the $[\text{O III}]$ filter ($\lambda_0 = 5009$ Å, FWHM = 52 Å), and also 4800 s in the $\text{H}\alpha$ filter ($\lambda_0 = 6565$ Å, FWHM = 11 Å).

Narrow-band $\text{H}\alpha$ and $[\text{O III}]$ images of DeHt 2 were obtained on 2010 August 23 with the WFC at the INT on El Roque de Los Muchachos Observatory. We used the same configuration to that described in Chapter 2. Total exposure time was 5400 s in the $[\text{O III}]$ filter ($\lambda_0 = 5008$ Å, FWHM = 100 Å), and 3600 s in the $\text{H}\alpha$ filter ($\lambda_0 = 6568$ Å, FWHM = 95 Å). We note that the $\text{H}\alpha$ filter includes the $[\text{N II}]\lambda\lambda 6548, 6583$ emission lines. However, these $[\text{N II}]$ lines are not detected in the nebular spectra of DeHt 2 due to its high excitation (see Section 4.3.2.3) and, therefore, the $\text{H}\alpha$ filter registers only the $\text{H}\alpha$ emission line. Seeing was ≈ 1.5 arcsec.

In the case of RWT 152, narrow-band $\text{H}\alpha$ and $[\text{O III}]$ images were obtained on 2010 December 16 with CAFOS, with the same configuration to that described in Chapter 2. Total exposure time

was 900 s in [O III] filter ($\lambda_0 = 5007 \text{ \AA}$, FWHM = 87 \AA), and 1900 s in the H α filter ($\lambda_0 = 6563 \text{ \AA}$, FWHM = 15 \AA). Seeing was ≈ 1.5 arcsec.

The images were reduced following standard procedures within the IRAF and MIDAS packages.

4.2.2 Spectroscopy

4.2.2.1 High-resolution long-slit spectroscopy

High-resolution long-slit spectra of Abell 36, DeHt 2, and RWT 152 were obtained with the Manchester Echelle Spectrometer at the 2.1 m telescope on the OAN-SPM during two different campaigns between 2011 and 2012: Abell 36 was observed on 2012 May 12–17, DeHt 2 on 2012 May 11–13, and RWT 152 on 2011 February 17. A 2k \times 2k Marconi CCD was used as detector in 4 \times 4 binning (0.702 arcsec pixel $^{-1}$) in the case of Abell 36 and DeHt 2, and in 2 \times 2 binning (0.338 arcsec pixel $^{-1}$) in the case of RWT 152. Two filters were used: (1) a $\Delta\lambda = 60 \text{ \AA}$ filter to isolate the H α emission line (87th order), with a dispersion of 0.11 \AA pixel^{-1} (in 4 \times 4 binning) and 0.05 \AA pixel^{-1} (in 2 \times 2 binning) and (2) a $\Delta\lambda = 50 \text{ \AA}$ filter to isolate the [O III] emission line (114th order), with a dispersion 0.08 \AA pixel^{-1} (in 4 \times 4 binning) and 0.04 \AA pixel^{-1} (in 2 \times 2 binning). Spectra of Abell 36 and DeHt 2 were obtained with the [O III] filter and an exposure time of 1800 s for each individual spectrum. Spectra of RWT 152 were acquired with the H α and [O III] filters and exposures times of 1200 and 1800 s, respectively. For all spectra, the slit was centred on the CS of each PN and oriented at different position angles (PAs) to cover relevant morphological structures of each object. The observed PAs for each object and their choice will be described in the corresponding section dedicated to each object. The spectra were wavelength calibrated to an accuracy of $\pm 1 \text{ km s}^{-1}$ using a Th-Ar lamp. The resulting spectral resolution (FWHM) is 12 km s^{-1} . Seeing was ≈ 1.5 –2 arcsec during the observations.

The spectra were reduced with standard routines for long-slit spectroscopy within the IRAF and MIDAS packages. Position-velocity (PV) maps have been obtained from these high-resolution, long-slit spectra. The origin of radial velocities in the PV maps is the systemic velocity obtained for each PN (see below), and the origin for projected angular distances is the position of the CS, as given by the intensity peak of the stellar continuum that is detected in all long-slit spectra. Internal radial velocities will be quoted hereafter with respect to the heliocentric systemic velocity of each nebula. The rest wavelengths adopted to rescale the radial velocity are 5006.84 \AA for [O III] and 6562.82 \AA for H α .

4.2.2.2 Intermediate-resolution, long-slit spectroscopy

Intermediate-resolution, long-slit spectra of DeHt 2 and Abell 36 were obtained with the Boller and Chivens spectrograph mounted on the 2.1m telescope at the OAN-SPM on 2013 June 5 and 6, respectively. The detector was a Marconi CCD with $2k \times 2k$ pixels and a plate scale of $1.18 \text{ arcsec pixel}^{-1}$. We used a $400 \text{ lines mm}^{-1}$ dispersion grating, giving a dispersion of $1.7 \text{ \AA pixel}^{-1}$, and covering the $4100\text{--}7600 \text{ \AA}$ spectral range. In the case of DeHt 2, a spectrum with the slit at PA 55° was obtained with the slit centred on the CS. In the case of Abell 36, a spectrum with the slit at PA 90° was obtained covering the CS and the eastern part of the nebula. For both objects, the slit width was 2 arcsec and exposure time was 1800 s for each spectrum. Seeing was $\simeq 3 \text{ arcsec}$.

Intermediate-resolution, long-slit spectra of RWT 152 were obtained using CAFOS on 2010 December 17. The detector was an SITe $2k \times 2k$ -CCD with a plate scale of $0.53 \text{ arcsec pixel}^{-1}$. Gratings B-100 and R-100 were used to cover the $3200\text{--}6200 \text{ \AA}$ and $5800\text{--}9600 \text{ \AA}$ spectral ranges, respectively, both at a dispersion of $\simeq 2 \text{ \AA pixel}^{-1}$. The spectra were taken with the slit at PA 0° and exposure times was 900 s for each grism. The slit width was 2 arcsec and it was centred on the CS. Seeing was $\simeq 2 \text{ arcsec}$. Spectrophotometric standards stars were observed each night for flux calibration.

The spectra were reduced using standard procedures for long-slit spectroscopy within the IRAF and MIDAS packages. For each PN, the observed emission line fluxes were dereddened using the extinction law of Seaton (1979) and the corresponding logarithmic extinction coefficient $c(\text{H}\beta)$, as obtained from the $\text{H}\alpha/\text{H}\beta$ observed flux ratio, assuming Case B recombination ($T_e=10^4 \text{ K}$, $N_e=10^4 \text{ cm}^{-3}$) and a theoretical $\text{H}\alpha/\text{H}\beta$ ratio of 2.85 (Brookhurst, 1971).

4.3 Results

4.3.1 Abell 36

4.3.1.1 Imaging

Figure 4.1 shows our $\text{H}\alpha$ and $[\text{O III}]$ images of Abell 36. Due to the high excitation of the nebula (see Sect. 4.3.1.3), our $[\text{N II}]$ image does not show nebular emission and, therefore, it is not presented here. Abell 36 presents an elliptical morphology with the major axis oriented at PA $\simeq 350^\circ$, and a size of $\simeq 7.4 \times 5.3 \text{ arcmin}^2$. Two particularly bright point-symmetric knotty arcs are observed, giving a spiral appearance to Abell 36, as already noted by Hua & Kwok (1999). Our images also suggest that a faint elliptical envelope could encircle the rest of components. The nebular emission is dominated, particularly in $[\text{O III}]$, by a distorted ring-like structure of \simeq

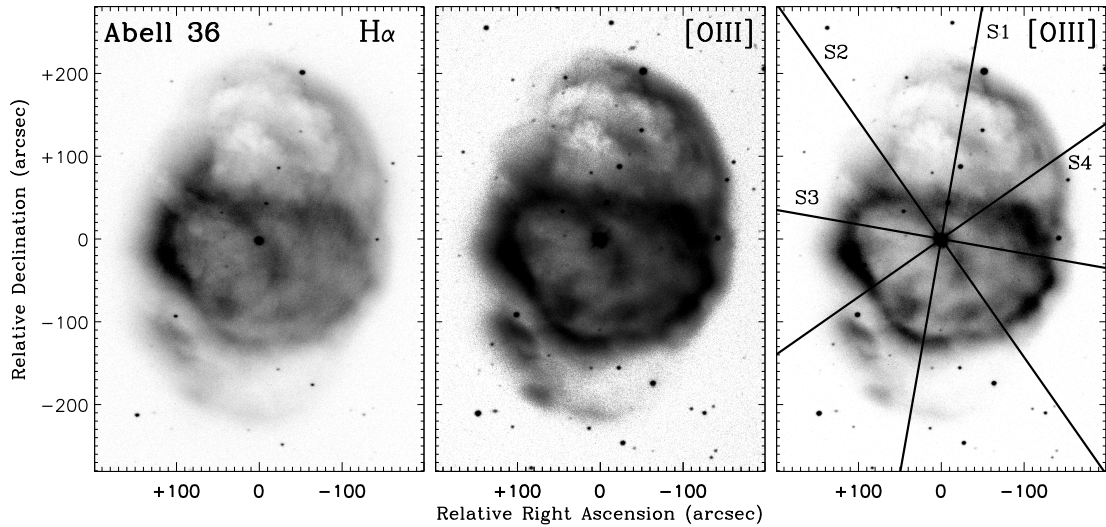


FIGURE 4.1: Grey-scale reproductions of the $H\alpha$ (left) and $[O\text{III}]$ (middle and right) images of Abell 36. Grey levels are linear on the left and right panels and logarithmic on the middle one. Slit positions used for high-resolution, long-slit spectroscopy are drawn in the right panel (slit width not to scale).

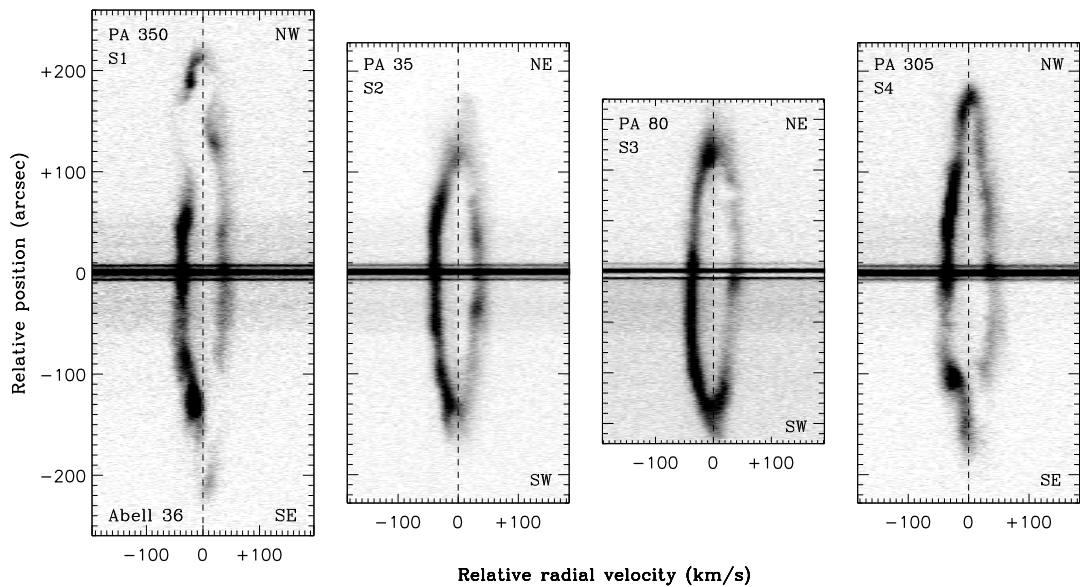


FIGURE 4.2: Grey-scale, PV maps derived from the high-resolution, long-slit $[O\text{III}]$ spectra of Abell 36 at four different PAs (upper left corner in each panel, see also Fig. 1). Grey levels are linear. The origin is at the systemic velocity (see text) and position of the CS, as indicated by the stellar continuum. The two horizontal emission features parallel to the continuum of the CS is a well characterized reflection of the instrument.

3.3×5.3 arcmin² in size, that appears displaced towards the south with respect to the CS. Several bright knots are also observed inside this ring. Towards the north, a bubble-like structure can be recognized inside the elliptical shell, that apparently emanates from the ring. The bubble extends up to ≈ 2.6 arcmin from the CS and is oriented at PA $\approx 12^\circ$

4.3.1.2 High-resolution, long-slit spectroscopy

Spectra of Abell 36 were obtained at PAs 35° , 80° , 305° , and 350° . The slit positions are shown in Fig. 4.1 (right-hand panel) overimposed on the [O III] image of the nebula, and are denoted from S1 to S4 starting at PA 350° counterclockwise. The slit PAs were chosen to cover the major and minor axis (S1 and S3, respectively) of the ellipse as well as two intermediate PAs (S2 and S4). It should be noted that in the cases of PAs 35° , 305° , and 350° , two spectra were secured with the slit on the CS but displaced from each other along the corresponding PA to cover the whole nebula. These two spectra were combined during the reduction process into a single long-slit spectrum. Figure 4.2 shows the PV maps of the [O III] emission line at the four observed PAs. From the radial velocity centroid of the [O III] emission feature, we derive a heliocentric systemic velocity $V_{\text{HEL}} = +34.8 \pm 1.4$ km s⁻¹, in agreement with the value obtained by Bohuski & Smith (1974).

The PV maps show a velocity ellipse with maximum velocity splitting of ≈ 74 km s⁻¹ at the stellar position and with no particular tilt with respect to the angular axis. The spatio-kinematical properties of the velocity ellipse vary with PA. In addition, outer structures are also distinguished. We describe below the PV maps in more detail.

The velocity ellipses at PAs 35° and 80° (S2 and S3 in Figs. 4.1 and 4.2) present similar properties to each other. They extend up to ≈ 130 arcsec towards the north-east (NE) and ≈ 105 arcsec towards the south-west (SW). The size of the velocity ellipses fits very well the size of the bubble and the southern part of the distorted ring (see Fig. 4.1), suggesting a spatio-kinematical relationship between both structures.

The PV map at 350° (S1 in Fig. 4.1) reveals a more complex kinematics. The velocity ellipse extends between $\approx \pm 130$ arcsec from the CS. Two bright knots are observed close to its tips with radial velocities of $\approx \pm 20$ km s⁻¹ (NW knot redshifted). A comparison with the images in Fig. 4.1 shows that these knots correspond to cuts of slit S1 with the bright edge of the northern bubble and with the southern edge of the distorted ring. This result reinforces those obtained at PAs 35° and 80° that the northern bubble and the southern half of the observed ring form a unique spatio-kinematic structure that may be defined as a spheroid. It is noteworthy that this spheroid has been identified through an analysis of PV maps based on high-resolution spectra and that it can be hardly recognized in the direct images. In addition, these spectra also demonstrate that the distorted ring observed in the direct images is a projection effect and does not correspond

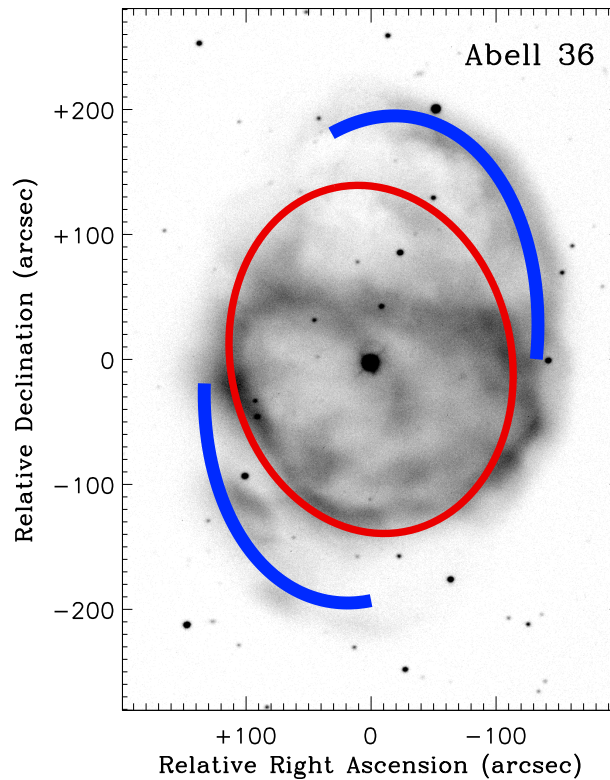


FIGURE 4.3: Sketch of Abell 36 as derived from our morphokinematical analysis. The spheroidal shell is displayed in red and the bright arcs are represented by thick blue lines.

to a real nebular structure. We also note that the velocity ellipse appears to be open at two point-symmetric locations on the PV map, with the north-west (NW) ‘hole’ mainly blueshifted and the south-east (SE) one mainly redshifted. Moreover, towards the NW, faint emission, with an arcuate shape in the PV map, and radial velocities up to $\approx -55 \text{ km s}^{-1}$, connects the velocity ellipse with emission from the NW point-symmetric arc. The NW arc itself presents two radial velocity components centred at the systemic velocity, with the brightest component being slightly blueshifted. The emission feature due to the SE arcs is similar to that of the NW arcs, but fainter and slightly redshifted.

At PA 305° (S4 in Fig. 4.1), the velocity ellipse may also be recognized, although it appears open at its tips and connected to emission from the point-symmetric arcs. This velocity ellipse is also compatible with the spheroidal structures identified at the other PAs. Emission from the NW arc present two velocity components, although it is centred close to the systemic velocity. Emission from the SE arc shows a single velocity component at the systemic velocity.

Some of the bright knots observed in the inner nebular regions have been covered by the slits (see Fig. 4.1). These knots do not appear as separated entities in the PV maps but share the kinematics of the velocity ellipses, suggesting that they are a part of the spheroidal structure.

The PV maps (Fig. 4.2) reveal that the [O III] emission is noticeable stronger in the blueshifted part of the nebula than in the redshifted one, as observed in other PNe (e.g., IC 2149 [Vázquez et al., 2002](#)). This could be related to dust absorption of the redshifted emission. Alternatively, interaction of the front (blueshifted) half of Abell 36 with the interstellar medium (ISM) could be causing this effect. To test this possibility, we compare the radial velocity of the local ISM at the position of Abell 36 with that of the nebula itself, assuming a distance of 150–770 pc (see [Abell, 1966](#), [Cahn & Kaler, 1971](#), [Cahn et al., 1992](#), [Acker et al., 1998](#), [Phillips, 2005](#)) and a standard rotation curve of the Galaxy. Following the formulation by [Nakanishi & Sofue \(2003\)](#), we obtain a heliocentric radial velocity of $\approx +26 \text{ km s}^{-1}$ for the ISM around Abell 36, that is lower than that of the nebula ($\approx +35 \text{ km s}^{-1}$). These values suggest that Abell 36 is encroaching on the ISM, although one would expect that the rear (redshifted) half of Abell 36 was the brighter one, while the opposite is observed.

The analysis of the PV maps implies a physical structure for Abell 36 that is quite different from what could be expected from the images. Figure 4.3 shows a sketch of the nebula overimposed on the [O III] image. As already mentioned, the velocity ellipse observed at all PAs is compatible with a spheroidal structure. Its major axis should be almost perpendicular to the line of sight, as indicated by the lack of tilt of the velocity ellipse in the PV maps, and oriented at PA around 12° , as suggested by the orientation of the northern bubble. The arcs resemble the point-symmetric structures observed in other PNe (e.g., NGC 6309; [Vázquez et al., 2008](#)). [Hua & Kwok \(1999\)](#) compared Abell 36 with NGC 6543 and our results strength this comparison and extend it to IC 4364 as well. These three PNe show a/an spheroidal/ellipsoidal shell that is accompanied by outer and extended point-symmetric regions [components DD' in NGC 6543 ([Miranda & Solf, 1992](#)) and in IC 4364 ([Guerrero et al., 2008](#)) and point-symmetric arcs in Abell 36], which appear twisted with respect to the orientation of the spheroidal shell. Following these authors, the point-symmetric arcs of Abell 36 may be interpreted as due to a collimated bipolar outflow that has been ejected along a rotating axis. If so, the axis has rotated mainly in a plane (the plane of the sky) as indicated by the low radial velocity of the arcs, while a relatively large rotation angle of $\approx 100^\circ$ is inferred from the images.

The velocity ellipses appear disrupted at PAs 305° and 350° , where the bright arcs are observed, but not at PAs 35° and 80° , where the bright arcs do not extend. This strongly suggests a relationship between the bright arcs and the disrupted regions of the spheroid. In particular, this disruption could be originated by a collimated outflow that is able to go through the spheroid, perforating parts of it. The kinematics of the faint emission connecting the velocity ellipse and the emission features from the arcs observed in the PV map at PA 305° strongly suggests an acceleration of material from the spheroid followed by a more or less sudden deceleration that could be due to interaction with the faint elliptical envelope. It is worth noting that, if this interpretation is correct, the collimation degree of the bipolar outflow should have been very

TABLE 4.2: Emission line intensities in Abell 36.

Line	$f(\lambda)$	$I(\lambda) (I(\text{H}\beta)=100)$
H γ λ 4340	0.129	46.5 \pm 0.7
He II λ 4686	0.042	123.0 \pm 1.0
He I+[Ar IV] λ 4711	0.036	16.7 \pm 0.3
[Ar IV] λ 4740	0.029	8.4 \pm 0.4
H β λ 4861	0.000	100.0 \pm 1.0
[O III] λ 4959	-0.023	96.9 \pm 1.0
[O III] λ 5007	-0.034	278.6 \pm 2.2
He II λ 5411	-0.118	9.5 \pm 0.3
H α λ 6563	-0.323	285.0 \pm 1.4
$c(\text{H}\beta) = 0.17$		
$\log F_{\text{H}\beta}(\text{erg cm}^{-2} \text{s}^{-1}) = -13.34$		

high because only “relatively” small portions of the spheroid are disrupted at each PA and a velocity ellipse can still be recognized in the PV maps at PAs 305° and 350°.

The equatorial expansion velocity of the spheroid ($\sim 37 \text{ km s}^{-1}$), its equatorial radius (~ 1.7 arcmin), and the distance (150–770 pc, see above) yield a kinematical age of $\sim 2\text{--}10 \times 10^3$ yr, a broad range of ages given by the uncertainty in the distance, that is compatible with a relatively young or very evolved PN. Finally, if our interpretation of the bright arcs is correct, the corresponding collimated outflows should be younger than the spheroid. However, their kinematical age is impossible to obtain because their original velocity as well as the changes that their velocity may have suffered through collimated outflow–shell interaction are unknown.

4.3.1.3 Intermediate-resolution, long-slit spectroscopy

The intermediate-resolution, long-slit nebular spectrum of Abell 36 is presented in Figure 4.4. A logarithmic extinction coefficient $c(\text{H}\beta)$ of $\simeq 0.17$ was obtained (see Sect. 4.2.2.2). The dereddened line intensities and their Poissonian errors are listed in Table 4.2. In addition to the hydrogen and [O III] $\lambda\lambda$ 4959,5007 emission lines, strong high excitation emission lines are observed as He II λ 4686 and [Ar IV] $\lambda\lambda$ 4711,4740. We note that [O III] λ 4363 and [Ar V] λ 7005 line emissions could also be present but deeper spectra are needed to confirm them. The spectrum indicates a high-excitation nebula, which is compatible with the non-detection of the nebula in the [N II] filter.

The normalized spectrum of the CS of Abell 36 is shown in Figure 4.5. As already mentioned, this star is included in the Subdwarf Database by Østensen (2006). The presence of narrow He II absorption lines (specially He II λ 4686) as well as the atmospheric parameters (Table 4.1) are indeed compatible with an sdO nature.

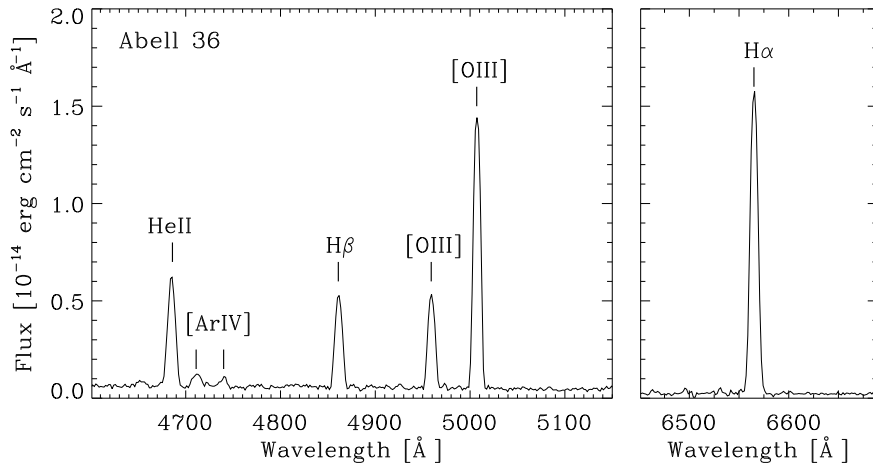


FIGURE 4.4: Nebular spectrum of Abell 36 obtained by integrating the emission lines between 77 and 124 arcsec eastern from the CS along the slit position. The emission lines are labelled.

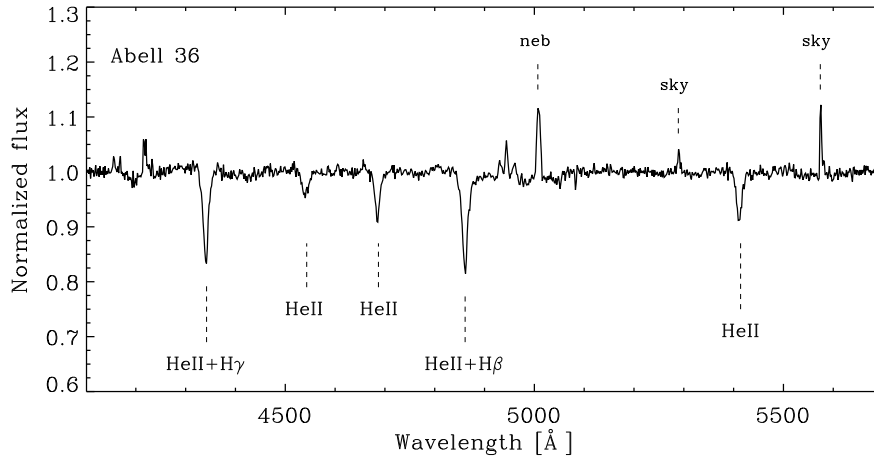


FIGURE 4.5: Normalized optical spectrum of the CS of Abell 36. Poorly subtracted sky lines and nebular emission lines are marked as well as some absorption lines.

4.3.2 DeHt 2

4.3.2.1 Imaging

Figure 4.6 shows our $H\alpha$ and $[O\text{ III}]$ images of DeHt 2 that reveal more details than previous ones (Manchado et al., 1996a). They show an elliptical shell with a size of $\approx 1.9 \times 1.5$ arcmin² and major axis oriented at $PA \approx 55^\circ$, although the polar regions seem to protrude and deviate from a “pure” elliptical geometry, in particular at the SW region. The shell shows a limb-brightening that is more noticeable along the northern edge. This could be a result of interaction of the nebula with the ISM (Wareing et al., 2007), an idea that is supported by the fact that the limb-brightening is more noticeable in $[O\text{ III}]$ than in $H\alpha$. Two bright filaments are observed in $[O\text{ III}]$ (much weaker in $H\alpha$) at the NE tip of the shell. They are parallel to each other, separated ≈ 0.1 arcmin, and oriented perpendicular to the major nebular axis. Furthermore, the

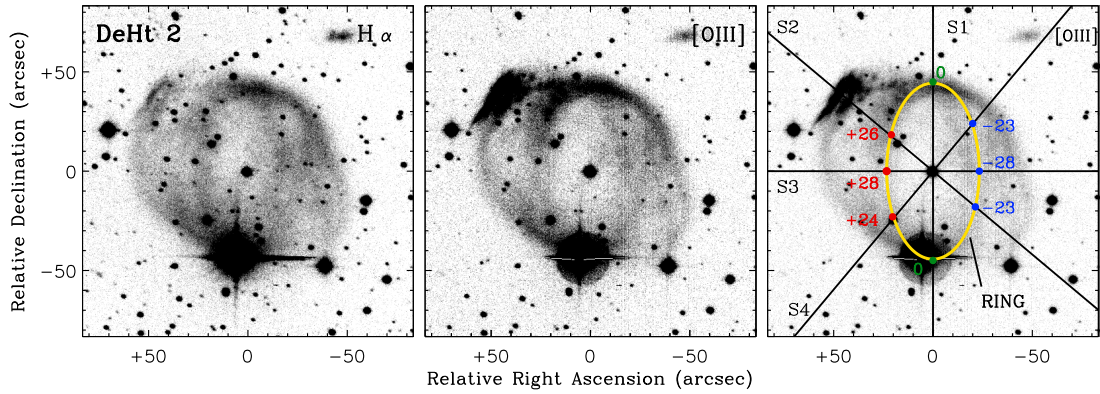


FIGURE 4.6: Grey-scale reproductions of the $H\alpha$ (left) and $[O\text{ III}]$ (middle and right) images of DeHt 2. Grey levels are linear. Slit positions used for the high-resolution, long-slit spectroscopy are drawn on the right panel (slit width not to scale). The small nebulosity towards the northwestern of DeHt 2 could be a galaxy.

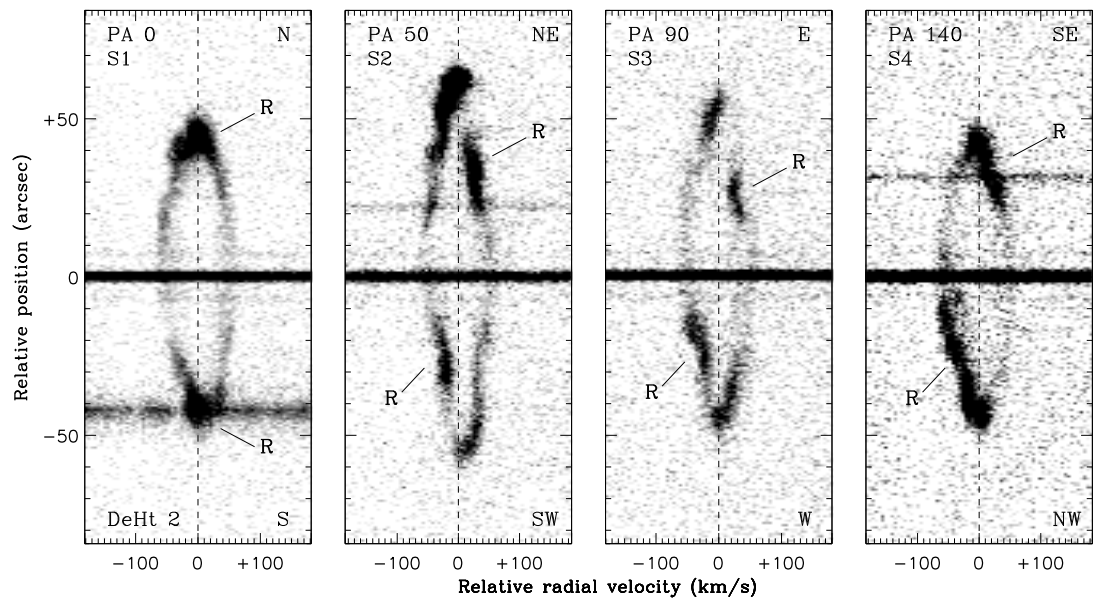


FIGURE 4.7: Grey-scale, PV maps derived from the high-resolution, long-slit $[O\text{ III}]$ spectra of DeHt 2 at four different PAs (upper left, see also Fig. 6). The bright features related to the ring-like structure are indicated by ‘R’.

images reveal the existence of an (elliptical) ring embedded in the elliptical shell, that is mainly distinguished by its relative brightness. The size of the ring is $\approx 1.5 \times 0.7 \text{ arcmin}^2$ and its minor axis is oriented E–W approximately. This ring is drawn in Fig. 4.6. The orientations of the ring and the elliptical shell are quite different from each other, indicating that the ring does not trace the equatorial plane of the elliptical shell.

4.3.2.2 High-resolution, long-slit spectroscopy

Spectra of DeHt 2 were obtained at PAs 0° , 50° , 90° , and 140° . These slit positions (denoted S1 to S4, respectively) are plotted in Fig. 4.6 (right-hand panel), on the [O III] image of the nebula. Slits S1 and S3 were chosen to cover the major and minor axes of the ring, respectively, while S2 covers the main axis of the elliptical shell and S4 its minor axis. Figure 4.7 shows the PV maps of the [O III] emission line at the four observed PAs. From the radial velocity centroid of the line emission feature, we derive a heliocentric systemic velocity $V_{\text{HEL}} = +47 \pm 2 \text{ km s}^{-1}$.

The PV maps at PAs 0° and 140° mainly show a velocity ellipse. The ellipse does not appear tilted on these PV maps, although some asymmetries with respect to the velocity axis are observed. At PA 50° the emission line feature shows a spindle-like shape slightly tilted in the PV map such the NE (SW) regions present an excess of blueshifted (redshifted) radial velocities. At PA 90° the emission line feature shows a shape halfway between that observed at PA 50° and PA 140° . Maximum line splitting of $\approx 100 \text{ km s}^{-1}$ is observed at the stellar position at all PAs. The PV maps also show that the CS is displaced from the nebular centre $\approx 3 \text{ arcsec}$ towards the SW at PA 50° and $\approx 5 \text{ arcsec}$ towards the west at PA 90° , which is difficult to recognize in the direct images. By combining these shifts, the CS appears displaced $\approx 7.5 \text{ arcsec}$ towards PA $\approx 255^\circ$.

The [O III] emission feature is generally weak in the PV maps except at particular positions that correspond to well-identified regions in the images. The two bright filaments at the NE tip of the elliptical shell can be recognized on the PV map at PA 50° , as two knots with radial velocities of $\approx -18 \text{ km s}^{-1}$ at $\approx 0.9 \text{ arcmin}$ from the CS and -10 km s^{-1} at $\approx 1 \text{ arcmin}$. The SW tip of the elliptical shell also appears bright in the PV map with a radial velocity of $\approx +16 \text{ km s}^{-1}$ at $\approx 0.9 \text{ arcmin}$. The rest of bright regions on PV maps coincide with the ring identified in the images. Although these features appear elongated in the spatial direction (particularly at PA 140°) and the radial velocity is difficult to measure, we have considered the position observed in the direct images to obtain the radial velocity that is indicated in Fig. 4.6 (right-hand panel). The western half of the ring is blueshifted while the eastern half is redshifted. Moreover, the radial velocity presents systematic variations in the ring reaching a maximum (in absolute value) of $\approx 28 \text{ km s}^{-1}$ at the minor axis, a minimum value of $\approx 0 \text{ km s}^{-1}$ at the major axis, and intermediate values at PAs 50° and 140° . This kinematics coincides with that expected from a tilted circular ring. Under this assumption, we obtain an inclination angle of $\approx 30^\circ$ for the plane of the ring with respect to the line of sight, an expansion velocity of $\approx 36 \text{ km s}^{-1}$, and a PA of $\approx 96^\circ$ for the orientation of the ring axis. It is noteworthy that the expansion velocity of the ring is lower than the expansion velocity measured at the stellar position, $\approx 50 \text{ km s}^{-1}$, as indicated by the maximum radial velocity splitting of the velocity ellipse.

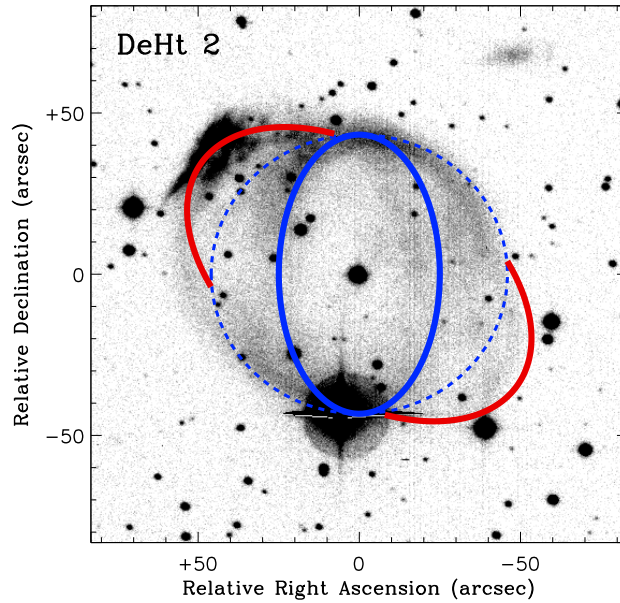


FIGURE 4.8: Sketch of the PN DeHt 2 as derived from our morphokinematical analysis. The spheroidal shell (dashed blue line), the ring-like structure (solid blue line), and the bipolar outflow (solid red line) are drawn.

The spatio-kinematical properties of DeHt 2 indicate that its formation has been complex with at least two different ejection processes being involved. In Figure 4.8, we show a schematic representation of the structures that compose DeHt 2, as inferred from the analysis of the PV maps. We suggest that the original structure of this PN was a spheroid on which a bright, ring-like region defined its equatorial plane. The fact that the expansion velocity of the ring (36 km s^{-1}) is lower than that measured at the stellar position (50 km s^{-1} , at some latitude above the equator), strongly suggests that the original structure was not spherical but probably an ellipsoid with the major axis oriented approximately E–W. Taken into account the spatio-kinematical properties of the ring and assuming a distance of 1.9–3.2 kpc (Dengel et al., 1980, Napiwotzki, 1999, 2001), its kinematical age results to be $1.3\text{--}1.9 \times 10^4$ yr, compatible with an evolved PN. Probably later, another bipolar ejection has taken place, that interacted with and deformed the original spheroid, as suggested by the protruding regions that are now observed as the polar regions of the apparent elliptical shell. The second ejection should have been collimated and along a bipolar axis oriented at $\text{PA} \simeq 50^\circ$, that is different from the orientation of the previous structure.

4.3.2.3 Intermediate-resolution, long-slit spectroscopy

Figure 4.9 shows the intermediate-resolution, long-slit spectra of the NE filaments of DeHt 2. Only the $\text{H}\alpha$, $\text{H}\beta$, $[\text{O III}]\lambda\lambda 4959, 5007$, and $\text{He II}\lambda 4686$ emission lines are detected. A logarithmic extinction coefficient $c(\text{H}\beta) \simeq 0.33$ was obtained (see Sect. 4.2.2.2). The dereddened line intensities and their Poissonian errors are listed in Table 4.3. The spectrum indicates a very high

TABLE 4.3: Emission line intensities in DeHt 2.

Line	$f(\lambda)$	$I(\lambda) (I(\text{H}\beta)=100)$
He II $\lambda 4686$	0.042	103.7 ± 2.7
H β $\lambda 4861$	0.000	100.0 ± 2.8
[O III] $\lambda 4959$	-0.023	308.5 ± 3.6
[O III] $\lambda 5007$	-0.034	921.1 ± 6.5
H α $\lambda 6563$	-0.323	285.0 ± 4.3
$c(\text{H}\beta) = 0.33$		
$\log F_{\text{H}\beta} (\text{erg cm}^{-2} \text{s}^{-1}) = -14.63$		

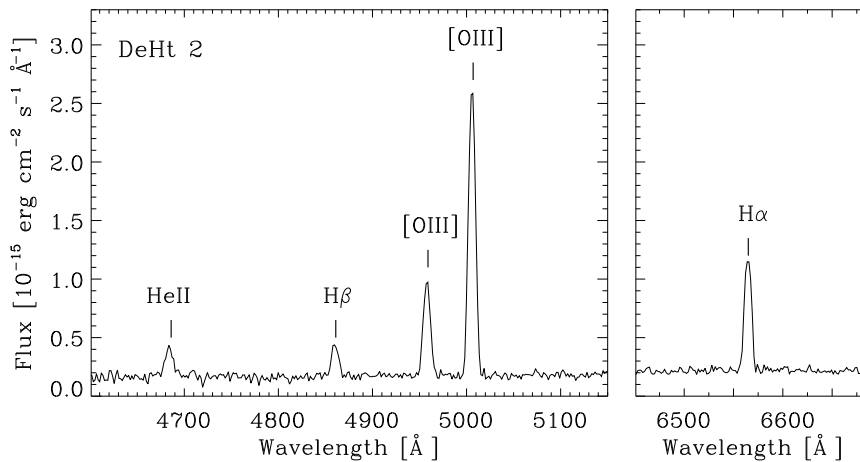


FIGURE 4.9: Nebular spectrum of DeHt 2 obtained by integrating the long-slit spectrum between 0.8 and 1.1 acmin from the CS along PA = 55°. The spectrum corresponds to the bright filaments at the northeastern (see Fig. 4.6).

excitation although other high-excitation emission lines (as in the case of Abell 36) are not observed. The same emission lines are detected in other nebular regions (spectra not shown here), suggesting a somewhat lower excitation than in the NE filaments.

The stellar spectrum is shown in Figure 4.10. It shows strong He II absorptions some of which can be blended with the Balmer absorptions. Although the spectrum of DeHt 2 does not have enough spectral resolution to resolve the Pickering and Balmer absorption lines, most probably the absorptions present in this spectrum mainly correspond to the Pickering ones, due to the high effective temperature of this CS (117 000 K, see Table 4.1). These spectral features and the atmospheric parameters (Table 4.1) are compatible with a very hot sdO star. To provide more support for this classification, we compare in Fig. 4.10 the normalized blue spectrum of the CS with that of BD+28°4211, a well-known sdO with $T_{\text{eff}} \simeq 82\,000$ K and $\log g \simeq 6.2$ cm s⁻² (Latour et al., 2013). The spectrum of BD+28°4211 was obtained with the CAFOS spectrograph in 2011 July. Spectra of both stars are also shown in Napiwotzki & Schoenberner (1995, their fig. 3). Both spectra are remarkably similar to each other, being the observed differences probably due to the signal to noise in each spectra and to the different atmospheric parameters of the stars. In any case, the spectral similarities strongly suggest an sdO nature for the CS of DeHt 2.

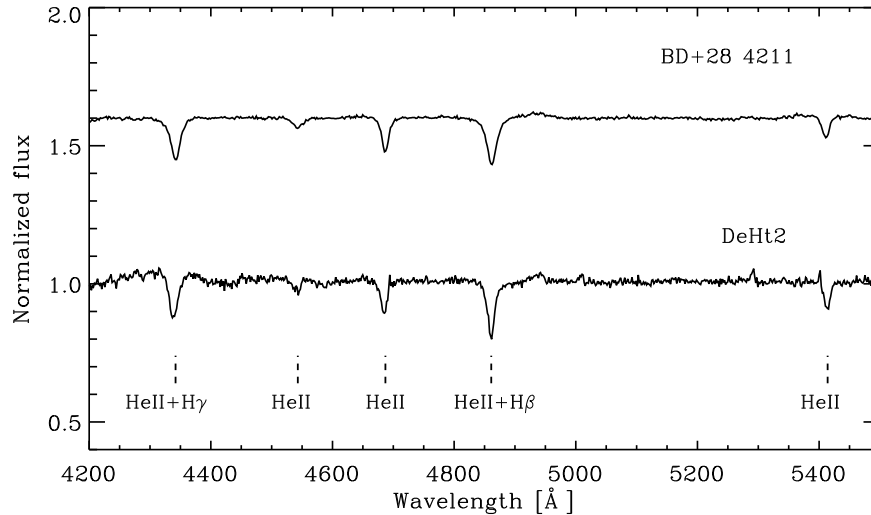


FIGURE 4.10: Normalized optical spectrum of the CS of DeHt 2 (bottom) compared to that of BD+28°4211 (top).

4.3.3 RWT 152

4.3.3.1 Imaging

Figure 4.11 shows the $H\alpha$ and $[O\text{ III}]$ images of RWT 152, in which details of the nebular morphology can be distinguished for the first time. Both images reveal a very faint PN. While in the $H\alpha$ image the nebula presents a diffuse, although non-spherical appearance, a more defined nebula can be discerned in the $[O\text{ III}]$ image. At low-intensity levels, the nebula seems to be almost circular whereas at higher intensity levels, it appears slightly bipolar with a size of $\approx 17 \times 21 \text{ arcsec}^2$, major axis oriented at $PA \approx 40^\circ$, and a rather uniform intensity distribution. It is worth noting that the CS is clearly displaced towards the NW with respect to the centre of the nebula (see also below).

4.3.3.2 High-resolution, long-slit spectroscopy

Spectra of RWT 152 were obtained at $PA 45^\circ$ (in $H\alpha$ and $[O\text{ III}]$) and $PA 135^\circ$ (in $[O\text{ III}]$) to cover the major and minor axis (S1 and S2, respectively, in Fig. 4.11) of the bipolar shell. Figure 4.12 shows the two PV maps in the $[O\text{ III}]$ emission line. We note that the $[O\text{ III}]$ emission line feature presents a much more knotty appearance in the PV maps than in the image. The PV map of $H\alpha$ emission line at $PA 45^\circ$ (not shown here) is very similar to that of the $[O\text{ III}]$ emission line at the same PA , but the large thermal width in the $H\alpha$ line does not allow us a detailed analysis of the kinematics. From the velocity centroid of the line emission features, we derive a heliocentric systemic velocity of $V_{\text{HEL}} = +134.5 \pm 1.8 \text{ km s}^{-1}$.

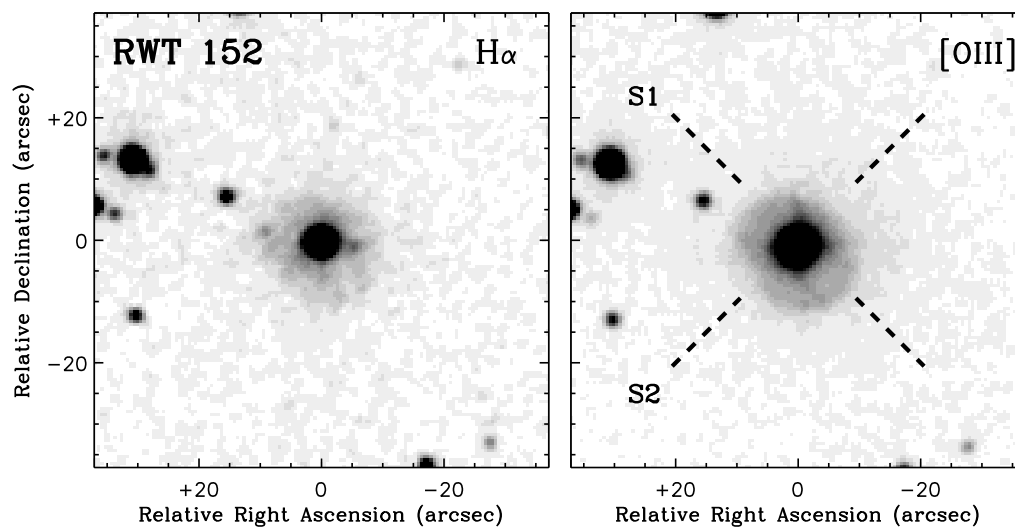


FIGURE 4.11: Grey-scale reproductions of the $H\alpha$ and $[O\text{ III}]$ images of RWT 152. Grey-levels are linear. A 3×3 box smooth was used for the representation. The slit positions used for the high-resolution, long-slit spectroscopy (S1 and S2) are drawn in the right-hand panel.

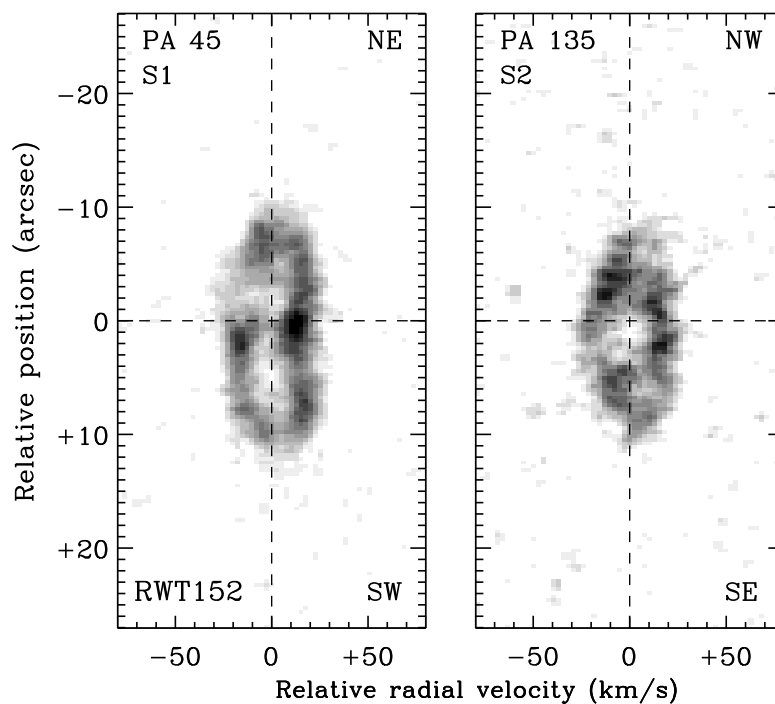


FIGURE 4.12: Grey-scale, PV maps derived from the high-resolution, long-slit $[O\text{ III}]$ spectra of RWT 152. Grey-levels are linear. The continuum of the central star has been removed (using the *background* IRAF task) and its position is marked with a dashed horizontal line. A 3×3 box smooth was used for the representation.

In the PV map at PA 45° , the [O III] emission feature presents an hour-glass like shape with a size of ≈ 22 arcsec, although deviations from a pure hour-glass shape are noticed, particularly in the NE lobe. Radial velocity at the tips of the emission feature is $\approx \pm 7 \text{ km s}^{-1}$. Two bright knots can be distinguished in the central region, that are symmetric in radial velocity but not centred on the CS: the redshifted knot presents a radial velocity of $\approx +14 \text{ km s}^{-1}$ and is located ≈ 0.12 arcsec NE from the CS; the blueshifted one has a radial velocity of $\approx -14 \text{ km s}^{-1}$ and is located ≈ 1.8 arcsec SW from the CS. The PV map at PA 135° presents a velocity ellipse with a maximum line splitting of $\approx 34 \text{ km s}^{-1}$ at the stellar position and a size of ≈ 18 arcsec as measured between the intensity peaks at the systemic velocity. The centre of the velocity ellipse is displaced ≈ 1.2 arcsec towards the SE with respect to the CS.

The displacements of nebula's centre with respect to the CS as measured in the PV maps are consistent with the off-centre position of the CS observed in the direct images. Taken into account the two observed PAs, a shift of ≈ 1.4 arcsec towards PA $\approx 348^\circ$ is obtained.

Both images and PV maps are compatible with a bipolar PN. The two bright knots observed in the central regions in the PV map at PA 45° suggest the existence of an equatorial enhancement. If we assume circular cross-section for the equator, the equatorial plane of the nebula is tilted by $\approx 6^\circ$ with respect to the line of sight. Assuming homologous expansion, a polar velocity of 19 km s^{-1} is obtained. There is no reliable determination for the distance of RWT 152 and estimates are 1.4 and 6.5 kpc (Ebbets & Savage, 1982, Pritchett, 1984). In consequence, only a lower limit of $\approx 4 \times 10^3$ yr can be obtained for its kinematical age, which suggests (at least) a relatively evolved PN.

4.3.3.3 Intermediate-resolution, long-slit spectroscopy

The intermediate-resolution nebular spectrum of RWT 152 is presented in Figure 4.13. Only the $H\alpha$, $H\beta$, and [O III] $\lambda\lambda 4959, 5007$ emission lines are identified. A logarithmic extinction coefficient $c(H\beta)$ of ≈ 0.46 was derived (see Sect. 4.2.2.2). Table 4.4 lists the dereddened line intensities and their Poissonian errors. The [O III]/ $H\beta$ line intensity ratio is ≈ 8 (Table 4.4), suggesting a low excitation.

The normalized spectrum of the CS is shown in Figure 4.14. In contrast to the CS spectrum of DeHt 2, the CS spectrum of RWT 152 is dominated by hydrogen Balmer lines. The narrowness of the absorption lines, and the presence of He I (e.g. He I $\lambda\lambda 4386, 4471$) and He II absorption lines (specially He II $\lambda 4686$) confirm the sdO nature of the CS. The CS was analysed by Ebbets & Savage (1982) who determined a relatively low (for an sdO) T_{eff} of ≈ 45000 K (see Table 4.1) that is compatible with the presence of He I $\lambda 4471$.

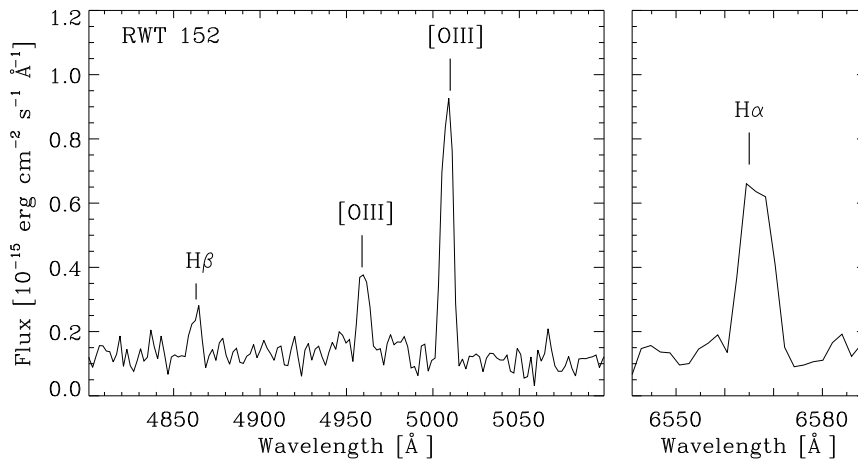


FIGURE 4.13: Nebular spectrum of RWT 152 obtained by integrating the detected emission lines 4.3 and 8.6 arcsec northern of RWT 2 along PA = 0°.

4.4 Discussion

The data presented and analysed in the previous sections have allowed us to deduce the basic physical structure and emission properties of Abell 36, DeHt 2, and RWT 152 and their CSs. Moreover, the spatio-kinematical analysis has been able to recover relevant information about the processes involved in the formation of the three objects. In addition, the spectra of the three CSs show characteristics that allow us to classify them as sdOs. In particular, the narrowness of the absorption lines and the presence of prominent He II absorption are typical of sdOs. This classification is corroborated by the atmospheric parameters of the CSs (Table 4.1), that are within the range of the sdOs atmospheric parameters (see Heber, 2009).

RWT 152 seems to be a result of a typical bipolar ejection as observed in many PNe. The formation of Abell 36 and DeHt 2 appears more complex and requires multiple ejection events, changes in the orientation of main ejection axis between events, and a different collimation degree of the ejections. In Abell 36, the bright arcs indicate a very large and ‘continuous’ change in the collimated ejection axis, whereas in DeHt 2 the bipolar outflows seem to have acted along a constant direction that is different from the main axis of the previous shell. Interestingly, evidence is found in both PNe that the collimated outflows might have been ejected after the main nebular shell was formed. Moreover, in both cases, the collimated outflows seem to have disrupted or deformed the previous shell. This situation is similar to that found in other PNe (e.g., Guerrero & Miranda, 2012, Ramos-Larios et al., 2012, Guillén et al., 2013) in which young collimated outflows seem to have disrupted a previous nebular structures. The origin of collimated outflows in PNe after the formation of the main nebular shell is difficult to explain within current scenarios for PN formation and is still matter of debate (see Tocknell et al., 2014).

TABLE 4.4: Emission line intensities in RWT 152.

Line	$f(\lambda)$	$I(\lambda) (I(\text{H}\beta)=100)$
H β λ 4861	0.000	100 \pm 3
[O III] λ 4959	-0.023	209 \pm 3
[O III] λ 5007	-0.034	591 \pm 3
H α λ 6563	-0.323	285 \pm 4
$c(\text{H}\beta) = 0.46$		
$\log F_{\text{H}\beta}(\text{erg cm}^{-2} \text{s}^{-1}) = -14.97$		

Multiple ejection events, as those identified in Abell 36 and DeHt 2, are observed in many PNe. The idea that complex PNe are related to the evolution of binary CSs has been present during many years and it has received strong support with recent detections of new binary CSs in PNe with multiple structures and jets (see [Miszalski et al., 2009b](#), and references therein). Within this context, it could be suggested that the CSs of Abell 36 and DeHt 2 are also binaries, although, to the best of our knowledge, no direct evidence exists for such binaries. It is interesting to note that both Abell 36 and DeHt 2 contain off-centre CSs, which could be considered as an indirect evidence for a binary CS (e.g., [Soker et al., 1998](#)). Although it is true that some binary CSs appear off-centre, inferring a binary CS from its off-centre position only should be seen with caution. Given that DeHt 2 and, perhaps, Abell 36 are evolved PNe, the off-centre CSs could be caused by deformation in the shell due to, for instance, interaction with the ISM ([Jones et al., 2010](#), [Frew et al., 2014](#)), and/or amplification through evolution of (originally small) asymmetries in the ejection process. In the case of Abell 36, interaction shell-collimated outflows could also contribute to create asymmetries in the shell. The case of the off-centre CS of RWT 152 looks different because of the more symmetric shell. However, RWT 152 may be a very distant PN and a higher spatial resolution is necessary to investigate possible asymmetries in the shell, which are already suggested by the distortions in the kinematics. In any case, these three PNe are good candidates to host binary CSs (see also below), and dedicated observations of their CSs should be obtained to search for possible companions.

The nebular spectra of Abell 36 indicates high excitation, as shown by the presence of [Ar IV] and strong He II λ 4686 emission lines. The nebular spectra of DeHt 2 and RWT 152 indicate high and low excitation respectively, but no emission lines from heavy elements (except [O III]) are detected. If other emission lines exist in these two PNe, they should be very faint. The CSs of Abell 36 and DeHt 2 present very similar atmospheric parameters (Table 4.1). Therefore, similar emission lines could be expected, unless the physical conditions and/or chemical abundances are very different in both PNe. The CS of RWT 152 has a relatively low T_{eff} and, in principle, low-excitation emission lines should be present in the nebula. The nebular spectra of DeHt 2 and RWT 152 are very similar to that of PN G 075.9+11.6 (see Chapter 3), in which only [O III] and Balmer emission lines have been detected. Following these authors, a probable explanation for the peculiar nebular spectra of DeHt 2 and RWT 152 is a deficiency in heavy elements in the nebula. Such a deficiency may be expected in PNe that originate from low-mass progenitors

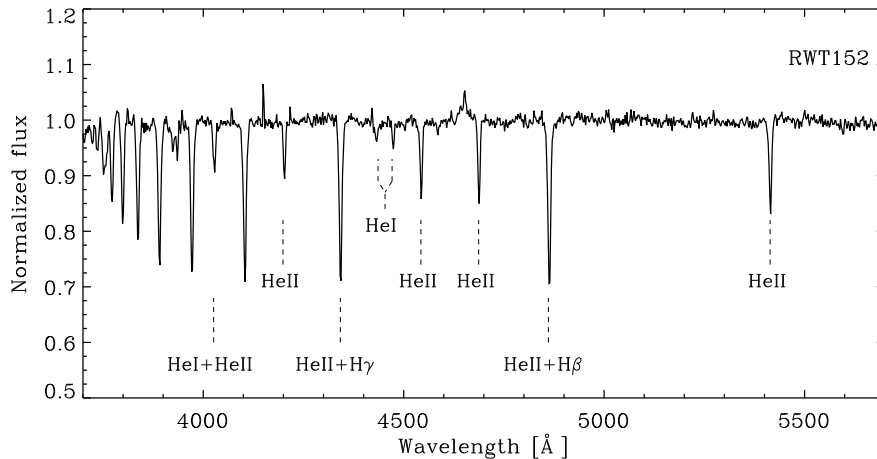


FIGURE 4.14: Normalized optical spectrum of the central star of RWT 152. Some of the absorption lines (specially He I and He II) are marked.

(see e.g., IC 2149; Vázquez et al., 2002) and it would be consistent with the idea that sdOs evolve from low-mass progenitors (see, e.g., Heber, 2009). Deep spectroscopy of these PNe is crucial to detect faint emission lines and to obtain their chemical abundances.

It is interesting to compare the properties of PN+sdO systems. If we restrict to those objects with a more confident classification, the number of PN+sdO systems is 18, that are those classified as “confirmed” in Table 2.3, together with the newly classified DeHt 2. Table 4.5 lists these PNe (columns 1 and 2), their morphology and some comments about nebular structures present in them (column 3), the binary nature of the CSs (column 4), and the corresponding references (column 5). We emphasize that the discussion below does not critically depend on whether some of the possible PN+sdO systems are added to the list and/or whether some of the objects in Table 4.5 are removed. We note that our Table 4.5 shares several objects with Table 1 by Miszalski et al. (2009b). These authors analyse the morphology of PNe with close binary CSs while we focus in the morphology and presence of binaries in sdO CSs.

An inspection of the properties of PN+sdO systems reveals that most of these PNe are very faint, suggesting that they are in a moderately or very evolved stage. A noticeable exception is the Stingray nebula (Hen 3–1357), a very young PN (Parthasarathy et al., 1995) whose CS (SAO244567) has recently been identified as an sdO (Reindl et al., 2014). If we attend to the morphology, the sample is dominated by elliptical and bipolar shapes with only an object (DS 2) presenting a round morphology. Moreover, many of these PNe show multiple structures, jet-like outflows or point-symmetric structures that could be related to the action of bipolar collimated outflows. It is also remarkable that many PN+sdO systems host binary CSs, suggesting that binary CSs may play an important role in the formation of PN+sdO systems. Finally, a large fraction of these systems are observed at a relatively high Galactic latitude. In particular, 11 PNe in Table 4.5 have $|b| > 10^\circ$ and 15 have $|b| > 7^\circ$. Although the number of objects is small to draw

firm conclusions, the relatively high Galactic latitudes are more typical of round PNe evolving from low-mass progenitors (Corradi & Schwarz, 1995, Stanghellini et al., 2002). Remarkably, low-mass progenitors are generally expected for sdOs (see above) and, in addition, sdOs are normally located at high Galactic latitudes. However, one would not expect a large fraction of complex PNe resulting from low-mass progenitors. These results and the large fraction of binary CSs in PN+sdO systems point out that the key parameter to form a complex PN is a binary CS rather than the mass of the progenitor. This conclusion is reinforced by recent results by, e.g., Miszalski et al. (2009b), Boffin et al. (2012), Corradi et al. (2014), Jones et al. (2014), who found that most PNe with close binary CS present complex morphologies.

sdOs associated with PNe represent a very small fraction ($\sim 3\%$) of the ≥ 800 known sdOs (Østensen, 2006). This number could increase as more CSs may be classified as sdO (e.g., Reindl et al., 2014). In this respect, we note the lack of firm classifications for many CS of PNe, which are crucial to identify new sdO among CSs.

4.5 Summary and outcomes of this chapter

We have presented and analysed narrow-band direct images, and high- and low-resolution, long-slit spectra of Abell 36, DeHt 2, and RWT 152, three PNe for which detailed spatio-kinematical analysis had not been carried out before. This analysis has been complemented with low-resolution, long-slit spectra that have allowed us to describe the spectral characteristics of the nebula and their CSs. The main conclusions of this chapter can be summarized as follows.

Abell 36 presents a point-symmetric elliptical morphology but the spatio-kinematical analysis reveals that it consists of a spheroidal shell and two bright point-symmetric arcs, attributable to bipolar, rotating outflows; the collimated outflows seem to have bored parts of the spheroid. DeHt 2 appears as an elliptical PN in direct images but our analysis strongly suggests that it has formed through two different ejection events, with the last one being more collimated than a previous ellipsoidal shell; evidence also exists in DeHt 2 for collimated outflow–shell interaction. RWT 152 is a bipolar PN with an equatorial ring. The complex structures of Abell 36 and DeHt 2 suggest that binary CSs may be involved in their formation.

The nebular spectra of Abell 36 and DeHt 2 indicate high excitation but only Abell 36 exhibits emission lines different from those due to Balmer, [O III], and He II. In DeHt 2 and RWT 152, the nebular spectra suggest a possible deficiency in heavy elements.

The spectra of the three CSs present narrow absorption lines, being the He II $\lambda 4686$ absorption particularly prominent. These characteristics, and the published atmospheric parameters strongly suggest an sdO nature for these CSs. Thus, these sdOs have most probably evolved through AGB and post-AGB phases.

We have compared properties of the 18 more confident PN+sdO systems and found that most of them are relatively or very evolved PNe, present collimated outflows or signs that collimated outflows have been involved in their formation, host binary CSs, and are observed at relatively high Galactic latitudes. These properties and other published results reinforce the idea that the formation of complex PNe is related to binary stars rather than to the progenitor mass. More studies of PN+sdO systems could provide interesting information about formation of complex PNe and sdO evolution.

TABLE 4.5: Properties of PN+sdO systems

PN G	Name	Morphology / Comments	Binary CS	References
009.6+10.5	Abell 41	Bipolar	Y	(1), (2), (3)
009.8–07.5	GJC 1	Irregular / Cometary-like	?	(4),(5)
027.6+16.9	DeHt 2	Elliptical / Spheroidal shell and bipolar outflows at different orientations	?	(6)
053.8–03.0	Abell 63	Bipolar / Jets	Y	(7),(8),(9), (10)
055.4+16.0	Abell 46	Elliptical-Bipolar	Y	(9),(11),(12),(13)
065.0–27.3	K 648	Elliptical / Two elliptical shells and halo	?	(14)
075.9+11.6	2M1931+4324	Multishell / Bipolar and elliptical shell at different orientations	Y	(15),(16)
136.3+05.5	HFG 1	Irregular	Y	(17),(18)
215.6+03.6	NGC 2346	Bipolar	Y	(9),(12),(19)
219.2+07.5	RWT 152	Bipolar	?	(6),(20)
272.1+12.3	NGC 3132	Elliptical	Y	(21),(22)
273.6+06.1	LSS 1362	Irregular-Elliptical	N	(23),(24)
279.6–03.1	He 2-36	Elliptical / Point-symmetry	?	(25),(26)
283.9+09.7	LSS 2018 (DS 1)	Bipolar-Irregular / Low-ionization structures	Y	(9),(27)
318.4+41.4	Abell 36	Elliptical / Spheroidal shell and point-symmetric arcs	?	(6),(20)
331.3–12.1	Hen 3–1357	Multishell / Bipolar and elliptical shells and jets	?	(28),(29)
335.5+12.4	LSE 125 (DS 2)	Round	N	(27),(30)
339.9+88.4	LoTr 5	Bipolar	Y	(31),(32)

(1) [Bruch et al. \(2001\)](#); (2) [Shimanskii et al. \(2008\)](#); (3) [Jones et al. \(2010\)](#) (4) [Borkowski et al. \(1993\)](#); (5) [Rauch et al. \(1998\)](#); (6) This chapter; (7) [Pollacco & Bell \(1997\)](#); (8) [Tsessevich \(1977\)](#); (9) [Miszalski et al. \(2009b\)](#); (10) [Mitchell et al. \(2007\)](#); (11) [Stanghellini et al. \(2002\)](#); (12) [Bond & Livio \(1990\)](#); (13) [Ritter & Kolb \(2003\)](#); (14) [Alves et al. \(2000\)](#); (15) [Aller et al. \(2013\)](#); (16) [Jacoby et al. \(2012\)](#); (17) [Heckathorn et al. \(1982\)](#); (18) [Grauer et al. \(1987\)](#); (19) [Kohoutek & Senkbeil \(1973\)](#); (20) [Østensen \(2006\)](#); (21) [Ciardullo et al. \(1999\)](#); (22) [Monteiro et al. \(2000\)](#); (23) [Chu et al. \(2009\)](#); (24) [Heber et al. \(1988\)](#); (25) [Corradi & Schwarz \(1993\)](#); (26) [Méndez \(1978\)](#); (27) [Drilling \(1983\)](#); (28) [Bobrowsky et al. \(1998\)](#); (29) [Reindl et al. \(2014\)](#); (30) [Hua et al. \(1998\)](#); (31) [Van Winckel et al. \(2014\)](#); (32) [Graham et al. \(2004\)](#)

Observations of RWT 152 with OSIRIS/GTC

In this chapter we present a more detailed morphological description and a chemical abundance analysis of RWT 152, based on subarcsecond red tunable filter imaging and deep intermediate-resolution, long-slit spectra, respectively, obtained with OSIRIS/GTC. The new $H\alpha$ image reveals new structures not observed in the previous images, with a main bipolar shape surrounded by a circular halo. The nebular spectra reveal a very low-excitation nebula with weak emission lines from H^+ , He^+ , and double-ionized metals, and absence of emission lines from neutral and single-ionized metals, except for $[N\ II]\lambda\ 6584$, which can be explained if RWT 152 is a density-bounded planetary nebula. Low abundances of S, O, Ar, N, and Ne are obtained that, together with the deduced high peculiar velocity, indicate that RWT 152 is a halo planetary nebula. This chapter is based on Aller et. al 2015c (submitted to MNRAS).

5.1 Introduction

As we concluded in Chapter 4, PNe around sdO CSs appear to share some characteristics. They are generally evolved or relatively evolved PNe with a very low surface brightness; most of them present elliptical and bipolar shapes, often with multiple structures, including signs of collimated outflows; and a high fraction of confirmed (or suspected) binary CSs is also observed in these PN+sdO systems. In addition, a possible deficiency of heavy elements is suggested in some of them. These common characteristics strongly suggests a common formation process for these PNe. However, more detailed studies of these systems, specially chemical abundance analysis of their PNe, are required to obtain information about their progenitor stars. In particular, given the faintness of these PNe, very deep spectra are needed to detect (if present) the emission lines required to trace the properties and the chemistry of these objects.

In this framework, large telescopes represent a very useful tool to carry out detailed analyses of such faint PNe, since they provide high signal-to-noise ratio data with relatively short-exposure times. We have obtained imaging and spectroscopy of the PN RWT 152 with the 10-m class GTC telescope. These data allow us to analyze its morphology in detail as well as to detect faint emission lines not detected in our previous CAFOS spectra.

5.2 Observations and data reduction

5.2.1 Optical imaging

Images of RWT 152 were obtained on 2013 November 6 in service mode with OSIRIS (Optical System for Imaging and low-Intermediate-Resolution Integrated Spectroscopy), mounted on the Nasmyth-B focus of the 10.4 m Gran Telescopio Canarias (GTC), at the Observatorio Roque de los Muchachos (La Palma, Canary Islands, Spain). The detector of OSIRIS consists of two Marconi CCD42-82 (2048×4096 pixels) with a 37 pix (binned) gap between them. The maximum unvignetted field of view (FOV) is 7.8×7.8 arcmin. In order to increase the signal-to-noise we chose the standard 2×2 binning mode which provides a plate scale of 0.254 arcsec pixel⁻¹.

The red tunable filter (RTF, [Cepa et al., 2003](#)) was used, which covers the 6510–9345Å wavelength range. The RTF allows to reduce this spectral range and isolate the desired order by selecting the available Order Sorter (OS) filters. We selected the OS filter f657/35 nm that provides a wavelength range of 6490–6600Å, thereby isolating the H α + [N II] $\lambda\lambda$ 6548,6584 emission lines. The RTF was sintonized with a full width at half-maximum (FWHM) of 20 Å.

It should be noted that with the RTF the wavelength along the FOV is not uniform, decreasing radially outwards from the optical centre following the law

$$\lambda = \lambda_0 - 5.04 \times r(\text{arcmin})^2, \quad (5.1)$$

where λ_0 is the central wavelength and r the distance to the optical centre (see [González et al., 2014](#)).

Figure 5.1 shows the circular FOV available for TF observations. In this figure, taken at 7325 Å, the bright rings correspond to prominent sky lines (also known as sky rings) each at a different wavelength. They are concentric to the TF optical centre, which is located within the gap of the CCDs, at pixel (-10, 976) of CCD2 (the right one). The radial wavelength variation over the FOV is thus clear in this image.

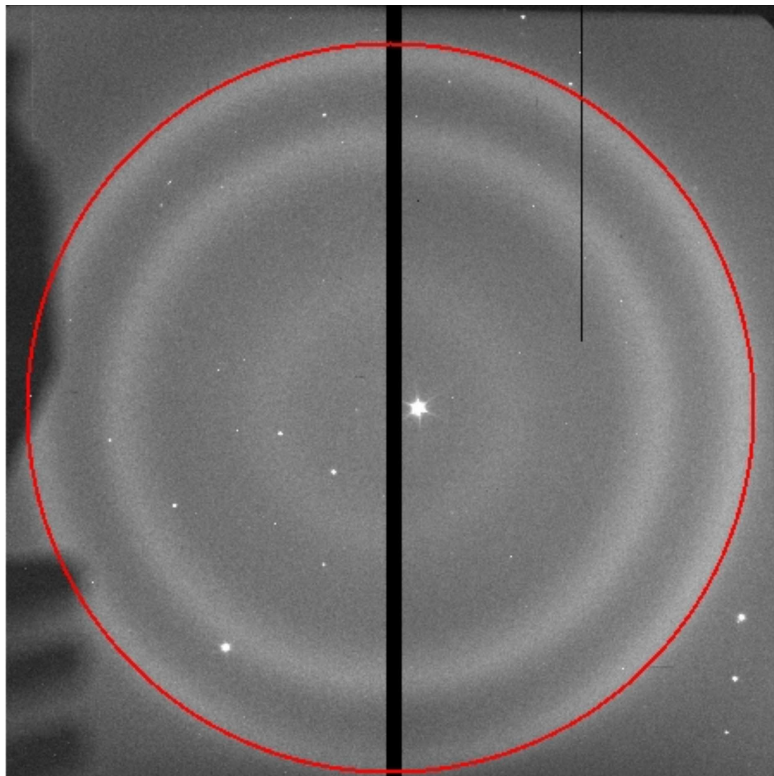


FIGURE 5.1: OSIRIS circular field of view available for TF mode. Each of the bright rings corresponds to a strong sky emission line at a specific wavelength. Credit image: <http://www.gtc.iac.es/instruments/osiris/osiris.php>

This quadratic decrease of the wavelength is particularly critical in extended objects such as PNe, since the light collected from each point of the nebula comes from different wavelengths depending on the distance to the optical centre. Taking this into account, the observations were designed to cover the $H\alpha$ and $[N\text{ II}]\lambda 6584$ emissions from all the points of RWT 152. The observing strategy was to obtain images with the optical centre at six different central wavelengths ($\lambda_0 = 6550, 6560, 6570, 6580, 6590,$ and 6600 \AA), hereafter referred to as individual bands. Figure 5.2 shows the spectral response of the selected OS filter centred at these individual bands (black lines). The intermediate-resolution, long-slit spectrum of RWT 152 (see Sect. 5.3.2) has also been plotted in Fig. 5.2 to show the contribution of the $H\alpha$ and $[N\text{ II}]\lambda 6584$ emission lines on each individual band. However, we note that the observed flux of the $[N\text{ II}]\lambda 6584$ emission line is practically negligible, only $\sim 0.5\%$ of $H\alpha$ (see Sect. 5.3.2), thus making the $H\alpha$ emission line the main contributor in this OS filter. The CS of RWT 152 was placed at ~ 1 arcmin from the optical centre, corresponding to $\sim 5 \text{ \AA}$ bluer than the central wavelength of each band (see equation 1). However, the small size of RWT 152 (see Sect. 5.3.1) implies that the wavelength along the nebula hardly varies, so we can assume that all points of the nebula are covered by approximately the same wavelength. Therefore, for this particular case, by adding the images of all individual bands we obtain an $H\alpha$ image of RWT 152. Three images were taken in each individual band, each with an exposure time of 80 s, allowing a dithering of ~ 5 arcsec between

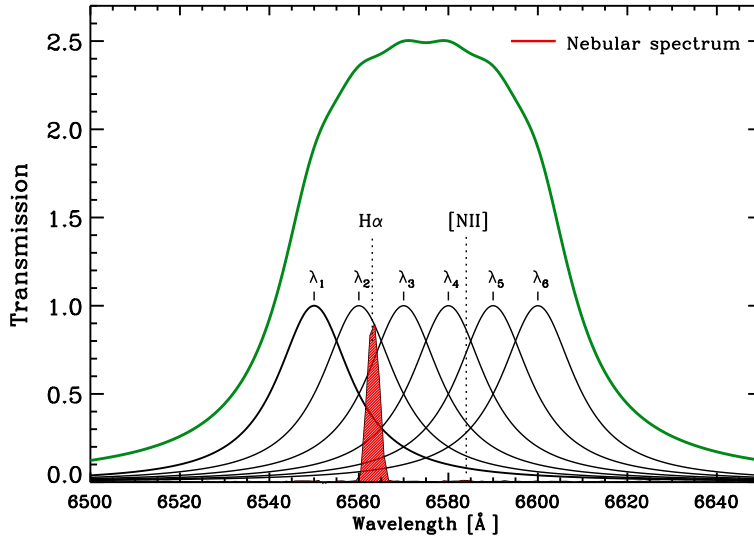


FIGURE 5.2: Transmission curves of the OS filter at the six selected bands (labelled as λ_1 , λ_2 , λ_3 , etc.) are plot in black. The scaled nebular spectrum of RWT 152 (see Sect. 5.3.2) is over-imposed in red and the position of the $H\alpha$ and $[NII]$ emission lines is indicated to highlight the contribution of these lines to the different bands. The resulting band of adding each individual band is plotted in green.

images to properly remove the diametric ghosts produced in the images.

The images were reduced using IRAF procedures for direct image. After correcting each individual frame from bias and flat-field, the three images of each individual band were aligned and median combined. Then, we added all images of all individual bands to obtain a deep $H\alpha$ image within the total band plotted as a green line in Fig. 5.2. The total exposure time for the final $H\alpha$ image is 1440 s (i.e., 6(bands) \times 3(images) \times 80 s) and the spatial resolution is 0.7 arcsec, as indicated by the FWHM of field stars in the image. Figure 5.3 shows the $H\alpha$ image at two different grey levels.

5.2.2 Intermediate-resolution, long-slit optical spectra

Intermediate-resolution, long-slit spectra of RWT 152 were obtained with OSIRIS. The volume-phased holographic gratings (VPHs) R2500U, R2500V, R2500R, R2500I were used. They cover the spectral ranges 3440–4610, 4500–6000, 5575–7685, and 7330–10000 Å, respectively, at dispersions of 0.62, 0.80, 1.04, and 1.36 Å pixel⁻¹. The standard 2 \times 2 binning mode was used, which provides a plate scale of 0.254 arcsec pixel⁻¹.

Spectra were obtained on 2013 November 6 (R2500R, R2500I) and 7 (R2500U, R2500V). The slit width was 0.8 arcsec and the spectra were obtained with the slit oriented at PA 90° and centred 7 arcsec south of the CS (see Fig. 5.3), covering the southwestern lobe of the nebula. The exposure time was 1200 s for each VPH and the seeing was \approx 0.9 arcsec.

The spectra were reduced following standard procedures for long-slit spectroscopy within the IRAF and MIDAS. The spectrophotometric standard Hiltner 600 was used for flux calibration. Some differences (around 10%) were found in the calibrated fluxes of the standard star in the overlapping range of the VPHs, which translate to the flux calibration of the nebular spectra. Nevertheless, these differences are within the uncertainties of the flux calibration process. Finally, we note that strong sky lines in the nebular spectrum could not be completely removed, leaving some residuals that prevent us from a clear identification or measurement of some nebular emission lines. This problem is particularly accused in the spectrum obtained with the VPH R2500I where most sky lines could not be removed (see Sect. 5.3.2).

5.3 Results

5.3.1 Morphology

The high quality and subarcsecond resolution of the new $H\alpha$ image (Fig. 5.3) allow us to describe new morphological structures in RWT 152 not detected so far, improving substantially the previous description explained in Chapter 4. The nebula shows a clear bipolar morphology in the light of $H\alpha$ with a size of $\approx 17 \times 21$ arcsec² and the major axis oriented at PA $\sim 45^\circ$, that are compatible with the size and orientation measured in our previous [O III] image. However, the new image reveals that the bipolar lobes are slightly different to each other, being the SW lobe broader than the NE one and that the bipolar lobes are composed by many bubbles, specially well defined in the SW lobe. No point-symmetric distribution of the bubbles is noticed in the $H\alpha$ image. The presence of these small bubbles may explain the deviations from a pure hour-glass geometry observed in the high-resolution, long-slit spectrum along the major nebular axis (see Sect. 4.3.3.2), implying a more complex internal kinematics.

The $H\alpha$ image also shows that the equatorial region of the bipolar shell is particularly bright (Fig. 5.3). To check the veracity of this structure and to discard possible effects produced by the brightness of the CS, we inspected the RTF image in the individual band with the optical centre at $\lambda_6=6600$ Å, where the emission should be dominated by the nebular continuum. In this image, shown in Fig. 5.4, the bright equatorial region cannot be recognized, indicating that this region corresponds to a real nebular structure that is most probably associated to the equatorial torus identified in the high-resolution, long-slit spectra (Sect. 4.3.3.2). In the image, the CS appears displaced ~ 3 arcsec northwards with respect to the centre of the nebula. This value slightly differs from the displacement inferred from the high-resolution spectra, where a shift of ≈ 1.4 arcsec towards PA $\approx 348^\circ$ was obtained. However, as the new image does not allow us to trace clearly the torus, the displacement obtained from the high-resolution spectra should be considered as a more precise value.

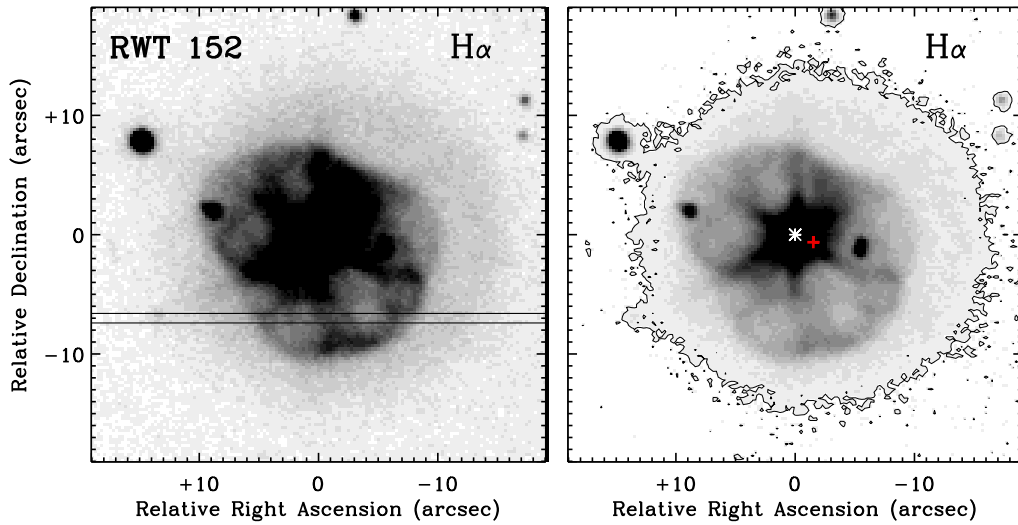


FIGURE 5.3: Grey-scale reproductions of the $H\alpha$ image of RWT 152 (north is up; east to the left). Grey levels are linear on the left-hand panel and logarithmic on the right-hand one. The origin (0,0) is the position of the central star marked with a white asterisk. The long slit used for spectroscopy is indicated by the horizontal lines in the left-hand panel (see text). The contour in the right-hand panel traces the size of the halo at the 3σ level above the background; the geometrical centre of the halo is indicated by a red plus symbol.

Finally, a very faint circular halo of ~ 29 arcsec in diameter can be recognized in the new $H\alpha$ image (Fig. 5.3). Neither the main nebula nor the CS are centred in the halo but are clearly displaced towards the northeast with respect to the geometrical centre of the halo. Displacements of a halo with respect to the CS and PN have been traditionally attributed to interaction of the PN with the ISM (see, e.g., Ramos-Larios & Phillips, 2009). In the case of RWT 152, the image suggests that the east/southeast part of the halo is interacting with the ISM. Nevertheless, if so, one would expect that the east/southeast part of the halo would be the brightest one, which is not observed in our image. In addition, the halo does not show departures from a circular symmetry, as it could be expected from that interaction. Higher-resolution images would be helpful to confirm this possible interaction.

5.3.2 The optical spectrum: physical conditions and chemical abundances

Figure 5.5 shows the intermediate-resolution, long-slit spectrum of RWT 152, obtained by combining the VPHs R2500U, R2500V and R2500R. The VPH R2500I is not shown here because of strong contamination by the sky lines (Sect. 5.2.2, but see also below). The spectra have been obtained by integrating the detected emission lines between 4 and 6.4 arcsec west of RWT 152 along the slit. This region corresponds to that showing the highest signal-to-noise ratio for the weakest lines. Whereas only $H\alpha$, $H\beta$ and $[O\text{ III}]\lambda\lambda 4959,5007$ emission lines had been previously

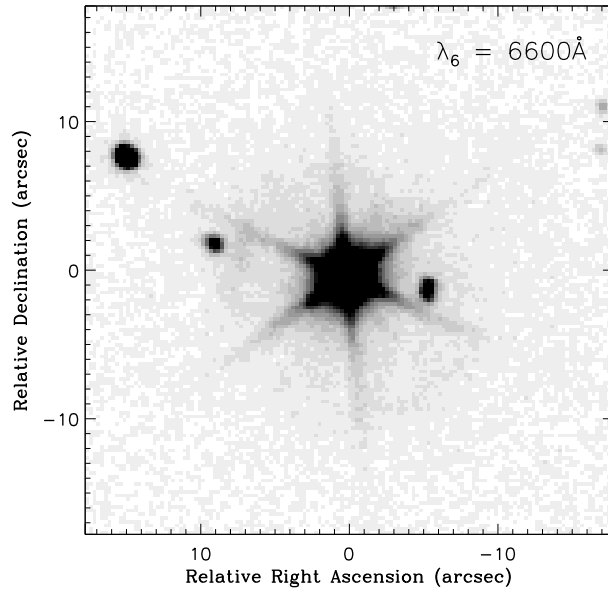


FIGURE 5.4: Grey-scale reproduction of the RTF image with the optical centre at $\lambda_6=6600 \text{ \AA}$, where the contribution of the $H\alpha$ emission line is minimum (see Fig. 5.2). Grey levels are linear.

detected in our previous nebular spectrum (see Sect. 4.3.3.3), the long-exposure OSIRIS/GTC spectra reveal other faint nebular emissions. In particular, $[\text{Ar III}]$, $[\text{Ne III}]$ and He I emission lines are detected. The $[\text{N II}]\lambda 6584$ emission line could also be present, although its extreme faintness (observed flux $\sim 1.32 \times 10^{-17} \text{ erg cm}^{-2} \text{ s}^{-1}$) suggests to take this identification with caution. In the VPH R2500I the $[\text{S III}]\lambda\lambda 9069, 9532$ emission lines are clearly identified and relatively isolated from strong sky lines whereas other faint emission lines ($[\text{Ar III}]\lambda 7751$, some Paschen lines) could also be present. Emission lines due to $[\text{O I}]$ and $[\text{S II}]$ are not identified. The $[\text{N I}]\lambda\lambda 5198, 5200$ and $[\text{O II}]\lambda\lambda 7320, 7330$ emission lines are contaminated by sky lines and their presence cannot be established directly. To check if these emission lines could be present, we have used the long-slit spectra before sky subtraction to compare the flux level measured in the nebula with that in nearby regions outside the nebula, at the wavelengths of the $[\text{N I}]$ and $[\text{O II}]$ emission lines. An upper limit of $\sim 6 \times 10^{-18} \text{ erg cm}^{-2} \text{ s}^{-1}$ for the observed flux of the $[\text{N I}]$ emission lines and an even smaller value for the $[\text{O II}]$ emission lines has been obtained. These values are much lower than the observed flux in $[\text{N II}]\lambda 6584$ mentioned above and allow us to conclude that emission lines from neutral and single-ionized metals are not present in the spectrum of RWT 152. This result is entirely compatible with the lack of $[\text{N I}]$ and $[\text{O II}]$ emission lines in the CAFOS spectra (see Chapter 4). Finally, He II emission lines are neither identified.

The spectra have been analyzed using the nebular analysis software ANNEB (Olguín et al., 2011), which also integrates the NEBULAR package of IRAF/STSDAS (Shaw & Dufour, 1995), for deriving physical conditions and both ionic and elemental abundances. A set of extinction laws are also included and a proper error propagation through the calculations is performed. Briefly, ANNEB

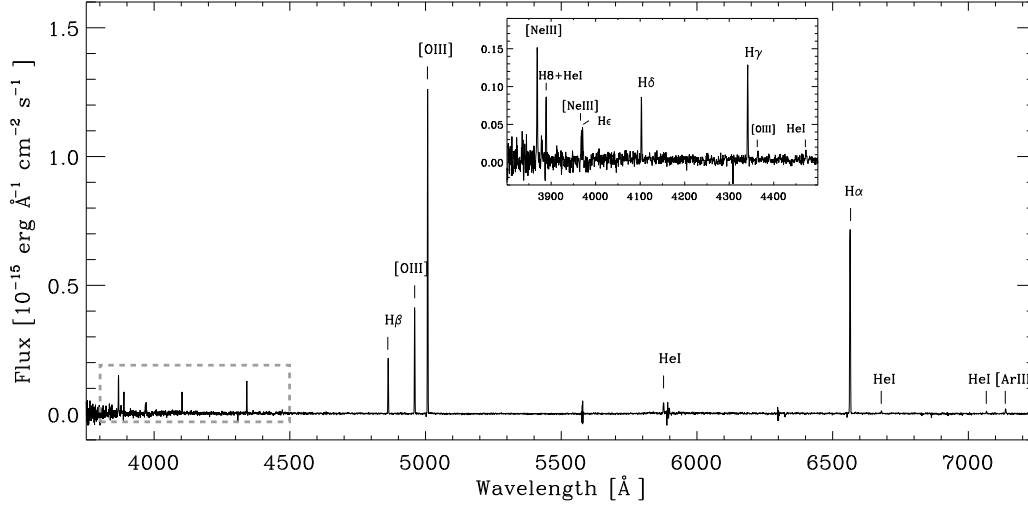


FIGURE 5.5: Optical spectrum of RWT 152 in the spectral range 3800–7250 Å. The VPHs R2500U, R2500V and R2500R have been combined. The detected emissions lines are labelled. The inset shows the spectrum in the range 3800–4500 Å.

obtains the logarithmic extinction coefficient $c(\text{H}\beta)$ and the electron temperature from the $[\text{O III}]$ lines $T_e([\text{O III}])$ iteratively, starting with the values derived for $T_e = 10^4$ K and the theoretical $\text{H}\alpha/\text{H}\beta$ line intensity ratio for case B recombination (Osterbrock, 1989); then, it derives the dereddened line intensities that are used to calculate the values of $c(\text{H}\beta)$ and $T_e([\text{O III}])$ again. The process is repeated until $c(\text{H}\beta)$ and $T_e([\text{O III}])$ converged to the final values.

A value for the electron density (N_e) is also necessary for the calculations. Unfortunately, the lack of the $[\text{S II}]$, $[\text{Ar IV}]$ or $[\text{Cl III}]$ emission lines from RWT 152 prevents us from deriving N_e from the forbidden lines. Therefore, we have used the observed flux in $\text{H}\alpha$ ($F(\text{H}\alpha)$) to calibrate the image and the formulation by Hua & Kwok (1999) to calculate the mean electron density in RWT 152. We considered a $F(\text{H}\alpha)$ of 6.27×10^{-15} erg cm $^{-2}$ s $^{-1}$ observed in a region of 0.8×29 arcsec 2 (defined by the slit width and the angular size of the nebula, including the halo), and obtained $N_e = 83/D[\text{kpc}]^{-1/2}$. For distances of 2.4 kpc (Ebbets & Savage, 1982) and 6.5 kpc (Pritchett, 1984), the electron density is 55 and 32 cm $^{-3}$, respectively, with an estimated error of about 10% in both cases. No particular differences were noticed in the resulting parameters and ionic and elemental abundances by using one or other of the derived electron density values. We have adopt $N_e = 55 \pm 10$ cm $^{-3}$.

After this procedure, we obtain $c(\text{H}\beta) = 0.60 \pm 0.04$ and $T_e([\text{O III}]) = 14400 \pm 750$ K that are listed in Table 5.1. The value for $c(\text{H}\beta)$ derived from the OSIRIS spectra is slightly higher than that obtained from the CAFOS spectra presented in Sect. 4.3.3.3 ($c(\text{H}\beta) \sim 0.46$), suggesting internal variations of the extinction in the nebula. Table 1 also lists the dereddened emission line intensities and their Poissonian errors, as obtained with $c(\text{H}\beta) = 0.60$ and the extinction law of

TABLE 5.1: Dereddened emission line intensities in RWT 152.

Line	$f(\lambda)$	$I(\lambda) (I(H\beta)=100)$
[Ne III] $\lambda 3869$	0.228	70.7 ± 4.3
He I + H8 $\lambda 3889$	0.223	42.9 ± 2.6
[Ne III] $\lambda 3968$	0.203	11.9 ± 1.2
H ϵ $\lambda 3970$	0.203	18.9 ± 1.4
H δ $\lambda 4101$	0.172	31.5 ± 1.4
H γ $\lambda 4340$	0.129	48.4 ± 1.9
[O III] $\lambda 4363$	0.124	9.0 ± 0.6
He I $\lambda 4471$	0.115	6.7 ± 0.4
H β $\lambda 4861$	0.000	100.0 ± 2.9
[O III] $\lambda 4959$	-0.023	188.1 ± 4.7
[O III] $\lambda 5007$	-0.034	552.3 ± 14.4
He I $\lambda 5876$	-0.216	20.1 ± 0.7
H α $\lambda 6563$	-0.323	280.5 ± 11.0
[N II] $\lambda 6584(?)$	-0.326	1.5 ± 0.1
He I $\lambda 6678$	-0.338	3.2 ± 0.2
He I $\lambda 7065$	-0.383	2.8 ± 0.2
[Ar III] $\lambda 7135$	-0.391	6.4 ± 0.3
[S III] $\lambda 9069$	-0.606	3.0 ± 0.2
[S III] $\lambda 9532$	-0.620	9.2 ± 0.6

$c(H\beta) = 0.60 \pm 0.04$
 $\log F_{H\beta}(\text{erg cm}^{-2} \text{s}^{-1}) = -15.85$
 $T_e([O III]) = 14400 \pm 750 \text{ K}$
 $N_e = 55 \pm 10 \text{ cm}^{-3}$

Seaton (1979). We further note that the use of other extinction laws (e.g., Cardelli et al., 1989) does not produce appreciable differences in the dereddened emission line intensities and other parameters.

The absence of the He II $\lambda 4686$ emission line and the [O III]/H β line intensity ratio of $\simeq 8$ (Table 5.1) indicate a very low-excitation PN, with an excitation class of 2 according to Gurzadian & Egikian (1991). The very low-excitation is compatible with the relatively low effective temperature of the CS of RWT 152 ($\simeq 45000 \text{ K}$, Ebbets & Savage 1982). In these circumstances, the non-detection of neutral and single-ionized emission lines (e.g., [S II], [O I], [N I], [O II]) and the extremely faintness of the (possible) [N II] $\lambda 6584$ emission line is highly peculiar for this excitation class.

The derived ionic abundances, calculated as a weighted average by the signal-to-noise ratio of each line for species with more than one line, are listed in Table 5.2. To obtain the helium abundance, we used the method by Kwitter & Henry (2001), while for the argon abundance, we followed the icf method by Kingsburgh & Barlow (1994). These elemental abundances are listed in Table 5.3, where $\epsilon(X/H) = \log(X/H) + 12$ is given. For the rest of the elements, the absence of some emission lines prevents to calculate the icfs and, therefore, the elemental abundances. Nevertheless, the low effective temperature of the CS and the observed spectrum allow us to make some reasonable assumptions to obtain approximate values for the abundances.

TABLE 5.2: Mean ionic abundances relative to H⁺ of RWT 152.

Ion	Ionic abundance
He ⁺	0.140±0.004
O ⁺⁺	(6.5±0.1)×10 ⁻⁵
N ⁺	(1.3±0.1)×10 ⁻⁷
Ar ⁺⁺	(2.8±0.1)×10 ⁻⁷
Ne ⁺⁺	(1.7±0.1)×10 ⁻⁵
S ⁺⁺	(2.8±0.1)×10 ⁻⁷

TABLE 5.3: Elemental abundances of RWT 152 (see text) and average abundances for type III and type IV PNe taken from [Costa et al. \(1996\)](#).

Element	Abundance	Type III PNe	Type IV PNe
He/H	0.140±0.004	0.099	0.104
ε(O/H)	7.81±0.02	8.42	8.08
ε(N/H)	5.11±0.03	7.74	7.41
ε(Ar/H)	5.72±0.02	6.07	5.22
ε(Ne/H)	7.23±0.03	7.71	7.27
ε(S/H)	5.45±0.02	6.74	5.64

In particular, the lack of He II and [Ar IV] emission lines in the spectra makes it highly improbable that ionization states as O³⁺, S³⁺, and Ne³⁺ may exist in the nebula. This, and the absence of emission lines from O⁰, O⁺, S⁺, and Ne⁺ in the spectrum of RWT 152 strongly suggest that O²⁺, S²⁺, and Ne²⁺ are the dominant excitation states. In consequence, their ionic abundances may be considered as representative of their elemental abundances. Using the same arguments, N²⁺ probably does not exist in the nebula. Taking into account that emission lines due to N⁰ neither exist, the N abundance should be similar to the abundance of N⁺, although given the extreme faintness of the [N II]λ6584 (see above), the existence of nitrogen in the nebula is questionable. In Table 5.3 we provide the values of the ionic abundances as the elemental abundances of O, S, Ne, and N, where the N abundance should be considered as an upper limit. Table 5.3 shows low elemental abundances of metals, confirming what we already suggested in Chapter 4. We will discuss below the implications of the elemental abundances. It is worth noting that this result provides strong support for a deficiency of metals in 2M1931+4324 (see Chapter 3), that presents a nebular spectrum very similar to that of RWT 152.

5.4 Discussion

One of the most noticeable characteristics of RWT 152 is its peculiar nebular spectrum. As already mentioned, the lack of low-excitation emission lines (e.g., [O I], [S II], [N I]) is difficult to understand in a PN with an excitation class of 2 and a relatively low effective temperature CS (≈ 45000 K, [Ebbets & Savage, 1982](#)). Under these conditions, one could expect that emission lines due to, e.g., O⁰, O⁺, S⁺, N⁰, were prominent, even though the abundances of O, S, N

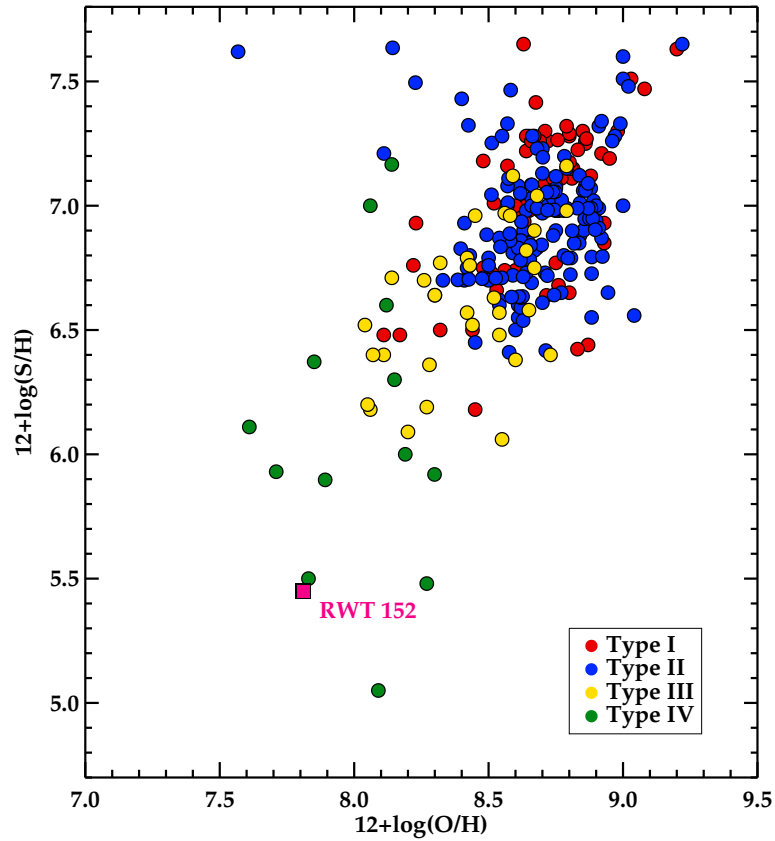


FIGURE 5.6: Plot of $12+\log(\text{Ar}/\text{H})$ versus $12+\log(\text{O}/\text{H})$ (left panel) and $12+\log(\text{S}/\text{H})$ versus $12+\log(\text{O}/\text{H})$ (right panel) for a sample of type I (red), type II (blue), type III (yellow) and type IV (green) PNe. Data from [Henry et al. \(2004\)](#), [Costa et al. \(1996\)](#), [Maciel & Koppen \(1994\)](#), [Howard et al. \(1997\)](#), and [Pereira & Miranda \(2007\)](#). The position of RWT 152 is marked with a pink square. Error bars of RWT 152 correspond to the size of the symbol.

are low. This spectrum can be understood if RWT 152 is a density-bounded PN with no low-excitation region (at least along the bipolar lobes, because the equatorial structure has not been studied). In fact, $[\text{O I}]$, $[\text{N II}]$, $[\text{S II}]$ emission lines become very weak in density-bounded models (see [Gesicki & Zijlstra 2003](#)), and, in addition, a PN becomes optically thin if the effective temperature of the CS is in the range 40000–50000 K ([Kaler & Jacoby 1991](#)), as it is the case of RWT 152.

To obtain information about the progenitor CS of RWT 152, it is interesting to classify RWT 152 according to the [Peimbert \(1978\)](#) types. The helium abundance derived for RWT 152 ($\text{He}/\text{H} \sim 0.140$, [Table 5.3](#)) indicates a type I or type II PNe. However, the extremely low nitrogen abundance rules out these two types. A comparison of the abundances of O, S, Ar and Ne with those typical of type III and type IV PNe, shown in [Table 5.3](#), clearly reveals that RWT 152 is a type PN. To reinforce this classification, we show in [Figure 5.6](#) the $12+\log(\text{S}/\text{H})$ versus $12+\log(\text{O}/\text{H})$ diagram for the four Peimbert types of PNe, in which RWT 152 is placed in the

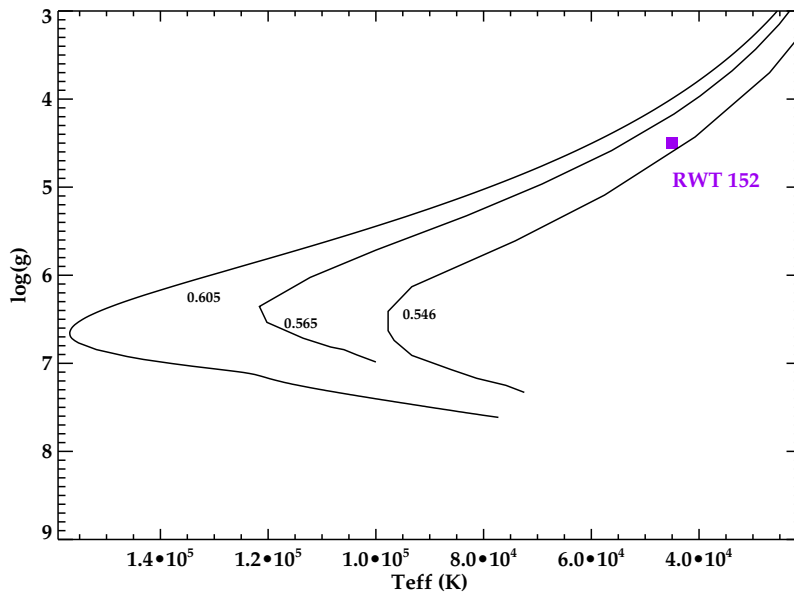


FIGURE 5.7: Position of RWT 152 in the $\log g - T_{\text{eff}}$ diagram according to [Ebbets & Savage \(1982\)](#). Post-AGB by evolutionary tracks by [Bloeker \(1995\)](#) and [Schoenberner \(1983\)](#) are drawn and labelled with the corresponding stellar mass (in M_{\odot}).

region of halo PNe. Finally, it is worth mentioning that the helium abundance in RWT 152 appears high for type IV PNe. However, some of these halo PNe present relatively high helium abundances, as, e.g., M2-7 with $\text{He}/\text{H} \sim 0.137$ ([Quireza et al., 2007](#)). The extremely low N abundance is noticeable. We have not found a reasonable explanation, although we have considered the possibility that the star had been formed in a nitrogen-poor environment, that N is depleted (forming part of the grains), and/or that N has not been dredged up.

Moreover, we have derived the peculiar velocity of RWT 152 from its heliocentric radial velocity $V_{\text{HEL}} \sim +134.5 \pm 1.8 \text{ km s}^{-1}$ (see Sect. 4.3.3.2), following the formulation explained in [Peña et al. \(2013\)](#), and the resulting value is $\sim 92 - 131 \text{ km s}^{-1}$ for distances of 2.4 kpc and 6.5 kpc, respectively. This interval of peculiar velocities clearly is expected for a type IV PNe. Finally, we note that the height above the Galactic plane of RWT 152 is 0.2–0.8 kpc for the mentioned distances. Although type IV PNe are usually located at $z > 0.8$ ([Peimbert, 1990](#)), we note that other halo PNe are located at comparable heights above that plane (see [Pereira & Miranda, 2007](#), and references therein). Summarizing, the chemical abundances and the peculiar velocity add RWT 152 as a new member of the few known halo PNe.

A comparison of the He and O abundances in RWT 152 with evolutionary models of stellar yields by [Marigo \(2001\)](#) suggests a progenitor star with an initial mass of $\sim 1.3 M_{\odot}$ and very low metallicity $Z = 0.004$. The stellar mass is compatible with that expected for sdOs ([Heber, 2009](#)) and the low metallicity indicates that the progenitor was formed in a poor-metal environment. In contrast, similar models of initial mass $\sim 1.25 M_{\odot}$ and $Z = 0.004$ by [Karakas \(2010b\)](#)

predict abundances considerably different from that found in RWT 152. Therefore, it is clear that drawing conclusions about the progenitor star of RWT 152 taking into account simply the chemical abundances of the nebula may be a bit misleading. For this reason, we have attempted to obtain information of the progenitor from the current status of the CS. Figure 5.7 shows the position of RWT 152 in the HR diagram $\log g - T_{\text{eff}}$ with the post-AGB tracks by [Bloeker \(1995\)](#) and [Schoenberner \(1983\)](#). The location of the star ($T_{\text{eff}} \simeq 45\,000$ K, $\log g \simeq 4.5$; [Ebbets & Savage, 1982](#)) is consistent with a current mass of $M \sim 0.55 M_{\odot}$ which implies an initial mass in the main sequence of $\sim 1 M_{\odot}$. For such a low-mass star, the ejected mass during the AGB evolution is expected to be small. In fact, with the electron density derived above and the size of the nebula we obtain values of $1.6 \times 10^{-2} - 1.8 \times 10^{-1} M_{\odot}$ for the ionized nebular mass (assuming 2.4 and 6.5 kpc, respectively) and a filling factor of 0.6. These values are much smaller than ionized masses usually obtain for PNe (see, e.g., [Hua & Kwok, 1999](#)), which is compatible with a low-mass progenitor. Moreover, taking into account that 0.1-0.3 M_{\odot} are lost in the RGB phase for a low-mass star ([Dorman et al., 1993](#)), the current mass of the CS and the obtained ionized mass, we recover a progenitor star with a ~ 0.8 -1.0 M_{\odot} as indicated by the position of the CS in the $\log g - T_{\text{eff}}$ diagram. Such a low ionized mass could also explain the low surface brightness of RWT 152. If a low-mass progenitor is involved in the evolution of other PNe+sdO systems, it is not surprising that these PNe are very faint and, in some cases, may have faded beyond detection.

The GTC image shows that RWT 152 presents multiple bubbles in its bipolar lobes. The number of PNe with multiple bubbles (or lobes) has largely increased, mainly due to increasing resolution of imaging capabilities. PNe with multiple bubbles/lobes can be classified in two broad categories: (1) those with a point-symmetric distribution of the bubbles/lobes as, e.g., NGC 6058 ([Guillén et al., 2013](#)), starfish-like PNe ([Sahai, 2000](#)), and other young PNe ([Sahai & Trauger, 1998](#)); and (2) those with a random (non-point-symmetric) distribution of the bubbles/lobes as, e.g., NGC 1514 ([Ressler et al., 2010](#)), NGC 7094 and Abell 43 ([Rauch, 1999](#)). RWT 152 seems to be an intermediate case: it shares with NGC 1514 and Abell 43 the random distribution of the bubbles but also shares with starfish PNe the existence of a bright equatorial region (torus) separating two main lobes (or multiple point-symmetric lobes). Several scenarios have been proposed to explain the presence of multiple bubbles/lobes, including bipolar jets at several directions with variable ejection velocity (e.g., [Velázquez et al., 2012](#)), interaction of a fast wind with a warped circumstellar disk ([Rijkhorst et al., 2005](#)), and interaction of a fast wind with an inhomogenous spherical shell ([Steffen et al., 2013](#)). Multiple point-symmetric bubbles/lobes appear more compatible with a bipolar jet model or warped disk model than with an inhomogenous shell scenario; the latter would require an extremely point-symmetric density distribution in the spherical AGB shell, which could be difficult to explain. PNe with randomly distributed bubbles could be better explain by an inhomogenous shell. In the case of RWT 152, the random distribution of the bubbles points out to a model in which a dense equatorial torus exists in the spherical

shell while the rest of the shell presents an inhomogeneous density distribution. Alternatively, wind interaction with a warped disk could also explain random bubbles if material in the two sides of the disk is distributed in an inhomogeneous manner. Nevertheless, a definitive conclusion about the shaping of RWT 152 is difficult to be reached because it is an already evolved PNe and the original shaping mechanism could be masked by other processes (e.g., hydrodynamical instabilities). Images of RWT 152 at higher spatial resolution and, in particular, of its equatorial region would be very useful to complete description of the nebula and to constrain its shaping.

5.5 Summary and outcomes of this chapter

We have presented OSIRIS/GTC red tunable filter $H\alpha$ imaging and intermediate-resolution, long-slit spectroscopy of RWT 152, one of the few known PNe hosting an sdO central star. The data, obtained at subarcsec spatial resolution, allowed us to describe the detailed morphology and to obtain the physical conditions and chemical abundances of the nebula. The main conclusions of this chapter can be summarized as follows:

- (1) The new $H\alpha$ image shows that RWT 152 is a bipolar PN with a bright equatorial torus, surrounding by a circular halo. The bipolar lobes consist of multiple bubbles with a non point-symmetric distribution. The centre of the halo does not coincide with the centre of nebula and with the central star, suggesting interaction of the halo with the interstellar medium.
- (2) The nebular spectra reveal very faint [Ar III], [Ne III], He I, [S III], and, perhaps, [N II] λ 6584 emission lines which had not been previously detected. Emission lines due to neutral and single-ionized metals are not detected while the lack of He II emission lines indicates that high ionization states (e.g., O^{3+} , S^{3+} , N^{3+}) are probably not present in the nebula. These results strongly suggest that RWT 152 is a density-bounded PN, at least in the direction of the bipolar lobes.
- (3) An electron temperature $T_e([O III])$ of ~ 14400 K was derived and $N_e \sim 32 - 55 \text{ cm}^{-3}$ depending on the distance. Except for helium, the derived chemical abundances of S, O, Ne and Ar are low. Remarkably, the abundance of N is extremely low and an explanation for this fact has not been found yet.
- (4) The low abundances and the high peculiar velocity we calculate for the object ($|\Delta V_{pr}| \sim 92 - 131 \text{ km s}^{-1}$) strongly suggest that RWT 152 is a halo PN, adding a new member to the small number of known PNe in this type.

-
- (5) A comparison of the atmospheric parameters of the CS with post-AGB evolutionary tracks suggests a $\sim 1.0 M_{\odot}$ progenitor for RWT 152, that should be formed in a metal-poor environment. This low-mass progenitor would be compatible with the low ionized nebular mass ($1.6 \times 10^{-2} - 1.8 \times 10^{-1} M_{\odot}$) derived for RWT 152.
 - (6) The multiple, non-point-symmetric bubbles observed in the bipolar lobes could be attributed to interaction of a fast wind with an inhomogeneous distribution of material at both sides of the equatorial torus. Nevertheless, the original mechanism for the formation of the bubbles could be masked through the evolution.

Spectral analysis of BD+30°623, the peculiar binary central star of the planetary nebula NGC 1514

In this chapter we present a detailed spectral analysis of the binary central star BD+30°623, consisting of a cool star and a hot companion that has been previously classified as sdO by some authors. This analysis, based on intermediate-resolution optical spectra and low-resolution ultraviolet spectra, has allowed us to derive accurately the parameters of the two components in a simultaneous way for the first time. This chapter has been adapted from [Aller et al. \(2015b\)](#) (MNRAS, 448, 2822).

6.1 Introduction

Among the different types of binary CSPNe, ones of special interest are those named *peculiar central stars* ([Lutz, 1977](#)). This class refers to cool (spectral type A through K) CSs that are not hot enough to ionize their associated nebulae. Lutz suggested that these stars may belong to binary systems, where a hot (and faint) component would be the responsible for the photoionization while the cooler (and brighter) star would account for the absorption spectrum. Many works can be found regarding these stars (see, e.g., [Méndez, 1978](#), [De Marco, 2009](#), [Pereira et al., 2010](#)). However, the complexity of these systems makes their analyses difficult because the determination of the stellar parameters is laborious.

BD+30°623 ($\alpha = 04^{\text{h}} 09^{\text{m}} 16^{\text{s}}.9$, $\delta = +30^{\circ} 46' 33''$, equinox 2000.0; $\ell = 165^{\circ}.53$, $b = -15^{\circ}.2$), the exciting CS of NGC 1514, is one of these peculiar binary stars. It has been studied extensively but the physical parameters of the two components had not been determined accurately to date. It was initially classified as a single star and several spectral types were proposed in the literature

ranging from B8 (Seares & Hubble, 1920), to B9 (McLaughlin, 1942) or A0 (Chopinnet, 1963). In contrast, Payne (1930) proposed an O8 classification.

Because of its peculiar spectrum, Kohoutek (1967) proposed, for the first time, the double star hypothesis for BD+30°623 based on photoelectric photometry. He reported the existence of a fainter and hotter companion and described the pair as A0 III + blue subdwarf (sdO) with effective temperatures (T_{eff}) of 10800 K for the A-star and 60000 K for the hot star, and radii of 4.1 and 0.45 R_{\odot} , respectively. Later, Kohoutek & Hekela (1967) confirmed these values based on a spectral analysis of the CS within the interval $\lambda\lambda$ 3650–5000 Å. In contrast, Greenstein (1972) reported that the ultraviolet luminosity of the sdO required a higher T_{eff} (100000 K), and that the cool star was, in fact, an Horizontal-Branch (HB) A star (A3–A5) with $T_{\text{eff}} \leq 10000$ K. Further evidence of the binary nature of this system was provided by the International Ultraviolet Explorer (IUE) observations obtained by Seaton (1980). With these UV spectra and broad-band photometry from the Dutch ANS satellite, he constructed a model and described the system as an A0–A3 III star with $T_{\text{eff}} \sim 9000$ K, and $\log g = 3.0$, and a hot star with $T_{\text{eff}} \geq 60000$ K. To do this, he used a line blanketed model for the cool star and a blackbody for the hot companion. Besides, weak P Cygni profiles were detected. Later, Feibelman (1997) also used IUE spectra to report a considerable variability of the UV flux (by a factor of 2) but he was not able to explain it. In strong contrast with previous determinations, Grewing & Neri (1990) used different methods to estimate T_{eff} of 27000, 28000 and 38000 K for the hot component. These values are too low to account for the observed He II emission from the nebula (Kaler, 1976), which requires $T_{\text{eff}} > 60000$ K (see Pottasch, 1984). In a most recent work, Taranova & Shenavrin (2007) proposed a spectral type B(3–7) main-sequence for the cool star based on infrared photometry. In these circumstances, it is clear that a new and detailed spectral analysis is necessary in order to determine the properties of this pair.

In this framework, we present an innovative spectral analysis of BD+30°623 by means of IUE ultraviolet and intermediate-resolution optical spectra. For this purpose, grids of synthetic spectra for the cool and hot stars were used and combined making use of the latest and state-of-the-art synthetic model atmospheres. As far as we know, this is the first time that such analysis is done for one of these peculiar binary CSs.

6.2 Observations and results

6.2.1 Intermediate-resolution optical spectra

Intermediate-resolution, long-slit spectra were obtained on 2011 January 16 with CAFOS at the 2.2-m telescope at Calar Alto Observatory (Almería, Spain). A SITe 2k×2k–CCD was used as detector. Gratings B-100 and R-100 were used to cover the 3200–6200 Å and 5800–9600 Å

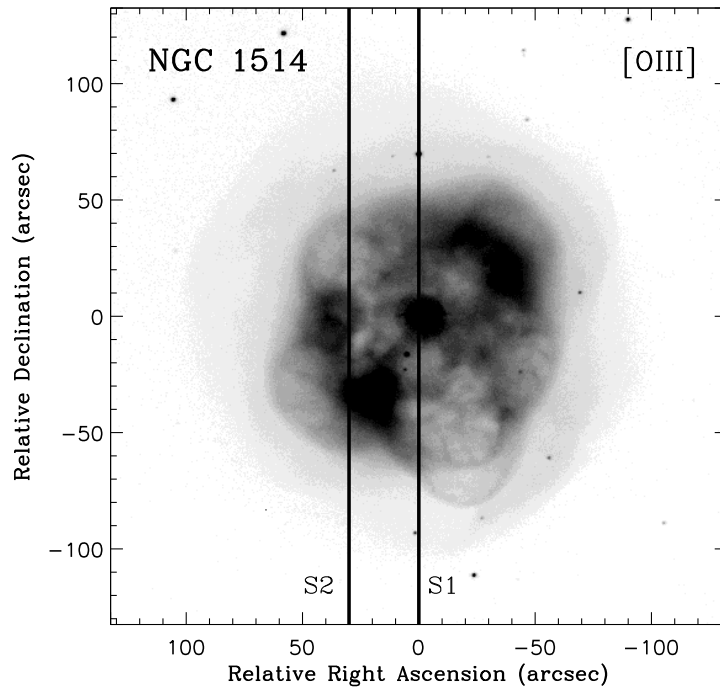


FIGURE 6.1: Grey-scale reproduction of the [O III] image of NGC 1514. Grey levels are linear. The two vertical lines S1 and S2 mark the slit positions used for intermediate-resolution, long-slit spectroscopy (see the text).

spectral ranges, respectively, both at a dispersion of $\approx 2 \text{ \AA pixel}^{-1}$. The slit width was 2 arcsec and the spectra were obtained at two slit positions, both oriented north–south: one (denoted S1) with the slit centred on the CS and with an exposure time of 100 s for each grism; and another (S2) displaced ~ 30 arcsec eastern from BD+30°623 and with an exposure time of 1800 s for each grism in order to cover the nebula. The projections of the slits on the sky are plotted in Figure 6.1, which shows an [O III] ($\lambda_0 = 5007 \text{ \AA}$, full width at half-maximum = 87 \AA) image of NGC 1514 also obtained with CAFOS in imaging mode. Seeing was ≈ 2 arcsec during the observations.

The spectra were reduced with standard routines for long-slit spectroscopy within the IRAF and MIDAS packages. For the absolute flux calibration, the spectrophotometric standards G191B2B and Feige 34 were observed the same night. We note that the red part of the spectrum (above $\sim 6200 \text{ \AA}$) presents an unexpected behaviour that we were unable to correct in the flux calibration process. Therefore, the wavelength range beyond 6200 \AA has not been taken into account for the analysis. However, the normalized uncalibrated spectrum at these wavelengths, in particular around $H\alpha$, is still usable to estimate the gravity of the cool component (see Sect. 6.4.2). Finally, we note that no problems with light losses in the flux calibration are present, since the available photometry in the blue part of the spectrum is compatible with our flux calibration.

The optical spectrum of BD+30°623 (Figure 6.2), obtained at S1, shows strong hydrogen absorption lines which are typical of A- or B-type stars. The Ca II K $\lambda 3933$ absorption line, also

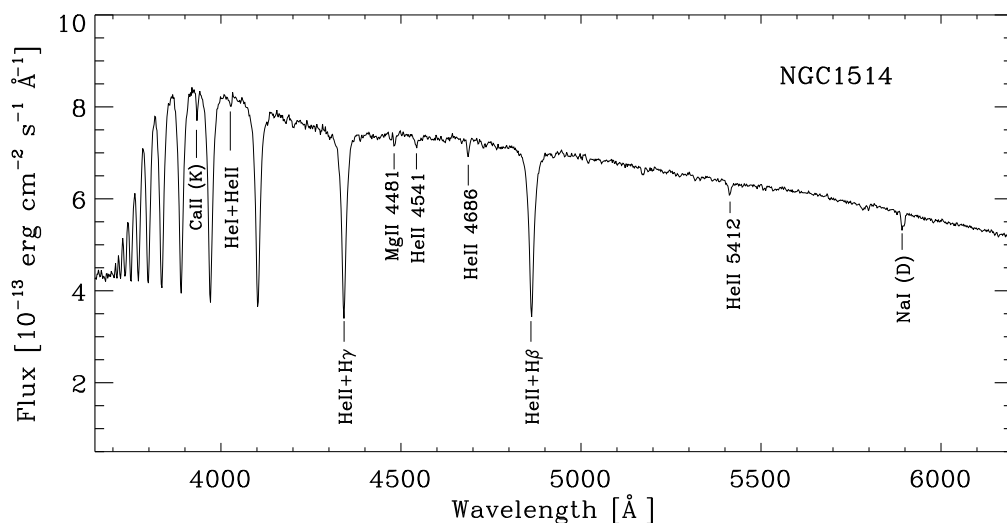


FIGURE 6.2: CAFOS CAHA blue spectrum of *BD+30°623* in the range 3500–6200 Å. Some helium and hydrogen absorption lines are indicated, as well as the $\text{Ca II } \lambda 3968$, and $\text{Mg II } \lambda 4481$. The Na I doublet ($\lambda 5889$ – 5895) is caused by interstellar absorption.

characteristic of these stars, is present. The spectrum also reveals other spectral features like $\text{He II } \lambda 4686$ and $\lambda 5412$ which are not expected in a typical spectrum of an A- or B-type star. They only appear (specially $\text{He II } \lambda 4686$) in stars with $T_{\text{eff}} \gtrsim 40000$ K (Eisenstein et al., 2006).

On the other hand, the spectrum shows very weak features of neutral helium. It is the case of $\text{He I } \lambda 4026$ (whose contribution cannot be separated from that of $\text{He II } \lambda 4025$ at this resolution) and $\text{He I } \lambda 4471$ (that seems to be also present although with a smaller contribution). These neutral helium absorption lines may originate either from the cool star or from the hot companion. Once the spectral analysis is concluded (see Sect. 6.4), we will see that these neutral helium features come from the cool companion.

We note that no nebular emission lines are observed in Fig. 6.2 because of the very short exposure time of this spectrum (100 s), but they are clearly observed in the long-exposure spectrum obtained at S2 (Fig. 6.1). We used this spectrum (not shown here) to determine the logarithmic extinction coefficient $c(\text{H}\beta)$. Because the $\text{H}\alpha$ emission line flux is unreliable (see above), we used the integrated $\text{H}\beta$ and $\text{H}\gamma$ fluxes observed at slit position S2 (see Fig. 6.1) to derive $c(\text{H}\beta) \simeq 0.97$, assuming Case B recombination ($T_e=10^4$ K, $N_e=10^4$ cm $^{-3}$) and a theoretical $\text{H}\gamma/\text{H}\beta$ ratio of 0.466 (Osterbrock, 1989). If we derive the colour excess from the relationship proposed by Seaton (1979) $c(\text{H}\beta) = 1.47 E(B-V)$, we obtain that $E(B-V) = 0.66$, in agreement with the value derived from the analysis of the CS (see Sect. 6.4.7). We also note that a slightly lower value for the logarithmic extinction coefficient ($c(\text{H}\beta) = 0.885$) was derived by Muthu (2001) from the observed $\text{H}\alpha/\text{H}\beta$ ratio. Finally, the detection of the $\text{He II } \lambda 4686$ emission line allows us to set a lower limit of $T_{\text{eff}} = 60000$ K for the hot companion (see above).

6.2.2 Low-resolution ultraviolet spectra

Since the T_{eff} of the hot companion of BD+30°623 should be higher than 60000 K, observations in the ultraviolet range are crucial to achieve a good characterization of this star. For this purpose, we have retrieved spectra from the IUE (Kondo et al., 1989) available in the IUE Newly Extracted Spectra (INES¹) System. INES provides spectra already calibrated in physical units.

We have retrieved the available low-dispersion ($\sim 6 \text{ \AA}$) IUE SWP (short wavelength) and LWP (long wavelength) spectra, which were obtained from 1978 to 1989. The SWP and LWP cover the ranges 1150-1975 \AA and 1910-3300 \AA , respectively. Only the pairs of spectra which were obtained consecutively, i.e., the same day were used. They are listed in Table 6.1. A mean of all spectra was calculated for the spectral analysis. Unfortunately, the LWP spectra beyond $\sim 2400 \text{ \AA}$ could not be used since most of them appear to be saturated and/or with many bad pixels at those wavelengths.

Figure 6.3 shows the SWP spectra listed in Table 6.1. Surprisingly, we have not found variability in the SWP spectra, in contrast with Feibelman (1997), who reported a variation in the flux of a factor ~ 2 . In order to discard possible reduction errors in the INES spectra, the same IUE SWP spectra available from the MAST² archive were retrieved. These spectra are reduced in an independent way to that of the INES archive. No sign of flux variability was found in MAST spectra either. Therefore, we consider that the variability found by Feibelman (1997) should be reassessed.

6.3 Synthetic stellar spectra

In order to carry out an accurate spectral analysis of the composite spectrum of BD+30°623, three synthetic model atmosphere grids have been used.

For the cool component, high-resolution spectra were synthesized in the range 3000–8000 \AA using the suite of programs SYNTH (Kurucz, 1993, Castelli & Kurucz, 2003).

For the ultraviolet range (1150–3200 \AA), low-resolution models from the ATLAS9 grid of model atmospheres³ by Castelli & Kurucz (2003) were used. Finally, each ultraviolet spectrum was combined with the corresponding optical one to build a grid in the range of 1150-8000 \AA .

For the hot component, we used TMAW⁴, a service recently developed in the framework of the German Astrophysical Virtual Observatory (GAVO), to calculate theoretical stellar spectra

¹<http://sdc.cab.inta-csic.es/ines/>

²<https://archive.stsci.edu/iue/search.php>

³<http://user.oat.ts.astro.it/castelli/grids.html>

⁴<http://astro.uni-tuebingen.de/~TMAW/>

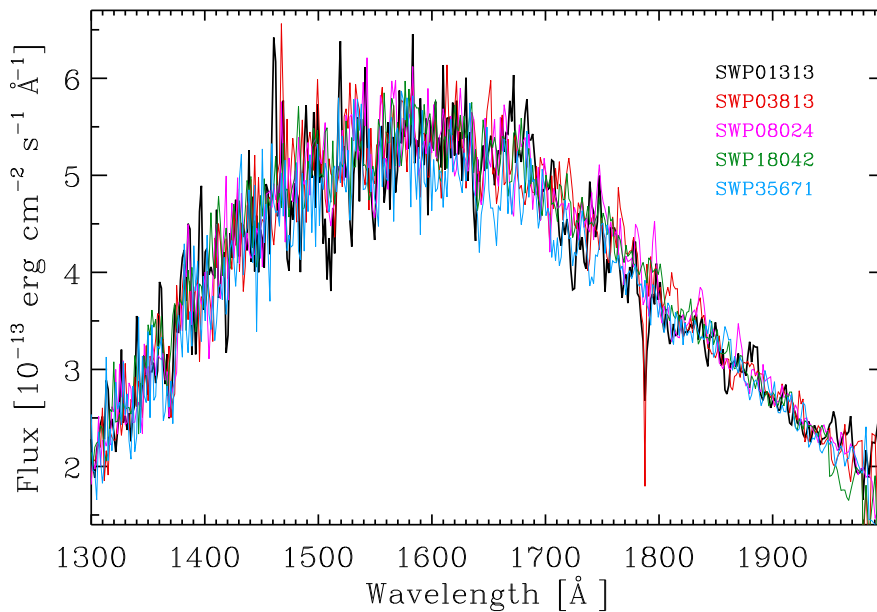


FIGURE 6.3: Plot of the five SWP spectra of BD+30°623 listed in Table 6.1 and used for the spectral analysis. No variability is observed in the SWP spectra, in contrast with that reported by Feibelman (1997).

of hot, compact stars. The service provides access to TMAP⁵ (Tübingen NLTE - Model Atmosphere Package; Werner et al., 2003), a collection of models successfully used for spectral analysis of hot, compact stars (e.g. Rauch et al., 2007, 2013, Ziegler et al., 2012).

We requested for a H+He, high-resolution grid, via TMAW, with $50000 \text{ K} \leq T_{\text{eff}} \leq 120000 \text{ K}$ in the range $1000 - 55000 \text{ Å}$. The spectral resolution was 0.1 Å in the range $1000 - 8000 \text{ Å}$ and 1 Å in the rest of the wavelengths. Since the H and He lines are not very sensitive to T_{eff} beyond 70000 K , we sampled from 50000 K to 70000 K in steps of 2000 K and from 70000 K to 120000 K in steps of 5000 K . Surface gravity in this grid ranges from $3.0 \leq \log g \leq 7.0$ in steps of 0.2 dex . However, we note that those models above the Eddington limit could not be calculated with the TMAW procedure. Therefore, the lower limit in $\log g$ is in fact set by the Eddington limit. The abundance ratio (by mass) of hydrogen to helium was varied as follows: H/He = 1/0, 0.9/0.1, 0.8/0.2, ... , 0.1/0.9, 0/1. No other elements have been taken into account for the calculation.

Before starting the spectral analysis, the synthetic spectra were degraded and rebinned to the resolution of the observations, which is $\approx 2 \text{ Å pixel}^{-1}$.

⁵<http://astro.uni-tuebingen.de/~TMAP/>

TABLE 6.1: IUE spectra used for the spectral analysis. The LWP spectra beyond $\sim 2400 \text{ \AA}$ could not be used for the spectral analysis (see the text).

Spectrum	Date (dd/mm/yyyy)
SWP01313 + LWR01279	04/04/1978
SWP03813 + LWR03394	05/01/1979
SWP08024 + LWR06984	23/02/1980
SWP18042 + LWR14219	20/09/1982
SWP35671 + LWR15127	04/03/1989

6.4 Spectral analysis

6.4.1 Composite models

The observed flux of a composite spectrum can be reproduced by the sum of two terms, each one referring to each individual spectrum, following the relation:

$$\begin{aligned}
 F_{\lambda} &= \left(\frac{R_{\text{cool}}}{d}\right)^2 S_{\lambda}(T_{\text{eff}(\text{cool})}, g_{\text{cool}}) + \left(\frac{R_{\text{hot}}}{d}\right)^2 S_{\lambda}(T_{\text{eff}(\text{hot})}, g_{\text{hot}}) \\
 &= k_{\text{norm}}[S_{\lambda}(T_{\text{eff}(\text{cool})}, g_{\text{cool}}) + a S_{\lambda}(T_{\text{eff}(\text{hot})}, g_{\text{hot}})],
 \end{aligned} \tag{6.1}$$

where R_{cool} , $T_{\text{eff}(\text{cool})}$, g_{cool} , R_{hot} , $T_{\text{eff}(\text{hot})}$, g_{hot} are the radius, the T_{eff} and the surface gravity of each object, d is the distance to the system (assuming that both objects are at the same distance) and S_{λ} the monochromatic surface flux emission of each component. In this way, the parameter a is defined as $(R_{\text{hot}}/R_{\text{cool}})^2$ and k_{norm} is the normalization constant defined as $(R_{\text{cool}}/d)^2$. Each composite model will be normalized to the observed spectrum following the procedure described by [Bertone et al. \(2004\)](#).

The last term of equation (1) has five unknowns, namely both T_{eff} and gravities, and the parameter a . In addition, the extinction affecting the observed spectrum – both R_V and $E(B-V)$ – is also unknown. This amounts to a total of seven unknowns, which poses a difficult problem to be tackled. Therefore, to arrive the final and sensible solution(s), we have devised a method to explore the whole range of parameters by building a grid of composite models from the individual grids, and by applying a suite of filters that allows us to select, among all possible combinations, those matching the observed spectral features, both at an overall level (the shape of the spectrum, the position of the Balmer jump) and lines (equivalent width of some absorption lines). The outcome of the analysis will be the T_{eff} , gravities and the ratio between the radii of the components.

In what follows, we will explain in detail the fitting procedure, until the final solutions are reached. Figure 6.4 shows a flowchart describing the whole process. Note that an iterative

process is needed because each cycle hinges on the parameters of the cool component that must be revised once each iteration is completed, until convergence is reached.

6.4.2 Parameters of the cool component

As it can be seen in Fig. 6.4, and is described in detail in the next subsections, the whole fitting process is based on the computation of grids of composite models where, in each one, the Kurucz synthetic spectrum of the cool star remains fixed and it is combined with all the TMAP models. The composite models undergo several filters imposed by the observations and only the small subset that fulfills all the observational constraints is accepted as a final solution for the problem. Therefore, the first step is to constrain the parameters of the cool star. These parameters are reassessed at the end of each cycle. We note that an approach from the point of view of the hot star (i.e. fixing the parameters of the hot star and combining with the whole grid of the Kurucz models) is not possible since we do not have enough spectral criteria to adjust the corresponding pairs of T_{eff} and gravity for the hot component.

The Ca II K $\lambda 3933$ line is generally one of the prime temperature criteria in A- or B-type stars (Gray & Corbally, 2009). In the case of single stars, an estimate of T_{eff} can be obtained by comparing the equivalent width (EW) of the line in the observed spectrum with that measured on a grid of synthetic spectra or templates. However, this simple procedure cannot be applied in this case, because superimposed to the spectrum of the cool component, there is an unknown contribution of the continuum and lines of the hot component. The only information we can extract in the first step is an upper limit to the $T_{\text{eff(cool)}}$, since composite models –or combinations of templates– containing a cool star whose $\text{EW}(\text{Ca II}) \leq 0.34 \text{ \AA}$ (which is the EW of the line in the observed spectrum) will have the EW of this line decreased below that value when the spectrum of the hot companion is added. An inspection of the grid of synthetic models (see Sect. 6.3) with solar metallicity sets a rough upper limit of $T_{\text{eff(cool)}} \sim 11000 \text{ K}$. The Ca II K line dependence on gravity and metallicity was found negligible.

Since the wings of the Balmer lines are very sensitive to gravity in A- and B-type stars (Gray & Corbally, 2009), we have explored which value of $\log g$ for the cool component is consistent with each potential T_{eff} . We have computed synthetic models for $\text{H}\alpha$, $\text{H}\beta$, $\text{H}\gamma$ and $\text{H}\delta$ for $T_{\text{eff(cool)}} = 9000 - 11500 \text{ K}$, in steps of 500 K, and values of $\log g_{\text{cool}} = 2.50 - 4.00$, in steps of 0.25 dex. Such intervals were chosen according to the typical parameters of A- and B-type stars. The widths of the lines in the spectrum have been compared with those in the synthetic models, and the pairs $(T_{\text{eff(cool)}}, \log g_{\text{cool}})$ that are consistent with the observations are (9000 K, 2.50), (9500 K, 2.75), (10000 K, 3.00), (10500 K, 3.25), (11000 K, 3.50) and (11500 K, 3.75). Typical errors in the determination of $\log g_{\text{cool}}$ are ± 0.25 dex.

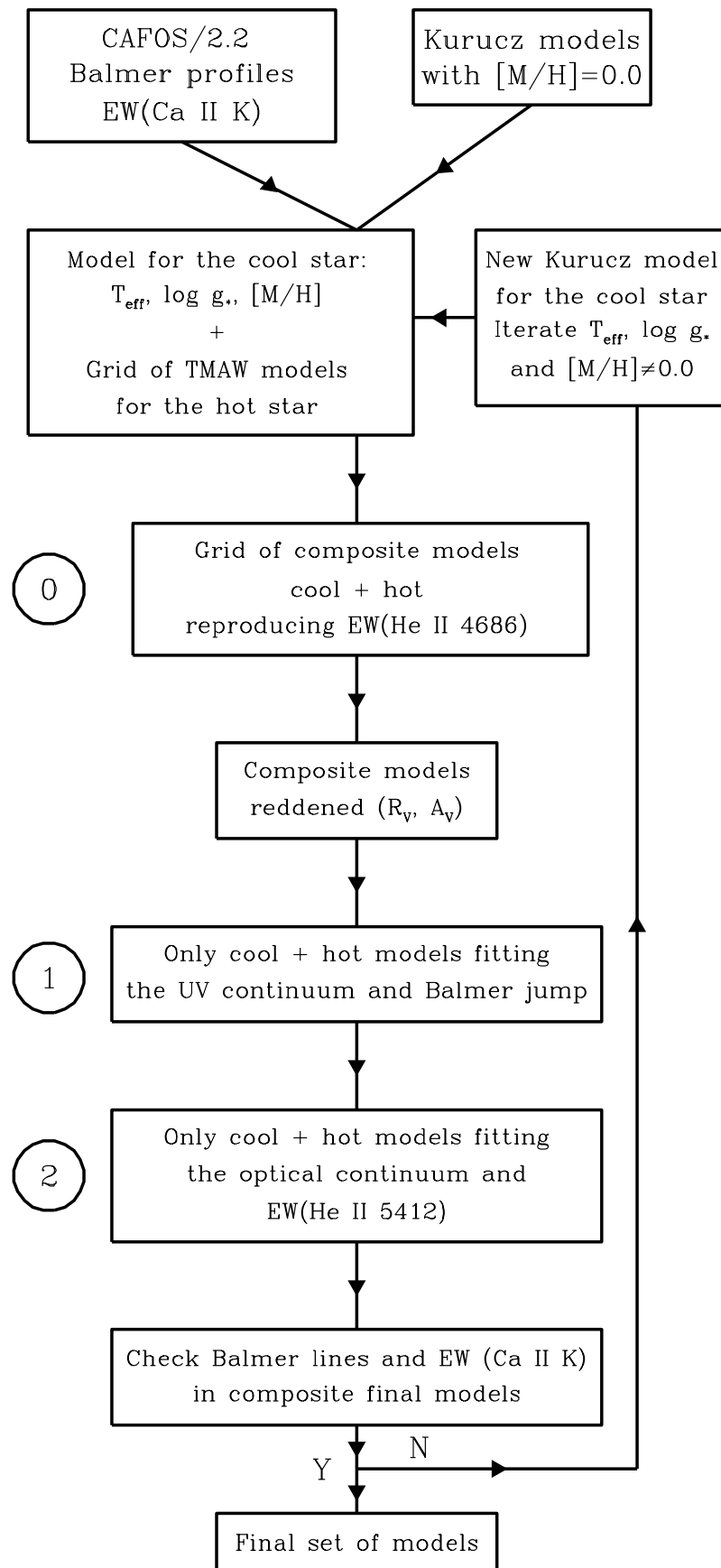


FIGURE 6.4: Flow chart with all the steps of the fitting procedure. See the text for details.

We would like to stress that we are comparing models computed with a single T_{eff} and gravity with the observed spectrum, that is a composite of two stars. The assumption underlying this exercise is that the cool component is the main contributor to the Ca II K and the Balmer lines. We also note that a possible interstellar contribution to this absorption line was not taken into account in the analysis. Although the low resolution of our spectrum does not allow us to quantify this contribution, Greenstein (1972) concluded that the cool component has a considerable strong stellar line by comparing the velocity of the observed Ca II K line and the expected interstellar line velocity.

Once the complete filtering process is done and the contributions of both components to the observed spectrum are evaluated, the Ca II K line and the Balmer profiles are analysed again and the values of $T_{\text{eff}(\text{cool})}$ and $\log g_{\text{cool}}$ are reassessed to fit the observations (see Sect. 6.4.5). The whole fitting and filtering process is started again (see Fig. 6.4).

6.4.3 First filter: UV continuum and Balmer jump

Before starting with the filtering procedure, we imposed the condition that the EW of the He II $\lambda 4686$ line of *all* composite models matches that of the observed line, namely $\sim 0.42 \text{ \AA}$. Therefore, for each pair $S_{\lambda}(T_{\text{eff}(\text{cool})}, g_{\text{cool}}), S_{\lambda}(T_{\text{eff}(\text{hot})}, g_{\text{hot}})$, the parameter $a(T_{\text{eff}(\text{cool})}, T_{\text{eff}(\text{hot})}, g_{\text{cool}}, g_{\text{hot}})$ is computed in such a way that the synthetic EW matches the observed one. The outcome of this step, – marked as ‘0’ in Fig. 6.4 – is a grid of composite models that will be passed to the first filter.

Since the ultraviolet and blue wavelengths are the most sensitive to the interstellar and nebular extinction, we carried out first an initial analysis fitting only the UV shape and the Balmer jump. To do this, we explored a wide range of reddening values and applied those to the models. In principle we shall not assume the unique Galactic average value of 3.1 for R_V (see Sect. 6.5 for further discussions) then, we varied this parameter and the colour excess $E(B-V)$. The values adopted for this analysis range from 1.5 to 5.0 in steps of 0.1 in the case of R_V , and from 0.2 to 1.5 in steps of 0.05 in the case of $E(B-V)$. The parametrization of the extinction by Fitzpatrick (1999) has been used.

A least squares fit with a confidence level of 99.73% (3σ), yields a first effective filtering over the total grid. We obtained that only those models with $E(B-V)$ between 0.5 and 0.6 and R_V between 2.3 and 2.6 fitted well the UV shape, and pass to the next filter. This step is marked as ‘1’ in Fig. 6.4.

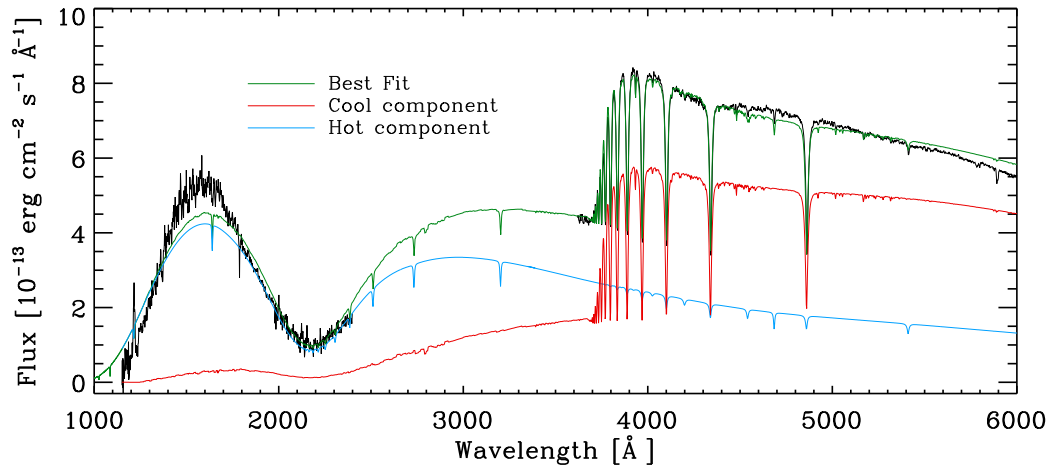


FIGURE 6.5: Observed spectrum of BD+30°623 (black) and one of the best fits (green) chosen between the models for the hot component that pass the filters described in Sect. 6.4, which corresponds to $T_{\text{eff}(\text{hot})} = 90000$ K, $\log g_{\text{hot}} = 5.6$ and $\text{H/He} = 0.4/0.6$. The parameters for the cool component are $T_{\text{eff}(\text{cool})} = 9850$ K and $\log g_{\text{cool}} = 3.5$. All the other solutions are virtually identical and are not plotted to avoid confusion. In red and blue, the separate contributions of the cool and hot stars, respectively, are plotted.

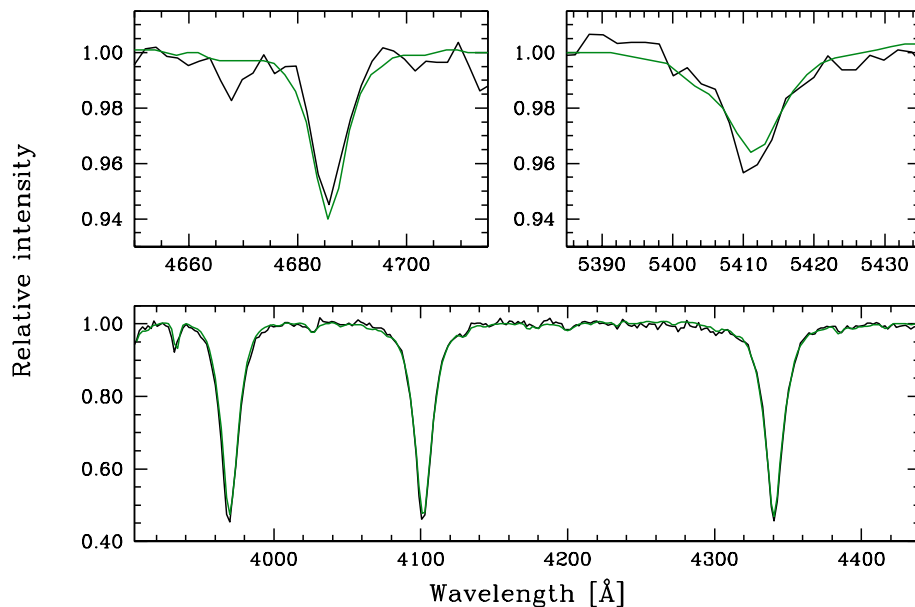


FIGURE 6.6: Profiles of the observed absorption lines (black) used for the spectral analysis together with the synthetic profiles (green) of one of the final solutions. In the upper part of the figure the He II $\lambda 4686$ and He II $\lambda 5412$ lines. In the lower part, the Ca II K line and the Balmer lines H ϵ , H δ and H γ .

6.4.4 Second filter: optical continuum and He II $\lambda 5412$

After the first filter, we performed a second fitting – ‘2’ in Fig. 6.4 – to match the optical continuum. Once again, a least squares fit with a confidence level of 3σ was carried out. At this point, we also imposed the requirement of a good fitting to the He II $\lambda 5412$ absorption line.

6.4.5 Reassessment of the parameters of the cool star

As mentioned in Sect. 6.4.2, in the first iteration we repeated the fitting procedure keeping fixed all the pairs $(T_{\text{eff(cool)}}, \log g_{\text{cool}})$ of the cool star that seemed to be compatible with the observations, combining them with the whole grid of synthetic spectra for the hot star.

After that first iteration, the EW of the Ca II K line and the widths of the wings of the Balmer lines were measured on each of the composite spectra that passed all the filters. As expected, the EW of the Ca II line is less, and the wings of the Balmer lines were narrower, than those in the observed spectrum – and on each of the individual models with $(T_{\text{eff(cool)}}, \log g_{\text{cool}})$ – due to the fact that a contribution of the hot component had been added to each cool model. The comparison of the features of the composite spectra with those observed helped to tune the parameters of the cool star. A new iteration was then started with the revised set of parameters, as shown in Fig. 6.4.

After a few cycles, it turns out that convergence in the procedure, and an excellent agreement with the observed spectrum, are achieved for $T_{\text{eff(cool)}} = 9850 \pm 150$ K and $\log g_{\text{cool}} = 3.50 \pm 0.25$. These parameters are compatible with both an A0 star ascending the giant branch (as reported by, e.g., Kohoutek, 1967) and a HB A0 star (as reported by Greenstein, 1972). We will see below that the HB A0 classification appears to be the most probable one. The strength of the Ca II K and other weak blends point to a subsolar metallicity. A value of $[M/H]_{\text{cool}} = -0.5$, which seems to match the observed features, has been adopted; however, high-resolution spectra would be needed to confirm or reject this.

6.4.6 Final results for the hot star

For that particular set of parameters of the cool star, seven successful solutions were obtained for the hot companion, with $T_{\text{eff(hot)}}$ between 80000 and 95000 K, $\log g_{\text{hot}}$ between 5.4 and 5.6 and compositions compatible with a helium-rich star (H/He= 0.0/1.0, 0.2/0.8, 0.3/0.7, 0.4/0.6, 0.5/0.5, 0.6/0.4). These final solutions together with the corresponding values of the parameter a (see equation 1) are listed in Table 6.2. The derived stellar parameters are compatible with most of the different known types of CSPNe, so we would need more information (e.g., mass, radius, luminosity) to classify the hot component in a definite way (see Sect. 6.5).

TABLE 6.2: Spectroscopic solutions for the hot component of BD+30°623.

$T_{\text{eff(hot)}} \text{ (K)}$	$\log g_{\text{hot}}$	H/He	a
80000	5.4	0.6/0.4	0.01445
85000	5.6	0.5/0.5	0.01328
90000	5.6	0.4/0.6	0.01211
95000	5.6	0.0/1.0	0.01172
95000	5.6	0.2/0.8	0.01113
95000	5.6	0.3/0.7	0.01113
95000	5.6	0.4/0.6	0.01094

Figure 6.5 shows one of these final solutions, namely that with $T_{\text{eff(hot)}} = 90000$, $\log g_{\text{hot}} = 5.6$ and H/He= 0.4/0.6, plotted in green. All the other solutions are virtually identical and are not included in the figure to avoid confusion. We have also plotted the individual contributions of the cool and hot stars in red and blue, respectively. As mentioned in Sect. 6.2, the neutral helium lines (e.g., He I $\lambda 4471$) come from the cool companion. This is in agreement with the high T_{eff} derived for the hot star.

In Figure 6.6, the profiles of the He II $\lambda 4686$, He II $\lambda 5412$, Balmer lines He ϵ , H δ and H γ , and Ca II K line, together with the corresponding fits are shown.

6.4.7 Extinction

As it can be seen in Fig. 6.4 and Sect. 6.4.3, each composite model is reddened with a range of values of R_V and colour excess $E(B-V)$ to match the shape of the UV continuum and the intensity of the Balmer jump. All final models matching successfully the observed spectrum had to be reddened with values of $R_V = 2.3 \pm 0.1$ and $E(B-V) = 0.60 \pm 0.05$, which imply $A_V \simeq 1.4$. Note that the value of the extinction does not have any impact on those filters matching the EW of lines, since on narrow regions around absorption lines the extinction correction can be considered as constant and its effect cancels out when computing EWs.

The resulting value of $\simeq 1.4$ for A_V is in good agreement with the value of 1.6 obtained by Ressler et al. (2010). Our estimations are also consistent with the colour excess obtained from the nebular extinction coefficient derived from the CAFOS spectrum ($E(B-V) = 0.66$, see Sect. 6.2). We note that the colour excess derived from the best fit is slightly higher than the previous values proposed in the literature, which ranges from 0.44 to 0.5 (Seaton, 1980, Feibelman, 1997).

We also note that while the bump at 2200 Å is successfully reproduced, the fitting around ~ 1600 Å does not reach the intensity levels of the observed spectrum. This can be a consequence of the parametrization used, since only a value of R_V has been taken into account. Besides, the lack of an accurate knowledge about the behaviour of the extinction laws in this spectral range makes difficult this kind of analysis.

TABLE 6.3: Stellar parameters of the two components of BD+30°623.

Stellar parameters	Cool star	Hot star
T_{eff} (K)	9850 ± 150	90000 ± 10000
$\log g$	3.5 ± 0.25	5.5 ± 0.1
M/M_{\odot}	0.55 ± 0.02	0.56 ± 0.03
R/R_{\odot}	2.1 ± 0.6	0.22 ± 0.03
$\log(L/L_{\odot})$	1.60 ± 0.25	3.4 ± 0.2
R_V		2.3 ± 0.1
$E(B-V)$		0.60 ± 0.05
d [pc]		285 ± 85

6.5 Discussion

The spectral analysis described above provides values of the T_{eff} and gravities of both components of BD+30°623. While it is true that the $T_{\text{eff(cool)}}$ has been already determined in a quite accurately way by several authors (see above), this is the first time that the parameters of the hot component have been spectroscopically derived. In Table 6.3, we list the results derived from the spectral analysis described in the previous sections (T_{eff} and gravities of the two components, and extinction) as well as the stellar parameters derived below from the evolutionary tracks (mass, radius, luminosity of the two components and the distance to the system). Note that the $T_{\text{eff(hot)}}$ is not an strict average of the T_{eff} listed in Table 6.2, we prefer to give a round number that represents all the solutions with an uncertainty bracketing all of them. Also note that the error in $\log g_{\text{hot}}$ comes from an average of the different values of the $\log g$ of the models that have passed all the filters in the analysis. In what follows, we adopt between the seven successful solutions matching the observed spectrum, that shown in Fig. 6.5, namely, $T_{\text{eff(hot)}} = 90000$ K, $\log g_{\text{hot}} = 5.6$, $T_{\text{eff(cool)}} = 9850$ K and $\log g_{\text{cool}} = 3.5$. These parameters allow us to compare with the appropriate evolutionary tracks and isochrones.

Figure 6.7 shows the position of the hot component of BD+30°623 in the HR diagrams $\log g_* - T_{\text{eff}}$ (top) and $\log(L_*/L_{\odot}) - T_{\text{eff}}$ (bottom) on the evolutionary tracks for post-AGB tracks by [Bloeker \(1995\)](#) and [Schoenberner \(1983\)](#). The location of the star is consistent with a mass of $M_{\text{hot}} = 0.56 \pm 0.03 M_{\odot}$, which implies a radius $R_{\text{hot}} = 0.22 \pm 0.03 R_{\odot}$, and a luminosity $\log(L_{\text{hot}}/L_{\odot}) = 3.4 \pm 0.2$. The luminosity and the dereddened integrated flux of the model fitting this component lead to a distance $d_{\text{hot}} = 253 \pm 88$ pc. The derived stellar mass indicates a progenitor of $\sim 1 M_{\odot}$ in the main sequence and, therefore, an age of about $10^9 - 10^{10}$ yr. The parameters derived from the evolutionary tracks agree with those typical of sdOs ([Heber, 2009](#), [Geier et al., 2011a](#)). Also, the narrowness of the He II $\lambda 4686$ absorption line is compatible with an sdO classification (as previously proposed by, e.g., [Kohoutek, 1967](#), [Greenstein, 1972](#)), rather than with a white dwarf. However, other classifications (like, e.g, O(He)-type) may also be compatible. Therefore, an analysis of high-resolution spectra in the UV range, as that carried

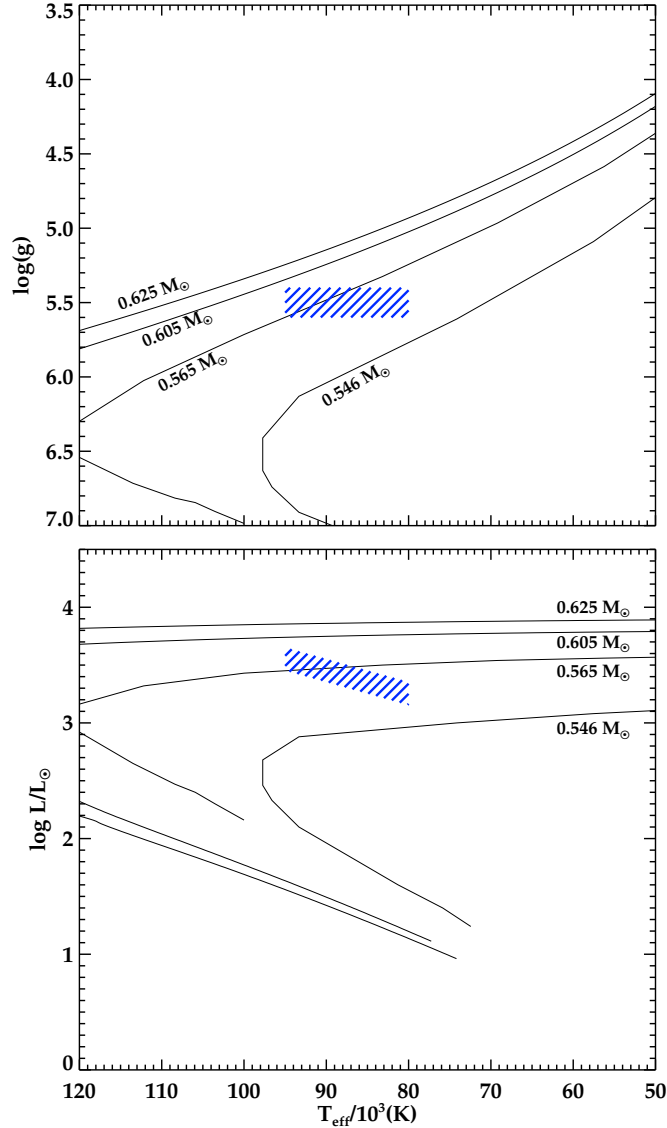


FIGURE 6.7: Location of the hot component on the evolutionary tracks by [Bloeker \(1995\)](#) and [Schoenberner \(1983\)](#). The blue solid lines indicates the region of the possible parameters of the hot star derived from the final solutions. Each evolutionary track is labelled with the corresponding stellar mass (in M_{\odot}).

out by [Latour et al. \(2013\)](#) for the sdO BD+28°4211, could allow us to confirm or rule out a possible sdO classification.

Figure 6.8 shows the position of the cool component in the HR diagrams $\log g_* - T_{\text{eff}}$ (top) and $\log(L_*/L_{\odot}) - T_{\text{eff}}$ (bottom) on the post main-sequence evolutionary tracks by [Girardi et al. \(2000\)](#) with $Z = 0.004$ (black) and the post-HB evolutionary tracks by [Dorman et al. \(1993\)](#) with $Z = 0.006$ (red). The stellar parameters derived are compatible, a priori, with two possible scenarios: an A0 star ascending the giant branch and a A0 star in the HB.

In the hypothesis that the cool component were an A0 star ascending the giant branch, the comparison with the [Girardi et al. \(2000\)](#) tracks gives a mass $M_{\text{cool}} = 2.9 \pm 0.5 M_{\odot}$, which

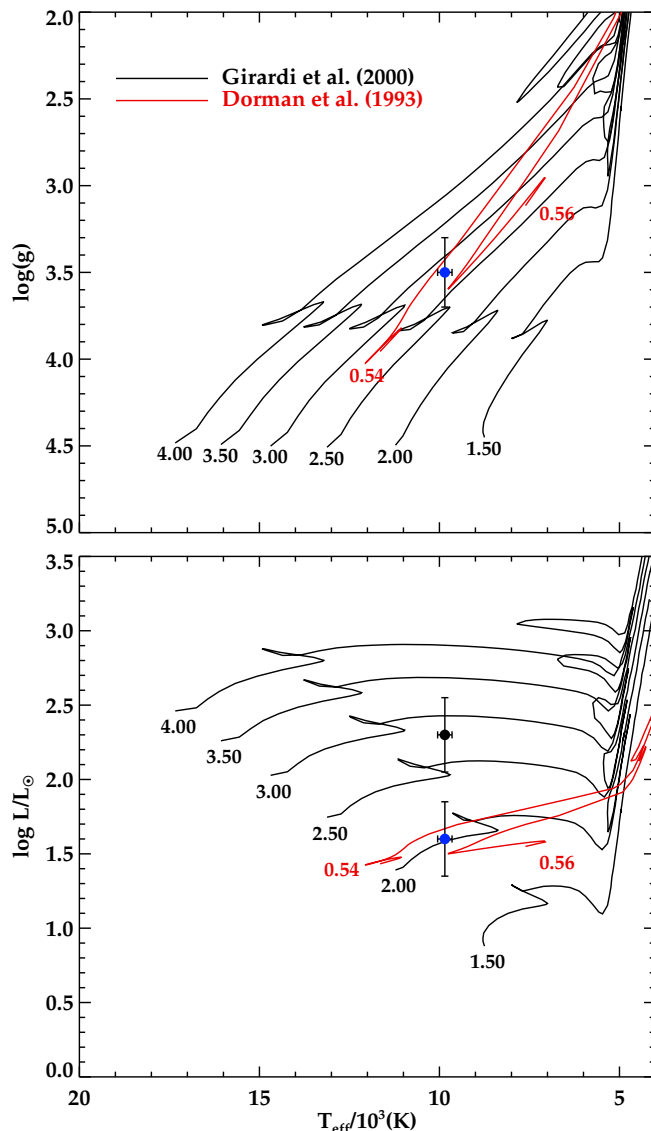


FIGURE 6.8: Location of the cool component on the evolutionary tracks calculated by Girardi et al. (2000) (black lines) and the post-HB evolutionary tracks by Dorman et al. (1993, red lines). Each evolutionary track is labelled with the corresponding stellar mass (in M_{\odot}). The location of the cool component in the top panel corresponds to two positions in the bottom panel depending on the evolutionary track with which we are comparing it (see the text).

implies a radius $R_{\text{cool}} = 4.9 \pm 1.5 R_{\odot}$, a luminosity $\log(L_{\text{cool}}/L_{\odot}) = 2.3 \pm 0.3$ and an age ~ 300 Myr. These parameters lead to a number of inconsistencies when compared with those of the hot star. If the CS is a physical pair, the age of the cool star is incompatible with the much longer time span required by the hot star to reach its current evolutionary status. Therefore, interaction between the stars (e.g., mass transfer) should be invoked to explain the age difference. This inconsistency in the age has been already reported for other similar CSs (see e.g., NGC 3132, Ciardullo et al., 1999). However, the luminosity and the dereddened integrated flux of the cool star lead to a distance $d_{\text{cool}} = 710 \pm 280$ pc that is incompatible with the CS being a physical binary but a coincidental alignment. This scenario is also difficult to reconcile with the observations. In

particular, it would be hard to explain that the *Hubble Space Telescope* does not resolve the pair, *and, simultaneously*, that the mean radial velocity of the cool star ($V_{\text{LSR}} = +47.6 \pm 1.6 \text{ km s}^{-1}$) and the systemic velocity of the nebula ($V_{\text{LSR}} = +41 \pm 5 \text{ km s}^{-1}$) are in agreement (Greenstein, 1972). In addition, the complex nebular morphology is difficult to understand within a single-star hypothesis but strongly suggests the presence of a binary system (see below). Moreover, the radii derived from the evolutionary tracks yield a value of 0.002 for the parameter a , defined as $(R_{\text{hot}}/R_{\text{cool}})^2$ under the assumption that both components form a binary system (equation 7.1); that value is a factor of 6.0 lower than the mean value $a=0.012$ obtained from the spectral analysis (Table 6.2). In view of all these arguments, we can discard the scenario of the cool component being a giant-branch star.

Alternatively, in the hypothesis that the cool component were an A0 star in the HB, the comparison with the Dorman et al. (1993) tracks gives a mass $M_{\text{cool}} = 0.55 \pm 0.02 M_{\odot}$ (Fig. 6.8, red lines), $R_{\text{cool}} = 2.1 \pm 0.6 R_{\odot}$ and $\log(L_{\text{cool}}/L_{\odot}) = 1.60 \pm 0.25$. The luminosity and the dereddened integrated flux lead to a distance $d_{\text{cool}} = 294 \pm 69 \text{ pc}$ that agrees very well with that derived above for the hot component ($d_{\text{hot}} = 253 \pm 88 \text{ pc}$) and is compatible with both stars forming a binary system. Moreover, in contrast with the giant-branch scenario, the radius derived for the HB star gives $a = 0.011$, in very good agreement with the mean value of a obtained from the spectral analysis (see Sect. 6.4). Besides, the normalization constant between the best-fitting models and the observed spectrum is $k_{\text{norm}} \simeq 2.77 \times 10^{-20}$, which is defined as $(R_{\text{cool}}/d)^2$ (equation 7.1). Taking $R_{\text{cool}} = 2.1$, we obtain a distance to the system $d = 285 \pm 85 \text{ pc}$, in agreement with the values derived independently for each component. This result also agrees with the range 200-300 pc considered by Ressler et al. (2010) based on the *Hipparcos* parallax (185 pc) and, alternatively, on the observed m_V magnitude and the assumption that the cool star is an HB A star with $M_V \simeq 1.0$ (240 pc). The fact that we obtain a very similar distance from an independent way – in our case, a spectral analysis – strongly reinforces the validity of our results. Finally, it should be noted that the parallax from the *Hipparcos* catalogue is $\pi = 5.40 \pm 1.70 \text{ mas}$ and the new reduction of the *Hipparcos* astrometric data by van Leeuwen (2007) provides $\pi = 3.79 \pm 1.61 \text{ mas}$. In both cases, $\sigma_{\pi}/\pi > 0.17$ and the Lutz–Kelker bias (Lutz & Kelker, 1973) prevents from using the *Hipparcos* parallax to obtain a reliable distance.

Concerning the age of the cool component, we note that the Dorman et al. (1993) evolutionary tracks do not provide neither the masses of the progenitor stars in the main sequence (ZAMS) nor their current ages. However, according to the evolutionary models by Serenelli & Weiss (2005), stars with masses between 0.8 and 0.9 M_{\odot} in the ZAMS might evolve (depending on the metallicity and the mass-loss) to HB stars with masses around 0.55 M_{\odot} – as it is our case – in periods between 8 and 12 Gyr. This range of ages is comparable to the age estimated for the hot component of BD+30°623. Therefore, the classification of the cool component as an HB A0 star is completely coherent with both the spectral analysis and the subsequent evolutionary study based on tracks and isochrones.

Another interesting point is the complex morphology of NGC 1514, consisting of numerous bubbles in the optical range (see Fig. 6.1) and a pair of axisymmetric rings recently discovered at mid-infrared wavelengths (Ressler et al., 2010). As mentioned above, a binary nature of BD+30°623 could already be tentatively inferred from this complex morphology, since binary interactions are generally believed to be the origin of non-spherical structures in PNe (see, e.g., De Marco, 2009, Miszalski et al., 2009b). It is true that neither radial velocity variations nor photometric and spectroscopic variability have been found in BD+30°623 (Greenstein, 1972, Purgathofer & Schnell, 1983, see also Sect. 6.2.2), which does not favour an association. However, in our case, the binary could be relatively close or have evolved through a common envelope phase (see Muthu & Anandarao, 2003) but being observed pole-on (or nearly) so that no variability can be observed whereas binary interactions can shape the complex nebula. We note that a pole-on binary is compatible with the narrowness of the absorption lines in the A0 star reported by Greenstein (1972), who concluded that the rotational velocity has to be small ($\leq 40 \text{ km s}^{-1}$). Alternatively, the pair could be a wide binary. This scenario would explain the lack of variability but have difficulties to account for the nebular complexity, unless particular orbital properties are considered (e.g., a highly eccentric orbit). In any case, conclusions about the characteristics of the binary and its relationship to nebular shaping should await for higher resolution images of this object.

NGC 1514 is not unique among PNe and cases of PNe with ‘cool’ CSs are well known (Lutz, 1977, De Marco, 2009). In particular, He 2-36, NGC 2346, NGC 3132 and PC 11 (Méndez, 1978, Pereira et al., 2010) contain an A-type star like NGC 1514. Moreover, most of these PNe present bipolar or complex morphologies that are much easier to explain in a binary scenario than in a single star one. We note that the knowledge of the stellar parameters for the hot components in these peculiar CSPNe is very scarce and the analysis of these CSs has been mainly focused on the cool components (see Table 4 in De Marco, 2009). In this context, the detailed spectral analysis presented in this work introduces a remarkable improvement since it allows us to obtain the stellar parameters of both cool and hot component simultaneously. Besides, this kind of analysis is useful to refine the spectral classification and the evolutionary status of the cool components in these systems. The future application of this method to similar peculiar CSs will be highly interesting to search for common properties in these systems and to constrain the formation and evolution of these enigmatic pairs of stars.

6.6 Summary and outcomes of this chapter

We have analysed ultraviolet IUE and CAFOS optical spectra of BD+30°623, the peculiar binary central star of NGC 1514. BD+30°623 shows an unusual central star spectrum whose main features correspond to an A-type star but also presents He II lines that must originate in a much

hotter companion. Previous studies of this central star have been unable to provide unambiguous parameters for its two components. Making use of state-of-the-art model-atmospheres for hot, compact stars (Tübingen NLTE - Model Atmosphere Package) and Kurucz synthetic models, we have carried out a detailed analysis of the ultraviolet and optical spectra with the aim of constraining the properties of this object. Grids of composite models of a cool+hot star were built. A χ^2 -fit and an iterative procedure based on filters imposed by observational constraints was devised to find the solutions that best reproduce both the shape of the ultraviolet and optical continuum and the main spectral features. To our knowledge, this kind of detailed analysis has not been done before for any of the peculiar binary central stars. The main results of this work can be summarized as follows:

1. The spectroscopic analysis leads to $T_{\text{eff}(\text{cool})} = 9850 \pm 150$ K, $\log g_{\text{cool}} = 3.50 \pm 0.25$ and $[M/H] \simeq -0.5$. For the hot component, solutions for $T_{\text{eff}(\text{hot})}$ between 80000 K and 95000 K, $\log g_{\text{hot}}$ between 5.4 and 5.6 and compositions pointing to a helium-rich star were found. An unique value for the extinction towards the two stars has been assumed, namely, $R_V = 2.3 \pm 0.1$ and $E(B-V) = 0.60 \pm 0.05$. Besides, the extinction coefficient derived from the nebular spectrum is $c(H\beta) \simeq 0.97$.
2. By comparing the stellar parameters derived for both components with the appropriate evolutionary tracks, we conclude that the cool component is compatible with an HB A0 star with mass $M_{\text{cool}} = 0.55 \pm 0.02 M_{\odot}$, radius $R_{\text{cool}} = 2.1 \pm 0.6 R_{\odot}$ and luminosity $\log(L_{\text{cool}}/L_{\odot}) = 1.60 \pm 0.25$. A distance $d_{\text{cool}} = 294 \pm 69$ pc is also derived. In the hypothesis underlying all this work that the stars form a physical pair, the scenario with an A0 star ascending the giant branch proposed by other authors seems to be inconsistent and therefore, should be discarded. On the other hand, the parameters of the hot component are $M_{\text{hot}} = 0.56 \pm 0.03 M_{\odot}$, $R_{\text{hot}} = 0.22 \pm 0.03 R_{\odot}$, and $\log(L_{\text{cool}}/L_{\odot}) = 3.4 \pm 0.2$. A distance of $d_{\text{hot}} = 253 \pm 88$ pc is derived. Although an sdO nature seems to be the most plausible one for this component, it is difficult to establish this classification firmly without high-resolution observations. The analysis is compatible with the two stars forming a physical pair.
3. A reanalysis of the IUE spectra shows that no variability is seen at short wavelengths, in contrast with the variation of the continuum flux by a factor of ~ 2 reported by Feibelman (1997).

The analysis presented in this chapter improves noticeably previous studies carried out for this object. However, further observations, like high-resolution spectra, will help to determine with a better accuracy parameters such as the metal abundance of the cool component and the rotation velocities. New long- and short-term observations would be also required in order to study the possible variability of this system and the properties of the binary. Theoretical studies addressing the evolution of this kind of systems are also imperative.

An updated catalogue of Galactic Planetary Nebulae by means of VO tools

The purpose of this chapter is to describe the catalogue of Galactic Planetary Nebulae that we have compiled during this thesis. To date, the most used catalogues of Galactic PNe are those presented by [Acker et al. \(1992\)](#) and [Kohoutek \(2001\)](#), with 1143 and 1510 objects, respectively. However, the number of newly discovered PNe has steadily increased during the last years and the census has not been correspondingly updated. Collecting the information to build up a new updated catalogue has been one of the aims of this thesis and it will be described in this chapter. Our compilation includes more than 2900 objects classified (when available) as confirmed, probable and possible Galactic PNe. The compilation has been made taking advantage of Virtual Observatory tools. The first purpose of this catalogue is to centralize all the known PNe with their most relevant information. As a second goal, we attempt to classify the whole sample of CSPNe in an automatic way, on basis of archival data. The ultimate aim of this classification is to obtain potential sdO CSs candidates by using existent data, which could be prioritized for subsequent spectroscopic follow-up. We describe the classification methods designed for this purpose as well as their application and validation in a sample of field blue stars. While the selected criteria are successful for the field star sample, we found difficulties in their applicability to CSPNe sample, concluding that spectra are necessary to classify them.

7.1 Introduction

The first (known) catalogue of Galactic PNe (CGPN) was published by [Perek & Kohoutek \(1967\)](#) and contained 1063 objects. Later on, [Acker et al. \(1992\)](#) presented the *Strasbourg-ESO Catalogue of Galactic PNe* (SECGPN), with 1143 true or probable PNe, which was updated by [Kohoutek \(2001\)](#) in his *Version 2000 of the Catalogue of Galactic PN*, containing 1510 PNe.

This population has nearly doubled in almost two decades. This spectacular increment in the detection of new PNe has been mainly possible thanks to exhaustive and recent surveys like the Macquarie/AAO/Strasbourg $H\alpha$ Planetary Nebula Catalogues (MASH-I, [Parker et al. 2006](#); and MASH-II, [Miszalski et al. 2008](#)) and the INT Photometric $H\alpha$ Survey (IPHAS, [Drew et al., 2005](#)).

Currently, the number of known confirmed or probable PNe in the Milky Way is estimated to be roughly 3000 (~ 3300 according to [Sabin et al. \(2014\)](#), < 2850 according to [Miszalski et al. \(2012\)](#)). However, due to the absence of an updated catalogue of Galactic PNe, it is difficult to know the complete census of this population. This lack of a unique and centralized database was the main motivation for this work. The construction of such a catalogue is not an easy task due to the large amount of objects and to the dispersion of the information among many individual catalogues and publications. In addition, many PNe appear duplicated in several catalogues. All of this makes it extremely difficult to do the compilation “by hand”.

In this context, the Virtual Observatory¹ (VO) provides a perfect framework to deal with huge amount of data in an efficient and user-friendly way. VO is an international astronomical community initiative whose main aim is to provide global electronic access to the available astronomical data archives of both ground- and space-based observatories. For that purpose, VO offers a broad set of services and tools for data mining, visualization and analysis (e.g., TOPCAT, ALADIN, VOSA, etc). We have taken advantage of the VO framework by using some of these tools to assemble a more up-to-date catalogue of Galactic PNe. This catalogue is described in Sect. 7.2.

As a first application of this catalogue, we attempted to classify the whole sample of CSPNe. As we described in detail in Chapter 1, CSPNe exhibit a wide diversity of spectral features, which is reflected by the numerous attributed spectral types. [Weidmann & Gamen \(2011\)](#) reported 26 different spectral types for their compilation of 492 spectroscopically classified CSs of both confirmed and probable PNe. However, this number represents just $\sim 13\%$ of all known PNe. This low fraction of spectroscopically classified CSs is a direct consequence of their faintness and the highly contaminated stellar spectra by the nebular emission lines in many cases. For these reasons, the development of an alternative classification procedure based on archival information is crucial. This methodology could be applied to a large sample of CSPNe providing a great advantage on this topic.

¹<http://www.ivoa.net/>

TABLE 7.1: Previous catalogues and works used for the preparation of our catalogue.

Catalogue or work	Objects
Version 2000 of the Catalogue of Galactic PN (Kohoutek, 2001)	1510
Kerber et al. (2003)	1312
Frew et al. (2013)	1258
MASH Catalogues (Parker et al., 2006, Miszalski et al., 2008)	1238
SECGPN (Acker et al., 1992)	1143
Cahn et al. (1992)	780
Tylenda et al. (1994)	768
Stanghellini et al. (2008)	563
Weidmann & Gamen (2011)	492
Phillips (2004)	447
van de Steene & Zijlstra (1994)	433
Beaulieu et al. (1999)	373
Kerber et al. (2008)	274
Mal'Kov (1997)	170
IPHAS (Sabin et al., 2014)	159
Ratag et al. (1997)	108
MACHO (Lutz et al., 2010)	102
Holovaty & Havrilova (2005)	87
Napiwotzki (1999)	50
Stasińska et al. (1997)	49
Escudero & Costa (2001)	45
Guerrero et al. (2013)	44
Hora et al. (1999)	41
De Marco et al. (2013)	31
Boumis et al. (2003)	25
Górny (2006)	24
Boumis et al. (2006)	19
Boumis et al. (2006)	19
Acker et al. (2012)	5
Aller et al. (2013)	1
This catalogue	2951

7.2 The PN Catalogue: gathering data from archives

The compilation of the PN sample was achieved by gathering data from different already published catalogues and works by means of the services provided by the VO. For this task, we used TOPCAT², an interactive VO-tool designed to work with tabular data.

Table 7.1 lists the different catalogues and works that have been used to conform the catalogue, together with the number of objects included in each of them. The CGPN by Perek & Kohoutek (1967) is not included in the list as the *Version 2000 of the Catalogue of Galactic PN* by Kohoutek (2001) is an update of that catalogue and so, all the objects included in the former are also included in the later. The catalogues were selected following mainly two procedures: First, we explored the results of VIZIER searching by the keyword “planetary nebula”. From these results, we selected those related with Galactic planetary nebula. Second, we intensively inspected the literature and selected those works containing a large number of PNe.

²<http://www.star.bris.ac.uk/~mbt/topcat/>

We note that many of these objects have multiple entries among several catalogues, an issue that can be easily ruled out using the cross-match capability of TOPCAT. We used a search radius of 5 arcsec in the cross-matching of the tables to be sure of not rejecting different PN with similar coordinates in different catalogues. In the cross-matching process, the SECGPN was selected as the reference catalogue, in a compromise between the number of objects and their available information. Then, the cross-matches with the rest of the catalogues were done on basis of the number of objects. Once all the catalogues were cross-matched, a visual inspection of the final catalogue was carefully carried out. This visual inspection consisted in rejecting duplicated PNe that may have different coordinates (separated by more than 5 arcsec) in their original catalogues, although being the same object. This could have been done by cross-matching the whole catalogue by the “name” column, but this is not an easy task since PNe generally have more than one common name.

After the visual inspection, the final catalogue contains 2951 Galactic PNe. Many of these objects are flagged in their original catalogues as true, probable or possible Galactic PNe. We keep these flags in our catalogue when available. In addition, we have also compiled a list of 121 misclassified PNe in the literature, which are also included in some of the catalogues listed in Table 7.1.


With the aim of facilitating the query to the catalogue, we have taken advantage of the data publishing tools developed by the Spanish Virtual Observatory (SVO). These tools allow to easily publish images and spectra (with MySpec-MyImg application) as well as tables and catalogues (with SVOCat). In this case, we have made use of the SVOCat³ tool, which allows the publication of our catalogue both as a web page and as a VO Cone Search service. In the following, we briefly describe the characteristics of these two accesses:

- *Web page access*: A basic interface allows the user to search by specific criteria, such as coordinates, PNG designation or common name. The default search radius for the query is 5 arcsec, although it can be user-defined. As the number of columns in the catalogue is really large (= 100), we have also implemented three available levels of verbosity: *minimum*, *medium* and *maximum*. The *minimum* option will display those columns with the basic information such as equatorial coordinates and name. The *medium* option (by default), will also show other columns containing additional informations such as photometric values and proper motions. Finally, if a *maximum* verbosity is selected, the whole table will be displayed. In the query, the number of sources to be returned can be also selected (with values ranging from 10 to unlimited).

The output format of the query is an HTML table that contains all the objects accomplishing the requirements. The header of each column provides a brief explanation of its

³<http://svo2.cab.inta-csic.es/vocats/SVOCat-doc>

Catalogue of Galactic PNe
New and updated catalogue of Galactic PNe



Home | Data retrieval | News | Documentation | Coverage Map | Help-Desk

RA (?) DEC (?) Radius (?) Search Reset
00 00 180 all results default verb. (Maximum Search Radius allowed: 180 degrees)

[-] Hide additional search fields

Name (?)
Flag_PN (?)

* List of rejected PN candidates (previously misclassified).

2951 data found.

Δ (?) (arcsec)	RA (J2000) (deg)	DEC (J2000) (deg)	RA (J2000) (hh:mm:ss)	DEC (J2000) (hh:mm:ss)	GAL_LONG (?) (deg)	GAL_LAT (?) (deg)	PNG (?)	Name (?)	Lum [Mal'kov] (?) (Lsun)
59511.33	9.31679	-13.71628	00:37:16.03	-13:42:58.61	108.371	-76.1858	108.4-76.1	BoBn 1	3700
59952.75	11.76390909	-11.8719284	00:47:03.34	-11:52:18.94	118.8646	-74.709	118.8-74.7	NGC 246	
76613.32	18.0954	11.3936	01:12:22.90	11:23:36.96	131.13	-51.1445		PG 0109+111	
109284.72	337.410588	-20.837122	22:29:38.54	-20:50:13.64	36.1612	-57.1179	036.1-57.1	NGC 7293	77
111609.66	353.97221	30.46844	23:35:53.33	30:28:06.38	104.2076	-29.6416	104.2-29.6	Jn 1	
112639.97	29.49612	10.94394	01:57:59.07	10:56:38.18	148.1113	-48.6473		GR 0155+10	
135744.73	324.22071	12.78861	21:36:52.97	12:47:19.00	66.778	-28.2022	066.7-28.2	NGC 7094	
140943.69	322.49742	12.17431	21:29:59.38	12:10:27.52	65.022	-27.3113	065.0-27.3	Ps 1	3300
150596.47	319.625	12.0267	21:18:30.00	12:01:36.12	62.9330580069826	-25.2133682993338		Fr 2-16	
151849.00	327.79592259	28.86398793	21:51:11.02	28:51:50.36	81.8738	-19.2931		BD+28 4211	
155594.95	351.4733	42.535	23:25:53.59	42:32:06.00	106.5584	-17.6006	106.5-17.6	NGC 7662	6200
162387.47	316.045321	-11.363406	21:04:10.88	-11:21:48.26	37.7623	-34.5715	037.7-34.5	NGC 7009	6500
166663.98	319.217808	24.147719	21:16:52.27	24:08:51.79	72.6626	-17.1519	072.7-17.1	A 74	
167717.95	323.87242	31.69592	21:35:29.38	31:41:45.31	81.296	-14.9127	081.2-14.9	A 78	

FIGURE 7.1: Snapshot of the catalogue available in the webpage.

content, by simply placing the mouse over the question mark of the column. The archive also implements the Simple Application Messaging Protocol (SAMP, Taylor et al., 2015). SAMP, developed within the context of the VO, enables VO applications to interoperate and communicate with each other, for instance by sending data or tables from one to another. Thanks to the SAMP, the HTML table provided in the query can be easily transferred to other VO applications in order to deal with the data in an efficient way. The catalogue is accessible through the public website:

http://svo2.cab.inta-csic.es/vocats/pn_aller.

Figure 7.1 shows a snapshot of the catalogue available in the webpage.

- *VO access*: It provides an important advantage to be efficiently retrieved by the astronomical community. We have implemented the International Virtual Observatory Alliance⁴ (IVOA) standards, like the Simple Cone Search (SCS) service. The SCS allows the user to search for sources in a range of right ascension and declination specified by an angular separation (named cone). The query through this service returns a VOTable with all the sources of the catalogue matching the coordinates within this cone⁵. With this service, the user can access the catalogue directly from VO tools like, for instance, TOPCAT.

The catalogue provides information about the common PN name, the official IAU PNG designation, when exists, the equatorial and galactic coordinates, as well as some of the most relevant information available in the original catalogues. The catalogue also provides photometric data

⁴<http://www.ivoa.net/>

⁵An example of this access would be
http://svo2.cab.inta-csic.es/vocats/pn_aller/cs.php?RA=18&DEC=11&SR=60&VERB=2

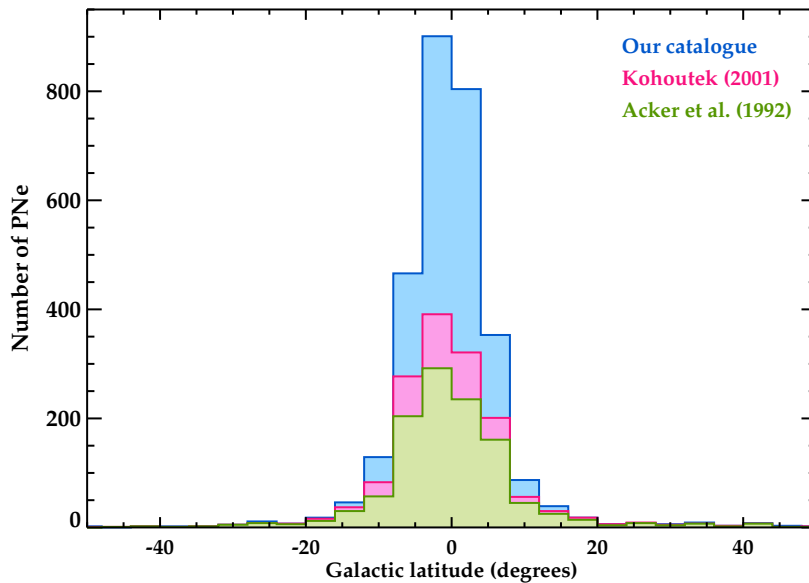


FIGURE 7.2: Galactic latitude distribution of PNe in our catalogue (blue) as compared with those PNe included in [Acker et al. \(1992\)](#) (green) and [Kohoutek \(2001\)](#) (pink).

in different bands from the 2MASS, SDSS DR9 and UCAC4 surveys, when available, as well as proper motion information from PPMXL survey. A flag column is also included (where applicable) to indicate the reliability of the detection. Finally, the catalogue offers direct access to the corresponding SIMBAD page for each object. This is a first version of the catalogue and we aim to keep it updated with the new discoveries, thus making it the reference catalogue for PNe.

In order to illustrate the improvement of our catalogue with respect to previous compilations of PNe, we compare in figure 7.2 the Galactic distribution of PNe in our catalogue (blue) and those included in the catalogues from [Acker et al. \(1992\)](#) in green and [Kohoutek \(2001\)](#) in pink. It is clear from this histogram the significant increment in the number of PNe which represent our compilation.

We expect that this catalogue will be an important referent for future investigations on PNe. Its almost completeness with respect to the whole sample of known PNe to date, provides a perfect framework to carry out, for instance, statistically significant morphological analysis of PNe and their association with galactic distribution, as well as binarity analysis of CSPNe, among others.

7.3 Classification of CSPNe

Spectral classification of CSPNe is usually based on spectroscopy, which demands a large amount of telescope time. In addition, spectroscopy is often not possible due to the faintness of the star or to the contamination of the nebular emission lines. Therefore, a primary goal of our

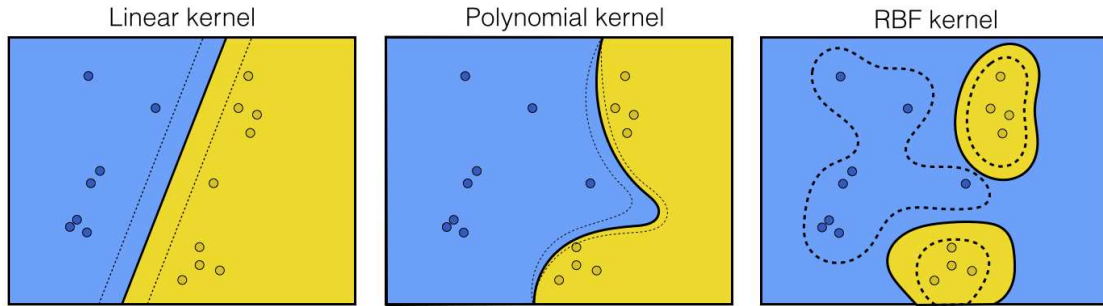


FIGURE 7.3: Examples of linear (left), polynomial (middle) and RBF (right) kernel functions available in Support Vector Machines. Kernel functions refers to those mathematical functions that trace the decision boundaries in the classification of a set of data. In this example, these kernels are able to separate the blue and yellow circles according to the function used (see the text for details).

catalogue of Galactic PNe is to provide the spectral type of all CSs without the need of obtaining spectra for these stars but using archive data instead. There are several classifications algorithms that can be used for this purpose. We selected three of them in order to independently compare the results and validate the efficiency of the classifiers. Once the classification algorithms were selected, we applied them to a known sample of blue stars in order to validate their application.

7.3.1 The machine-learning algorithms

Several methods are designed to classify a sample of data on basis of one or more criteria. The three classification algorithms used in this work are briefly described as follows:

- **Support Vector Machines** (SVMs, [Vapnik, 1995](#)) are a set of supervised learning methods that can be used for different purposes as classification, regression and outlier detection. SVMs are based on the idea of learning patterns and finding decision boundaries in a set of data. Basically, given a training data with a previously known classification, the algorithm is capable of finding which hyperplane (or a set of hyperplanes) better separates the different classes or memberships. Therefore, a new set of data can be classify by the algorithm on basis of these hyperplanes. However, the data are not always easily separable by simple hyperplanes, and non-linear decision functions are then required. These decision (or mathematical) functions are built up by the so-called kernel functions. Different kernel functions like linear, polynomial, radial basis function -RBF- and sigmoid, specifically designed for different purposes, are available to achieve the best classification in an efficient way. [Figure 7.3](#) shows three of these kernel functions in a two-dimensional case. This method, however, has the important disadvantage that all the targets to be classified need to have information in all the attribute fields. This could result in a high decrease of

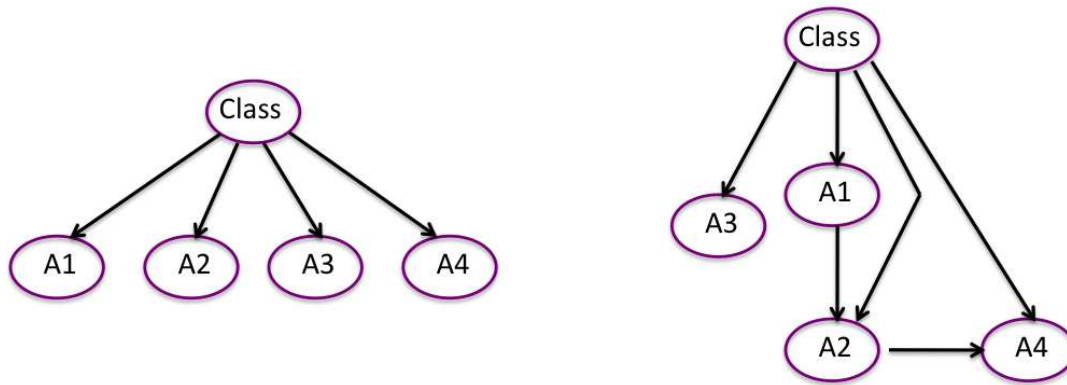


FIGURE 7.4: Examples of graphics constructed with Bayesian Networks. The superior node in each graph is the class we want to classify, and the other nodes represent the attributes (A1, A2, A3, A4) we are using for the classification. These attributes can be completely independent to each other (left panel) or they can be connected through a dependence relationship (see the text for details).

the training sample, since it is possible that many of the objects do not have data in some of the attributes.

- **Random Forests** (RF, [Breiman, 2001](#)) is a classification method that consists in building several decision trees for the training sample. These decision trees are predictive models to split data into different classes, based on a number of attributes or properties of the data. RF combines the bagging ([Breiman, 1996](#)) approach and a random selection of features (attributes). In other words, it uses several random subsamples of the training sample and predict the class of each individual subsample. The final classification is given by the mode of the classes of the individual predictions.
- **Bayesian Networks** (BN, [Korb & Nicholson, 2010](#)) are probabilistic graphical classification models. The corresponding graphs are formed by nodes and conditional arcs which link the relationships between the nodes. Figure 7.4 shows two example of BN graphs. Each node represents an attribute and two nodes connected to each other means that they have a dependence relationship. Usually, the superior node (or parent node) represents the class, whose value is obtained by combining the conditional probabilities according to the graph. In the most simple case, in which all attributes are independent, the probability of belonging to a specific class is calculated by:

$$P(\text{Class}=C_i|\text{Attributes}) = P(A_1|\text{class}=C_i) \times P(A_2|\text{class}=C_i) \times \dots \times P(A_N|\text{class}=C_i),$$

where A_N represents the attributes. The method is able to discover automatically the dependences between attributes and provide an associated graph of these dependencies in order to facilitate the visualization and the probabilities determination. Figure 7.4 shows

an example of a graph with independent attributes (left panel) and another one with dependencies between the attributes (right panel).

7.3.2 Application and validation of the methods

7.3.2.1 The field star sample

This first step prior to apply these algorithms to the CSPNe sample is to prove their feasibility, given the attributes available in astronomical archives, in a sample of known objects. We selected five different types of spectroscopically well-classified blue stars from *bona fide* catalogues. This sample includes white dwarfs, sdOs, PG1159, O, and WR stars. All the stars in the training sample do not have, *a priori*, associated PNe, except for the case of the PG1159 sample, in which 17 of 40 stars are CSPNe (see below). The catalogues used for the training sample were the following:

- The *Galactic O-Star Spectroscopic Survey* (GOSSS, [Sota et al., 2014b](#)), which contains 448 O stars with a *bona fide* classification. This catalogue is the result of combining the objects presented in [Sota et al. \(2011\)](#) and [Sota et al. \(2014a\)](#).
- The *Sloan Digital Sky Survey Data Release 7 White Dwarf Catalog* (SDSS DR7, [Kleinman et al., 2013](#)) provides information of 19 712 spectroscopically confirmed white dwarfs. From this large sample, only those WDs with $T_{\text{eff}} \geq 30000$ K were selected as they are blue objects and have similar colours than the rest of the stars in the training sample. This criterium reduced the sample to 1 648 WDs.
- For the sdOs sample, we used the whole sample described in Chapter 2, that contains 774 objects.
- The *7th Catalog of Galactic Wolf-Rayet stars* ([van der Hucht, 2001](#)), which contains 227 Population I Wolf Rayet stars.
- For the *PG1159-type sample*, no catalogue is available as far as we know, so we used the list included in [Werner & Herwig \(2006\)](#), the most complete compilation of PG1159 stars to date. It contains 40 of such stars (17 of them with associated PNe). We are aware that other new PG1159 stars have been possibly catalogued since then. However, the number remains very low and our classification method is not affected by it.

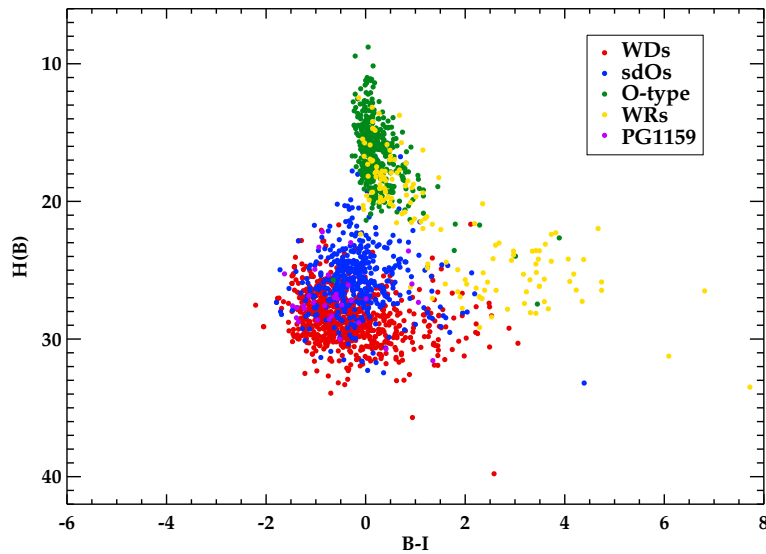


FIGURE 7.5: Reduced proper motion diagram for the field star sample (sdOs, white dwarfs, O stars, Wolf-Rayet stars and PG1159) used for the classification.

7.3.2.2 Selection criteria

In order to distinguish and classify the different object classes conforming the field star sample, choosing the optimal set of attributes (or parameters) in the sample is crucial. The final selected attributes were the following:

- **Proper motions**

Following the procedure described in Oreiro et al. (2011), we used proper motions in order to distinguish among different kinematic populations in the sample. For that, we matched our list of objects with the PPMXL catalogue (Roeser et al., 2010) by using a maximum of 5 arcsec as a radius for the cross-match. PPMXL provides positions, proper motions, 2MASS (J , H , K_s) and photographic (USNO B, R, and I-band) photometry of 900 million stars and galaxies, aiming to be complete for stars with $V \leq 20$.

To separate among the different classes of objects, we used the reduced proper motion (H) which is calculated, for a given filter, as follows:

$$H(\text{filter}) = m + 5 \log_{10}(\mu) + 5, \quad (7.1)$$

where m is the apparent magnitude in the filter and μ the total proper motion measured in milliarcsec per year.

In Fig. 7.5 we show $H(B)$ against $(B-I)$ for the field star sample. In a quick look, one can distinguish two main groups in the diagram. On the one hand, white dwarfs (red) and sdOs (blue) seem to cluster in the bottom left part of the diagram, while Wolf-Rayet

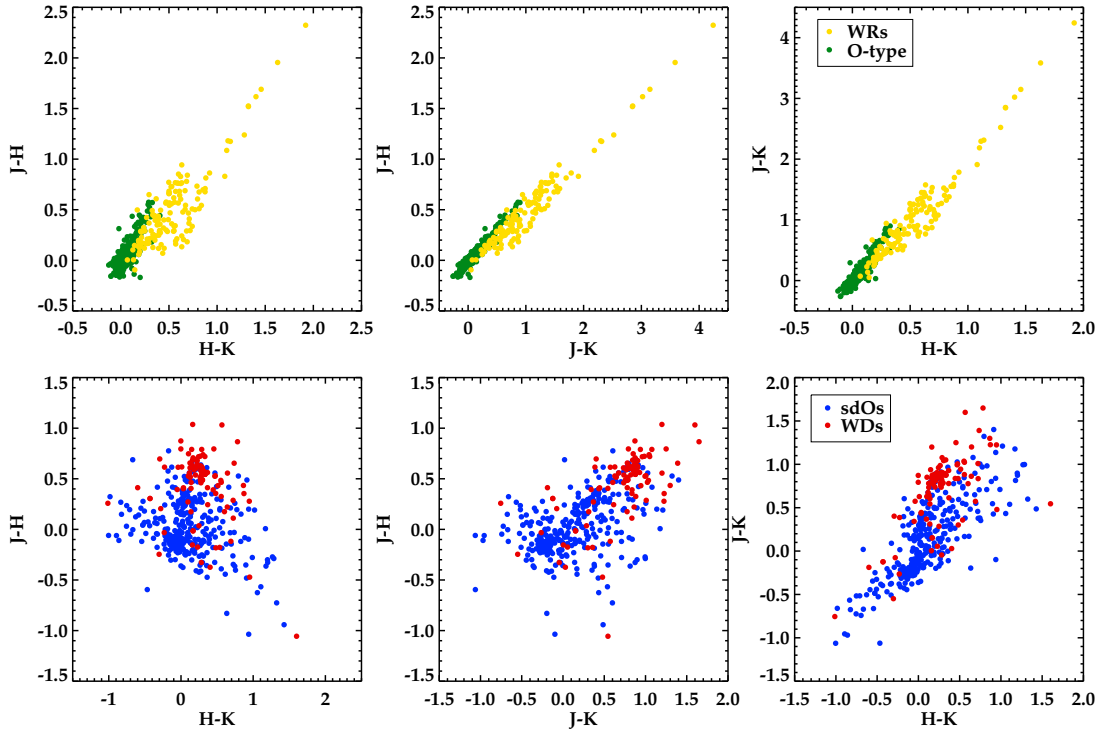


FIGURE 7.6: Colour-colour diagrams from 2MASS photometry for the O-type and WR field stars (upper panels) and for the sdOs and WDs field stars (lower panels).

(yellow) and O-type (green) stars lie in the upper right region. Moreover, a borderline around $H(B) \sim 28$ could be traced to separate between WDs and sdOs.

- **Infrared colours**

After cross-match our sample of field stars with the Two Micron All-Sky Survey (2MASS) of Point Sources (Cutri et al., 2003), we inspected whether the 2MASS photometry contributed to separate the classes included in the sample. We selected infrared photometry in order to minimize the influence of extinction. Figure 7.6 shows the colour-colour diagram using 2MASS photometry for the two main groups obtained in the proper motion diagram (i.e., O-type and WR on the one hand, and sdOs and WDs on the other hand). As can be seen in the figure, these colours clearly separated O (green dots) and WR (yellow dots), as well as sdOs and WDs, although in this case with a bit more contamination. This is, therefore, a relevant filter in the classification method, since it allows distinguishing between these two samples (O-type and WR) that appear mixed in a large region of the reduced proper motion diagram (see Fig. 7.5).

- **Galactic distribution**

We also noted that the two main groups in the sample are easily distinguished on basis of their galactic distribution. Figure 7.7 shows this distribution of the sample in the same colour code than Figure 7.5. There is a clear segregation between O and Wolf-Rayet

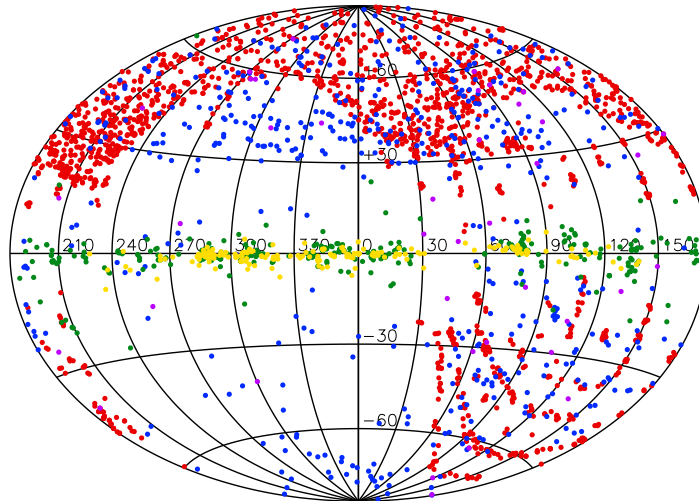


FIGURE 7.7: Galactic distribution of the field star sample.

stars (located near the galactic plane) and the sdOs and WDs (located at high latitudes). Although it is not easily identified, the PG1159 sample are also included in the plot and they are also mainly located at high latitudes. This evident difference in the distribution of the objects is just a consequence of their evolutionary state. While all sdO, WD and PG1159 sample are very evolved objects, the O and WR stars are younger, coming from a different population. In fact, the WD (and maybe the sdO) sample in this plot, very probably represent the ultimate stage of the low- and intermediate-mass star that passed through the planetary nebula phase long time ago.

7.3.2.3 Results of the classification for the field star sample

Once the attributes have been selected they will be the input parameters for the classification algorithms. Hence, these input parameters are the following: $H(B)$, $B-I$, $J-H$, $H-K$, and galactic latitude l . In addition, the proper motion in right ascension and declination was used. Not all the parameters were used in all the classification algorithms. For the implementation of the algorithms, we used the data mining software WEKA (Hall et al., 2009).

For the SVM algorithm, a RBF kernel was set to classify on basis of 4 attributes ($H(B)$, $B-I$, $J-H$, $H-K$). The introduction of l as input parameter led to a strong misclassification of the sample, although the reasons could not be identified. In any case, taking into account the other four attributes, we obtained a mean accuracy of the classification of $\sim 85\%$ with this method.

For the RF algorithm, we set to 100 the number of trees generated. The attributes $H(B)$, $B-I$, $J-H$, $H-K$, l , pm_{RA} and pm_{DEC} were used. Due to the small number of attributes in our training

set, the random selection of features was not important as every attribute was necessary for the classification. The mean accuracy obtained in this case was $\sim 88\%$.

Finally, for the BN algorithm we did not put any restriction to the maximum number of parents for each attribute. The attributes $H(B)$, $B-I$, $J-H$, $H-K$, l , pm_{RA} and pm_{DEC} were used. The mean accuracy achieved was $\sim 85\%$.

We used cross-validation in all the classification algorithms. We can conclude that the three classification algorithms have achieved a high success rate in the classification of the field star sample. In the next section we will use the same algorithms and attributes for the classification of CSPNe.

7.3.3 Our case study: classification of CSPNe

Once we have validated the classification methods for a known sample of field stars, the next step is to apply them to the sample of CSPNe of our catalogue. In the following we describe this classification.

7.3.3.1 The CSPNe sample

We selected those CSPNe with known spectral classification. We take as reference the list of classified CSPNe compiled by [Weidmann & Gamen \(2011\)](#). Although that work contains 492 stars of both confirmed and possible PN with spectral-type determinations, they are dispersed in 26 different classes which makes it very difficult to obtain significant samples. As an example, 19 out of these 26 spectral types include less than 20 objects. In addition, some of the most populated classes are not, indeed, spectral types, as it is the case of the “weak emission lines”(wels) with 72 objects or the “Blue” class with 50. Therefore, we grouped some of the classes into a more general class with the aim of expanding the sample significantly. For instance, the groups of DA+WD (12 objects), DAO (14 objects) and DO (4 objects) were grouped in the WD group. We proceeded similarly for all the subtypes of WR stars and O stars, respectively. In addition, we also used the sample of sdOs compiled by [Aller et al. \(2015a\)](#), which includes 18 of these objects. In total, we obtained these samples:

- 82 objects in the group of O-type stars.
- 30 objects in the group of WD stars.
- 102 objects in the group of WR stars.
- 15 objects in the group of PG1159 stars.

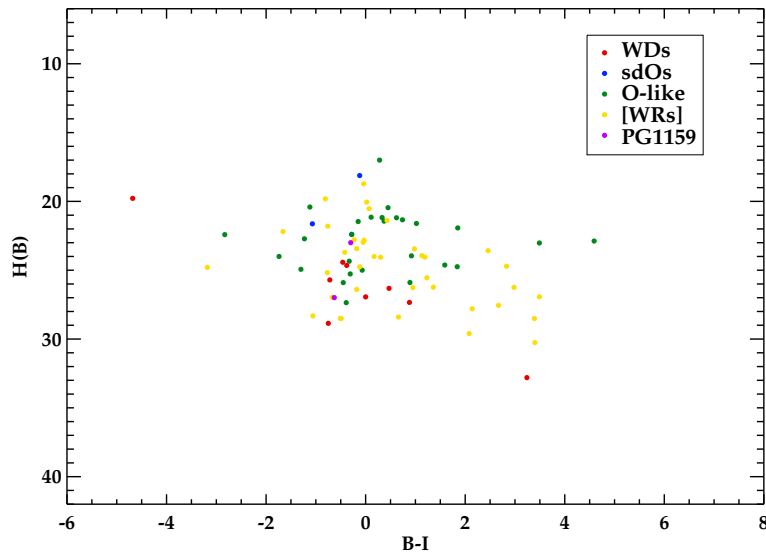


FIGURE 7.8: Reduced proper motion diagram for CSPNe training sample used for the classification.

- 18 objects in the group of sdO stars.

7.3.3.2 Selection criteria

The next step is to apply the selection criteria described in Sect. 7.3.2.2 to the different classes of CSPNe in order to get an optimal classification of them.

- **Proper motions**

In Fig. 7.8 we show $H(B)$ against $(B-I)$ for the CSPNe training sample. In contrast to the training sample for the field stars, the proper motion filter does not distinguish the groups in the CSPNe sample. This result could be explained taking into account that the CSPNe groups previously defined are objects in a similar evolutionary stage and, therefore, hard to distinguish from a kinematical point of view.

- **Infrared colours**

As in the case of field stars, we also investigated the possible segregation of CSPNe classes on basis of their 2MASS photometry. Figure 7.9 shows the corresponding colour-colour diagrams. This figure should be compared with Fig. 7.6 in which we show the same diagram but for field stars (note that we have set the same axis range in both figures for comparison purposes). In the case of CSPNe, both [WRs] and O-like stars appear mixed in the upper panels of Fig. 7.9 in contrast to what we see in field stars (see Sect. 7.3.2.2). The larger dispersion in the case of CSPNe could be due to extinction effects because

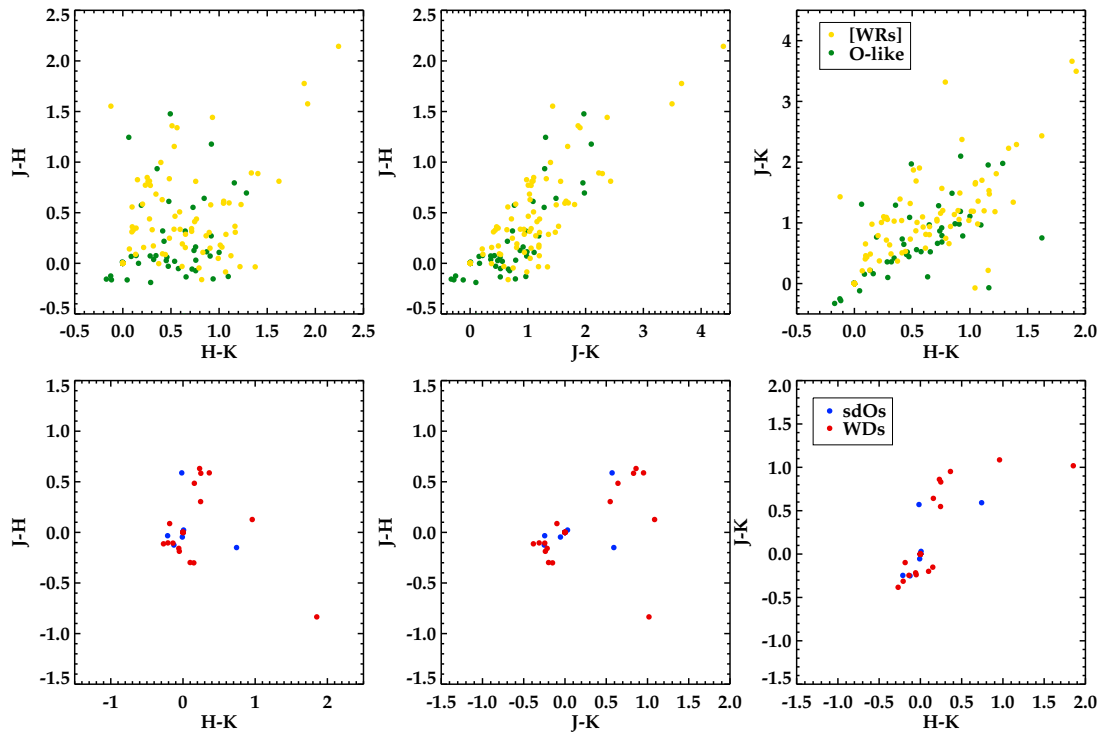


FIGURE 7.9: Colour-colour diagrams from 2MASS photometry for the O-like and [WR] CSPNe (upper panels) and for the sdOs and WDs CSPNe (lower panels).

of the presence of dust from the PNe around them. We also do not find any segregation between the sdOs and WDs CSPNe (lower panels of Fig. 7.9), although these results can be affected by the low number statistics.

- **Galactic distribution**

Figure 7.10 shows the galactic distribution of all classes of the CSPNe sample. It is clear from this figure that there is not segregation of the different classes according to the latitude, as it was in the case of the training sample for field stars. This was already expected since as we mentioned in Chapter 1, PNe are mainly located near the Galactic plane. Therefore, this filter is neither applicable to the sample of CSPNe.

7.3.3.3 Results of the classification for the CSPNe sample

In view of the lack of criteria that segregates the CSPNe training sample, the classification algorithms could not be applied in this case to obtain a classification of the whole sample of CSPNe. The reason for this can be ascribed to the fact that selected criteria are completely

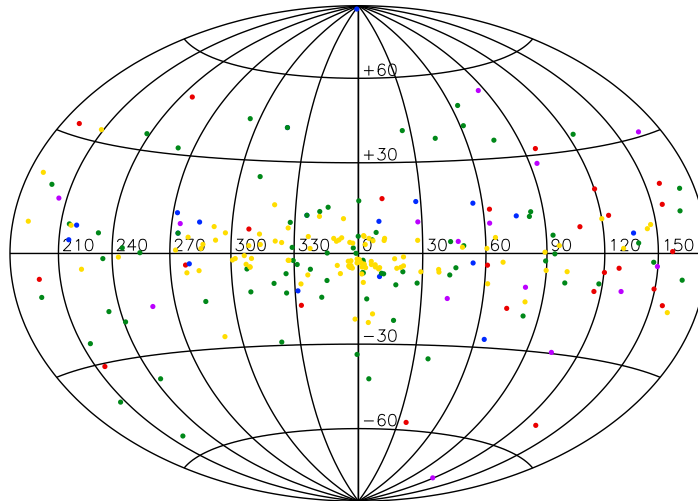


FIGURE 7.10: Galactic distribution of the CSPNe sample.

dependent on the stellar properties to be studied. Thus, while in the case of the field stars, the O and WR sample are massive objects belonging to Population I, the O-like and [WRs] stars found in CSPNe are low-mass, evolved stars. Therefore, they are currently in two different evolutionary states and have very different properties (e.g., mass, radius, etc.). Then, it is clear that different criteria have to be applied for the two samples. On the other hand, the sdOs and WDs used in the case of the field stars seem to be much more evolved objects than those sdOs and WDs found in CSPNe (i.e., the former may have already passed through the PN phase). This is easily concluded from their spatial distribution in the Galaxy, since the former are usually located at high latitudes and the later are mainly located near the Galactic plane. In short, the photometric and kinematic information available in astronomical archives is not enough by itself to distinguish between the different classes in the CSPNe sample. However, we note that the low number of CSPNe spectroscopically classified prevents a statistically valid analysis and selecting the appropriate criteria. Currently, we need a larger spectroscopically classified sample of CSPNe in order to obtain larger subsamples of the different spectral types.

7.4 Summary and outcomes of this chapter

In this chapter we have presented an updated catalogue of 2951 true, probable and possible Galactic planetary nebulae, which is the result of combining about thirty individual catalogues and works by using VO tools. The catalogue, which is accessible online, provides the most relevant information of these individual works as well as data from 2MASS, SDSS, UCAC4 and PPMXL archives and offers direct access to SIMBAD for each object.

As a second part of the work, we have developed a classification method with the main aim of classifying the whole sample of CSPNe. This method is based in three different classification algorithms, which are capable of classifying a sample of objects on basis of certain criteria. We have applied these classification algorithms to a known sample of blue objects with a successful result. Unfortunately, the criteria required to separate the samples are not easily recognizable in the CSPNe sample, which makes impossible the application of the classification method to this sample.

Conclusions and Future Work

To close this dissertation, we review the whole research objectives and results presented in this work. We also give some prospective ideas and projects for the future work of this research.

8.1 General Conclusions

Along this thesis, we have investigated several topics on formation and evolution of PNe that host sdOs central stars. In this work, we have made use of different observational techniques, like narrow-band and red tunable filter imaging, as well as low-, intermediate-, and high-resolution long slit spectroscopy, which has provided us a large experience in the data acquisition and reduction. This has allowed us to acquire background in the morphological and kinematical analysis of PNe, crucial to investigate their 3D structure and the processes involved in their formation.

From a theoretical point of view, we have also used the state-of-the-art non-LTE stellar-atmosphere models for hot, compact stars developed by the German Astrophysical Virtual Observatory (GAVO) and accessible through the TheoSSA service. Working with these sophisticated models has allowed us to obtain a substantial background in the spectroscopic analysis of CSPNe, crucial to constrain their origin and current evolutionary status. In addition, we have also made use of the nebular analysis software ANNEB, which has provided us expertise in the calculations and interpretation of the physical nebular properties and chemical abundances. Finally, and also in the framework of the Virtual Observatory (VO), we have used some of the VO tools (e.g., Topcat, Aladin) which provide a great advantage in the data mining and visualization, specially when handling a huge amount of data.

The main scientific contributions of this thesis can be summarized as follows:

- We have carried out an observational survey to search for new PNe around sdOs in the optical range. This kind of searches were not conducted since the late eighties and this is the first time that this topic is tackled with “modern” instrumentation. In our survey, more than 100 sdOs have been imaged with 2-m class telescopes. This search was complemented with a careful visual inspection of a sample of roughly 700 sdOs in the WISE public archive, which provides mid-infrared images in four bands (from 3.4 to 22 μm). All these searches resulted in the discovery of a new PNe around the sdO 2M 1931+4324 as well as 11 more candidates that present hints of nebulosity in the WISE images. We also obtained imaging and intermediate-resolution, long-slit spectra of some of the already known PNe with confirmed or possible sdO CSs, in order to constrain the sdO nature of these objects. As a result of this work, we classified as sdO the CS of the PN DeHt 2 and tentatively propose the same classification for the CS of PN K 2-2.
- Based on narrow-band imaging and high-resolution, long-slit spectra, we report the first detailed morpho-kinematic analyses of four PN+sdO systems: our recently discovered 2M 1931+4324, Abell 36, DeHt 2 and RWT 152. Complementary low- and intermediate-resolution, long-slit spectra were also analyzed in all cases, which have allowed us to confirm the sdO nature of their CSs and to obtain the properties of the nebulae. These studies have allowed us to reconstruct the formation history of these four objects and conclude that different ejection processes with different properties have been involved.
- In the case of RWT 152, an additional and detailed abundance analysis based on deep intermediate-resolution, long-slit spectra from a 10-m class telescope is also presented. This analysis reveals that RWT 152 is a new halo PNe. Its low chemical abundances, the very low ionized mass and the faintness of the nebula, as well as its atmospheric parameters clearly point out a low-mass progenitor ($\leq 1 M_{\odot}$). This result could be compatible with the scarcity of PN+sdO systems.
- We compiled a total of ~ 18 reliable PN+sdO systems, taking into account data from the literature and our newly classified objects. For all these sdOs with associated PNe a post-AGB origin is proposed. We suggest that this low number could be biased by (1) the extreme faintness of the PNe, (2) the lack of a spectral classification of many CSs and/or (3) the fact that the nebulae has vanished before being photoionized by the CSs, due to the slow evolution of their possible low-mass progenitors.
- We have analyzed the properties of these 18 PN+sdO systems. For the first time, we have found that these systems share some common characteristics: (1) most of the objects are evolved or relatively evolved PNe with a very low surface brightness; (2) most of them present elliptical and bipolar morphologies, often revealing complex and multiple

structures as well as signs of collimated outflows; (3) they usually present nebular spectra which suggest a possible deficiency in heavy metals; (4) a high fraction of them belong (or are suspected to belong) to binary systems.

- For the first time, a pioneering spectral analysis procedure has been developed for tackling *peculiar* central stars. These CSPNe, are thought to host binary systems consisting of a cool (A- to K-spectral type) and bright star, responsible for the observed absorption spectrum and a hot and faint companion responsible for the photoionization of the nebula. The presence of the hot companion is usually hardly suspected in the optical spectrum, which makes it difficult the analysis of both components. In this context, we have presented an innovative detailed spectral analysis methodology for these kind of objects, which allows us to simultaneously obtain the atmospheric parameters of both stars. This ultimately provides information about the origin and current evolutionary status of the pair. We have successfully applied this spectral analysis procedure to BD+30°623, the central star of the complex PN NGC 1514. We found that the sdO classification for the hot component is uncertain, that the cool star is an A0 horizontal branch star and not an A0 red giant star, as usually classified. Moreover, the coincidence between the derived distance for each star, confirms that this CSs is a binary. This method opens up a novel window to study other similar complex systems.
- We have built up a new catalogue of Galactic PNe, that updates the last compilation published 15 years ago. It contains a total of 2951 PNe, to be compared with the 1510 PNe in the last compilation. Additionally, we have designed a classification method to distinguish different classes of blue stars with the ultimate goal of classifying the whole sample of CSPNe in an automatic way, on basis of archival data and without the need of obtaining spectra. While the selected criteria are successful for the blue field stars, we found difficulties to apply this technique to the CSPNe sample, concluding that spectra are necessary to obtain their spectral types.

8.2 Future prospects

Apart from the work included and described in this thesis, we have been also involved in other side projects related to the main topic of this dissertation, which are still ongoing. Additionally, part of the analysis carried out during this period provides the basis for future research in several interesting lines. In the following, we briefly point out some highlights concerning this future work.

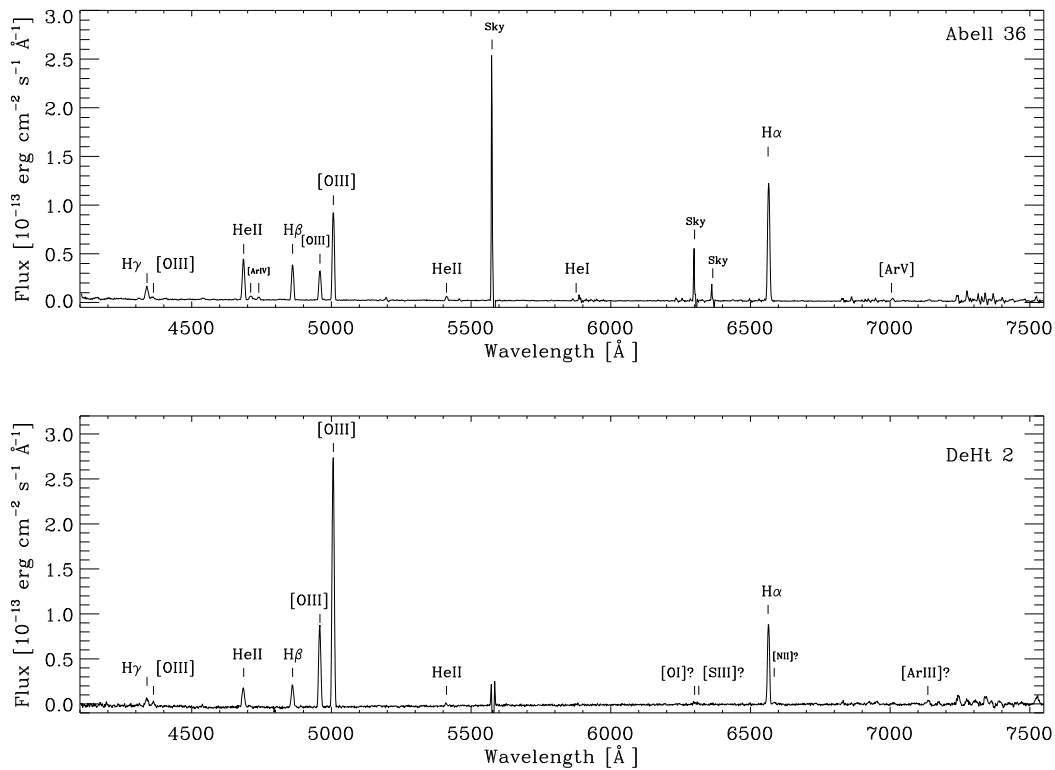


FIGURE 8.1: Deep nebular spectra of PN Abell 36 (upper panel) and DeHt 2 (lower panel).

1. Analysis of very deep nebular spectra of PNe around sdOs

In the course of this thesis we have obtained a series of intermediate-resolution, long-slit spectra of some of the confirmed or possible PN+sdO systems by using the Boller & Chivens spectrograph (OAN-SPM). These data are still to be analyzed. The main goal of these observations is to obtain a very deep spectrum of each PN by combining the individual spectra, which will allow us to detect very faint emission lines and to obtain chemical abundances.

Figure 8.1 shows the reduced spectra for Abell 36 (top) and DeHt 2 (bottom), in the range 4100 - 7550 Å. Total exposure times are 2.5 h (5 individual spectrum \times 1800 s each) for the case of Abell 36 and 4.5 h (9 \times 1800 s) for the case of DeHt 2. Indeed, faint emission lines (e.g. H γ and [OIII] λ 4363) are detected in these deep spectra, which were not observed in the spectra presented in Chapter 4.

2. Spectral analysis and classification of CSPNe

As we have extensively discussed in this dissertation, spectral classification of CSPNe is one of the open challenges in the PNe field today. Spectroscopy of a large number of CSPNe would significantly improve our knowledge about their formation and evolution scheme, by determining their physical properties and peculiarities instead of considering them just as ionization sources.

We aim to obtain high-resolution spectroscopy and carry out spectral analysis of a large number of CSPNe in order to derive their atmospheric parameters (T_{eff} , $\log g$) and chemical abundances, by using the latest state-of-the-art synthetic models which we have already used in this thesis. This investigation could significantly increase the number of sdOs as CSPNe.

On the other hand, it is highly interesting to apply the innovative spectral analysis that we have developed for the case of the CS of NGC 1514, to the rest of the sample of *peculiar central stars*. This will provide information about the evolutionary status of these objects.

3. Morpho-kinematic analysis of NGC 1514

Besides the detailed analysis of the binary CSs of NGC 1514 presented in this thesis (Chapter 6), we also obtained high-resolution, long-slit spectra of this complex PN to carry out a detailed morpho-kinematic analysis of the nebula. The observations are already reduced and we are working in the corresponding kinematic analysis. Figures 8.2 and 8.3 show the slits used for the high-resolution spectra and the resulting PV maps at each slit, respectively. We will use the software `SHAPE`¹ (Steffen et al., 2011), a 3D morpho-kinematic modeling tool that allows us to obtain synthetic PV maps and images that can be compared with the observed ones.

4. Building up an updated catalogue of hot subdwarf stars

Also under construction is a new and updated catalogue of hot subdwarf stars. Almost ten years have passed since the publication of the Subdwarf Database by Østensen (2006) and many new hot subdwarf stars have been identified in the last years. Many of these new discoveries are the result of searches by means of VO (see, e.g., Oreiro et al., 2011, and Pérez et al., submitted). Following the methodology presented in Chapter 7, it would be very useful to compile, by using the VO tools, a new updated and complete database that accounts for these new discoveries and reports the information (magnitudes, proper motions, stellar parameters, binarity) for all these stars.

5. Binary central stars

Finally, as a long-term project, we would like to explore the role of binarity on the shape of PNe from an observationally point of view. As we have explained throughout this thesis, binary interactions have been the main proposed mechanism to explain this diversity of shapes in PNe. However, the number of observed objects is still very low to draw firm conclusions about the influence of binary interactions in the shape of PNe. For this purpose, we will use different techniques (radial velocity, light curves modulations and infrared excess) to detect and follow-up a large amount of binary systems in the nuclei of PNe.

¹<http://www.astrosen.unam.mx/shape/>

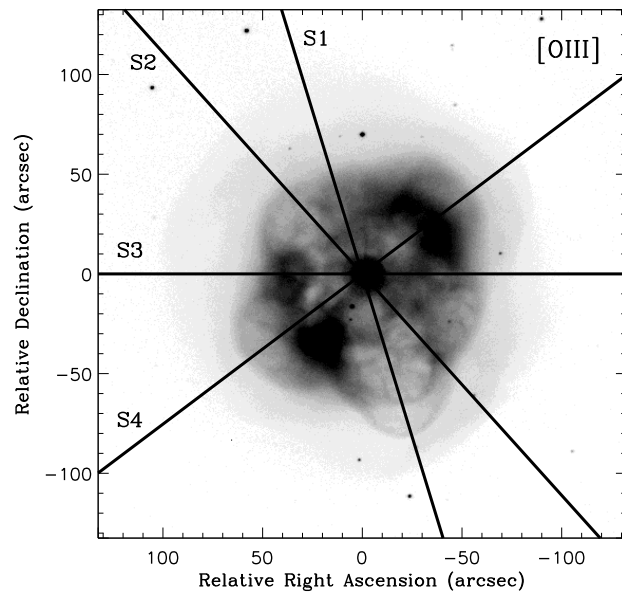


FIGURE 8.2: Grey-scale reproduction of the [O III] image of NGC 1514. grey levels are linear. The lines S1, S2, S3 and S4 mark the slit positions used for high-resolution, long-slit spectroscopy.

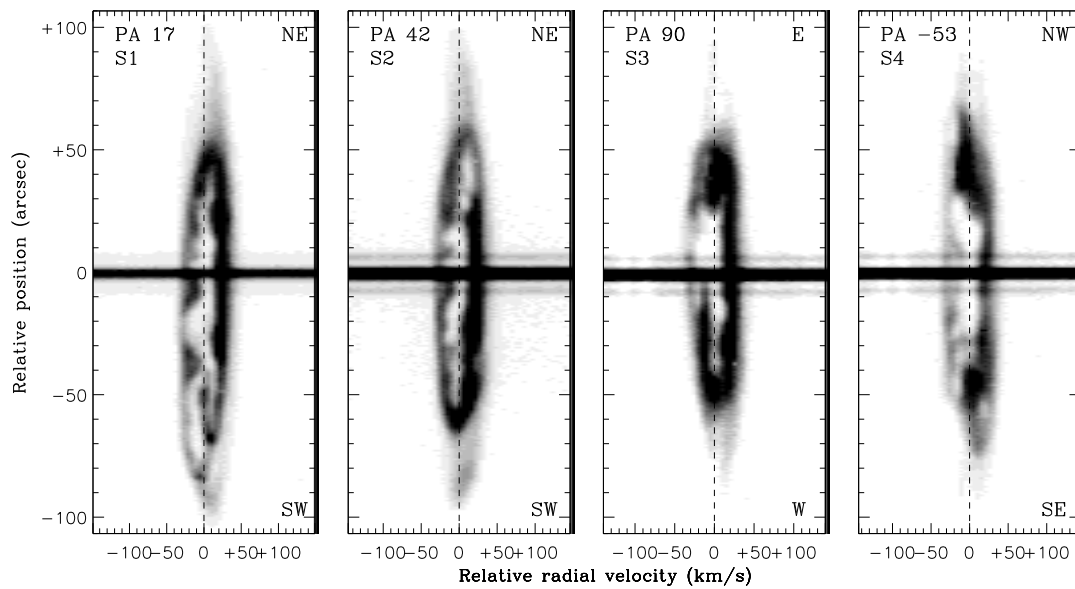


FIGURE 8.3: Grey-scale, PV maps derived from the [O III] $\lambda 5007$ high-resolution, long-slit spectra of NGC 1514.

List of Publications

In the course of this thesis, I have participated in 4 refereed articles so far, all of them as first author. The list of publications is presented below in inverse chronological order of publication. Currently, I have one more paper in preparation (as first author and not listed below). My contributions to scientific conferences are also listed below.

Refereed publications

- [1] **“Observations of the planetary nebula RWT 152 with OSIRIS/GTC”**.
A. Aller L. F. Miranda, L. Olguín, E. Solano, and A. Ulla
Submitted to MNRAS.

- [2] **“Spectral analysis of BD+30°623, the peculiar binary central star of the planetary nebula NGC 1514”**.
A. Aller, B. Montesinos, L. F. Miranda, E. Solano, and A. Ulla.
2015, MNRAS, 448, 2822A; DOI: 10.1093/mnras/stv196

- [3] **“The physical structure of planetary nebulae around sdO stars: Abell 36, DeHt 2, and RWT 152”**.
A. Aller L. F. Miranda, L. Olguín, R. Vázquez, P. F. Guillén, R. Oreiro, A. Ulla, and E. Solano
2015, MNRAS, 446, 317A; DOI: 10.1093/mnras/stu2106

- [4] **“Detection of a multishell planetary nebula around the hot subdwarf O-type star 2MASS J19310888+432457”**.
A. Aller, L. F. Miranda, A. Ulla, R. Vázquez, P. F. Guillén, L. Olguín, C. Rodríguez-López, P. Thejll, R. Oreiro, M. Manteiga, and E. Pérez.
2013, A&A, 552A, 25A; DOI: 10.1051/0004-6361/201219560

Conference contributions

- [1] **“GTC/OSIRIS observations of RWT 152, a case study of a planetary nebula with an sdO central star”**.
A. Aller, L. F. Miranda, L. Olguín, E. Solano, and A. Ulla
Proceedings of *The physics of evolved stars: A conference dedicated to the memory of Oliver Chesneau*, held in Nice (France) June 8-12, 2015.
In press.

- [2] **“A new planetary nebula around the hot subdwarf star 2MASS J19310888+4324577”**.
A. Aller, A. Ulla, L. F. Miranda, P. Thejll, R. Oreiro, C. Rodríguez-López, M. Manteiga, and E. Pérez
Proceedings of the *Highlights of Spanish Astrophysics VII*, held in Valencia (Spain) July 9-13, 2012
2013, pg. 511-515.
- [3] **“Search for planetary nebulae around hot subdwarf stars”**.
A. Aller, A. Ulla, L. F. Miranda, R. Oreiro, M. Manteiga, E. Pérez, C. Rodríguez-López.
Proceedings of the *XXXIII Meeting of the Spanish Royal Society of Physics*, held in Santander (Spain), September 19-24, 2011
ISBN 978-84-86116-44-6 (T.4)
- [4] **“Statistical analysis of temple orientation in Ancient India”**.
A. Aller and J. A. Belmonte.
Proceedings of the SEAC 19th annual meeting *Stars and Stones: A voyage in Archeoastronomy and Cultural Astronomy – A meeting of different worlds*, held in Évora (Portugal), September 19-24, 2011
BAR S2720, 2015; ISBN 978-1-4073-1373-3.
- [5] **“Gaia future contribution to the study of PNe”**.
M. Manteiga, B. Arcay, A. Ulla, A. Aller, L. F. Miranda, Y. Isasi and Gaia DPAC.
Proceedings of the IAU Symposium No. 283: *Planetary nebulae: an eye to the future*, held in Puerto de la Cruz, Tenerife (Spain) July 25-29, 2011
Volume 283, pg. 428-429.
- [6] **“Rule or exception? Planetary nebulae around hot subdwarf stars”**.
A. Aller, L. F. Miranda, A. Ulla, R. Oreiro, M. Manteiga, E. Pérez, and C. Rodríguez-López.
Proceedings of the IAU Symposium No. 283: *Planetary nebulae: an eye to the future*, held in Puerto de la Cruz, Tenerife (Spain) July 25-29, 2011

Bibliography

- Abell, G. O. 1966, *ApJ*, 144, 259
- Acker, A., Boffin, H. M. J., Outters, N., et al. 2012, *RMxAA*, 48, 223
- Acker, A., Fresneau, A., Pottasch, S. R., & Jasniewicz, G. 1998, *A&A*, 337, 253
- Acker, A., Marcout, J., Ochsenbein, F., et al. 1992, *The Strasbourg-ESO Catalogue of Galactic Planetary Nebulae. Parts I, II.*
- Aller, A., Miranda, L. F., Olguín, L., et al. 2015a, *MNRAS*, 446, 317
- Aller, A., Miranda, L. F., Ulla, A., et al. 2013, *A&A*, 552, A25
- Aller, A., Montesinos, B., Miranda, L. F., Solano, E., & Ulla, A. 2015b, *MNRAS*, 448, 2822
- Alves, D. R., Bond, H. E., & Livio, M. 2000, *AJ*, 120, 2044
- Bains, I., Gledhill, T. M., Richards, A. M. S., & Yates, J. A. 2004, in *Astronomical Society of the Pacific Conference Series, Vol. 313, Asymmetrical Planetary Nebulae III: Winds, Structure and the Thunderbird*, ed. M. Meixner, J. H. Kastner, B. Balick, & N. Soker, 186
- Balick, B. 1987, *AJ*, 94, 671
- Balick, B. & Frank, A. 2002, *A&A Annual Review*, 40, 439
- Balick, B., Gonzalez, G., Frank, A., & Jacoby, G. 1992, *ApJ*, 392, 582
- Banse, K., Crane, P., Grosbol, P., et al. 1983, *The Messenger*, 31, 26
- Baschek, B. & Norris, J. 1975, *ApJ*, 199, 694
- Beaulieu, S. F., Dopita, M. A., & Freeman, K. C. 1999, *ApJ*, 515, 610
- Bernard Salas, J., Pottasch, S. R., Beintema, D. A., & Wesselius, P. R. 2001, *A&A*, 367, 949
- Bertone, E., Buzzoni, A., Chávez, M., & Rodríguez-Merino, L. H. 2004, *AJ*, 128, 829

- Blackman, E. G., Frank, A., Markiel, J. A., Thomas, J. H., & Van Horn, H. M. 2001a, *Nature*, 409, 485
- Blackman, E. G., Frank, A., & Welch, C. 2001b, *ApJ*, 546, 288
- Blöcker, T., Osterbart, R., Weigelt, G., Balega, Y., & Men'shchikov, A. 2001, in *Astrophysics and Space Science Library*, Vol. 265, *Astrophysics and Space Science Library*, ed. R. Szczerba & S. K. Górný, 241
- Bloecker, T. 1995, *A&A*, 299, 755
- Bobrowsky, M., Sahu, K. C., Parthasarathy, M., & García-Lario, P. 1998, *Nature*, 392, 469
- Boffin, H. M. J., Miszalski, B., Rauch, T., et al. 2012, *Science*, 338, 773
- Bohuski, T. J. & Smith, M. G. 1974, *ApJ*, 193, 197
- Bond, H. E. 2000, in *Astronomical Society of the Pacific Conference Series*, Vol. 199, *Asymmetrical Planetary Nebulae II: From Origins to Microstructures*, ed. J. H. Kastner, N. Soker, & S. Rappaport, 115
- Bond, H. E., Liller, W., & Mannery, E. J. 1978, *ApJ*, 223, 252
- Bond, H. E. & Livio, M. 1990, *ApJ*, 355, 568
- Borkowski, K. J., Tsvetanov, Z., & Harrington, J. P. 1993, *ApJ Letters*, 402, L57
- Borucki, W. J., Koch, D., Basri, G., et al. 2010, *Science*, 327, 977
- Borucki, W. J., Koch, D. G., Lissauer, J. J., et al. 2003, in *Society of Photo-Optical Instrumentation Engineers (SPIE) Conference Series*, Vol. 4854, *Future EUV/UV and Visible Space Astrophysics Missions and Instrumentation.*, ed. J. C. Blades & O. H. W. Siegmund, 129–140
- Boumis, P., Akras, S., Xilouris, E. M., et al. 2006, *MNRAS*, 367, 1551
- Boumis, P., Meaburn, J., Lloyd, M., & Akras, S. 2009, *MNRAS*, 396, 1186
- Boumis, P., Paleologou, E. V., Mavromatakis, F., & Papamastorakis, J. 2003, *MNRAS*, 339, 735
- Brassard, P., Fontaine, G., Billères, M., et al. 2001, *ApJ*, 563, 1013
- Breiman, L. 1996, *Machine learning*, 24, 123
- Breiman, L. 2001, *Machine learning*, 45, 5
- Brocato, E., Matteucci, F., Mazzitelli, I., & Tornambe, A. 1990, *ApJ*, 349, 458
- Brocklehurst, M. 1971, *MNRAS*, 153, 471

- Brown, T. M., Bowers, C. W., Kimble, R. A., Sweigart, A. V., & Ferguson, H. C. 2000, *ApJ*, 532, 308
- Brown, T. M., Latham, D. W., Everett, M. E., & Esquerdo, G. A. 2011, *AJ*, 142, 112
- Brown, T. M., Sweigart, A. V., Lanz, T., Landsman, W. B., & Hubeny, I. 2001, *ApJ*, 562, 368
- Bruch, A., Vaz, L. P. R., & Diaz, M. P. 2001, *A&A*, 377, 898
- Cahn, J. H. & Kaler, J. B. 1971, *ApJ Supplements*, 22, 319
- Cahn, J. H., Kaler, J. B., & Stanghellini, L. 1992, *A&A, Supplement*, 94, 399
- Cardelli, J. A., Clayton, G. C., & Mathis, J. S. 1989, *ApJ*, 345, 245
- Castellani, M. & Castellani, V. 1993, *ApJ*, 407, 649
- Castelli, F. & Kurucz, R. L. 2003, in *IAU Symposium, Vol. 210, Modelling of Stellar Atmospheres*, ed. N. Piskunov, W. W. Weiss, & D. F. Gray, 20P
- Cepa, J., Aguiar, M., Bland-Hawthorn, J., et al. 2003, in *Revista Mexicana de Astronomia y Astrofisica Conference Series, Vol. 16, Revista Mexicana de Astronomia y Astrofisica Conference Series*, ed. J. M. Rodriguez Espinoza, F. Garzon Lopez, & V. Melo Martin, 13–18
- Charpinet, S., Fontaine, G., Brassard, P., & Dorman, B. 1996, *ApJ Letters*, 471, L103
- Chevalier, R. A. & Luo, D. 1994, *ApJ*, 421, 225
- Chopinnet, M. 1963, *Journal des Observateurs*, 46, 27
- Chromey, F. R. 1980, *AJ*, 85, 853
- Chu, Y.-H., Gruendl, R. A., Guerrero, M. A., et al. 2009, *AJ*, 138, 691
- Ciardullo, R., Bond, H. E., Sipior, M. S., et al. 1999, *AJ*, 118, 488
- Corradi, R. L. M., Rodríguez-Gil, P., Jones, D., et al. 2014, *MNRAS*, 441, 2799
- Corradi, R. L. M. & Schwarz, H. E. 1993, *A&A*, 273, 247
- Corradi, R. L. M. & Schwarz, H. E. 1995, *A&A*, 293, 871
- Costa, R. D. D., Chiappini, C., Maciel, W. J., & de Freitas Pacheco, J. A. 1996, *A&A, Supplement*, 116, 249
- Cutri, R. M., Skrutskie, M. F., van Dyk, S., Beichman, C. A., & Carpenter, J. M. 2003, *VizieR Online Data Catalog*, 2246, 0
- D’Cruz, N. L., Dorman, B., Rood, R. T., & O’Connell, R. W. 1996, *ApJ*, 466, 359

- De Marco, O. 2009, *PASP*, 121, 316
- De Marco, O., Long, J., Jacoby, G. H., et al. 2015, *MNRAS*, 448, 3587
- De Marco, O. & Moe, M. 2005, in *American Institute of Physics Conference Series*, Vol. 804, *Planetary Nebulae as Astronomical Tools*, ed. R. Szczerba, G. Stasińska, & S. K. Gorny, 169–172
- De Marco, O., Passy, J.-C., Frew, D. J., Moe, M., & Jacoby, G. H. 2013, *MNRAS*, 428, 2118
- Delgado-Inglada, G., Morisset, C., & Stasińska, G. 2014, *MNRAS*, 440, 536
- Dengel, J., Hartl, H., & Weinberger, R. 1980, *A&A*, 85, 356
- Dorman, B., Rood, R. T., & O’Connell, R. W. 1993, *ApJ*, 419, 596
- Douchin, D., De Marco, O., Frew, D. J., et al. 2015, *MNRAS*, 448, 3132
- Drew, J. E., Greimel, R., Irwin, M. J., et al. 2005, *MNRAS*, 362, 753
- Drilling, J. S. 1983, *ApJ Letters*, 270, L13
- Drilling, J. S. 1996, in *Astronomical Society of the Pacific Conference Series*, Vol. 96, *Hydrogen Deficient Stars*, ed. C. S. Jeffery & U. Heber, 461
- Drilling, J. S., Jeffery, C. S., Heber, U., Moehler, S., & Napiwotzki, R. 2013, *A&A*, 551, A31
- Drilling, J. S., Moehler, S., Jeffery, C. S., Heber, U., & Napiwotzki, R. 2003, in *The Garrison Festschrift*, ed. R. O. Gray, C. J. Corbally, & A. G. D. Philip, 27
- Ebbets, D. C. & Savage, B. D. 1982, *ApJ*, 262, 234
- Eisenstein, D. J., Liebert, J., Koester, D., et al. 2006, *AJ*, 132, 676
- Escudero, A. V. & Costa, R. D. D. 2001, *A&A*, 380, 300
- Feibelman, W. A. 1997, *PASP*, 109, 659
- Fitzpatrick, E. L. 1999, *PASP*, 111, 63
- Frew, D. J., Bento, J., Bojičić, I. S., & Parker, Q. A. 2014, *MNRAS*, 445, 1605
- Frew, D. J., Bojičić, I. S., & Parker, Q. A. 2013, *MNRAS*, 431, 2
- Frew, D. J. & Parker, Q. A. 2006, in *IAU Symposium*, Vol. 234, *Planetary Nebulae in our Galaxy and Beyond*, ed. M. J. Barlow & R. H. Méndez, 49–54
- Frew, D. J. & Parker, Q. A. 2010, *PASA*, 27, 129
- Garcia-Segura, G. 1997, *ApJ Letters*, 489, L189

- García-Segura, G., Langer, N., Różyczka, M., & Franco, J. 1999, *ApJ*, 517, 767
- García-Segura, G., Villaver, E., Langer, N., Yoon, S.-C., & Manchado, A. 2014, *ApJ*, 783, 74
- Geier, S. 2013, in *European Physical Journal Web of Conferences*, Vol. 43, *European Physical Journal Web of Conferences*, 4001
- Geier, S., Heber, U., Tillich, A., et al. 2011a, in *American Institute of Physics Conference Series*, Vol. 1331, *American Institute of Physics Conference Series*, ed. S. Schuh, H. Drechsel, & U. Heber, 163–169
- Geier, S., Hirsch, H., Tillich, A., et al. 2011b, *A&A*, 530, A28
- Giesecking, F., Becker, I., & Solf, J. 1985, *ApJ Letters*, 295, L17
- Girardi, L., Bressan, A., Bertelli, G., & Chiosi, C. 2000, *A&A, Supplement*, 141, 371
- Girven, J., Steeghs, D., Heber, U., et al. 2012, *MNRAS*, 425, 1013
- Gleizes, F., Acker, A., & Stenholm, B. 1989, *A&A*, 222, 237
- Goldman, D. B., Guerrero, M. A., Chu, Y.-H., & Gruendl, R. A. 2004, *AJ*, 128, 1711
- Gómez, J. F., Suárez, O., Bendjoya, P., et al. 2015, *ApJ*, 799, 186
- Gómez, Y., Tafoya, D., Anglada, G., et al. 2009, *ApJ*, 695, 930
- González, J. J., Cepa, J., González-Serrano, J. I., & Sánchez-Portal, M. 2014, *MNRAS*, 443, 3289
- Górny, S. K. 2006, in *IAU Symposium*, Vol. 234, *Planetary Nebulae in our Galaxy and Beyond*, ed. M. J. Barlow & R. H. Méndez, 409–410
- Gourgouliatos, K. N. & Jeffery, C. S. 2006, *MNRAS*, 371, 1381
- Graham, M. F., Meaburn, J., López, J. A., Harman, D. J., & Holloway, A. J. 2004, *MNRAS*, 347, 1370
- Grauer, A. D., Bond, H. E., Ciardullo, R., & Fleming, T. A. 1987, in *Bulletin of the American Astronomical Society*, Vol. 19, *Bulletin of the American Astronomical Society*, 643
- Gray, R. O. & Corbally, J., C. 2009, *Stellar Spectral Classification*
- Green, E. M., Fontaine, G., Hyde, E. A., For, B.-Q., & Chayer, P. 2008, in *Astronomical Society of the Pacific Conference Series*, Vol. 392, *Hot Subdwarf Stars and Related Objects*, ed. U. Heber, C. S. Jeffery, & R. Napiwotzki, 75
- Green, R. F., Schmidt, M., & Liebert, J. 1986, *ApJ Supplements*, 61, 305

- Greenstein, J. L. 1966, *ApJ*, 144, 496
- Greenstein, J. L. 1972, *ApJ*, 173, 367
- Greggio, L. & Renzini, A. 1990, *ApJ*, 364, 35
- Grewing, M. & Neri, R. 1990, *A&A*, 236, 223
- Groth, H. G., Kudritzki, R. P., & Heber, U. 1985, *A&A*, 152, 107
- Guerrero, M. A., Chu, Y.-H., & Miranda, L. F. 2004, *AJ*, 128, 1694
- Guerrero, M. A. & Miranda, L. F. 2012, *A&A*, 539, A47
- Guerrero, M. A., Miranda, L. F., Ramos-Larios, G., & Vázquez, R. 2013, *A&A*, 551, A53
- Guerrero, M. A., Miranda, L. F., Riera, A., et al. 2008, *ApJ*, 683, 272
- Guillén, P. F., Vázquez, R., Miranda, L. F., et al. 2013, *MNRAS*, 432, 2676
- Gurzadian, G. A. & Egikian, A. G. 1991, *Astrophysics & Space Science*, 181, 73
- Hall, M., Frank, E., Holmes, G., et al. 2009, *SIGKDD Explorations*, 11, 10
- Han, Z., Podsiadlowski, P., Maxted, P. F. L., Marsh, T. R., & Ivanova, N. 2002, *MNRAS*, 336, 449
- Haro, G. & Luyten, W. J. 1962, *Boletín de los Observatorios Tonantzintla y Tacubaya*, 3, 37
- Heber, U. 1986, *A&A*, 155, 33
- Heber, U. 2009, *A&A Annual Review*, 47, 211
- Heber, U. & Drilling, J. S. 1984, *Mitteilungen der Astronomischen Gesellschaft Hamburg*, 62, 252
- Heber, U. & Hunger, K. 1987, in *IAU Colloq. 95: Second Conference on Faint Blue Stars*, ed. A. G. D. Philip, D. S. Hayes, & J. W. Liebert, 599–602
- Heber, U., Werner, K., & Drilling, J. S. 1988, *A&A*, 194, 223
- Heckathorn, J. N., Fesen, R. A., & Gull, T. R. 1982, *A&A*, 114, 414
- Henry, R. B. C., Kwitter, K. B., & Balick, B. 2004, *AJ*, 127, 2284
- Herald, J. E. & Bianchi, L. 2004, *ApJ*, 609, 378
- Herrero, A., Machado, A., & Mendez, R. H. 1990, *Astrophysics & Space Science*, 169, 183
- Herwig, F. 2005, *A&A Annual Review*, 43, 435

- Hillwig, T. C., Bond, H. E., Afşar, M., & De Marco, O. 2010, *AJ*, 140, 319
- Holmberg, E. B., Lauberts, A., Schuster, H.-E., & West, R. M. 1978, *A&A*, Supplement, 31, 15
- Holovaty, V. V. & Havrilova, N. V. 2005, *Astronomy Reports*, 49, 390
- Hora, J. L., Latter, W. B., & Deutsch, L. K. 1999, *ApJ Supplements*, 124, 195
- Howard, J. W., Henry, R. B. C., & McCartney, S. 1997, *MNRAS*, 284, 465
- Hua, C. T., Dopita, M. A., & Martinis, J. 1998, *A&A*, Supplement, 133, 361
- Hua, C. T. & Kwok, S. 1999, *A&A*, Supplement, 138, 275
- Huarte-Espinosa, M., Carroll-Nellenback, J., Nordhaus, J., Frank, A., & Blackman, E. G. 2013, *MNRAS*, 433, 295
- Huarte-Espinosa, M., Frank, A., Balick, B., et al. 2012, *MNRAS*, 424, 2055
- Hubeny, I. & Lanz, T. 1995, *ApJ*, 439, 875
- Humason, M. L. & Zwicky, F. 1947, *ApJ*, 105, 85
- Husfeld, D. 1987, in *IAU Colloq. 95: Second Conference on Faint Blue Stars*, ed. A. G. D. Philip, D. S. Hayes, & J. W. Liebert, 237–246
- Husfeld, D., Butler, K., Heber, U., & Drilling, J. S. 1989, *A&A*, 222, 150
- Iben, Jr., I. 1990, *ApJ*, 353, 215
- Iben, Jr., I., Kaler, J. B., Truran, J. W., & Renzini, A. 1983, *ApJ*, 264, 605
- Iben, Jr., I. & Livio, M. 1993, *PASP*, 105, 1373
- Iben, Jr., I. & Tutukov, A. V. 1986, *ApJ*, 311, 753
- Icke, V. 1988, *A&A*, 202, 177
- Icke, V., Preston, H. L., & Balick, B. 1989, *AJ*, 97, 462
- Jacoby, G., De Marco, O., Howell, S., & Kronberger, M. 2012, in *American Astronomical Society Meeting Abstracts*, Vol. 219, *American Astronomical Society Meeting Abstracts #219*, #418.02
- Jacoby, G. H., Kronberger, M., Patchick, D., et al. 2010, *PASA*, 27, 156
- Jacoby, G. H. & van de Steene, G. 1993, in *Bulletin of the American Astronomical Society*, Vol. 25, *American Astronomical Society Meeting Abstracts*, 1369
- Jacoby, G. H. & van de Steene, G. 1995, *AJ*, 110, 1285

- Jeffery, C. S. 2002, in *Astronomical Society of the Pacific Conference Series*, Vol. 279, *Exotic Stars as Challenges to Evolution*, ed. C. A. Tout & W. van Hamme, 53
- Jeffery, C. S., Drilling, J. S., Harrison, P. M., Heber, U., & Moehler, S. 1997, *A&A, Supplement*, 125, 501
- Jones, D., Boffin, H. M. J., Miszalski, B., et al. 2014, *A&A*, 562, A89
- Jones, D., Lloyd, M., Santander-García, M., et al. 2010, *MNRAS*, 408, 2312
- Kahn, F. D. & West, K. A. 1985, *MNRAS*, 212, 837
- Kaler, J. B. 1976, *ApJ Supplements*, 31, 517
- Karakas, A. I. 2010a, in *Principles and Perspectives in Cosmochemistry*, ed. A. Goswami & B. E. Reddy, 107
- Karakas, A. I. 2010b, *MNRAS*, 403, 1413
- Kerber, F., Mignani, R. P., Guglielmetti, F., & Wicenec, A. 2003, *A&A*, 408, 1029
- Kerber, F., Mignani, R. P., Smart, R. L., & Wicenec, A. 2008, *A&A*, 479, 155
- Kilkenny, D., Koen, C., O'Donoghue, D., & Stobie, R. S. 1997a, *MNRAS*, 285, 640
- Kilkenny, D., O'Donoghue, D., Koen, C., Stobie, R. S., & Chen, A. 1997b, *MNRAS*, 287, 867
- Kingsburgh, R. L. & Barlow, M. J. 1994, *MNRAS*, 271, 257
- Kleinman, S. J., Kepler, S. O., Koester, D., et al. 2013, *ApJ Supplements*, 204, 5
- Kohoutek, L. 1967, *Bulletin of the Astronomical Institutes of Czechoslovakia*, 18, 103
- Kohoutek, L. 2001, *A&A*, 378, 843
- Kohoutek, L. & Hekela, J. 1967, *Bulletin of the Astronomical Institutes of Czechoslovakia*, 18, 203
- Kohoutek, L. & Senkbeil, G. 1973, *Memoires of the Societe Royale des Sciences de Liege*, 5, 485
- Kondo, Y., Boggess, A., & Maran, S. P. 1989, *A&A Annual Review*, 27, 397
- Korb, K. B. & Nicholson, A. E. 2010, *Bayesian artificial intelligence* (CRC press)
- Kudritzki, R. P. 1976, *A&A*, 52, 11
- Kurucz, R. 1993, *ATLAS9 Stellar Atmosphere Programs and 2 km/s grid*. Kurucz CD-ROM No. 13. Cambridge, Mass.: Smithsonian Astrophysical Observatory, 1993., 13

- Kwitter, K. B., Congdon, C. W., Pasachoff, J. M., & Massey, P. 1989, *AJ*, 97, 1423
- Kwitter, K. B. & Henry, R. B. C. 2001, *ApJ*, 562, 804
- Kwok, S. 2004, *Nature*, 430, 985
- Kwok, S., Purton, C. R., & Fitzgerald, P. M. 1978, *ApJ Letters*, 219, L125
- Kwok, S., Zhang, Y., Koning, N., Huang, H.-H., & Churchwell, E. 2008, *ApJ Supplements*, 174, 426
- Lanz, T., Brown, T. M., Sweigart, A. V., Hubeny, I., & Landsman, W. B. 2004, *ApJ*, 602, 342
- Lanz, T. & Hubeny, I. 2003, *ApJ Supplements*, 146, 417
- Lanz, T. & Hubeny, I. 2007, *ApJ Supplements*, 169, 83
- Latour, M., Fontaine, G., Chayer, P., & Brassard, P. 2013, *ApJ*, 773, 84
- Latour, M., Fontaine, G., Green, E. M., Brassard, P., & Chayer, P. 2014, *ApJ*, 788, 65
- Lawlor, T. M. & MacDonald, J. 2001, in *Astronomical Society of the Pacific Conference Series*, Vol. 226, 12th European Workshop on White Dwarfs, ed. J. L. Provencal, H. L. Shipman, J. MacDonald, & S. Goodchild, 20
- Liebert, J., Tweedy, R. W., Napiwotzki, R., & Fulbright, M. S. 1995, *ApJ*, 441, 424
- Lopez, J. A., Meaburn, J., & Palmer, J. W. 1993, *ApJ Letters*, 415, L135
- Lutz, J., Fraser, O., McKeever, J., & Tugaga, D. 2010, *PASP*, 122, 524
- Lutz, J. H. 1977, *A&A*, 60, 93
- Lutz, T. E. & Kelker, D. H. 1973, *PASP*, 85, 573
- Luyten, W. J. & Miller, W. C. 1951, *ApJ*, 114, 488
- Maciel, W. J. & Koppen, J. 1994, *A&A*, 282, 436
- Mal'Kov, Y. F. 1997, *Astronomy Reports*, 41, 760
- Manchado, A., Guerrero, M. A., Stanghellini, L., & Serra-Ricart, M. 1996a, The IAC morphological catalog of northern Galactic planetary nebulae
- Manchado, A., Stanghellini, L., & Guerrero, M. A. 1996b, *ApJ Letters*, 466, L95
- Marigo, P. 2001, *A&A*, 370, 194
- Mastrodemos, N. & Morris, M. 1998, *ApJ*, 497, 303
- Mastrodemos, N. & Morris, M. 1999, *ApJ*, 523, 357

- Maxted, P. f. L., Heber, U., Marsh, T. R., & North, R. C. 2001, MNRAS, 326, 1391
- Mclaughlin, D. B. 1942, PASP, 54, 31
- Meaburn, J., López, J. A., Gutiérrez, L., et al. 2003, RMxAA, 39, 185
- Mellema, G. & Frank, A. 1995, MNRAS, 273, 401
- Méndez, R. H. 1978, MNRAS, 185, 647
- Méndez, R. H. 1989, in IAU Symposium, Vol. 131, Planetary Nebulae, ed. S. Torres-Peimbert, 261–272
- Mendez, R. H. 1991, in IAU Symposium, Vol. 145, Evolution of Stars: the Photospheric Abundance Connection, ed. G. Michaud & A. V. Tutukov, 375
- Mendez, R. H., Gathier, R., Simon, K. P., & Kwitter, K. B. 1988, A&A, 198, 287
- Mendez, R. H. & Niemelä, V. S. 1977, MNRAS, 178, 409
- Miranda, L. F., Gómez, Y., Anglada, G., & Torrelles, J. M. 2001a, Nature, 414, 284
- Miranda, L. F. & Solf, J. 1992, A&A, 260, 397
- Miranda, L. F., Torrelles, J. M., Guerrero, M. A., Vázquez, R., & Gómez, Y. 2001b, MNRAS, 321, 487
- Miszalski, B. 2012, in IAU Symposium, Vol. 283, IAU Symposium, 107–110
- Miszalski, B., Acker, A., Moffat, A. F. J., Parker, Q. A., & Udalski, A. 2009a, A&A, 496, 813
- Miszalski, B., Acker, A., Ochsenbein, F., & Parker, Q. A. 2012, in IAU Symposium, Vol. 283, IAU Symposium, 442–443
- Miszalski, B., Acker, A., Parker, Q. A., & Moffat, A. F. J. 2009b, A&A, 505, 249
- Miszalski, B., Corradi, R. L. M., Boffin, H. M. J., et al. 2011, MNRAS, 413, 1264
- Miszalski, B., Crowther, P. A., De Marco, O., et al. 2013, in Astronomical Society of the Pacific Conference Series, Vol. 469, 18th European White Dwarf Workshop., ed. Krzesiń, J. ski, G. Stachowski, P. Moskalik, & K. Bajan, 281
- Miszalski, B., Parker, Q. A., Acker, A., et al. 2008, MNRAS, 384, 525
- Mitchell, D. L., Pollacco, D., O’Brien, T. J., et al. 2007, MNRAS, 374, 1404
- Moe, M. & De Marco, O. 2006, ApJ, 650, 916
- Moehler, S., Richtler, T., de Boer, K. S., Dettmar, R. J., & Heber, U. 1990, A&A, Supplement, 86, 53

- Monteiro, H., Morisset, C., Gruenwald, R., & Viegas, S. M. 2000, *ApJ*, 537, 853
- Morales-Rueda, L., Maxted, P. F. L., Marsh, T. R., North, R. C., & Heber, U. 2003, *MNRAS*, 338, 752
- Morris, M. 1987, *PASP*, 99, 1115
- Muthu, C. 2001, *Bulletin of the Astronomical Society of India*, 29, 381
- Muthu, C. & Anandarao, B. G. 2003, *AJ*, 126, 2963
- Nakanishi, H. & Sofue, Y. 2003, *PASJ*, 55, 191
- Napiwotzki, R. 1997, *A&A*, 322, 256
- Napiwotzki, R. 1999, *A&A*, 350, 101
- Napiwotzki, R. 2001, *A&A*, 367, 973
- Napiwotzki, R. 2008, in *Astronomical Society of the Pacific Conference Series*, Vol. 392, *Hot Subdwarf Stars and Related Objects*, ed. U. Heber, C. S. Jeffery, & R. Napiwotzki, 139
- Napiwotzki, R., Karl, C. A., Lisker, T., et al. 2004, *Astrophysics & Space Science*, 291, 321
- Napiwotzki, R. & Schoenberner, D. 1995, *A&A*, 301, 545
- O'Connor, J. A., Redman, M. P., Holloway, A. J., et al. 2000, *ApJ*, 531, 336
- Olguín, L., Vázquez, R., Contreras, M. E., & Jiménez, M. Y. 2011, in *Revista Mexicana de Astronomía y Astrofísica*, vol. 27, Vol. 40, *Revista Mexicana de Astronomía y Astrofísica Conference Series*, 193–193
- Oreiro, R., Østensen, R. H., Green, E. M., & Geier, S. 2009, *A&A*, 496, 827
- Oreiro, R., Rodríguez-López, C., Solano, E., et al. 2011, *A&A*, 530, A2
- Østensen, R. H. 2006, *Baltic Astronomy*, 15, 85
- Østensen, R. H., Silvotti, R., Charpinet, S., et al. 2011, *MNRAS*, 414, 2860
- Østensen, R. H., Silvotti, R., Charpinet, S., et al. 2010, *MNRAS*, 409, 1470
- Osterbrock, D. E. 1989, *Astrophysics of gaseous nebulae and active galactic nuclei*
- Parker, Q. A., Acker, A., Frew, D. J., et al. 2006, *MNRAS*, 373, 79
- Parker, Q. A., Phillipps, S., Pierce, M. J., et al. 2005, *MNRAS*, 362, 689
- Parthasarathy, M., Garcia-Lario, P., de Martino, D., et al. 1995, *A&A*, 300, L25
- Payne, C. H. 1930, *Harvard College Observatory Bulletin*, 878, 1

- Peña, M., Rechy-García, J. S., & García-Rojas, J. 2013, *RMxAA*, 49, 87
- Peimbert, M. 1978, in *IAU Symposium*, Vol. 76, *Planetary Nebulae*, ed. Y. Terzian, 215–223
- Peimbert, M. 1990, *Reports on Progress in Physics*, 53, 1559
- Peimbert, M. & Costero, R. 1969, *Boletín de los Observatorios Tonantzintla y Tacubaya*, 5, 3
- Peimbert, M. & Torres-Peimbert, S. 1983, in *IAU Symposium*, Vol. 103, *Planetary Nebulae*, ed. D. R. Flower, 233–241
- Pereira, C. B., Baella, N. O., Daflon, S., & Miranda, L. F. 2010, *A&A*, 509, A13
- Pereira, C.-B. & Miranda, L.-F. 2007, *A&A*, 467, 1249
- Perek, L. & Kohoutek, L. 1967, *Catalogue of galactic planetary nebulae*
- Phillips, J. P. 2004, *MNRAS*, 353, 589
- Phillips, J. P. 2005, *MNRAS*, 357, 619
- Pollacco, D. L. & Bell, S. A. 1997, *MNRAS*, 284, 32
- Pottasch, S. R., ed. 1984, *Astrophysics and Space Science Library*, Vol. 107, *Planetary nebulae - A study of late stages of stellar evolution*
- Pritchett, C. 1984, *A&A*, 139, 230
- Purgathofer, A. & Schnell, A. 1983, *Information Bulletin on Variable Stars*, 2362, 1
- Quireza, C., Rocha-Pinto, H. J., & Maciel, W. J. 2007, *A&A*, 475, 217
- Ramos-Larios, G., Guerrero, M. A., Vázquez, R., & Phillips, J. P. 2012, *MNRAS*, 420, 1977
- Ramos-Larios, G. & Phillips, J. P. 2009, *MNRAS*, 400, 575
- Ratag, M. A., Pottasch, S. R., Dennefeld, M., & Menzies, J. 1997, *A&A, Supplement*, 126, 297
- Rauch, T. 1999, *A&A, Supplement*, 135, 487
- Rauch, T., Dreizler, S., & Wolff, B. 1998, *A&A*, 338, 651
- Rauch, T., Heber, U., Hunger, K., Werner, K., & Neckel, T. 1991, *A&A*, 241, 457
- Rauch, T., Reiff, E., Werner, K., et al. 2006, in *Astronomical Society of the Pacific Conference Series*, Vol. 348, *Astrophysics in the Far Ultraviolet: Five Years of Discovery with FUSE*, ed. G. Sonneborn, H. W. Moos, & B.-G. Andersson, 194
- Rauch, T., Werner, K., Bohlin, R., & Kruk, J. W. 2013, *A&A*, 560, A106

- Rauch, T., Werner, K., Ziegler, M., Kruk, J. W., & Oliveira, C. M. 2007, in *Asymmetrical Planetary Nebulae IV*, 18
- Reimers, D. 1975, *Circumstellar envelopes and mass loss of red giant stars*, ed. B. Baschek, W. H. Kegel, & G. Traving, 229–256
- Reindl, N., Rauch, T., Parthasarathy, M., et al. 2014, *A&A*, 565, A40
- Ressler, M. E., Cohen, M., Wachter, S., et al. 2010, *AJ*, 140, 1882
- Reyes-Ruiz, M. & López, J. A. 1999, *ApJ*, 524, 952
- Rijkhorst, E.-J., Mellema, G., & Icke, V. 2005, *A&A*, 444, 849
- Ritter, H. & Kolb, U. 2003, *A&A*, 404, 301
- Rodríguez-López, C., Moya, A., Garrido, R., et al. 2010, *MNRAS*, 402, 295
- Rodríguez-López, C., Ulla, A., & Garrido, R. 2007, *MNRAS*, 379, 1123
- Roeser, S., Demleitner, M., & Schilbach, E. 2010, *AJ*, 139, 2440
- Rozyczka, M. & Franco, J. 1996, *ApJ Letters*, 469, L127
- Sabin, L., Parker, Q. A., Corradi, R. L. M., et al. 2014, *MNRAS*, 443, 3388
- Sabin, L., Zijlstra, A. A., & Greaves, J. S. 2007, *MNRAS*, 376, 378
- Saffer, R. A., Bergeron, P., Koester, D., & Liebert, J. 1994, *ApJ*, 432, 351
- Sahai, R. 2000, *ApJ Letters*, 537, L43
- Sahai, R., Dayal, A., Watson, A. M., et al. 1999, *AJ*, 118, 468
- Sahai, R. & Trauger, J. T. 1998, *AJ*, 116, 1357
- Saio, H. & Jeffery, C. S. 2000, *MNRAS*, 313, 671
- Sargent, W. L. W. & Searle, L. 1968, *ApJ*, 152, 443
- Schoenberner, D. 1983, *ApJ*, 272, 708
- Schröder, K.-P. & Cuntz, M. 2005, *ApJ Letters*, 630, L73
- Schwarz, H. E. 1992, *A&A*, 264, L1
- Seares, F. H. & Hubble, E. P. 1920, *ApJ*, 52, 8
- Seaton, M. J. 1979, *MNRAS*, 187, 73P
- Seaton, M. J. 1980, *QJRAS*, 21, 229

- Serenelli, A. & Weiss, A. 2005, *A&A*, 442, 1041
- Shaw, R. A. & Dufour, R. J. 1995, *PASP*, 107, 896
- Shimanskii, V. V., Borisov, N. V., Sakhbullin, N. A., & Sheveleva, D. V. 2008, *Astronomy Reports*, 52, 479
- Silvotti, R., Solheim, J.-E., Gonzalez Perez, J. M., et al. 2000, *A&A*, 359, 1068
- Silvotti, R., Solheim, J.-E., Heber, U., et al. 2001, in *Astronomical Society of the Pacific Conference Series*, Vol. 226, 12th European Workshop on White Dwarfs, ed. J. L. Provencal, H. L. Shipman, J. MacDonald, & S. Goodchild, 177
- Soker, N. 1997, *ApJ Supplements*, 112, 487
- Soker, N. & Livio, M. 1994, *ApJ*, 421, 219
- Soker, N., Rappaport, S., & Harpaz, A. 1998, *ApJ*, 496, 842
- Sota, A., Maíz Apellániz, J., Morrell, N. I., et al. 2014a, *ApJ Supplements*, 211, 10
- Sota, A., Maíz Apellániz, J., Walborn, N. R., et al. 2014b, *VizieR Online Data Catalog*, 3274, 0
- Sota, A., Maíz Apellániz, J., Walborn, N. R., et al. 2011, *ApJ Supplements*, 193, 24
- Stanghellini, L., Shaw, R. A., & Villaver, E. 2008, *ApJ*, 689, 194
- Stanghellini, L., Villaver, E., Manchado, A., & Guerrero, M. A. 2002, *ApJ*, 576, 285
- Stark, M. A. & Wade, R. A. 2003, *AJ*, 126, 1455
- Stasińska, G., Gorny, S. K., & Tylenda, R. 1997, *A&A*, 327, 736
- Steffen, W., Koning, N., Esquivel, A., et al. 2013, *MNRAS*, 436, 470
- Steffen, W., Koning, N., Wenger, S., Morisset, C., & Magnor, M. 2011, *IEEE Transactions on Visualization and Computer Graphics*, Volume 17, Issue 4, p.454-465, 17, 454
- Stroeer, A., Heber, U., Lisker, T., et al. 2007, *A&A*, 462, 269
- Suárez, O., Gómez, J. F., Bendjoya, P., et al. 2015, *ApJ*, 806, 105
- Taranova, O. G. & Shenavrin, V. I. 2007, *Astronomy Letters*, 33, 584
- Taylor, M. B., Boch, T., & Taylor, J. 2015, *Astronomy and Computing*, 11, 81
- Toalá, J. A., Guerrero, M. A., Todt, H., et al. 2015, *ApJ*, 799, 67
- Tocknell, J., De Marco, O., & Wardle, M. 2014, *MNRAS*, 439, 2014

- Tody, D. 1986, in Society of Photo-Optical Instrumentation Engineers (SPIE) Conference Series, Vol. 627, Instrumentation in astronomy VI, ed. D. L. Crawford, 733
- Tody, D. 1993, in Astronomical Society of the Pacific Conference Series, Vol. 52, Astronomical Data Analysis Software and Systems II, ed. R. J. Hanisch, R. J. V. Brissenden, & J. Barnes, 173
- Traulsen, I., Hoffmann, A. I. D., Rauch, T., et al. 2005, in Astronomical Society of the Pacific Conference Series, Vol. 334, 14th European Workshop on White Dwarfs, ed. D. Koester & S. Moehler, 325
- Tsessevich, V. P. 1977, Information Bulletin on Variable Stars, 1320, 1
- Tylenda, R. & Gorny, S. K. 1993, Acta Astronomica, 43, 389
- Tylenda, R., Stasińska, G., Acker, A., & Stenholm, B. 1994, A&A, Supplement, 106, 559
- van de Steene, G. C. & Zijlstra, A. A. 1994, A&A, Supplement, 108, 485
- van der Hucht, K. A. 2001, New Astronomy Reviews, 45, 135
- van Leeuwen, F. 2007, A&A, 474, 653
- Van Winckel, H., Jorissen, A., Exter, K., et al. 2014, A&A, 563, L10
- Vapnik, V. 1995, The Nature of Statistical Learning Theory (Springer New York)
- Vázquez, R., López, J. A., Miranda, L. F., Torrelles, J. M., & Meaburn, J. 1999, MNRAS, 308, 939
- Vázquez, R., Miranda, L. F., Olguín, L., et al. 2008, A&A, 481, 107
- Vázquez, R., Miranda, L. F., Torrelles, J. M., et al. 2002, ApJ, 576, 860
- Velázquez, P. F., Raga, A. C., Riera, A., et al. 2012, MNRAS, 419, 3529
- Vos, J., Østensen, R. H., Degroote, P., et al. 2012, A&A, 548, A6
- Walton, N. A., Walsh, J. R., & Pottasch, S. R. 1993, A&A, 275, 256
- Wareing, C. J., Zijlstra, A. A., & O'Brien, T. J. 2007, MNRAS, 382, 1233
- Wawrzyn, A. C., Barman, T. S., Günther, H. M., Hauschildt, P. H., & Exter, K. M. 2009, A&A, 505, 227
- Webbink, R. F. 1984, ApJ, 277, 355
- Weidmann, W. A. & Gamen, R. 2011, A&A, 526, A6

- Werner, K. 2010, in *Recent Advances in Spectroscopy Theoretical, Astrophysical and Experimental Perspectives*, ed. R. K. Chaudhuri, M. V. Mekkaden, A. V. Raveendran, & A. Satya Narayanan, 199–209
- Werner, K., Deetjen, J. L., Dreizler, S., et al. 2003, in *Astronomical Society of the Pacific Conference Series, Vol. 288, Stellar Atmosphere Modeling*, ed. I. Hubeny, D. Mihalas, & K. Werner, 31
- Werner, K. & Dreizler, S. 1999, *Journal of Computational and Applied Mathematics*, 109, 65
- Werner, K. & Herwig, F. 2006, *PASP*, 118, 183
- Woudt, P. A., Kilkenny, D., Zietsman, E., et al. 2006, *MNRAS*, 371, 1497
- Wright, E. L., Eisenhardt, P. R. M., Mainzer, A. K., et al. 2010, *AJ*, 140, 1868
- Ziegler, M., Rauch, T., Werner, K., Köppen, J., & Kruk, J. W. 2012, *A&A*, 548, A109